Advanced Diffusion MRI for Microstructure Imaging: Theoretical Developments

Andrada Savickas (Ianuş)

A dissertation submitted in partial fulfillment
of the requirements for the degree of
Doctor of Philosophy
of
University College London.

Department of Medical Physics and Bioengineering,
Centre for Medical Image Computing
University College London
May 10, 2016

I, Andrada Savickas (Ianuş), confirm that the work presented in this thesis is my own. Where information has been derived from other sources, I confirm that this has been indicated in the work.

Abstract

An accurate characterization of tissue features at microscopic level is essential for understanding the brain structure or staging a large variety of diseases, such as Alzheimer's, multiple sclerosis or cancer. The aim of microstructure imaging is to provide information related to cellular structure from non-invasive imaging modalities, such as Magnetic Resonance Imaging (MRI). This can be achieved by developing accurate tissue models and relating them to imaging data. Diffusion weighted MRI (DW-MRI) measures the displacement of the water molecules inside the tissue which is sensitive to the configuration of cellular membranes, therefore it provides relevant information for characterizing tissue microstructure.

This PhD thesis presents my work on developing novel DW-MRI sequences and tissue models which provide improved sensitivity to cellular features such as pore size and shape. To model the DW-MRI signal, the tissue is regarded as a porous medium with cells described as fluid-filled pores separated by impermeable membranes. The first part of this thesis is concentrated on improving the estimation of intrinsic diffusivity and pore size. Specifically, it analyses a promising class of diffusion sequences, namely oscillating gradients, which measure diffusion on a short time scale and give access to small structures, such as cell nuclei. Additionally, it emphasises the benefits of low-frequency oscillating waveforms over the standard acquisition for estimating axon diameter.

The second part of my project focuses on estimating complex tissue features such as pore elongation and size distribution, and it demonstrates that these features are intrinsically linked and need to be explicitly modelled for accurate results. Moreover, it shows that pulse sequences with varying gradient orientation, such as double diffusion encoding, are able to separate these effects more effectively than standard sequences. The most recent study combines the benefits of both sequences in an innovative acquisition with double oscillating gradients. This supports estimates of cell size distribution and eccentricity for a wider range of substrates.

Acknowledgements

The past four years as a PhD student at UCL have been a fantastic experience, and there are many people who made this possible.

First, I would like to express my sincere gratitude to my primary supervisor Prof. Daniel Alexander for his constant support, invaluable advice and scientific skills that made a great contribution to everything I have learnt during the past four years, as well as for his help with this thesis, all the publications and the EPSRC fellowship application. I am grateful to my supervisor Dr. Ivana Drobnjak for a close collaboration on all the projects, a direct engagement in designing MISST as well as detailed feedback on this thesis and a very useful mock fellowship interview. I would also like to thank my supervisor Prof. David Hawkes for bridging the project with real world clinical applications and for his invaluable feedback during my first year and transfer vivas.

I am grateful to my examiners, Dr. Simon Walker-Samuel and Dr. Markus Nilsson, for a vivid scientific discussion of my work as well as valuable comments for this thesis and future research in diffusion MRI.

Many thanks to Dr. Gary Zhang for insightful conversations on mathematical modelling, diffusion MRI and data analysis, as well as for organizing many group dinners revealing the flavours of sichuan cuisine. I am also thankful to Dr. Bernard Siow for sharing his knowledge of MR physics and various practical aspects of imaging.

I would like to thank Dr. Eleftheria Panagiotaki for her help with implementing various diffusion models and for collaborating on the extension and optimisation of VERDICT. During the past year I had a fruitful collaboration with Dr. Noam Shemesh which lead to one chapter of this thesis.

I am also indebted to Dr. Matt Hall, Dr. Aurobrata Gosh, Răzvan Marinescu, Joseph Jacobs, Mark Graham, Maira Tariq and Lebina Kakkar for proofreading chapters of this thesis.

My experience at UCL wouldn't have been so delightful without my friends from the ’MIG foodies’ group: Lebina Kakkar, Maira Tariq and Jiaying Zhang. We had many lunch and coffee breaks together that would lift my mood on a rainy day. Moreover, I would like to thank the entire MIG group for being really nice and supportive with every occasion - the best colleagues I could have hoped for!

Many thanks to my friends in London, that definitely improved the entire experience of being a PhD student.

Very special thanks to my husband Vytautas Savickas. Thank you for understanding what it means to undertake a PhD, for being next to me at every step along the way, for making delicious coffee and breakfast in the morning, and most importantly for loving me.

I am very grateful to my parents, Mariana and Gelu Ianuş, as well as my grandparents and my entire family. It is the love, care and education you provided that made me who I am today.

I’m not ending the acknowledgements with the traditional ’last, but not least’, because there are many other people who contributed to my education and taught me many of the skills needed to perform this research.

Related publications

Journal publications and book chapters

- Ianuş, A., Drobnjak, I., Alexander, D.C. Model-based estimation of microscopic anisotropy using diffusion MRI. *NMR in Biomedicine, accepted.*
- Drobnjak, I., Zhang, H., Ianuş, A., Kaden, E., Alexander, D.C. PGSE, OGSE, and sensitivity to axon diameter in diffusion MRI: Insight from a simulation study. *Magnetic Resonance in Medicine, Early View*
- Ianuş, A., Drobnjak, I., Alexander, D.C. Model-based estimation of microscopic anisotropy in macroscopically isotropic substrates using diffusion MRI *Lecture Notes in Computer Science.* IPMI 2015.
- Ianuş, A., Siow, B., Drobnjak, I., Zhang, H., Alexander, D. C. Gaussian phase distribution approximations for oscillating gradient spin echo diffusion MRI. *Journal of Magnetic Resonance (2013) 227:25-34*
- Siow, B., Drobnjak, I., Ianuş, A., Christie, I. N., Lythgoe, M. F., Alexander, D. C. Axon radius estimation with Oscillating Gradient Spin Echo (OGSE) Diffusion MRI. *Diffusion Fundamentals (2013) 18:1-6*

Conference publications

- Ianuş, A., Drobnjak, I., Shemesh, N., Alexander, D.C. Metrics of microscopic anisotropy: a comparison study. *International Conference on Magnetic Resonance Microscopy (2015)* - oral presentation
- Drobnjak, I., Zhang, H., Ianuş, A., Kaden, E., Alexander, D.C. Why should axon diameter mapping use low frequency OGSE? Insight from simulation. *23rd Meeting of the International Society for Magnetic Resonance in Medicine (2015)* - poster pitch

- Ianuş, A., Drobnjak, I., Alexander, D.C. Model-based estimation of microstructure parameters from diffusion MRI data in a substrate with microscopic anisotropy and a distribution of pore sizes. *23rd Meeting of the International Society for Magnetic Resonance in Medicine (2015)*
- Shemesh, N., Ianuş, A., Alexander, D.C., Drobnjak, I. Double Oscillating Diffusion Encoding (DODE) augments microscopic anisotropy contrast. *23rd Meeting of the Proceedings of the International Society for Magnetic Resonance in Medicine (2015)* - oral presentation
- Drobnjak, I., Lyon, J., Zhang, H., Ianuş, A., Kaden, E., Alexander, D.C., Dyrby, T. Low frequency OGSE improves axon diameter imaging in monkey corpus callosum over simple PGSE method. *23rd Meeting of the International Society for Magnetic Resonance in Medicine (2015)*
- Panagiotaki, E., Ianuş, A., Jhonston, E., Chan, R.W., Stevens, N., Atkinson, D., Punwani, S., Hawkes, D., Alexander, D.C. Optimised VERDICT MRI protocol for prostate cancer characterisation. *23rd Meeting of the the International Society for Magnetic Resonance in Medicine (2015)*
- Ianuş, A., Siow, B., Drobnjak, I., Zhang, H., Alexander, D. C. (2012). Gaussian Phase Distribution Approximations of the Square Wave Oscillating Gradient Spin-Echo (SWOGSE) Diffusion Signal. *20th Meeting of the the International Society for Magnetic Resonance in Medicine (2012)*
- Siow, B., Drobnjak, I., Ianuş, A., Christie, I. N., Alexander, D. A. (2012). Pore Size Estimation with Oscillating Gradient Spin Echo (OGSE) Diffusion NMR. *11th International Bologna Conference on Magnetic Resonance in Porous Media.*
- Siow, B., Ianuş, A., Drobnjak, I., Christie, I. N., Lythgoe, M. F., Alexander, D. C. Optimised oscillating gradient diffusion MRI for the estimation of axon radius in an ex vivo rat brain. *20th Meeting of the International Society for Magnetic Resonance in Medicine (2012)*

In preparation:

- Ianuş, A., Shemesh, N., Drobnjak, I., Alexander, D.C. Double-Oscillating-Diffusion-Encoding (DODE) augments sensitivity towards microscopic anisotropy

Research software:

- MISST - Microstructure Imaging Sequence Simulation Toolbox. An open source software which computes the diffusion signal for any user defined diffusion gradient and a variety of compartment tissue models. Available at `https://www.nitrc.org/`

Academic awards:

- EPSRC Doctoral Prize research fellowship, starting in January 2015 for 2 years
- Finalist in the London Hopper research spotlight competition
- Prize for engagement and enthusiasm in the Medical Physics PhD Showcase, UCL

Statement of intellectual contribution

The material presented in this thesis is entirely my own work expect in the following chapters:

- Chapter 4 presents collaborative work and the contributions are divided as follows:

  Section 4.1 was carried out by Ivana Drobnjak and myself, with various inputs from the other co-authors. We had equal contributions in developing the concept of measuring signal sensitivity to axon diameter and designing the experiments presented in this thesis. The simulations are based on the MISST software, which is one of my contributions described in chapter 7, and were performed by Ivana Drobnjak.

  Section 4.2 was carried out by Lebina Kakkar and myself, with various inputs from the other co-authors. I contributed to the design of the diffusion protocol, as well as to the data analysis which uses the theoretical framework I have developed. Lebina Kakkar carried out the acquisition and analysis of the experimental data.

- Chapter 6 presents work that was performed in collaboration with Noam Shemesh and Ivana Drobnjak. We contributed equally to the design of the experiments, and I carried out all the simulations presented in this thesis.

- Chapter 7 presents the software MISST (Microstructure Imaging Sequence Simulation Toolbox), which I developed based on previous work by Daniel Alexander and Ivana Drobnjak. My contribution is the extension of the signal model for more geometries (parallel planes, cuboids, finite cylinders), as well as the entire modular layout of the software. I have also written all the example files, tutorials and documentation for MISST.

Contents

5 Model-based estimation of microscopic anisotropy 117

List of Figures

List of Tables

Chapter 1

Introduction

Studying tissue anatomy at the microscopic scale is essential for understanding brain structure or for diagnosing and monitoring diseases, such as Alzheimer's, multiple sclerosis or various tumours. Standard histology, which relies on different types of staining, is performed on tissue samples and is an invasive probe of microstructure. For instance, the histological analysis of brain structure is usually performed in post mortem specimens, which do not retain all characteristics of live tissue. In case of various pathologies, such as tumours, tissue biopsies are analysed under microscope to provide histological information. This procedure is invasive, provides only local details, and poses risks of infections and other complications. Microstructure imaging aims to use non-invasive imaging modalities to provide information similar to histological techniques which reveal the cellular structure.

Non-invasive imaging techniques, such as computed tomography (CT), positron emission tomography (PET) or magnetic resonance imaging (MRI) aim to probe tissue structure and function, in vivo. MRI is one of the most commonly used imaging modalities due to the large variety of contrast mechanisms, which can be tuned for various applications. Depending on the data acquisition, MRI can provide high resolution images of macroscopic tissue structure (T1 or T2 weighted images), measure blood flow and blood vessel anatomy (perfusion MRI, venography MRI), provide functional information about tissue activation (functional MRI) or estimate the drug uptake in the tissue (dynamic contrast enhanced MRI). By sensitising the MR signal to the diffusion of water molecules, the obtained contrast can also reflect tissue microstructure.

Diffusion weighted MRI (DW-MRI) probes molecular displacement, typically of water molecules which are abundant in biological tissue, and provides structural information at the microscopic level. In a homogeneous environment, particles can freely diffuse in all directions. In the tissue, cellular membranes restrict the molecular diffusion and affect the measured signal, therefore it is possible to extract microstructural information (e.g. cell size, shape, volume fraction, etc) from DW-MRI data. This can be achieved by developing realistic models of tissue architecture and relating them to the acquired signal. The paradigm of this framework is illustrated in Figure 1.1. Imaging tissue microstructure is an active research topic in DW-MRI with potential applications to cancer imaging to discern differences in tumour microstructure [2, 3, 4], white matter imaging to map axon diameter [5, 6, 7, 8, 9, 10] in the presence of orientation dispersion [11, 12] and undulation [13], grey matter imaging to discriminate cytoarchitectures [14], and muscle imaging to assess the degree of injury [15].

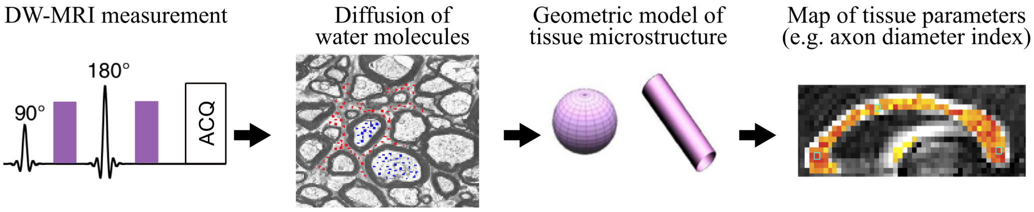

Figure 1.1: Schematic representation of the microstructure imaging paradigm using DW-MRI. Axon diameter index map adapted from [9]

The standard way of acquiring diffusion MRI data is single diffusion encoding (SDE), achieved by applying a pair of magnetic field gradients during the image acquisition process [16]. Most of current microstructure imaging techniques use a collection of SDE sequences. However, such an acquisition is sensitive only to a limited range of pore sizes and cannot characterize more complex tissue configurations which feature anisotropy at the sub-voxel scale, as in grey matter or various tumours.

Moreover, current microstructure imaging techniques use tissue models that are not specific enough to represent these complex substrates. For instance, white matter models assume diffusion inside infinite cylinders, while cancer models assume spherical restriction. Therefore, these techniques do not allow a simultaneous estimation of pore size and eccentricity which is important for accurate tissue characterization at the interface between white and grey matter or in cancer tumours.

1.1 Problem statement

The research question that motivates this work is identifying the capabilities of advanced diffusion MR sequences to inform on cellular architecture. The overall goal of this thesis is to develop microstructure imaging techniques that use advanced sequences and more complex tissue models in order to improve the estimation of pore size and shape.

Replacing the standard DW-MRI acquisition with more advanced sequences increases sensitivity to microstructural features. Oscillating diffusion encoding (ODE) probes diffusion on a shorter time scale and improves access to smaller structures, while double diffusion encoding (DDE), which varies the gradient orientation in one measurement, improves sensitivity to pore anisotropy at the microscopic scale. We adapt these sequences for microstructure imaging techniques which can provide biomarkers related to intrinsic tissue properties such as cellular size distribution, shape and volume fraction. This requires an accurate mathematical representation of the tissue architecture that captures its geometric complexity. Moreover the signal model linking the diffusion data and tissue model should evaluate quickly enough to allow model fitting in every voxel of an image volume to obtain parameter maps.

1.2 Project aims

The specific aims of this thesis are the following:

- adapt ODE sequences for microstructure imaging techniques and investigate their sensitivity to axon diameter.
- develop a tissue model and acquisition protocol which can be used to estimate pore size and shape.
- combine the benefits of diffusion gradients with oscillating waveform and varying orientation in one acquisition.

1.3 Contributions

A detailed description of the contributions I made towards solving these research questions is presented below:

- An analytical signal model of restricted diffusion for ODE with square and trapezoidal oscillating gradient waveforms, as well as sinusoidal gradients with arbitrary phase and frequency, using the Gaussian Phase Distribution (GPD) approximation (Ianus et al, JMR 2013).
- Analysis and optimal design of sinusoidal, square and trapezoidal waveforms for temporal diffusion spectroscopy which uses oscillating waveforms to measure the restricted diffusion spectrum (Ianus et al, JMR 2013).
- A sensitivity analysis of ODE sequences with respect to pore diameter for different configurations of cylindrical pores (Drobnjak et al, MRM 2015).
- An extension of the GPD approximation for DDE and DODE sequences for restricted diffusion (Ianus et al, IPMI 2015).
- A model-based framework for estimating pore size and eccentricity in complex substrates which feature a distribution of pore sizes and both microscopic and macroscopic anisotropy (Ianus et al, IPMI 2015, NMRBiomed *under review*).
- An analysis of the ability of current sequences (SDE and DDE) to recover micrstructural features such as pore size distribution and eccentricity (Ianus et al, IPMI 2015, NMRBiomed *under review*).
- A new class of diffusion encoding sequences, which combines the benefits of oscillating gradients and varying gradient orientation, namely double oscillating diffusion gradients (DODE) (Shemesh et al, ISMRM 2015).
- A comparison between two model-free metrics of microscopic anisotropy (Ianus et al, ICMRM 2015).
- As a tool to answer these research questions, I have developed MISST (Microstructure Imaging Sequence Simulation Toolbox) - a diffusion MRI simulator for non-standard acquisition sequences and a large variety of tissue models.

1.4 Report structure

The thesis is organized as follows. Chapter 2 presents the background information necessary to understand this work. It begins with a description of cellular architecture in brain and cancer tissue, which is of interest for microstructure imaging. Then it introduces the NMR phenomenon, as well as signal generation, detection and localization which are the basis for MRI. Further, it presents the theoretical framework of diffusion MRI and details various modelling approaches used in the literature. Chapter 3 describes my theoretical work on oscillating diffusion gradients. Chapter 4 presents two collaboration studies which analyse the sensitivity of sequences with respect to pore size and experimentally validate oscillating gradients, respectively. Chapter 5 discusses my work on a model-based approach for estimating pore size and eccentricity in complex substrates, and Chapter 6 is focused on the novel double oscillating diffusion sequences we have proposed. Chapter 7 presents MISST a research software to simulate diffusion signal in restricted environments. Chapter 8 provides a summary of the work presented in this thesis and future research.

Chapter 2

Background

This chapter provides the necessary information to understand the principles of diffusion MRI and discusses previous studies and state-of-the-art microstructure imaging techniques.

The first section discusses the histological properties of brain and cancer tissue which we aim to characterize and provides an overview of currently available imaging techniques. The second section presents the basic theory of MRI, including the nuclear magnetic resonance phenomenon, signal generation, detection and spatial localization. The following section discusses in detail diffusion weighted MRI, which is the modality of interest for this research. First, we introduce the basis of diffusion contrast, the standard way of acquiring such data, as well as the signal model in the case of free diffusion. Then we consider diffusion in restricted environments and present various signal models. As this work is focused on developing advanced diffusion acquisition, we provide an overview of the non-standard diffusion sequences developed so far and their applications. The last part of this chapter presents current applications of microstructure imaging technique for brain and cancer imaging.

2.1 Imaging tissue microstructure

Microstructure imaging uses non-invasive imaging techniques in order to extract information about the tissue structure and function at the micron level. This is possible because features of interest (e.g. cell size, shape, volume fraction, permeability, perfusion, etc) affect the measured data from various imaging modalities such as computed tomography (CT) [17, 18], positron emission tomography (PET) [19, 20] or magnetic resonance imaging (MRI) [21, 22, 23]. By using mathematical models which describe the effect of various tissue properties on the acquired signal and fitting them to the data, it is possible to infer microscopic features from images that have a much lower resolution (usually at the millimetre scale). In order to obtain meaningful results, the mathematical modelling of the acquired signal should provide an accurate representation of the underling tissue. For example, in DW-MRI methods that account for restricted diffusion in the tissue, the geometric model should resemble the cellular architecture [23], or in PET techniques that consider multiple signal compartments, they should reflect the kinetics of the tracer in the tissue [24] in order to estimate parameters such as permeability. Thus, a good understanding of the structure and function of the tissue is required in order to develop accurate imaging methods.

In the rest of this section we discuss structural and functional features of brain and cancer tissue, two applications of interest for the microstructure imaging techniques we are developing. Further we present an overview of current imaging techniques, both invasive and non-invasive, that are commonly used for brain and cancer imaging.

2.1.1 Brain tissue

Cells in the brain can be classified according to their structure and function in two major types: neurons and glia. Neurons are the main functional units of the brain that enable information transfer and complex computational functions, while glial cell provide the necessary support for the nervous system [25]. Between the brain and the skull there are three layers of membranes, called meninges, which have the role to protect the brain from external damage and are filled with cerebro-spinal fluid (CSF). Investigating brain slices shows that neural tissue is not uniform, but has some darker areas (grey matter) and some paler areas (white matter) [25]. Grey matter is mainly formed by neuron cell bodies which are the information processing centres of the brain, and are grouped according to structure and function in larger areas called nuclei. White matter mostly consists of axons, an extension of neurons that facilitates communication between different regions of the brain. Axons that connect the same regions tend to bundle together and form tracts. Figure 2.1 illustrates the main features of brain anatomy [26, 27], while Figure 2.2 presents a schematic diagram of a neuron [28].

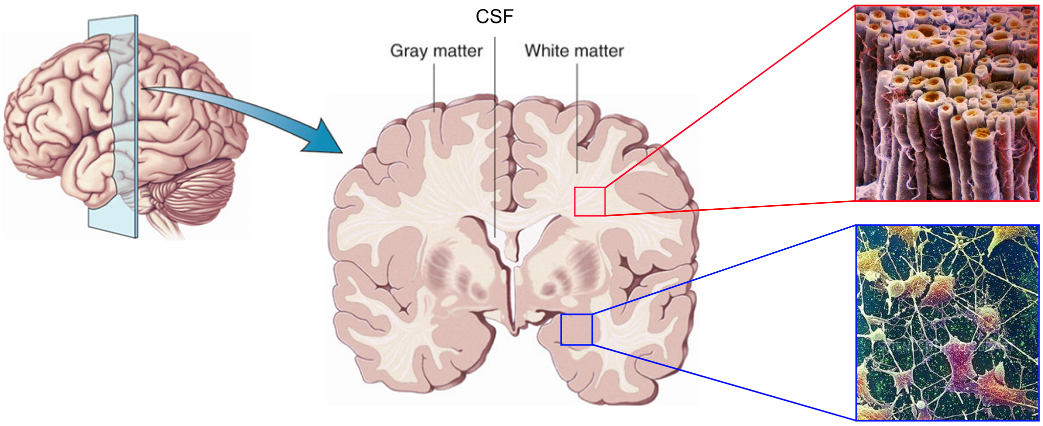

Figure 2.1: Illustration of brain anatomy in the coronal plane [27] showing white matter, grey matter and CSF. The structure of white and grey matter is illustrated using scanning electron microscope images [26].

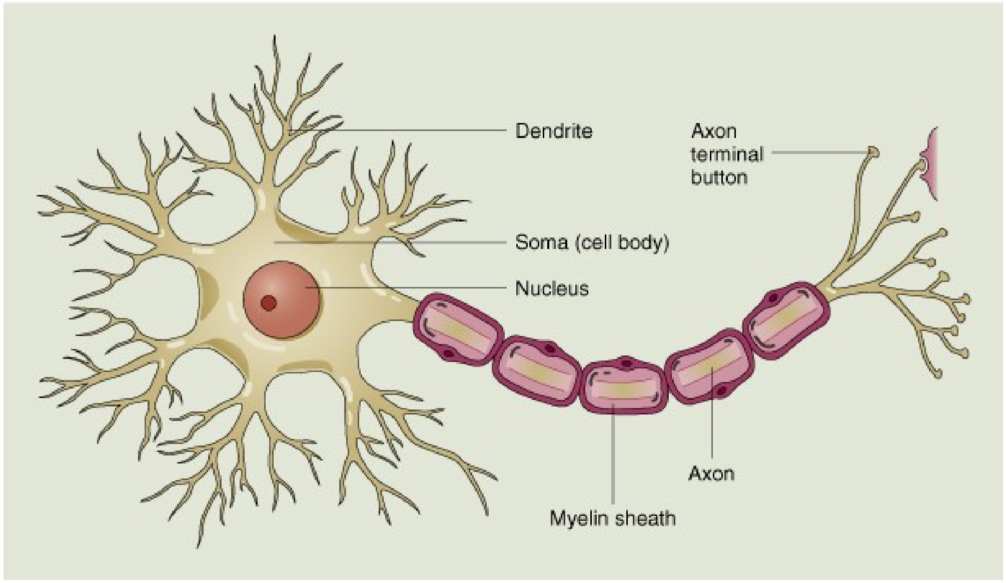

Figure 2.2: Schematic diagram of a neuron. The cell body features short, branched extensions (dendrites) which allow communication with nearby neurons and a long projection (axon) which facilitates communication over longer distances. Axons are usually covered in myelin sheaths which improve the conduction speed of electric impulses [28].

Grey matter

Grey matter contains mostly neuronal cell bodies, unmyelinated axons, glial cells and blood capillaries and serves to process information in the brain. As illustrated in Figure 2.1, the majority of grey matter is located at the surface of the brain where it forms the cerebral cortex, a sheet-like structure with thickness varying between 2 and 5 mm [29]. Islands of grey matter can also be found inside the brain in regions such as the thalamus or basal ganglia.

The cerebral cortex consists of many different types of neurons, which from the standpoint of cytology can be grouped in two main classes: pyramidal cells (neurons with long axons) and stellate cells (neurons with short axons). Staining cross-sections of tissue allows a direct visualisation of cell bodies which were thoroughly studied in the early 20th century and revealed the laminar structure of the cortex. The different layers are interconnected and form vertical columns that extend from the surface of the brain (plial surface) to white matter [29]. Vertical columns with similar cytoarchitecture are grouped together, making cortical parcellation possible. One of the most famous parcellations consists of the Broadmann areas, defined and numbered by the anatomist Korbinian Brodmann in the early 20th century [30]. The Broadman areas represent regions of the cerebral cortex which have a similar histological structure and organization of cells. Later studies have shown an overlap between functional properties of different areas and their cytoarchitecture [29]. The neuronal cell bodies vary in shape and size between different layers and cortical areas. For example pyramidal cells can be classified according to their diameter as small (1-12μm), medium (20-25 μm), large (45-50 μm) and giant (70-100 μm, characteristic for the motor cortex).

The structure and thickness of the cortex are of interest for studying normal brain development as well as a wide range of neurodegenerative diseases and psychiatric disorders, such as Alzheimer's and other dementias, Huntington's disease, schizophrenia, etc [31].

White matter

White matter is primarily composed of axons and supporting glial cells. As illustrated in Figures 2.1 and 2.2, axons are long and thin projections of neuron cell bodies that facilitate information transfer between cortical and subcortical regions. The tip of the axons consists of growth cones which sense chemical signals and determine the development in the desired direction [32]. They are organized in bundles which are commonly referred to as tracts. Glial cells are adjacent to axons and have an important role in determining the structure and function of white matter. For example, astrocytes maintain a balanced chemical environment of neurotransmiters and regulate the uptake of nutrients from the blood, while oligodendrocites produce the myelin sheath surrounding the axons which acts as electric insulation and increases the speed of signal conduction [33].

The key role of axons is to transfer chemical and electrical impulses between neurons, allowing long-distance communication. The length of axons in the body varies between millimetres to meters and their inner diameters are orders of magnitude smaller, ranging between 0.1 to 20 microns [34]. Light microscopy measurements of axon inner diameter in the human corpus callosum show size distributions with a mode between 0.5 to 1 μm and a range of values up to 9 μm [35]. Nevertheless, there is significant shrinkage during the fixation process (65% [35]) which needs to be accounted for when comparing histological images with in-vivo measurements. The conduction speed of electrical impulses increases with axon diameter, however, due to the complexity of neural network and limited volume, the axons in the brain cannot have a large diameter. This problem was solved by the myelin sheaths, a lipid-rich substance that is wrapped around the axons and insulates them. Myelination allows a dramatic increase in conduction velocity compared to unmyelinated axons, which has facilitated the evolution of human cerebral function [33]. The thickness of the myelin sheath increases with axon diameter, yielding a g-ratio (ratio between inner and outer axon diameters) between 0.6 and 0.8 [36, 37]. The myelin sheath is interrupted every 1-2 millimetres by unmyelinated segments called nodes of Ranvier. When axons have this structure, the signal propagates from node to node, which results in a higher conduction velocity. The white matter structure is closely related to its function, with the thickest axons originating in primary motor and somatosensory areas and the thinnest ones in prefrontal and temporal areas [38]. This suggests that fast conduction is required for movement and sensory processing which are important for survival, while higher cognitive tasks do not require the same conduction speed [38].

The structure and function of white matter can be affected by different pathologies that affect the myelin sheaths, axons or glial cells. For example dysmyelination is characterized by a defective chemical structure of the myelin and is a characteristic of leukodystrophies, a group of diseases that affect children and young adults. On the other hand, demyelination describes the loss of previously healthy myelin and can happen though different mechanisms in diseases such as multiple sclerosis or schizophrenia [39]. Axon and neural degeneration can also occur as a result of traumatic injuries. All these conditions result in an impaired function of white matter, however they all have different cellular mechanisms. In order to differentiate and track the progression of different lesions, first we need to localize and characterize them.

2.1.2 Brain imaging

In the late 19th, early 20th century, the development of staining procedures revealed the structure of individual neurons in dissected brain tissue as well as the laminar structure of the cortex [40]. Careful dissection and staining of brain tissue allowed a detailed parcellation of the cortical areas based on differences in cytoarchitecture (e.g. Brodmann areas [30]) as well as the visualization of white matter tracts from tracer studies [41]. The resolution of these images obtained by light microscopy is in the order of microns. More recent developments in electron microscopy (EM) provide resolution at the nanoscale, detailing the fine structure of axons and myelin [42]. This allows the quantification of axons size distribution [35], volume fraction as well as myelin content in different white matter tracts [42]. These imaging modalities offer great resolution, however, they pose some drawbacks. The tissue needs to be carefully handled and fixed within a short period of time after dissection in order to prevent neuronal degeneration [43]. Moreover, the tissue is subject to distortions and shrinkage caused by slicing and fixation [44]. Histological samples are also important for clinical use to distinguish between different types of pathology described above, however this is an invasive procedure which poses risks for the patient and cannot be easily performed in case of brain diseases.

Over the past decades, non-invasive imaging techniques such as computer tomography (CT), positron emission tomography (PET) and magnetic resonance imaging (MRI) have revolutionized in-vivo brain imaging. CT provides structural information based on different absorption rates of x-rays [45] and PET offers functional and metabolic information from the uptake of different radioactive tracers [46].

For brain imaging, MRI is the modality of choice as it offers very good structural contrast in soft tissue and can provide different contrast mechanisms depending on the application. For example, in T1-weighted images, which are often used to analyse brain macrostructure, compartments with greater water content appear darker, whereas compartments with increased lipid content (e.g. white matter) appear bright. T2-weighted images offer complementary contrast and are useful to visualize pathology such as white matter lesions and oedema which appear bright. Other types of data acquisition can provide additional structure information such as proton density [42]. MRI techniques can also be used to image blood flow. Arterial spin labelling (ASL) [47] has been applied to measure perfusion in the cortex [48], while the blood oxygen level-dependent (BOLD) contrast is the basis of functional MRI [49]. Tissue microstructure can by probed with diffusion weighted MRI. For instance, diffusion tensor imaging (DTI) [50] reveals the main fibre orientation and has been used in tractography to study white matter connectivity in-vivo, while more recent work shows the possibility of recovering microstructural parameters which reflect the axon diameter distribution and volume fraction [5, 9, 10] which are potential biomarkers for white matter diseases. Nilsson et al presents a comprehensive review of DW-MRI acquisition and modelling strategies for white matter [51]. The most commonly used techniques are discussed in detail in later sections.

2.1.3 Cancer tissue

The term cancer refers to a malignant growth, which is characterized by a continuous, uncontrolled and damaging proliferation of cells which are structurally and functionally different compared to the normal cells from which they develop [52]. Cancer tumours are classified in two ways, depending on the type of tissue where it originates (histological type) and on the location in the body where it first appeared. The most recent classification is presented in the *International Classification of Diseases for Oncology* [53].

From a histological standpoint, the most common type of cancer, accounting for 80 to 90 percent, is carcinoma which originates in the epithelial tissue. The majority of carcinomas affect organs or glands capable of secretion, such as breast, prostate, lung, pancreas, etc. [53]. The appearance and structure of tissue changes as the cancer becomes more aggressive, thus the disease is graded based on histological data which dictates the choice of treatment. In order to provide similar information to histology, non-invasive imaging techniques should be sensitive to these tissue changes and recover cellular features such as size, shape, volume fraction, etc.

Tumour detection, classification and grading highly depends on the affected organ, and here I exemplify this process for prostate cancer, which is an application of interest for my future work.

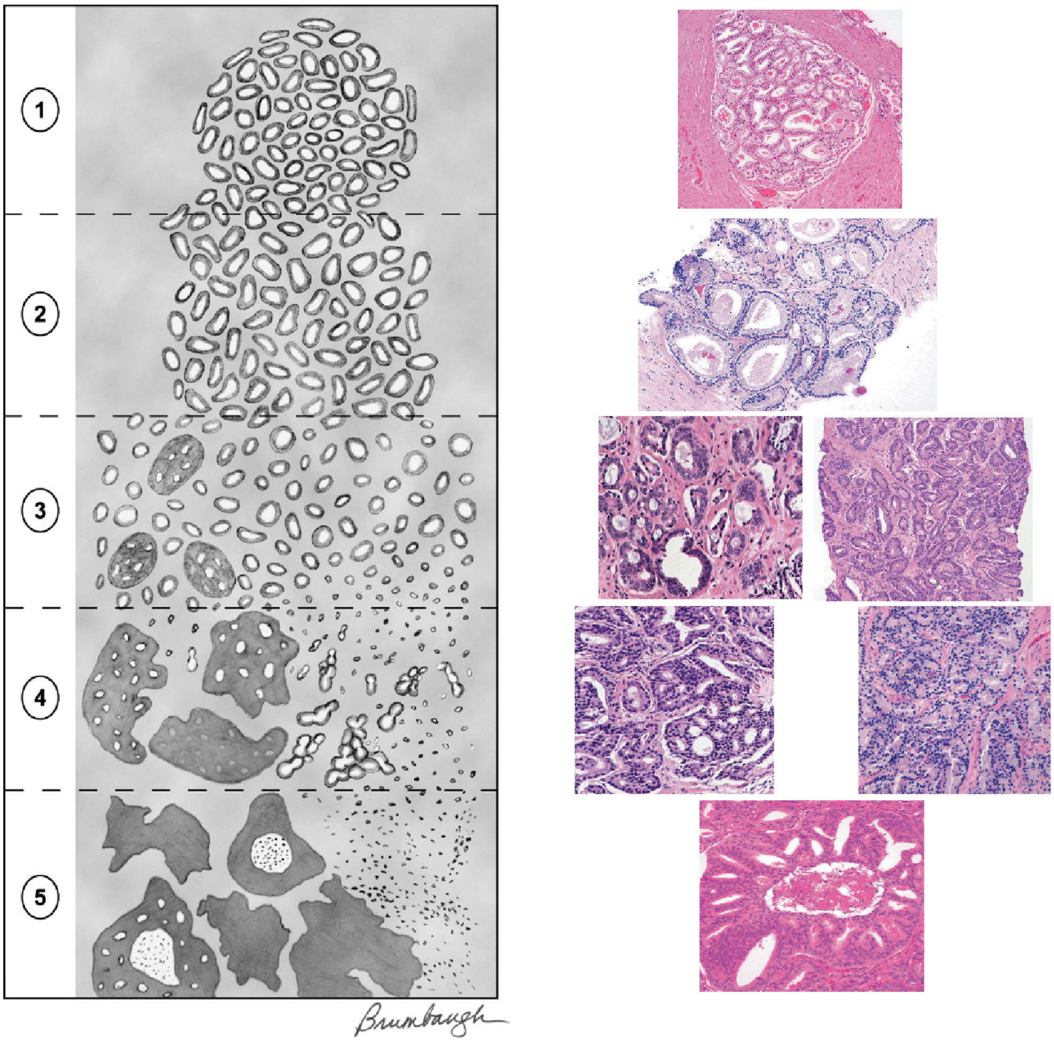

Figure 2.3: Modified Gleason grading scheme [1]. The aggressiveness of cancer increases with Gleason grade.

Prostate cancer

The structure of healthy prostate tissue is quite regular and consists of glands, which are made of a duct (lumen) surrounded by epithelial cells and are connected by muscular tissue (stroma). With cancer, the glandular structure is affected, the epithelial cells proliferate, the glands become fused with each other and the amount of healthy stroma decreases. These hystological changes can be visualized from tissue samples stained

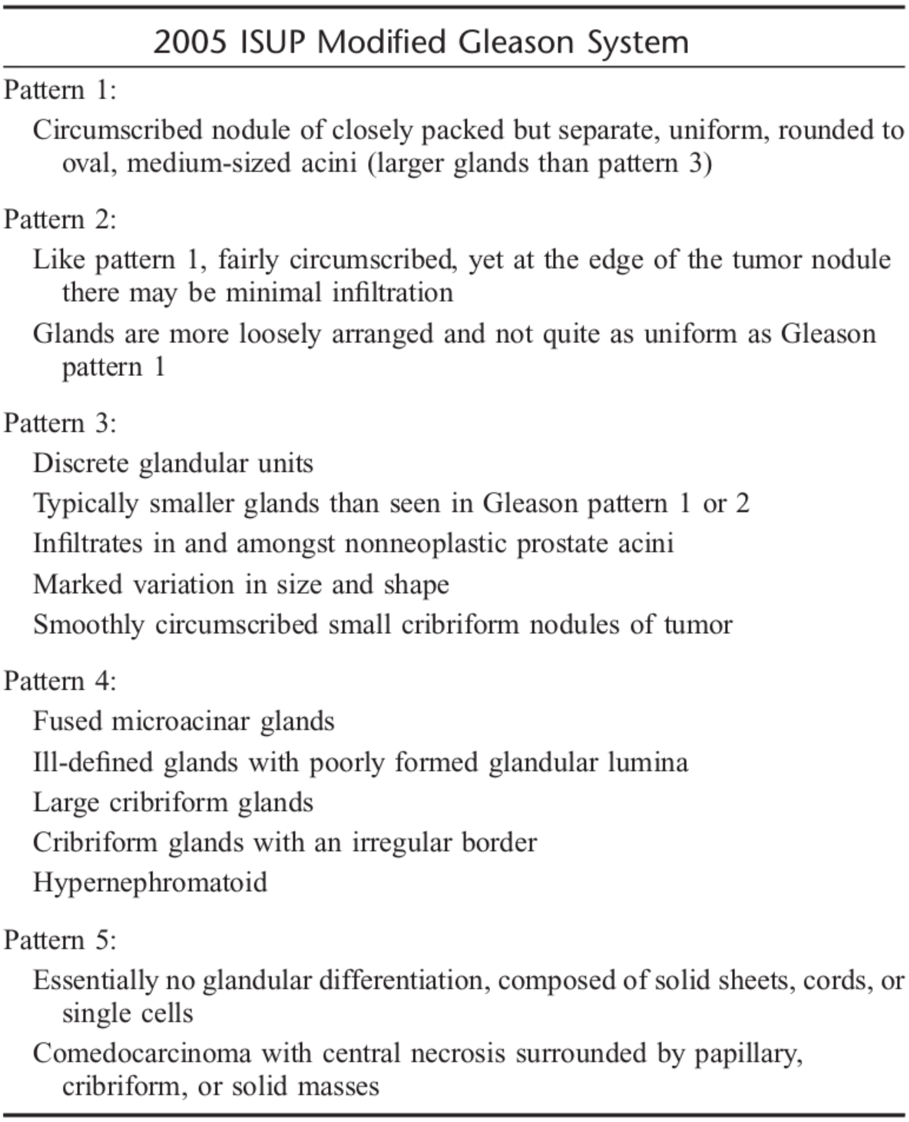

2005 ISUP Modified Gleason System

Pattern 1:
- Circumscribed nodule of closely packed but separate, uniform, rounded to oval, medium-sized acini (larger glands than pattern 3)

Pattern 2:
- Like pattern 1, fairly circumscribed, yet at the edge of the tumor nodule there may be minimal infiltration
- Glands are more loosely arranged and not quite as uniform as Gleason pattern 1

Pattern 3:
- Discrete glandular units
- Typically smaller glands than seen in Gleason pattern 1 or 2
- Infiltrates in and amongst nonneoplastic prostate acini
- Marked variation in size and shape
- Smoothly circumscribed small cribriform nodules of tumor

Pattern 4:
- Fused microacinar glands
- Ill-defined glands with poorly formed glandular lumina
- Large cribriform glands
- Cribriform glands with an irregular border
- Hypernephromatoid

Pattern 5:
- Essentially no glandular differentiation, composed of solid sheets, cords, or single cells
- Comedocarcinoma with central necrosis surrounded by papillary, cribriform, or solid masses

Figure 2.4: Tissue features of different prostate cancer grades [1]

with hematoxylin and eosin (H&E), which colours nuclei with dark blue, cytoplasm with purple and the stroma with pink. In H&E images, the lumen space remains white.

These aspects of tissue degeneration are captioned by the Gleason grading system [54, 1], which is visually depicted in Fig. 2.3, and classifies the aggressiveness of cancer into 5 grades based solely on the architectural properties of the tissue. The pathologist decides which is the most predominant and the second most predominant pattern of the cancerous tissue from the biopsy sample and assigns to each one a grade from 1 to 5. The final grade is the sum of the two, i.e. a score from 2 to 10, and is an important part of the pathological report which determines the most suitable treatment for the patient. A brief description of the tissue architecture for different cancer grades according to the most recent classification is presented in Fig. 2.4.

The Gleason grading system is specific for prostate cancer, however, there are similar histological grading schemes for cancer tumours affecting various organs. For example the Nottingham histological score classifies breast cancer based on tubule formation, nuclear pleomorphism and mitotic count [55]. In most other cancers the histological grade distinguishes between three different tissue types: well differentiated (cancer cells resemble normal cells), moderately differentiated (cancer cells look more abnormal) and poorly differentiated (cancer cells do not resemble normal cellular structure).

2.1.4 Cancer imaging

Diagnosing cancer takes into account histological data (grading) as well as information about the tumour size and its spread to surrounding tissue, lymph nodes or other organs (staging) [56].

The gold standard for cancer grading is tissue biopsy. The tissue sample is taken to a laboratory, where it is routinely stained with H&E, which reveals the tissue structure, and analysed under microscope [56]. Then, it is assigned a histological grade which reflects the malignancy of the cells. If necessary, other special stains, which can highlight different features such collagen fibres, iron content, melanin, fungi, etc, are used [57].

Cancer staging requires information at the macroscopic scale and relies on various non-invasive imaging techniques for localization and quantification of tumour spread. For example, X-rays and more recently CT are widely used for the thoracic region and especially for the lungs, as there is a big contrast between normal tissue filled with air and tumours. PET and other nuclear medicine techniques use small quantities of radioactive tracers to measure the metabolic rate which is higher in malignant tumours due to the increased vascularity and cell proliferation. Thus, cancerous areas appear very bright in PET images, which facilitates the detection of cancer spread and metastases. Once the tumour is localized and the treatment is planned, regular check-ups are necessary to assess the progression of the disease and/or the efficacy of treatment.

The drawback of the previously mentioned modalities is the limited repeatability due to ionizing radiation (X-ray, CT) or uptake of radioactive tracers (PET). MRI offers a great imaging flexibility and overcomes these issue as it uses non-ionizing radiation. Body MRI is a challenging task due to the artefacts caused by cardiac and respiratory motion. With the development of better data acquisition and analysis tools (e.g. cardiac gating [58], motion correction algorithms [59]), MRI has become an important tool for cancer imaging. Tumours have a different chemical composition compared to the normal tissue which affects the magnetic properties and consequently they have a different intensity on standard T1 and T2-weighted MRI images. Dynamic contrast enhanced (DCE) MRI measures the blood inflow after injecting a paramagnetic tracer, such as chelated gadolinium. In general, tumours show early enhancement due to the increased vascularity. Recent work showed the ability of MRI to provide functional information similar to PET by imaging sugar metabolism through glucose chemical exchange saturation transfer [60]. Diffusion MRI signal depends on the microstructural properties of the cancer lesion, such as cell size and density. Thus, low signal in DW-MRI indicates an area of highly packed cells which are usually characteristic for tumours. Various studies aim to correlate imaging biomarkers, derived from DW-MRI and DCE-MRI, with histological data [61, 62], while more recent microstructure imaging techniques based on DW-MRI, such as VERDICT, were able to produce maps of tissue parameters such as cellularity [63].

2.1.5 Summary

This section presents the main characteristics of brain and cancer tissue and illustrates the importance of imaging techniques for understanding normal and pathological tissue. Non-invasive imaging techniques, such as CT, PET and MRI, generate whole-organ maps illustrating various aspects of tissue structure and function and are being used for an increasing number of applications in brain and body imaging. Compared to the other modalities, MRI uses non-ionizing radiation, making it safer in terms of multiple repetitions and follow-up studies.

2.2 Magnetic Resonance Imaging

This section presents a semi-classical picture of nuclear magnetic resonance (NMR), the physical phenomenon explored in MRI, as well as the most common contrast mechanisms and data acquisition which are the building blocks of modern imaging techniques.

2.2.1 Nuclear magnetic resonance (NMR)

Nuclei with a non-zero magnetic moment (including hydrogen) can absorb and emit electromagnetic radiation of a certain frequency when placed in an external magnetic field. This phenomenon is known as nuclear magnetic resonance (NMR) and was demonstrated for the first time in 1946 in separate experiments designed by Edward Purcell and Felix Bloch [64, 65]. Protons and neutrons which build up the nucleus have an intrinsic angular momentum called spin, which gives rise to the magnetic moment. The state of each individual nucleus is described by quantum mechanics, however, the ensemble behaviour can be accurately described by classical models [66]. Most biomedical imaging applications exploit the NMR of hydrogen nuclei (protons), thus all constants are given for protons which are $\frac{1}{2}$-spin particles.

In a quantum mechanical description, the measured component of an individual spin along any direction (conventionally chosen as z-direction) has only discrete states. A $\frac{1}{2}$-spin particle has two eigenstates, spin-up $|\uparrow\rangle$ and spin-down $|\downarrow\rangle$ with eigenvalues $m = \pm\frac{1}{2}$. When no measurement is performed, the full spin-state is a superposition of the two eigenstates. The weights of the two states are complex numbers that express the direction of spins as precisely as nature allows in accordance with quantum mechanics [66].

The magnetic moment μ can be written in terms of the spin operator:

$$\boldsymbol{\mu} = \gamma \cdot \hbar \cdot \mathbf{S} \tag{2.1}$$

$\gamma = 2.675 \cdot 10^8\ \mathrm{s}^{-1}\mathrm{T}^{-1}$	gyromagnetic ratio for ^{1}H
$\hbar = \frac{h}{2\pi} = 1.054 \cdot 10^{-34}$ Js	reduced Planck constant
$\mathbf{S}$	particle spin

The interaction between this magnetic moment $\boldsymbol{\mu}$ and an external magnetic field $\mathbf{B}$ is described by the following Hamiltonian:

$$-\boldsymbol{\mu} \cdot \mathbf{B} = -\gamma \cdot \hbar \cdot B_0 \cdot S_z \tag{2.2}$$

where B_0 is the component of the magnetic field along the z-axis, which is conventionally chosen along the direction of the external magnetic field.

The eigenvalues of this Hamiltonian are $E = -\gamma\hbar B_0 m = \mp\frac{1}{2}\gamma\hbar B_0$ corresponding to $m = \pm\frac{1}{2}$. The energy difference between the two eigenstates is $\Delta E = \gamma\hbar B_0$ and the occupation of the two states follows the Boltzmann distribution:

$$\frac{N_+}{N_-} = e^{\frac{\Delta E}{kT}} = e^{\frac{\gamma\hbar B_0}{kT}} \tag{2.3}$$

N_+	occupation number of the parallel state
N_-	occupation number of the anti-parallel state
$k = 1.38 \cdot 10^{-23}$ J/K	Boltzmann constant

In a probe with N water protons per unit volumes, the difference in the occupation of the two energy states creates an equilibrium magnetization M_0, which is parallel to the external magnetic field:

$$M_0 = \frac{N\gamma^2\hbar^2 B_0}{4kT} \tag{2.4}$$

An NMR / MRI experiment measures the net magnetization of the spin ensemble, and not of individual spins. In this case, it can be shown that the mean of the expected outcomes of magnetization measurements derived from quantum mechanics follows the classical equation of motion [66].

2.2.2 Signal generation and detection

The total magnetic moment per unit volume gives rise to a macroscopic magnetization $\mathbf{M} = (M_x, M_y, M_z)$, which can be described by classical mechanics. In order to measure the magnetization and probe different magnetic properties of the sample, the net magnetization $\mathbf{M}$ is perturbed from equilibrium using radio-frequency (RF) pulses and the response of the system is recorded using receiver coils. This section presents the basics of generating and detecting the MR signal.

In analogy to classical mechanics, the evolution of magnetization $\mathbf{M} = (M_x, M_y, M_z)$ in the presence of an external magnetic field $\mathbf{B}(t)$ is described according to:

$$\frac{d\mathbf{M}(t)}{dt} = \gamma \cdot \mathbf{M}(t) \times \mathbf{B}(t) \tag{2.5}$$

If we consider the case of a constant magnetic field B_0 along z-axis, then the components of the magnetization are described by the following equations:

$$\frac{dM_x}{dt} = \gamma \cdot B_0 \cdot M_y; \qquad \frac{dM_y}{dt} = -\gamma \cdot B_0 \cdot M_x; \qquad \frac{dM_z}{dt} = 0 \tag{2.6}$$

Therefore, the component parallel to the magnetic field $M_{\|}$ is constant and the perpendicular component, which can be written as $M_{\perp} = M_x + iM_y$ with $i = \sqrt{-1}$, precesses around z-axis. The angular frequency of precession $\omega_0 = \gamma B_0$ is known as the Larmor frequency. Thus, the spin system can by manipulated by superimposing time varying magnetic fields.

Excitation and radio frequency (RF) pulses

By applying an alternative current with frequency ω_1 through the transmit coil, an oscillating magnetic field perpendicular to z-direction is produced:

$$\mathbf{B}_1(t) = \begin{bmatrix} B_1 \cos \omega_1 t \\ B_1 \sin \omega_1 t \\ 0 \end{bmatrix} \tag{2.7}$$

When this oscillating magnetic field, commonly referred to as a radio-frequency (RF) pulse, is superimposed to the initial constant field B_0, equation (2.5) can be rewritten as:

$$\frac{d\mathbf{M}(t)}{dt} = \gamma \cdot \mathbf{M}(t) \times \begin{bmatrix} B_1 \cos \omega_1 t \\ B_1 \sin \omega_1 t \\ B_0 \end{bmatrix} \tag{2.8}$$

This equation describes the manipulation of the magnetization $\mathbf{M}$ by transversal RF fields which is schematically represented in Fig. 2.5.

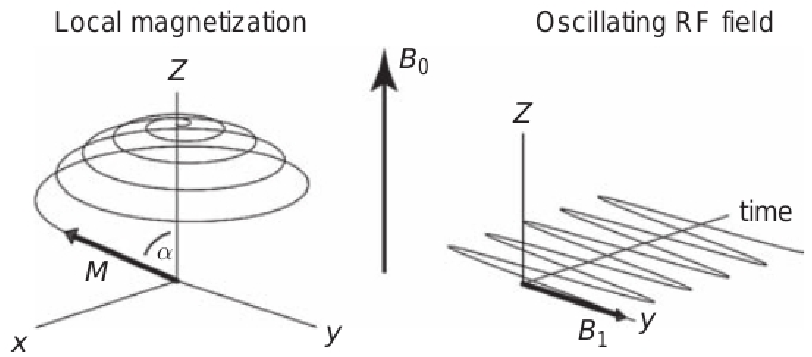

Figure 2.5: A transversal RF pulse causes the net magnetization to precess around z-axis. Figure adapted from [67]

Depending on the frequency ω_1 and on the duration of the pulse, different effects can be obtained. For $\omega_1 = \omega_0$ and a constant amplitude B_1, the magnetization $\mathbf{M}$ is deviated from the equilibrium by an angle α depending on the duration of the pulse. This is called the flip angle. The commonly used values in acquiring the MR images are $\alpha = 180^o$ -corresponding to magnetization inversion and $\alpha = 90^o$ -corresponding to transversal magnetization.

Bloch equations, $T1$ and $T2$ relaxation

The time-dependent behaviour of the net magnetization $\mathbf{M}$ in the presence of an applied magnetic field $\mathbf{B}(t)$ is described quantitatively by the Bloch equations, which include relaxation effects. If the net magnetization is disturbed from equilibrium then it has the tendency to realign with the external field. The evolution of the magnetization in parallel direction is characterized by the relaxation time $T1$:

$$\frac{dM_\parallel}{dt} = \frac{M_0 - M_\parallel}{T1} + \gamma \cdot (\vec{M} \times \vec{B})_z = \frac{M_0 - M_\parallel}{T1} + \gamma \cdot (M_x B_y - M_y B_x) \qquad (2.9)$$

The relaxation time $T1$ describes the interaction between the spins and the chemical bindings of the surrounding lattice ('spin-lattice interaction') and depends on the material as well as on the applied magnetic field. After the application of a 180° RF pulse which completely inverts the magnetisation, the solution of equation 2.9 with initial conditions $M_{||} = -M_0$ and $M_{\perp} = 0$, is:

$$M_{||}(t) = M_0(1 - 2 \cdot e^{-\frac{t}{T1}}), \tag{2.10}$$

and assuming infinite repetition time between measurements ($TR \to \infty$). This experiment is known as Inversion Recovery (IR) and probes $T1$ relaxation [67].

The evolution of the transverse magnetization is subject to relaxation with decay constant $T2$, which is a measure of spin-spin interactions, describing the effect of local field inhomogeneities and/or direct interactions between the spins without energy transfer to the lattice [68]:

$$\frac{dM_{\perp}}{dt} = -\frac{M_{\perp}}{T2} - i\gamma \cdot (M_{\perp}B_z - M_z B_{\perp}) \tag{2.11}$$

After a 90^o RF pulse which brings the magnetization to the transverse plane, the solution of equation 2.11, with initial conditions $M_{\perp} = M_0$ and $M_{||} = 0$, is:

$$M_{\perp} = M_0 \cdot e^{-\frac{t}{T2} - i\gamma B_0 t} \tag{2.12}$$

Thus, the transverse magnetization is precessing around the main magnetic field and its magnitude is subject to an exponential decay with time constant $T2$. This experiment is known as Free Induction Decay (FID) and is a measure of the relaxation time $T2$ [67].

Signal detection and spin echo

In order to perform an MR measurement, the magnetization needs to have a transverse component that precesses around the z-axis and according to Faraday's law will induce an oscillating voltage in the receiver coils that can be recorded [69].

In practice the signal in a FID experiment decays much faster than expected as a result of T2 decay alone, due to magnetic field inhomogeneities. Spins that experience different magnetic fields precess at different rates which results in a phase dispersion that reduces the overall signal magnitude. The apparent relaxation time is $T2^*$ and is much shorter than $T2$ [67]. If we denote the relaxation time due to field inhomogeneities as $T2'$, then we have the following relation between the relaxation times:

$$\frac{1}{T2^*} = \frac{1}{T2} + \frac{1}{T2'}. \tag{2.13}$$

It is possible to correct for $T2'$ and reverse the dephasing caused by field inhomogeneities by applying an additional 180^0 RF pulse after the initial 90^o pulse. The 180^0 RF pulse inverts the precession direction of the spins and creates an echo of the original FID signal at a moment called echo time (TE). The amplitude of the signal at echo time decays according to $T2$ relaxation [67]. This acquisition method is called a spin-echo sequence and is illustrated in Figure 2.6.

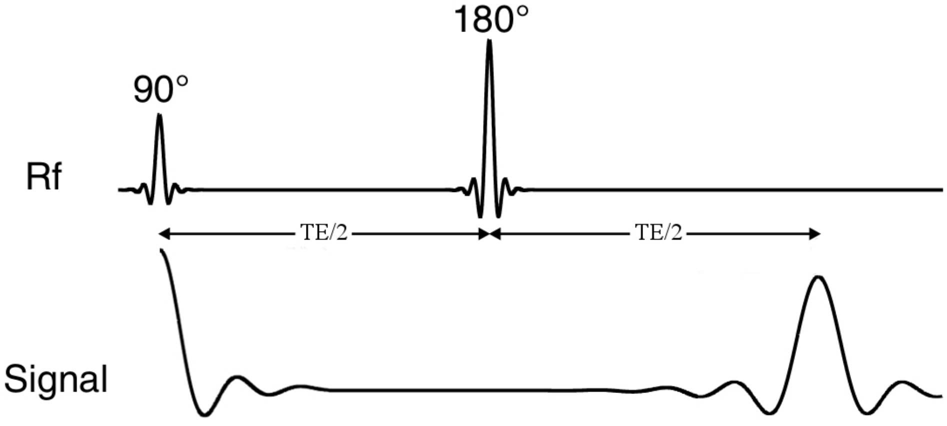

Figure 2.6: Schematic representation of the spin-echo sequence. (Figure adapted from [70])

2.2.3 Spatial localization

Acquiring the signal from the NMR experiment described above provides an average value for the entire sample. Thus the central task of MRI is to localize the MR signal and extract information about its spatial distribution.

As the Larmor frequency depends on the magnetic field, spatial localization can be achieved using magnetic field gradients $\mathbf{G} = (G_x, G_y, G_z)$. For a 3D volume, this is usually performed in three steps: slice encoding (usually in z direction), frequency encoding (x direction) and phase encoding (y direction) [69].

The slice selection is realized by applying a field gradient along the z-direction at the same time with the excitation RF pulse which has a narrow distribution of frequencies, referred to as bandwidth. The Larmor frequency varies linearly along the z-axis, thus the RF pulse will affect only the magnetization from a slice which has the resonant frequency within its bandwidth. Different slices can be selected by changing the frequency of the RF pulse. The spatial resolution in z-direction depends on the bandwidth of the RF pulse as well as the gradient strength.

Frequency encoding is used to provide information about the position along the x-axis. This works by superimposing a magnetic field gradient G_x during readout which makes the oscillation frequency linearly dependent on position [69]:

$$\omega(x) = \gamma(B_0 + G_x x) = \omega_0 + \gamma G_x x \tag{2.14}$$

The signal generated locally from spins in an infinitesimal interval dx at point x is:

$$S(x,t) = \rho(x) dx e^{-i(\omega_0 + \gamma G_x x)t}, \tag{2.15}$$

where $\rho(x)$ is a general notation for the spatial distribution of MR signal, accounting for spin density, T1 and T2 relaxation, flip angle, etc. In case of a spin-echo sequence, the frequency encoding gradient is applied after the echo time.

After demodulation (removal of the carrier signal $e^{-i\omega_0 t}$), the signal received from the entire object is:

$$S(t) = \int_{-\infty}^{\infty} S(x,t) dx = \int_{-\infty}^{\infty} \rho(x) e^{-i\gamma G_x x t} dx \tag{2.16}$$

Frequency encoding localizes the signal along x-direction, however it does not provide any information about the spatial distribution in y direction. Thus an additional encoding mechanism is necessary.

Phase encoding is realized by applying a magnetic field gradient G_y for a short time interval (preparatory time T_{PE}) between the excitation and readout. When the gradient is on, the frequency depends on the y-position, thus the accumulated phase is space dependent. The FID signal generated locally from spins in an infinitesimal interval dy at point y is:

$$S(y,t) = \rho(y) dy e^{-i(\omega_0 t + \phi(y))}, \quad \text{with } \phi(y) = \gamma G_y y T_{PE} \tag{2.17}$$

After demodulation the phase encoded signal is:

$$S(t) = \int_{-\infty}^{\infty} S(y,t) dy = \int_{-\infty}^{\infty} \rho(y) e^{-i\gamma G_y y T_{PE}} dy \tag{2.18}$$

Frequency and phase encoding can be used to localize the signal in the 2D plane. The total signal acquired at a a given time T_{FE} is:

$$S = \int\int I(x,y) e^{-i\gamma G_x x T_{FE}} e^{-i\gamma G_y y T_{PE}} dxdy, \tag{2.19}$$

$$\begin{aligned} k_x &= \frac{1}{2\pi}\gamma G_x T_{FE} \\ k_y &= \frac{1}{2\pi}\gamma G_y T_{PE} \end{aligned} \tag{2.20}$$

By substituting these spatial frequencies into equation 2.19, we obtain:

$$S(k_x, k_y) = \int\int I(x,y) e^{-2\pi i k_x} e^{-2\pi i k_y} dxdy \tag{2.21}$$

This demonstrates there is a Fourier relation between the image function $I(x, y)$ and the signal $S(k_x, k_y)$. Thus by measuring the signal at many values of k_x and k_y, also known as k-space, we can recover in the image function, which is the quantity of interest [69]. The k-space can be traversed by manipulating the magnetic gradients $G_x(t)$ and $G_y(t)$. Equations 2.14 to 2.19 show the concept of frequency and phase encoding for the simple case of constant gradients. The Fourier relationship between the signal and the image function holds for time dependent gradients as well, however the k-space sampling trajectory is no longer a straight line.

The are many different k-space sampling schemes including linear, radial or spiral [69], and the data can be acquired in multiple excitations (multi-shot) or in a single excitation (single-shot). Multi-shot acquisitions provide good image resolution, image contrast and signal-to-noise ratio (SNR), however they are not well suited for diffusion MRI due to the fact that diffusion gradients induce a spatially varying phase and shot-wise random over the sample that would interfere with the phase encoding [71]. Thus, the acquisition of choice for diffusion imaging is single-shot echo planar imaging (SS-EPI) which images the entire k-space in one excitation pulse. This is achieved with rapidly switching phase and frequency encoding gradients, as illustrated in Figure 2.7.

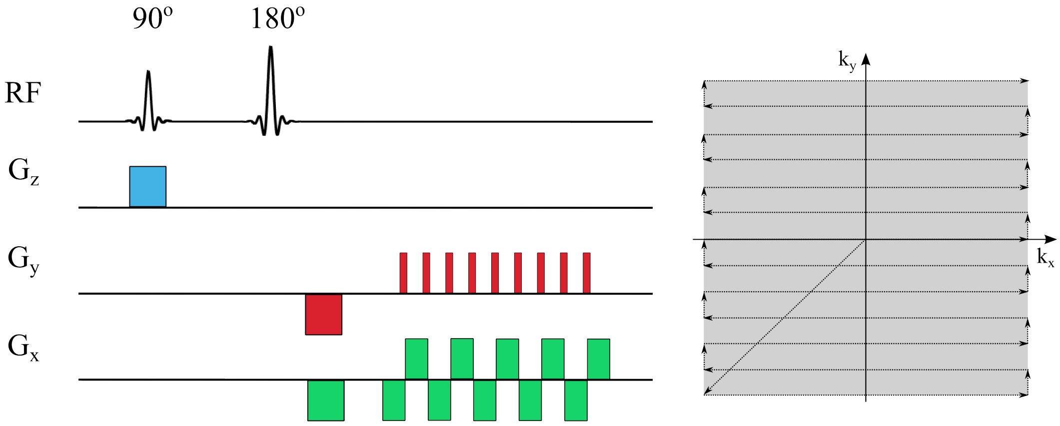

Figure 2.7: [Single-shot echo planar imaging readout]Schematic representation of a spin echo SS-EPI sequence and the resulting coverage of k-space.

Image reconstruction

The last step of MR imaging is to reconstruct the image function $I(x, y)$ from the raw k-space data $S(k_x, k_y)$. According to equation 2.21, this can be achieved using a two-dimensional inverse Fourier transform, which is applied for each slice. The resulting image function is complex valued and can be used to create both magnitude and phase images [69].

2.3 Diffusion MRI - Theory

This section provides the theoretical principles of diffusion MRI. It briefly introduces the mathematical description of diffusion and how to encode it using MRI techniques. Then it describes diffusion MRI signal models for free and restricted diffusion and presents a variety of non-standard acquisition protocols which are sensitive to different microstructural features such as pore anisotropy or permeability and exchange between different water pools.

2.3.1 Diffusion theory

Diffusion describes the random motion of particles from a region of high concentration to a region of low concentration and is mathematically described by Fick's law [72]:

$$\mathbf{J}(\mathbf{r},t) = -D\nabla c(\mathbf{r},t), \tag{2.22}$$

where $\mathbf{J}(\mathbf{r},t)$ is the particle flux, D is the diffusion coefficient, $c(\mathbf{r},t)$ is the particle concentration and the minus sign indicates that the direction of flow is from larger to smaller concentration [73]. Combining equation 2.22 with the conservation of mass law

$$\frac{\partial c(\mathbf{r},t)}{\partial t} = -\nabla \cdot \mathbf{J}(\mathbf{r},t), \tag{2.23}$$

we arrive at Fick's second law of diffusion

$$\frac{\partial c(\mathbf{r},t)}{\partial t} = D\nabla^2 c(\mathbf{r},t) \tag{2.24}$$

which is also commonly referred to as the diffusion equation.

In the absence of a net concentration gradient, random molecular motion still exists, a process known as Brownian motion, which was discovered by R. Brown and mathematically described by A. Einstein [74]. In this case molecules undergo a process of "self-diffusion" [72] and we are concerned with the probability $P(\mathbf{r}_1,t_1|\mathbf{r}_0,t_0)$ of a particle staring from $\mathbf{r}_0$ and moving to $\mathbf{r}_1$ in time $t_1 - t_0$. Thus, we can re-write equation 2.24:

$$\frac{\partial P(\mathbf{r}_1,t_1|\mathbf{r}_0,t_0)}{\partial t_1} = D\nabla^2 P(\mathbf{r}_1,t_1|\mathbf{r}_0,t_0). \tag{2.25}$$

$P(\mathbf{r}_0,t_0,\mathbf{r}_1,t_1)$ is commonly termed the Green's function of the diffusion propagator. For diffusion in a homogeneous and isotropic medium with initial condition $P(\mathbf{r}_1, 0|\mathbf{r}_0, 0) = \delta(\mathbf{r_1} - \mathbf{r_0})$ and boundary condition $R \rightarrow 0$ for $\mathbf{r} \rightarrow \infty$ the solution of equation 2.25 is: [73]

$$P(\mathbf{r_1}, t_1|\mathbf{r}_0, t_0) = (4\pi D(t_1 - t_0))^{-3/2} \exp\left(-\frac{(\mathbf{r}_1 - \mathbf{r}_0)^2}{4D(t_1 - t_0)}\right) \tag{2.26}$$

For free diffusion, the mean square displacement can be calculated from equation 2.26 as:

$$\begin{aligned}\left\langle(\mathbf{r}_1 - \mathbf{r}_0)^2\right\rangle &= \int_{-\infty}^{\infty} (\mathbf{r}_1 - \mathbf{r}_0)^2 P(\mathbf{r}_1, t_1|\mathbf{r}_0, t_0) d\mathbf{r}_0 d\mathbf{r}_1 \\ &= nD(t_1 - t_0), \text{ with } n = 2, 4, \text{ or 6 for one, two or three dimensions.}\end{aligned} \tag{2.27}$$

For example, for diffusion along a line $n = 2$, for diffusion in a plane $n = 4$ and for diffusion in a volume $n = 3$.

2.3.2 Diffusion contrast

This section presents how we can estimate molecular displacements using MR measurements. When the external magnetic field B_0 is homogeneous, the Larmor frequency and consequently the cumulative phase of individual spins are independent of the location $\phi(t) = \omega_0 \cdot t = \gamma B_0 t$. When in addition to the constant field B_0 there is a spatially dependent field with gradient $\mathbf{G}(t)$, then the Larmor frequency is spatially dependent, and so is the phase:

$$\phi(t) = \int_0^t (\omega_0 + \gamma \mathbf{G}(t')\mathbf{r}(t'))dt' = \omega_0 t + \gamma \int_0^t \mathbf{G}(t')\mathbf{r}(t'))dt'. \tag{2.28}$$

This approach is used to spatially encode the signal, as explained in section 2.2.3 and also offers the ground for quantifying molecular displacement due to diffusion.

The standard sequence used to measure diffusion was developed by Stejskal and Tanner in 1965 and modifies the spin-echo sequence by adding two equal gradient pulses of duration δ placed before and after the refocusing RF pulse, separated by the time interval Δ [16]. The Stejskal-Tanner sequence, which is also known in the literature as "single pulsed gradient", "pulsed gradient spin-echo" or "single diffusion encoding" is illustrated in Fig. 2.8. In this work we use the name "single diffusion encoding" (SDE), which was recently agreed upon in the diffusion MRI community [75].

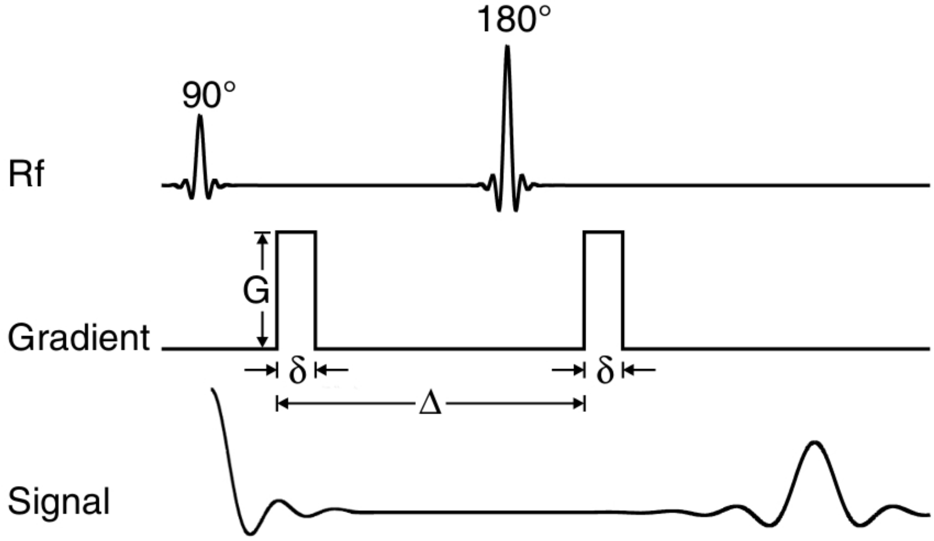

Figure 2.8: Schematic representation of the SDE sequence with gradient amplitude G pulse duration δ and diffusion time Δ. (Figure adapted from [70])

2.3.3 Free diffusion and Bloch-Torrey equation

The effect of self-diffusion in NMR was first described by Torrey (1956) by modifying the Bloch equation to account for the "transport of magnetization" [76]. Thus, in absence of RF pulses, the equation for the transverse magnetization ($M_\perp$) in the rotating frame (i.e. without the last term in equation 2.11) is:

$$\frac{\partial M_\perp}{\partial t} = -i\gamma M_\perp \mathbf{G} \cdot \mathbf{r} - \frac{M_\perp}{T_2} + D\nabla^2 M_\perp. \tag{2.29}$$

In this case $M_\perp$ is a function of both time and position. For free diffusion, equation 2.29 can be solved by making the substitution [72]:

$$M_\perp = E(t)\left(\exp(-i\gamma \mathbf{r} \cdot \int_0^t \mathbf{G}(t')dt')\exp(-t/T2)\right) \tag{2.30}$$

At the echo time of a spin-echo sequence, the integral of the effective gradient is 0 (accounting for the effect of the 180^o RF pulse). Thus, substituting $M(t)$ into equation 2.29, integrating the result and normalizing for $T2$ decay, we get the following expression for $E(t)$ [72]:

$$E(t) = \exp\left(-D\gamma^2 \int_0^t \left|\int_0^{t'} \mathbf{G}^*(t'')dt''\right|^2 dt'\right), \tag{2.31}$$

which can be expressed as

$$E(t) = \exp(-bD), \text{ where } b = \gamma^2 \int_0^t \left|\int_0^{t'} \mathbf{G}^*(t'')dt''\right|^2 dt' \tag{2.32}$$

is commonly referred to as the b-value and $\mathbf{G}^*$ is the effective gradient waveform accounting for the effect of the 180^o RF pulse.

For the standard SDE sequence illustrated in Fig. 2.8 with gradient amplitude G, duration δ and interval between gradients Δ, the b-value, calculated by integrating equation 2.32 from 0 to echo time TE and assuming infinite slew rates, evaluates to:

$$b = \gamma^2 G^2 \delta^2 (\Delta - \delta/3). \tag{2.33}$$

The b-value describes the amount of diffusion weighting in applications which assume Gaussian diffusion such as mapping the apparent diffusion coefficient (ADC) or diffusion tensor imaging (DTI).

2.3.4 Restricted diffusion

The free diffusion model is used in many DW-MRI studies, however it does not accurately represent tissue properties, especially the signal component coming from the intracellular water molecules which are restricted by the cell walls. Therefore it is important to construct a model for computing the diffusion signal inside bounded media in order to be able to infer the compartment size or shape from diffusion data, which is important for microstructure imaging techniques.

The effect of the boundaries on the positions of the spins can be described through the diffusion propagator $P(\mathbf{r}_0, t_0|\mathbf{r}_1, t_1)$ which represents the probability that a particle moves from position $\mathbf{r}_0$ at time t_0 to position $\mathbf{r}_1$ at time t_1 [77]. As seen in equation 2.25, the diffusion propagator satisfies Fick's second law. In case of restricted diffusion inside a pore with fully reflecting walls, the boundary condition which shows no particle flux through the membrane is

$$D\hat{\mathbf{n}} \cdot \nabla_{\mathbf{r_1}} P(\mathbf{r}_1, t_1|\mathbf{r}_0, t_0) = 0 \tag{2.34}$$

and the initial condition is

$$P(\mathbf{r}_1, 0|\mathbf{r}_0, 0) = \delta(\mathbf{r}_1 - \mathbf{r}_0), \tag{2.35}$$

where D is the diffusion coefficient, $\hat{\mathbf{n}}$ is the outward surface normal at the boundary, $\nabla_{\mathbf{r_1}} P(\mathbf{r}_1, t_1|\mathbf{r}_0, t_0)$ is the probability gradient in the direction of $\mathbf{r_1}$, and $\delta(\mathbf{r})$ is the Dirac delta function. The solution to equation 2.25 can be written as [78]

$$P(\mathbf{r}_1, t_1|\mathbf{r}_0, t_0) = \sum_{n=0}^{\infty} e^{-D\lambda|t_2 - t_1|} u_n(\mathbf{r}_0) u_n^*(\mathbf{r}_1) \tag{2.36}$$

where the $u_n(\mathbf{r})$ are the eigenfunctions of the diffusion equation parametrized by the eigenvalues λ_n.

In the literature there are several approaches which can be used to calculate the diffusion signal in bounded media [79, 80, 81, 82, 83]

Short pulse gradient (SPG) approximation

The SPG approximation assumes a sufficiently short gradient pulse $\delta \ll \Delta$ so that there is no displacement during the application of the gradients. The effect of the first gradient is to induce a phase which depends on location $\gamma\delta\mathbf{G} \cdot \mathbf{r}_0$ which is subsequently inverted by the 180° RF pulse. Thus, after the second gradient there is a net phase shift $\Delta\phi(\mathbf{r}_1 - \mathbf{r}_0) = \gamma\delta\mathbf{G} \cdot (\mathbf{r}_1 - \mathbf{r}_0)$.

After normalizing for $T2$ decay, the echo signal is given by the ensemble average of the phase term $\langle \exp(i\Delta\phi) \rangle = \langle \exp(i\gamma\delta\mathbf{G} \cdot (\mathbf{r}_1 - \mathbf{r}_0)) \rangle$. The ensemble average can be computed knowing the initial distribution of particles $\rho(\mathbf{r}_0)$ and the probability that a particle moves from position $\mathbf{r}_0$ to $\mathbf{r}_1$ in the time interval Δ [84]:

$$E(\mathbf{G}, \Delta) = \iint \rho(\mathbf{r}_0) P(\mathbf{r}_1|\mathbf{r}_0, \Delta) \exp(i\gamma\delta\mathbf{G} \cdot (\mathbf{r}_1 - \mathbf{r}_0)) d\mathbf{r}_0 d\mathbf{r}_1 \tag{2.37}$$

Making the substitution $\mathbf{r}_1 = \mathbf{r}_0 + \mathbf{R}$ and defining the average propagator as

$\bar{P}(\mathbf{R}, t) = \int \rho(\mathbf{r}_0)P(\mathbf{r}_0 + \mathbf{R}|\mathbf{r}_0)d\mathbf{R}$, equation 2.37 can be rewritten as:

$$E(\mathbf{G}, \Delta) = \int \bar{P}(\mathbf{R}, \Delta) \exp(i\gamma\delta\mathbf{G} \cdot \mathbf{R})d\mathbf{R}. \tag{2.38}$$

Thus, there is a Fourier relationship between $E(\mathbf{G}, \Delta)$ and the average propagator $\bar{P}(\mathbf{R}, \Delta)$ and we can define a reciprocal space $\mathbf{q} = (2\pi)^{-1}\gamma\delta\mathbf{G}$ so that

$$E(\mathbf{G}, \Delta) = \int \bar{P}(\mathbf{R}, \Delta) \exp(i2\pi\mathbf{q} \cdot \mathbf{R})d\mathbf{R}. \tag{2.39}$$

Using the SPG approximation, acquiring the signal in q-space allows the estimation of $\bar{P}(\mathbf{R}, t)$ [85, 77] in a similar way as acquisition in k-space allows the measurement of the image function, as discussed in section 2.2.3.

Gaussian phase distribution approximation

The SPG approximation provides a convenient theoretical framework to image the average propagator, however the condition of short pulse is rarely met in practice.

An analytical expression of the restricted DW signal can be constructed assuming the displacement of the spins $R(t)$, and therefore their phases $\phi(t)$, have a Gaussian distribution with the variance depending on the time t [80, 73, 86]. In this case the signal is

$$E = \exp\left(-\frac{\gamma^2}{2}\int_0^{TE} dt_1 \int_0^{TE} dt_2 \mathbf{G}^{\mathbf{T}^*}(t_1)\langle\mathbf{r}(t_1)\mathbf{r}(t_2)\rangle\mathbf{G}^*(t_2)\right) \tag{2.40}$$

where $\mathbf{G}^*(t)$ and $\mathbf{r}(t)$ are the effective gradient and the position of a molecule at time t and $\langle\cdot\rangle$ is the particle-particle correlation function, describing the correlation between particle positions. Under this formulation, the signal has the following form [78]:

$$\begin{aligned} E &= \exp\left(-\frac{\gamma^2}{2}\int_0^{TE} dt_1 \int_0^{TE} dt_2 \int_V d\mathbf{r_1} \int_V d\mathbf{r_2}\rho(\mathbf{r_1}, \mathbf{t_1})P(\mathbf{r_1}, t_1|\mathbf{r_2}, t_2)\left(\mathbf{r_1} \cdot \mathbf{G}^*(t_1)\right)\left(\mathbf{r_2} \cdot \mathbf{G}^*(t_2)\right)\right) \\ &= \exp\left(-\frac{\gamma^2}{2}\sum_{n=0}^{\infty} B_n \int_0^{TE} dt_1 \int_0^{TE} dt_2 e^{-D\lambda_n|t_2 - t_1|}G^*(t_2)G^*(t_1)\right) \end{aligned} \tag{2.41}$$

where $\mathbf{G}^*(t) = G^*(t)\hat{\mathbf{g}}$ is the effective gradient vector with magnitude $G^*(t)$ and direction $\hat{\mathbf{g}}$, V denotes the diffusion domain and B_n and λ_n are geometry dependent factors.

If the initial density of spins is constant, then B_n is defined as

$$B_n = \frac{1}{\rho} \int_V d\mathbf{r_1} \int_V d\mathbf{r_2} \, (\hat{\mathbf{g}} \cdot \mathbf{r_1}) \, (\hat{\mathbf{g}} \cdot \mathbf{r_2}) \, u_n(\mathbf{r_1}) u_n(\mathbf{r_2}). \tag{2.42}$$

where $u_n(\mathbf{r})$ are the eigenfunctions of the diffusion equation in the restricted domain. The factors B_n and λ_n have analytical expressions for simple geometries such as parallel planes, cylinders, spheres [80, 78, 81] and spherical shells [87]. The explicit formulae are given in the appendix A.1.

The GPD approximation is accurate for a wide range of gradient strengths used in practice [83, 86], however it cannot recover more complex signal features such as diffraction patterns. This formulation is useful for diffusion gradient waveforms which can be easily parametrized, and has been derived for SDE sequences [80], stimulated echos [88], dual spin echos [89], oscillating diffusion gradients [87, 90] and double diffusion encoding sequences [91].

Matrix method (MM)

In 1997 Callaghan developed a mathematical framework which allows the computation of the diffusion signal E in a closed form for an arbitrary pulse sequence [92]. The pulse sequence is divided into narrow intervals τ, as illustrated in Fig. 2.9 and the gradient amplitude $G_0(n\tau)$ is quantified into steps of size g_{step}. Thus, at time $n\tau$ the amplitude of the diffusion vector is $m_n q$ where $q = (2\pi)^{-1}\tau g_{step}$, and m_n is given by

$$m_n = \lfloor (g_0(n\tau)/g_{step}) \rfloor \tag{2.43}$$

The signal E is calculated as a product of matrix operators which describe the phase evolution inside the boundaries:

$$E = S(\mathbf{q}) R [A(\mathbf{q})]^{m_2} R ... R [A(\mathbf{q})]^{m_{N-1}} R S^T(-\mathbf{q}) \tag{2.44}$$

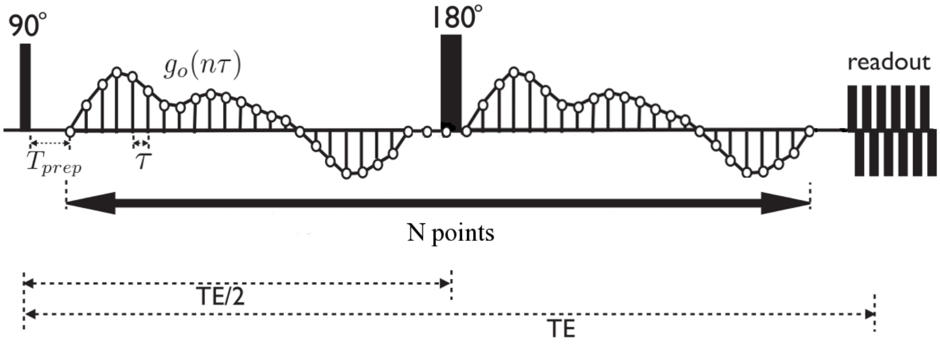

Figure 2.9: Schematic representation of a generalized waveforms with fixed gradient orientation. Adapted from [93]

where the elements of the matrices S, A and R have the following definitions

$$\begin{aligned} S_n(\mathbf{q}) &= V^{-1/2} \int u_n(\mathbf{r}) \exp(i2\pi\mathbf{q}\cdot\mathbf{r}) d\mathbf{r} \\ R_{nn} &= \exp(-\lambda_n D\tau) \\ A_{nn'}(\mathbf{q}) &= \int u_n * (\mathbf{r}) u_{n'}(\mathbf{r}) \exp(i2\pi\mathbf{q}\cdot\mathbf{r}) d\mathbf{r}, \end{aligned} \tag{2.45}$$

V is the pore volume and $\mathbf{q} = q\hat{\mathbf{g}}$ where $\hat{\mathbf{g}}$ is the unit gradient vector.

This approach is commonly known as the matrix method (MM), and has been implemented in recent pulse sequence optimization studies [93, 94] for restricted diffusion inside cylinders. Similar to the GPD approximation, MM can accommodate restricted diffusion inside geometries that have an analytical expression for the eigenfunctions $u_n(\mathbf{r})$ [95].

The above method has recently been extended for gradients with time varying orientation [96]. In the case of fixed orientation, the vector $\mathbf{q}$ is the same at every time point $n\tau$ which allows the precalculation of matrices $A(\mathbf{q})$ and $S(\mathbf{q})$. However, when the gradient orientation is time-dependant, the vector $\mathbf{q}$ is different at different time points and the matrices also depend on time. Thus equation 2.44 becomes:

$$E = S(q\hat{\mathbf{g}}_\mathbf{1}) R [A(q\hat{\mathbf{g}}_\mathbf{2})]^{m_2} R ... R [A(q\hat{\mathbf{g}}_\mathbf{N-1})]^{m_N - 1} R S^T(-q\hat{\mathbf{g}}_\mathbf{N}) \tag{2.46}$$

where $\hat{\mathbf{g}}_\mathbf{n}$ denotes the gradient orientation at time $n\tau$.

Calculating the matrices $A(q\hat{\mathbf{g}}_\mathbf{N})$ element-by-element at each time point is too computationally expensive. Drobnjak et al [96] shows an efficient implementation for cylindrical and spherical restriction, which we use for various experiments presented in this thesis, as well as in the implementation of MISST, detailed in chapter 7.

Multiple correlation function (MCF)

Multiple correlation function is another approach for computing restricted diffusion signal which has been introduced by Grebenkov [97]. Similarly to the method developed by Callaghan, it uses a matrix formalism to compute the signal for piece-wise constant gradients, however it is derived from a different theoretical starting point. MCF approach starts from the Bloch-Torrey equation:

$$\frac{\partial M_{\perp}(\mathbf{r},t)}{\partial t} = D\nabla^2 M_{\perp}(\mathbf{r},t) - i\gamma B(\mathbf{r},t)M_{\perp}(\mathbf{r},t), \tag{2.47}$$

where $M_{\perp}$ is the perpendicular magnetization, $B(\mathbf{r},t) = B_0 + G(t)\hat{\mathbf{g}} \cdot \mathbf{r}$ is a space-varying magnetic field (superposition of the main magnetic field and diffusion gradients) and the signal is normalized for $T2$ decay. This form of the Bloch-Torrey equation can also be considered as a diffusion equation, to which the effect of magnetic field encoding has been added [82]. The aim is to solve for the magnetisation $M_{\perp}$ which provides the MR signal:

$$E = \int_{\mathbf{r}} M_{\perp}(\mathbf{r},t)\rho(\mathbf{r})d\mathbf{r} \tag{2.48}$$

where $\rho(\mathbf{r})$ accounts for the effects of the initial distribution of the magnetization, the sampling sensitivity of the coils, etc [82].

The key to the solution is to represent the magnetisation $M_{\perp}$ in the basis of eigenfunctions of the Laplace operator within the restricted domain:

$$M_{\perp}(\mathbf{r},t) = \sum_m c_m(t)u_m(\mathbf{r}) \tag{2.49}$$

where $u_m(\mathbf{r})$ are the eigenfunctions of the Laplace operator and c_m are time dependent coefficients. Substituting the eigenfunction expansion in equation 2.47 to calculate the time-dependent coefficients and computing the integral in equation 2.49, the signal for a piece-wise constant gradient is given by the matrix product [82]:

$$E = U \prod_{n=0}^{N} \exp\left(-\left(\frac{\tau_n}{T} p\Lambda + i q_n \mathcal{B}\right)\right) U^* \tag{2.50}$$

where the product is computed over N intervals with constant gradient strength G_n and duration τ_n ($T = \sum_n \tau_n$). Vectors U and U^* encode the initial spin distribution $\rho(\mathbf{r})$, $p = \frac{DT}{L^2}$ with L the length scale of the pore, $q_n = \gamma G_n \delta_n$ and matrices Λ and $\mathcal{B}$ reflect the pore geometry and have the following expressions:

$$\begin{aligned} \Lambda_{m,m} =& \lambda_m L^2 \\ \mathcal{B}_{m,m'} =& \frac{1}{L} \int_{\mathbf{r}} d\mathbf{r} u_m^*(\mathbf{r})(\hat{\mathbf{g}} \cdot \mathbf{r}) u_{m'}(\mathbf{r}) \end{aligned} \tag{2.51}$$

where λ_m are the eigenvalues of u_m and * denotes the complex conjugate.

Monte Carlo simulation

Numerical simulations have been used in many studies to validate theoretical approaches of computing the diffusion signal or to understand the effects of various parameters are cannot be accurately described by analytic models (e.g. [83, 92, 95, 87, 98, 99, 100]). The majority of algorithms used to simulate the diffusion motion and compute the signal attenuation are part of the broad class of Monte Carlo (MC) Markov Chain algorithms. The numerical simulations are very flexible and are used to generate realistic synthetic diffusion data for arbitrary pulse sequences and restricting geometries. For example, Hall et al [101] study the convergence of the diffusion signal inside complex geometries depending on the simulation parameters and Panagiotaki et al [102] show the potential of the methods using realistic 3D meshes. The main drawback of MC simulation is the computational complexity. It usually requires a computer cluster for a reasonable running time, and therefore it is not suitable for voxel-based parameter fitting applications, though this can be mitigated by using a synthesized database approach [99, 103].

2.3.5 Diffusion spectrum

In the early 80s, Stepisnik [104] has studied the NMR signal when a train of 180^o RF pulses (Carr-Purcell-Meiboom-Gill CPMG sequence) was applied in addition to a constant magnetic field gradient, which resulted in an effective oscillating gradient waveform. The theoretical results showed that diffusion measurements can determine the spectrum of the particle velocity autocorrelation function $\langle \mathbf{v}(t)\mathbf{v}(0)\rangle$, where $\langle\cdot\rangle$ denotes the molecular ensemble average. This approach has been considered in a later study by Callaghan and Stepisnik [105] to investigate the diffusion spectrum of various oscillating gradients such as sinusoidal or square waveforms. This technique is known in the literature as "temporal diffusion spectroscopy".

The diffusion spectrum $\mathbf{D}(\omega)$, which is a generalisation of the diffusion coefficient in equation 2.31, is defined as the Fourier transform of the velocity autocorrelation function [105, 104]:

$$\mathbf{D}(\omega) = \frac{1}{2}\int_0^\infty \langle \mathbf{v}(t')\mathbf{v}(0)\rangle e^{i\omega t'} dt' \tag{2.52}$$

where $\langle \mathbf{v}(t)\mathbf{v}(t+dt)\rangle$ describes how dependent is $\mathbf{v}(t+dt)$ on $\mathbf{v}(t)$ and $\mathbf{D}(\omega)$ describes diffusion on the time scale of $2\pi/\omega$. For Brownian motion, the particle position and velocity are independent on the previous state, also known as the Markov property. This is true when dt is larger than a certain value called velocity auto-correlation time τ_c which depends on the molecular interactions and for the systems we are studying is on the order of $\approx 10^{-10}$ s [106]. Thus, for free diffusion the velocity autocorrelation function decays fast to 0 after the correlation time τ_c [106] and resembles a delta function. The resulting diffusion spectrum is constant. For restricted diffusion, the Markov property does not hold anymore, and there is a negative velocity autocorrelation caused by the reflection on the boundaries. In this case the diffusion spectrum is frequency dependent and exhibits a deficit at low frequencies. These two situations are illustrated in Fig. 2.10.

The normalized signal attenuation measured at the echo time can be calculated according to

$$\begin{aligned} &S(2\tau) = \exp(-\beta(2\tau)) \\ \text{with}\quad &\beta(2\tau) = \frac{\gamma^2}{\pi}\int_0^\infty \mathbf{F}'^T(\omega)\mathbf{D}(\omega)\mathbf{F}'(-\omega)d\omega \end{aligned} \tag{2.53}$$

In equation 2.53, the gradient modulation spectrum $\mathbf{F}(\omega)$ is the Fourier transform

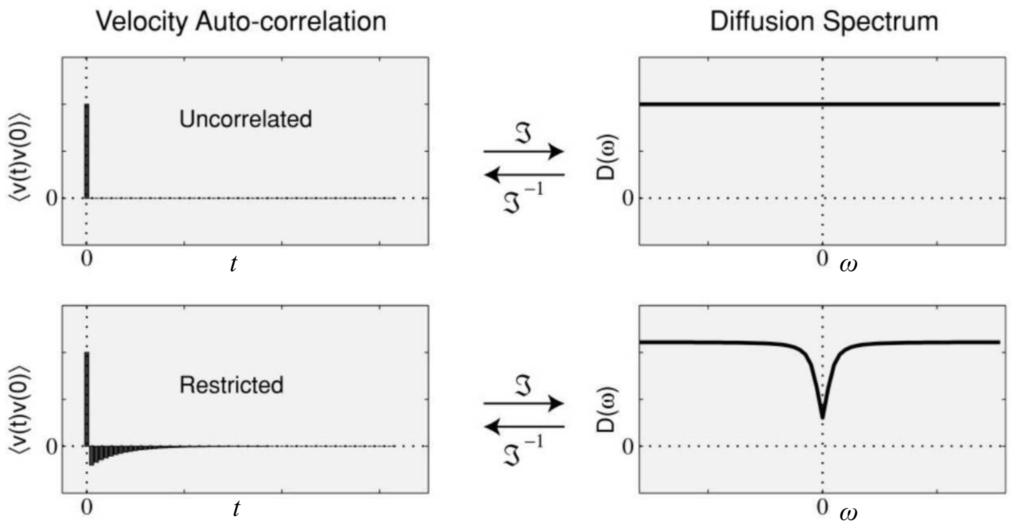

Figure 2.10: Velocity autocorrelation function and diffusion spectrum for free and restricted diffusion. (Figure from [106])

of the diffusion gradient integral $\mathbf{F}(t) = \int_0^t \mathbf{G}(t')dt'$.

$$\mathbf{F}'(\omega) = \int_0^{2\tau} e^{i\omega t}\mathbf{F}(t)dt \tag{2.54}$$

The spectral formulation is especially important for studying the effect of more complex gradient waveforms such as oscillating gradients, as it illustrates which diffusion times contribute to the ADC value.

2.3.6 Beyond standard sequences: oscillating gradients and double diffusion encoding

The standard diffusion encoding is the SDE sequence illustrated in Fig. 2.8. However, the sensitivity of the diffusion signal to various tissue characteristics such as cellular size, shape or volume fraction can be improved by using more advanced sequences. Here we introduce oscillating gradients and double pulsed field gradients, which are directly related to this work. If there is prior knowledge of the tissue architecture, the sensitivity of the diffusion measurements can be further increased by optimising the sequence parameters.

Oscillating diffusion gradients

Oscillating diffusion encoding (ODE) sequences [107] replace the pulsed gradient in the standard SDE sequence with oscillating gradient waveforms, such as sine, cosine, square or trapezoidal waveforms as illustrated in Fig. 2.11. This has the effect of reducing the diffusion time of the experiment from the interval Δ between the two rectangular pulses in the SDE measurement to half period of the oscillation (1/2ν). Thus by tuning the oscillation frequency, ODE sequences are more sensitive to intrinsic diffusivity for a wider range of pore sizes.

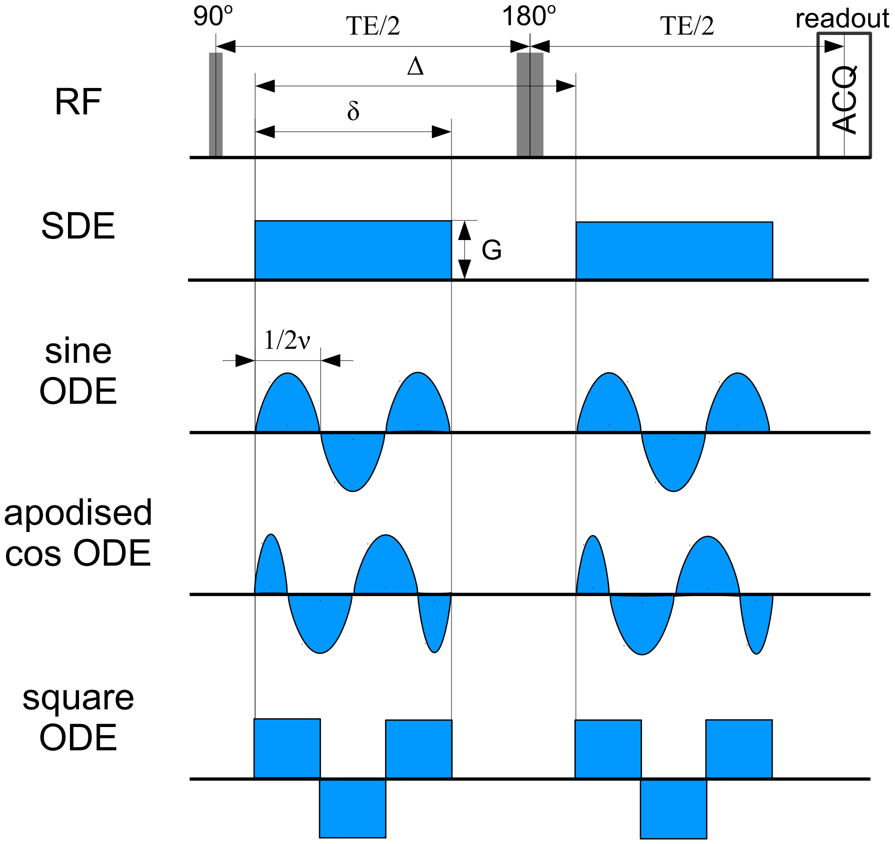

Figure 2.11: Schematic representation of single and oscillating diffusion encoding (ODE) sequences with sine, apodised cosine and square gradient waveforms.

The most common application of ODE sequences is to measure the diffusion spectrum $D(\omega)$, which is referred in the literature as 'temporal diffusion spectroscopy' [105, 106, 108]. As seen in equation 2.53, the gradient modulation spectrum $\mathbf{F}(\omega)$ indicates which components of $D(\omega)$ are measured in the experiment. For cosine-like oscillating gradients, $\mathbf{F}(\omega)$ has only one peak at the oscillation frequency and the measured ADC corresponds to $D(\omega)$. Thus studying the dependence of ADC on gradient frequency for cosine-like waveforms provides a measure of the diffusion spectrum. More recent studies use ODE sequences to estimate microstructural features, either by modelling the ADC dependence as a function of pore size [109] or by fitting a tissue model directly into the signal [87]. Previous work on modelling the diffusion signal acquired with ODE sequences is detailed in section 2.4.3

Double and multiple diffusion encoding

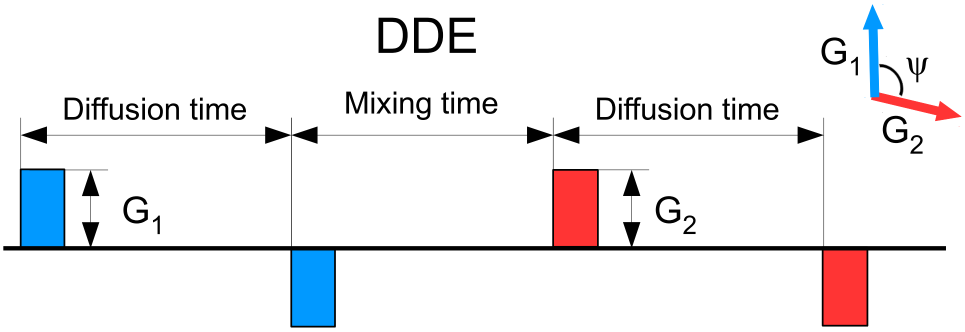

Figure 2.12: Schematic representation of a double diffusion encoding (DDE) sequence

The double diffusion encoding (DDE) sequence [110] in Fig. 2.12 concatenates two gradient pulses separated by a mixing time. This can be extended to multiple diffusion encoding (MDE) [111] which has an arbitrary number of concatenations of the SDE sequence separated by additional mixing times.

The motivation for the DDE sequence, and in general MDE, is that it probes the correlation of the water mobility at different time scales and in different directions, which can provide sensitivity to features invisible, or significantly less visible, to SDE, such as pore shape or exchange rate.

DDE - Theoretical aspects

The diffusion signal for an SDE sequence with narrow gradient pulses is given by equation 2.37, and can be easily extended for multiple gradient pulses [111, 112]. For DDE sequences with short gradient pulses and the same gradient separation Δ, the diffusion signal written in terms of $\mathbf{q} = (2\pi)^{-1}\gamma\delta G$ has the following form:

$$\begin{aligned} E(\mathbf{q}_1, \mathbf{q}_2, \Delta, \tau_m) = &\int d\mathbf{r}_0 \rho(\mathbf{r}_0) e^{i2\pi\mathbf{q_1 r_0}} \times \int d\mathbf{r}_1 P(\mathbf{r}_0|\mathbf{r}_1, \Delta) e^{-i2\pi\mathbf{q_1 r_1}} \\ &\times \int d\mathbf{r}_2 P(\mathbf{r}_1|\mathbf{r}_2, \tau_m) e^{-i2\pi\mathbf{q_2 r_2}} \times \int d\mathbf{r}_3 P(\mathbf{r}_2|\mathbf{r}_3, \Delta) e^{i2\pi\mathbf{q_2 r_3}} \end{aligned} \tag{2.55}$$

where r_i indicate the position during the application of the gradient pulses and $P(\mathbf{r}|\mathbf{r}', T)$ is the diffusion propagator which indicates the probability of a particle to move from position $\mathbf{r}$ to $\mathbf{r}'$ during time interval T.

In practice, protocols of DDE measurements cover different subsets of the full measurement space depending on what dispersion behaviour and/or microscopic sample features they intend to investigate. For example, the DD-COSY (Diffusion-Diffusion Correlation Spectroscopy) experiment [113] aims to reveal microscopic anisotropy in macroscopically isotropic samples by correlating diffusion measurements in different directions. The simplest version of the experiment is performed at short mixing times and it fixes the pulse durations and diffusion times. Then multiple measurements with varying gradient amplitudes are acquired with either aligned or perpendicular orientations [113, 114]. The data can be analysed assuming a diffusion signal model of microscopic anisotropy, or performing a 2D inverse Laplace transform. On the other hand, the DEXSY (Diffusion-Diffusion Exchange Spectroscopy) experiment [113, 114] aims to reveal exchange processes in compartmental systems. This experiment fixes the pulse durations and diffusion time and it varies the gradient amplitudes along a given direction. During the measurements the mixing time is long to allow for exchange between different water pools.

Another well known experiment for measuring diffusion correlation is angular DDE [111, 115, 116, 117, 118] which varies just one parameter, namely the angle between the two gradient orientations. In this case, the gradient amplitude, duration and diffusion time are the same for the two pulses. At short mixing time τ_m the difference between parallel and anti-parallel gradient orientation increases with pore size and at long τ_m the difference between parallel and perpendicular gradient orientation increases with pore eccentricity. To better understand this fact we can further analyse equation 2.55 for long diffusion and mixing times.

In the long time limit $P(\mathbf{r}|\mathbf{r}'|, \infty) = \rho(\mathbf{r}')$ and defining the reciprocal pore space as $\tilde{\rho}(\mathbf{q}) = \int d\mathbf{r}\rho(\mathbf{r}) \exp(i2\pi\mathbf{q}\mathbf{r})$ equation 2.55 becomes:

$$E(\mathbf{q}_1, \mathbf{q}_2) = |\tilde{\rho}(\mathbf{q}_1)|^2 |\tilde{\rho}(\mathbf{q}_1)|^2 \tag{2.56}$$

which gives the DDE signal for one pore. When we consider an ensemble of pores, the total signal is given by summing the individual contributions:

$$E_{tot}(\mathbf{q}_1, \mathbf{q}_2) = \sum_n |\tilde{\rho_n}(\mathbf{q}_1)|^2 |\tilde{\rho_n}(\mathbf{q}_1)|^2 \tag{2.57}$$

In the case of randomly oriented pores, the signal will not depend on the absolute orientation of $\mathbf{q_i}$, but may depend on the angle between $\mathbf{q}_1$ and $\mathbf{q}_2$ [111]. For spherical pores $\tilde{\rho_n}(\mathbf{q})$ depends only on the magnitude of $\mathbf{q}$, thus $E_{tot}(\mathbf{q}_1, \mathbf{q}_2)$ does not depend on the angle between the gradients. In contrast, for ellipsoids, $\tilde{\rho_n}(\mathbf{q})$ depends on the relative orientation of $\mathbf{q}$ to the main axis. After averaging over all possible pore orientation, the signal $E_{tot}(\mathbf{q}_1, \mathbf{q}_2)$ still depends on the relative angle between $\mathbf{q}_1$ and $\mathbf{q}_2$, as the product $|\tilde{\rho_n}(\mathbf{q}_1)|^2 |\tilde{\rho_n}(\mathbf{q}_1)|^2$ is taken before the summation. The effect appears in the fourth order expansion to the signal in $\mathbf{q}$ and is described in detail for various geometries in [117]. The signal difference between DDE with parallel and perpendicular gradients in the long mixing time limit is a signature of elongated pores. When the substrate is macroscopically anisotropic, as in brain tissue for example, a generalisation of the experiment also varies the orientation of G_1 [119, 120, 121]. Various approaches used for modelling microscopic anisotropy are discussed in section 2.4.4.

2.4 Diffusion MRI - Modelling

DW-MRI is one of the most computationally rich MRI modalities, as there are many different ways to acquire the data and to model the diffusion signal in order to extract meaningful information. Depending on the complexity of measurements and the way data is analysed, different tissue characteristics can be estimated. This section presents the most common models used to analyse the DW-MRI data, which can be separated into two main groups [122]:

- "signal models" expand the free diffusion model and introduce new parameters that enable increased agreement with the measured data;
- "biophysical models" generate a geometrical model of the underlying tissue and calculate the corresponding MR signal.

In the later part of the section we focus on the modelling approaches that are directly relevant to this work. Thus we describe previous studies which use ODE sequences to infer microstructural features and we present available modelling approaches to recover anisotropy at the subvoxel scale as well a distribution of pore sizes.

2.4.1 Signal models

Modelling diffusion MRI data works by developing analytic expressions of the signal and fitting them to the measurements. In case of signal models, the estimated parameters reflect the diffusion signal, however they are not necessarily related to histological tissue features. Here we present some of the commonly used approaches, starting with the simplest model of a mono-exponential function.

Apparent diffusion coefficient (ADC)

The simplest way to model the diffusion MRI signal is to assume free diffusion in an isotropic, homogeneous environment. In this case, equation 2.31 shows that the signal follows a mono-exponential decay and the metric that can be derived from such a measurement is the apparent diffusion coefficient (ADC):

$$ADC = -\frac{\log(S/S_0)}{b} \tag{2.58}$$

where S is the diffusion weighted signal, S_0 is the signal acquired without the diffusion encoding gradients and b is a measure of diffusion weighting which depends on sequence parameters, as shown in equation 2.31.

ADC is being used mainly for cancer imaging, as tumours are generally macroscopically isotropic [123, 124]. However, if the underlying tissue is anisotropic, such as white matter or muscle fibres, ADC depends on the direction of the gradient, thus the one-dimensional (1D) Gaussian model is not appropriate to describe the orientation dependence of molecular displacement [125].

Diffusion Tensor Imaging (DTI)

A more general description of free diffusion in anisotropic environments uses a three-dimensional (3D) Gaussian model of molecular displacement [125]. Thus, the scalar diffusivity D in equations 2.22 to 2.25 is replaced by a 3x3 symmetric tensor $\tilde{\mathbf{D}}$ with elements $D_{\alpha\beta}$, where α and β take each of the Cartesian coordinates [73]

$$\tilde{\mathbf{D}} = \begin{pmatrix} D_{xx} & D_{xy} & D_{xz} \\ D_{yx} & D_{yy} & D_{yz} \\ D_{zx} & D_{zy} & D_{zz} \end{pmatrix} \tag{2.59}$$

In this case the diffusion signal depends on the gradient direction:

$$S = S_0 \exp(-b\hat{\mathbf{g}}^T \tilde{\mathbf{D}} \hat{\mathbf{g}}), \tag{2.60}$$

where S_0 is the signal without diffusion encoding gradient, b is the diffusion weighting factor and $\hat{\mathbf{g}}$ denotes the gradient direction. Equation 2.60 has 7 independent parameters, thus at least 7 measurements are necessary to estimate the diffusion tensor $\tilde{\mathbf{D}}$: one measurement with $b = 0$ and 6 measurements with non-zero diffusion weighting and non-collinear gradient orientations ($\mathbf{g}_i \times \mathbf{g}_j \neq 0, for i \neq j$). In practice, for robust parameter estimates and to reduce the influence of noise and the orientational variance, at least 20-30 isotropically distributed gradient directions are necessary [126]. Most diffusion tensor imaging (DTI) studies use b-values in the range 600-1200 s/mm^2, which yields on average an approximate signal attenuation of 0.5 [127].

After the diffusion tensor is estimated from the data, we can perform an eigen decomposition of $\tilde{\mathbf{D}}$ in order to calculate the eigenvectors $\hat{\mathbf{d}}_1$, $\hat{\mathbf{d}}_2$ and $\hat{\mathbf{d}}_3$ and the corresponding eigenvalues $\lambda_1 \geq \lambda_2 \geq \lambda_3$. This representation provides the principal directions of diffusion and the corresponding diffusivities. In practice, different functions of the eigenvalues are used to characterize the size and shape of the diffusion tensor. The simplest metric is mean diffusivity:

$$MD = \frac{1}{3}\text{Trace}(\mathbf{D}) = \frac{D_{xx} + D_{yy} + D_{zz}}{3} = \frac{\lambda_1 + \lambda_2 + \lambda_3}{3}. \tag{2.61}$$

Another commonly used metric which is rotationally invariant is fractional anisotropy, which describes the departure of $\mathbf{D}$ from isotropic diffusion [128]:

$$FA = \sqrt{\frac{3}{2}} \frac{\sqrt{(\lambda_1 - \bar{\lambda})^2 + (\lambda_2 - \bar{\lambda})^2 + (\lambda_3 - \bar{\lambda})^2}}{\sqrt{\lambda_1^2 + \lambda_2^2 + \lambda_3^2}}. \tag{2.62}$$

DTI is widely used for brain imaging, however there are a number of clear limitations of this technique [125]. First, the DTI model provides only a voxel-averaged diffusion tensor which cannot accurately describe more complex tissue configurations such as crossing fibres in the brain. Second, as the b-value is increased there is a departure from mono-exponential decay due to diffusion in the intracellular space, and the Gaussian displacement model is no longer appropriate.

Next, we present some basic approaches to recover complex fibre configurations as well as signal models which aim to explain the deviation from Gaussianity of the signal, then we focus on the biophysical models which are more relevant to this work.

Reconstructing multiple fibres

With the introduction of High Angular Resolution Diffusion Imaging (HARDI) acquisition, which uses a larger number of gradient orientation, it is possible to image the intra-voxel heterogeneity of white matter fibres [129]. Various data analysis methods have been developed in order to estimate the configuration of fibres. One of the first proposed methods is a mixture of diffusion tensors [129], with the first eigenvector of each tensor providing the main direction of the fibre populations. Non-parametric techniques such as diffusion spectrum imaging (DSI) [130, 131] and QBall [132, 133] aim to recover the diffusion orientation distribution function (dODF) directly from q-space imaging, using an inverse Fourier Transform or a spherical Funk-Radon transform, respectively. On the other hand, spherical deconvolution methods [134, 135] aim to recover directly the fibre orientation distribution function (fODF).

Accounting for non-Gaussian diffusion

In free diffusion the probability distribution of the spin displacement follows a Gaussian distribution (equation 2.26), giving rise to a mono-exponential decay of the diffusion MRI signal as a function of b-value. However, in biological tissue, diffusion is restricted by cellular membranes and the spin displacements are no longer described by the same Gaussian probability distribution, therefore this regime is commonly referred in the literature [136] as non-Gaussian diffusion. In this case the diffusion MRI signal departs from a mono-exponential decay, and there are many different approaches proposed in the literature to model this effect.

Diffusion kurtosis imaging (DKI) is an extension of DTI that aims to quantify the departure from mono-exponential signal decay [137]. In addition to the apparent diffusion coefficient, the method provides an estimate of the excess kurtosis of the diffusion displacement probability distribution.

$$\ln S = \ln(S_0) - bD_{app} + \frac{1}{6}b^2 D_{app}^2 K_{app}^2 + O(b^3) \tag{2.63}$$

If the full kurtosis tensor is estimated, then the model has 22 parameters and requires measurements with at least two different non-zero b-values. Obtaining robust DKI estimates is more challenging than the simpler DTI metrics and there are various strategies discussed in the literature [138, 139]. Moreover, some kurtosis metrics can be correlated with microstructural features [140].

A bi-exponential model explains the departure from Gaussian diffusion by assuming two non-exchanging water pools with slow and fast diffusion [141]:

$$S = f_{slow} \exp(-b\hat{\mathbf{g}}^T \tilde{\mathbf{D}}_{slow} \hat{\mathbf{g}}) + f_{fast} \exp(-b\hat{\mathbf{g}}^T \tilde{\mathbf{D}}_{fast} \hat{\mathbf{g}}) \tag{2.64}$$

where $\tilde{\mathbf{D}}_{slow}$ and $\tilde{\mathbf{D}}_{fast}$ represent the slow and fast diffusion tensors and f_{slow} and f_{fast} are their respective volume fractions. The slow compartment is usually associated with diffusion in the intracellular space and the fast one with diffusion in the extracellular space. A bi-exponential model is also used to describe the intra-voxel incoherent motion (IVIM) [142] which arises due to blood flow through capillaries and can be measured with diffusion MRI at low b-values (b <200 s/mm^2).

Another approach to explain the deviation from mono-exponential decay is to assume a distribution of diffusivities, which is usually referred to as a statistical model [143]:

$$S = S_0 \int_0^\infty P(D) \exp(-bD) dD. \tag{2.65}$$

The model in [143] assumes a normal distribution of diffusivities with mean ADC and standard deviation σ and maps these parameters in the brain. Starting from a similar theoretical standpoint, other studies [144, 145] characterize the signal arising from a distribution of diffusivities using a stretched exponential model:

$$S = S_0 \exp -(bD)^\alpha. \tag{2.66}$$

where α is the stretching parameter, which characterizes the deviation of the signal attenuation from mono-exponential behaviour.

All these models explain well the diffusion signal and aim to find biomarkers that can differentiate regions of interest or correlate with the progression of pathology. However the estimated parameters do not necessarily correspond to microstructural tissue features.

2.4.2 Biophysical models

Biophysical models provide a geometrical representation of the underlying tissue. Then, they are used to calculate the corresponding MR signal and solve the inverse problem to estimate tissue features given the measured data. Depending on the application different tissue properties are modelled. Historically, biophysical models of diffusion MRI data were first developed to represent the signal in white matter. Here we present the most relevant models of white matter in a roughly chronological order, then we discuss biophysical models of non-brain tissue and cancer and we conclude this section with models of microscopic anisotropy and pore size distribution which are directly relevant to this thesis.

Stanisz' model of optic nerve

One of the first biophysical models that describe diffusion signal in white matter was proposed by Stanisz et al[23]. The study investigates bovine optic nerves and represents the tissue using three compartments: prolate ellipsoids (axons), spheres (glial cells) and hindered diffusion (extracellular space) with exchange between the compartments [146]. To calculate the restricted diffusion signal the model uses the SPG approximation discussed in 2.3.4. As there is no analytical solution for ellipsoids, the work approximates it as restricted diffusion in between parallel planes with an orientation dependent separation. The model estimates tissue related features such as average axon diameter and length (short and long axis of ellipsoids), the size of glial cells (sphere radius), diffusivities in the intra- and extra-cellular space as well as membrane permeabilities. Fitting this model requires high quality data with many different measurements. In this study, the nerve sample was carefully aligned parallel and perpendicular to the magnetic field and high quality NMR data with SNR > 1000 was acquired with multiple gradient strengths and diffusion times. Translating this model to in-vivo MRI with limited acquisition time and an SNR up to 50 is virtually impossible. Thus simpler models that describe the key features of tissue are necessary.

Ball and Stick model

The ball and stick model introduced by Behrens et al [147] is a simple two-compartment white matter model that is feasible for clinical MRI. In the intra-axonal space diffusion occurs only in the parallel direction (stick) with diffusivity d, while in the extra-axonal space diffusion is isotropic (ball), with the same diffusivity. Thus the signal can be written as the weighted sum of the two compartments:

$$S = S_0 \left(f \exp(-bd(\hat{\mathbf{n}} \cdot \hat{\mathbf{g}}) + (1-f) \exp(-bd) \right) \tag{2.67}$$

where f is the volume fraction of the anisotropic compartment, $\hat{\mathbf{n}}$ is the fibre direction and $\hat{\mathbf{g}}$ is the direction of the diffusion gradient. Ball an stick can be easily extended to model multiple fibre populations by adding additional "stick" compartments [148]. While simplicity is a key when having a limited amount of data, this model cannot represent microstructural tissue features such as axon diameter.

CHARMED and AxCaliber

Assaf's work builds on the idea of a multi compartment model and introduces a more realistic depiction of the intra-axonal space. Unlike ball and stick, composite hindered and restricted model of diffusion (CHARMED) [149] represents the intra-axonal space as a distribution of cylinders. Extracellular space is represented as hindered diffusion with a cylindrically symmetric diffusion tensor (Zeppelin compartment according to the taxonomy in [150]). For the intra-axonal space, the model assumes one or two fibre populations. The distribution of axon diameters and intracellular diffusivity perpendicular to the fibres are fixed to typical values for axons in the spinal cord. Thus the model recovers the fibre orientation, intracellular diffusivity parallel to the fibres, extracellular diffusivities and the corresponding volume fractions.

A later technique developed in the same research group, AxCaliber [5], extends the CHARMED model and estimates the distribution of axon diameters, assuming a known fibre direction. Based on previous histological work by Aboitiz [35], the axon diameters are assumed to follow a Gamma distribution. The restricted diffusion signal can be written as a volume weighted sum over the contributions from axons with different diameters:

$$S_r = \sum_i w_i \frac{f_i}{\pi(2R_i)^2} S_{r,i}, \quad \text{with, } w_i(\alpha,\beta) = \frac{(2R_i)^{\alpha-1} e^{-\alpha/\beta}}{\beta^\alpha \Gamma(\alpha)} \tag{2.68}$$

where S_r is the total restricted signal, $S_{r,i}$ is the restricted signal from axons with radius R_i and the weights w_i follow a Gamma distribution with shape parameter α and scale parameter β. Data is acquired perpendicular to the nerve fibres with multiple combinations of gradient strengths and diffusion times. The correspondence between histology and MR measurements of axon diameter in sciatic and optic nerve tissue specimens is really good. This technique has been further used in-vivo to estimate the axon diameter distribution in the rat corpus callosum [6]. This approach requires many measurements perpendicular to the nerves, assuming prior knowledge of the fibre orientation.

ActiveAx

To overcome these limitations, Alexander [151] developed a computational framework to optimise a rotationally invariant DW-MRI acquisition, which makes the estimation of axon diameter feasible in a clinical set-up. In order to increase the robustness of the parameter estimates, [151] simplified the tissue model and describes the fibre population as randomly packed, identical parallel cylinders. The extracellular space features hindered diffusion, as described in the CHARMED model. In order to account for partial volume effects from the cerebral spinal fluid (CSF), one more compartment

compartment featuring isotropic free diffusion is added. (In term of the taxonomy used in [150], this model is ZeppelinCylinderBall). Thus, ActiveAx estimates the axon diameter index, which correlates well with the mean volume-weighted diameter, fibre orientation and volume fractions of the different compartments. The intracellular diffusivity and extracellular diffusivity parallel to the axons are equal and fixed, and the hindered diffusivity perpendicular to the fibres is computed using a simple turtuosity constraint $d_{\perp} = d_{\|}(1-f)$ [152], where f is the axonal volume fraction. In a later study [9] Alexander et al uses the ActiveAx framework to estimate the axon diameter index in the human corpus callosum in-vivo and in the monkey brain ex-vivo. As previous models showed [23], an additional fully restricted water compartment is needed for the ex-vivo data. Although the model reduces the characterization of the axon diameter distribution to a single volume-weighted diameter index, it still requires high quality data and large gradient strengths in order to estimates small axon diameters. As the gradient strength increases, smaller sizes can be detected and measured using diffusion data [153]. Thus, in-vivo axon diameter estimation can be significantly improved by using data from the human Connectome scanner, which has higher diffusion gradients up to 300 mT/m [154] compared to standard clinical gradients of less than 100 mT/m.

Modelling fibre dispersion

Previous models assume one or more fibre populations with parallel axons in each voxels, however these configuration cannot accurately describes regions of bending or fanning fibre bundles which are widespread throughout the brain [155].

Jespersen et al [122] developed a model that can capture the distribution of axons and dendrites both in white matter, which can be highly anisotropic, as well as grey matter which is more isotropic. They use a two-compartment model with an isotropic tensor (ball) to describe diffusion in the extracellular space and a distribution of cylindrically symmetric anisotropic tensors to describe intra-axonal diffusion. To describe a general distribution, they chose to expand it in terms of spherical harmonics and to estimate the corresponding coefficients in addition to the tensor diffusivities and the volume fraction. The model prediction agrees very well with the experimental data which was acquired from a monkey brain ex-vivo with many different b-values and gradient orientations.

Zhang et al [11] extends the model proposed in ActiveAx and aims to recover the axon diameter index in the presence of dispersion. To this end, they use a parametric Watson distribution, which is a cylindrically symmetric directional distribution characterized by a single concentration parameter κ. Due to the reduced number of model parameters, the technique is suitable for estimating axon diameter index and orientation dispersion from in-vivo human data acquired with 4 different b-values and multiple gradient directions (4 HARDI shells).

In later work, Zhang et al [12] developed neurite orientation dispersion and density imaging (NODDI), a simplified version of the model above aimed for routine clinical imaging which requires only two different b shells. NODDI models the signal contribution from three compartments: Intra-neurite signal represented by sticks following a Watson distribution, extra-neurite signal modelled by a cylindrically symmetric tensor and CSF which exhibits free isotropic diffusion. Due to its simplicity and straightforward data acquisition, NODDI has been used in many different studies to characterize healthy and pathological brain tissue [156, 157, 158, 159].

The Watson distribution is symmetric around the main direction and cannot recover more complex fibre configurations featuring anisotropic dispersion such as fanning. Thus, the fibre orientation can be better described using a distribution that allows for anisotropic dispersion, such as Bingham, which is the analogue of a Gaussian distribution for directional data [160]. For instance Kaden et al [161] use a finite mixture of Bingham distributions in a parametric spherical deconvolution approach to separate crossing fibres which feature dispersion. The same orientation distribution is also used by Sotiropolous et al [162] to extend the ball-and-stick model and by Tariq et al [163] to extend the NODDI model.

General white matter compartment models

The models presented above are specific cases of multi-compartment models that capture various features of the tissue. In general, a multi-compartment model can be formed by suitable combinations of several compartments that represent the main water pools in the tissue such as intra- and extra-axonal space, CSF, glial cells, etc. This approach was taken by Panagiotaki et al [150] to describe the diffusion MR signal in the rat corpus callosum, ex-vivo. Ranking the models according to Bayesian Information Criterion (BIC), which accounts for the goodness of fit and number of parameters, shows that three compartment models with restriction along the fibre direction explain the data the best. A similar conclusion was drawn by Ferizi et al [164] for in vivo human data. A limitation of these two studies is that they investigated only models of coherently oriented fibres. A more recent work in the same group [165] includes fibre dispersion and shows that these model outperform the best models with coherent fibres. Many of these white matter models are discussed in a recent review study by Nilsson et al [51].

Restriction spectrum imaging

The multi-compartment models described above use a non-linear fitting algorithm to estimate the model parameters. Restriction spectrum imaging (RSI) extends the linear spherical deconvolution (SD) approach to obtain information at multiple length scales [166, 3]. This is achieved by replacing the single response function from conventional linear SD (usually a cylindrically symmetric diffusion tensor [167]) with a range of diffusion tensors. In later work [3] they also use response functions corresponding to cylindrical restriction for white matter modelling and spherical restriction for cancer modelling.

VERDICT and the emergence of cancer models

The majority of the diffusion MRI models described above have been developed for brain imaging. Vascular, extracellular and restricted diffusion for cytometry in tumours (VERDICT) [2] aims to extend the use of biophysical models for microstructure imaging in tumours. The VERDICT framework describes diffusion in three compartments:

- signal from intracellular water inside cells - modelled with restricted diffusion
- signal from water adjacent to cells and blood vessels (EES) - modelled with hindered diffusion
- signal from water in blood in the capillary network - modelled using perfusion

First the VERDICT method was demonstrated in xenograft colorectal tumours and the parameter estimates were in good agreement with histological finding and successfully differentiated between two tumour lines with different microstructures. The technique was translated to clinical imaging of prostate cancer patients [63] and the parameter estimates clearly differentiated between benign and cancer regions.

Estimating permeability

The biophysical models discussed above account for various tissue features, however, when modelling restriction they do not account for membrane permeability. The Kärger model [146] is a well-known approach for including permeability, however it assumes two well mixed pools of water and does not account for restriction, which yields biased estimates [99]. Modelling restricted diffusion inside pores with permeable membranes can be achieved by changing the boundary condition in equation 2.34, however there is no analytical model for the extracellular space. [168] includes the effects of restriction by modelling a time-dependent diffusivity in the Kärger model, while more recent work accounts for an infinite equidistant array of permeable barriers [169], however, it does not include extra-cellular space. A database approach with Monte Carlo simulations including restriction and exchange, has been used to test the accuracy of the Kärger model, showing that the analytical model yields biased estimates of volume fractions for exchange times < 350 ms. Moreover, the exchange time values are more difficult to estimate compared to other model parameters [99]. A more recent study which uses machine learning to estimate axon diameter and membrane permeability from Monte Carlo simulations has also shown that the two effects cannot be well separated using standard SDE measurements [103]. Another technique assumes two water pools with slow and fast diffusion and estimates the apparent exchange rate between them using DDE sequences with various mixing times [170]. In healthy white matter, Nilsson et al [171] suggest long exchange time on the order of seconds. Thus, for commonly used diffusion times which are in the range of tens of milliseconds, considering impermeable membranes is a valid assumption. The same study showed a lower exchange time for viable tissue in tumours (≈ 300 ms), thus assuming impermeable membranes in this case might lead to biased pore size estimates if the measurements have long diffusion times. When the measurements have shorter diffusion time, such as ODE sequences, then this effect is negligible [172].

2.4.3 Models for oscillating gradients

Temporal diffusion spectroscopy

The most common way of performing an ODE experiment is to study the diffusion spectrum. So far the diffusion spectrum has been studied for sinusoidal and rectangular modulation [105, 106]. For sine and square oscillations, the gradient spectrum has maxima at $\omega = 0$ and $\omega = \omega_0$, where ω_0 is the angular frequency of the gradient. If a $\pi/2$ phase is introduced, i.e. cosine waveform, the peak at $\omega = 0$ is cancelled, and the gradient probes the diffusion spectrum at a single frequency $\omega = \omega_0$. Thus, the apparent diffusion coefficient (ADC) measured with a cosine-like waveform corresponds directly to the value from the diffusion spectrum. In order to compute the ADC, the b-value for oscillating gradients is required. The expressions of the b-values for sinusoidal waveforms that have been used so far in temporal diffusion spectroscopy studies are given in Appendix A.

In the first in-vivo temporal diffusion spectroscopy study, Does et al [106] investigated the dependence of ADC on diffusion time in the normal and globally ischemic rat brain. They investigated three different gradient waveforms: sine, double sine and apodised cosine. As theory predicts, the dependence of ADC on diffusion time was less pronounced for sine gradients due to the $\omega = 0$ frequency peak in the power spectrum, as discussed above. Aggarwal et al [173] extends the analysis to a frequency dependent diffusion tensor and investigates separately the dependence of parallel ($\lambda_{||}$) and perpendicular ($\lambda_{\perp}$) diffusivities in normal and demyelinated rat brain tissue. The results show different frequency dependencies of $\lambda_{||}(\omega)$ and $\lambda_{\perp}(\omega)$ in various parts of the brain as well as for different stages of demyelination and remyelination. The data used in this study was acquired with one b-value $\approx$ 700 s/mm^2. In order to better characterise the complex tissue structure, Portnoy et al [174] acquired SDE and ODE data over a large range of diffusion times and b-values. To explain the deviation from monoexponential decay with increasing b-value, they fitted a kurtosis model to the data, and the results show decreasing apparent kurtosis with increasing gradient frequency. Moreover, by explicitly modelling the dependence of ADC(ω), they estimated the restriction size in various areas of the brain. The above mentioned studies implemented ODE sequences on pre-clinical scanners with high diffusion gradients $\approx$ 700 mT/m. More recent studies by Van et al [108] and Baron et al [175] implement ODE sequences with trapezoidal and sinusoidal waveforms on clinical scanners and investigate the dependence of ADC, $\lambda_{\|}$, $\lambda_{\perp}$ and FA on frequency. The studies also investigate how to optimise the sequence parameters δ and Δ in order to obtain a sharper peak in the power spectrum. This point is detailed in section 3.3.2, as it constitutes a part of my work accomplished before these research articles were published.

Pore size estimation using ODE sequences

Most of the previous studies investigated the dependence of ADC and/or other DT related metrics on diffusion time (or gradient frequency). It is possible to extract further information about the tissue structure by modelling the diffusion spectrum $D(\omega)$ as a function of pore size [78]. $D(\omega)$ can be written in terms of the diffusion coefficients in the long and short time limit and the geometric factors B_n and λ_n which describe restriction [174]:

$$D(\omega) = D_0 + \sum_n B_n \frac{a_n(D_\infty - D_0)\omega^2}{a_n^2(D_\infty - D_0)^2 + \omega^2}. \tag{2.69}$$

The explicit formulae for B_n and λ_n are given in the Appendix A. Thus, by explicitly modelling $D(\omega)$, Portnoy et al [174] also extracted pore size information from the ODE data.

Another approach to estimate pore size is to fit a biophysical model to the acquired ODE data, which requires an analytical signal model for ODE sequences. This can be achieved using the GPD approximation described in section 2.3.4. Xu et al [87] derived such expressions for sinusoidal gradient waveforms and validated them against Monte-Carlo simulations. The work also extended the model of restricted diffusion to spherical shells, which is a good representation of cells with a nucleus inside. Later simulation studies have investigated the effect of variations in cell nuclear size [87], intracellular volume fraction, intranucleus and intracytoplasm diffusion coefficients, membrane permeability and T2 relaxations [176]. Such thorough simulation studies may be helpful to elucidate the biophysical mechanisms underlying measured diffusion changes. The experimental study of Li et al [109] follows up on previous work and uses cosine ODE measurements to estimate pore size in phantoms with hollow microcapillaries of various diameters. The results showed that ODE sequences can be used to estimate both intrinsic diffusivity and pore size, however the gradient used in this experiment was as high as 1.88 T/m.

2.4.4 Models of microscopic anisotropy

The quantification of microscopic diffusion anisotropy aims to disentangle the effects of orientation distribution from microstructural features, which has potential for characterizing white matter integrity [119], grey matter cytoarchitectures [14] or distinguishing between different tumour types [177].

The techniques discussed so far use a collection of SDE or ODE measurements which are sensitive to pore-size distribution in known isotropic pores or coherently oriented anisotropic pores. However, SDE and ODE sequences, which have constant gradient orientation, fail to discriminate between more complex systems, such as certain configurations of isotropic pores with a size distribution and randomly oriented anisotropic pores [117]. This section illustrates the most common techniques used to estimate microscopic anisotropy and briefly discuss the sequences they use. It presents both biophysical models of restriction as well as signal models that can provide a measure of microscopic anisotropy.

Mitra showed theoretically that DDE sequences with varying angle between the two gradients provide sensitivity to pore size at short mixing times and to pore elongation at long mixing times [111], a fact that was experimentally verified for the first time in yeast cells [115]. This development lead to a number of modelling techniques that aim to recover microscopic anisotropy using DDE sequences.

Özarslan presents a comprehensive analysis of DDE signal in idealized experimental conditions (narrow gradient pulses, long diffusion time and long or vanishing mixing times) in closed pores [117] for simple geometries of spheres, ellipsoids and capped cylinders. The study also investigates the DDE signal for arbitrary sequence parameters when diffusion is restricted inside capped cylinders using the MCF signal model. Koch and Finsterbush [178] investigate in simulation the DDE signal dependence on sequence parameters and microstructural parameters such as pore size and eccentricity, and use DDE sequences with short mixing time to estimate pore sizes [116].

Shemesh et al uses DDE measurements to tell apart spherical pores from randomly oriented anisotropic pores using yeast cells and a phantom consisting of water-filled cylindrical compartments. Pore size is estimated using either a geometric model of spherical restriction or randomly oriented infinite cylinders [179].

Acquiring angular DDE measurements provide information regarding pore size and eccentricity only in the plane spanned by the gradient vectors, thus is not a suitable analysis for anisotropic substrates such as white matter. Lawrenz et al [119] provides a general description of the DDE signal behaviour in the presence of macroscopic anisotropy. They also extend the DDE acquisition to support the estimation of tensor elements and derive a rotationally invariant metric of microscopic anisotropy (MA), based on the difference between DDE measurements with parallel and perpendicular gradients. Jespersen et al [121] further extends the DDE acquisition to a rotationally invariant 5-design scheme that can applied to the cumulant expansion of the signal, which is more accurate than the Taylor expansion assumed in the previous work. Using again the difference between DDE measurements, they derive a rotationally invariant eccentricity metric (ϵ) and its normalized counterpart, fractional eccentricity (FE), which that is the same as FA in the case of coherent pores.

Another technique for estimating microscopic anisotropy has been recently introduced by Lasic et al [180]. This approach combines diffusion sequences that isotropically weight the signal in one measurement with directional sequences that have the same $q(t) = \int_0^t G(t)dt$ value, where $G(t)$ is the applied gradient waveform. Their derivation of a microscopic anisotropy metric, termed μFA, is based on the assumption that diffusion in each microdomain is Gaussian. Thus, this technique can disentangle the contribution to the diffusivity variance caused by the orientation dispersion of anisotropic microdomains and a distribution of diffusivities in each microdomain. More recent studies relax the assumption of directional and isotropic encoding and extend the computation of μFA to generalized gradients with varying orientation within one measurement [181, 182].

A similar idea is developed by Kaden et al [183], who proposed a method to disentangle the effect of orientation distribution and to estimate the microdomain diffusivity from a standard 2-shell HARDI acquisition. However this method assumes identical microdomains and cannot account for the variance that arises due to a distribution of diffusivities. This confirms the necessity of more advanced acquisition protocols in order to accurately characterize complex substrates.

2.4.5 Models of pore size distribution

Histological studies [35, 184] of the fibre composition in human corpus callosum have motivated white matter models such as CHARMED [149] and AxCaliber [5] to describe intra-axonal diffusion using a Gamma distribution of axon diameters. While this is a rather novel approach for biomedical imaging, diffusion NMR has been used for a long time to estimate pore size distributions in various emulsions, such as mixtures of water and oil [185, 186, 187]. Many studies assume a lognormal distribution which is a good approximation for homogeneously mixed emulsion systems, with a low-viscosity continuous phase [188].

A later study [188] presents a frameworks to estimate a non-parametric distribution of pore sizes in oil-in-water emulsions using standard SDE diffusion sequences. A more recent work [189] uses a similar framework to estimate size distribution in glass microcapillary arrays and shows that DDE sequences provide a more accurate estimation of the size distribution compared to SDE sequences. This study uses a model of infinitely long cylinders, a limitation that is addressed by estimating a joint radius-length distribution in order to account for finite pore eccentricities [190]. Although the distribution of sizes is estimated, the main orientation of the pores is assumed to be known, which is a major drawback in practical applications.

2.4.6 Summary

This section presents a wide range of modelling approaches to extract information from diffusion MRI signal. In a homogeneous medium, the diffusion signal decreases mono-exponentially with increasing diffusion weighting (b-value), however this is not the case in more complex substrates such as biological tissues. The signal models presented in the first part of this section aim to explain this deviation by including higher order terms in the signal expansion, adding more exponentials, considering a distribution of diffusivities, etc. The estimated parameters are correlated with the cellular features of interest however they are not a direct measure of microstructure. The biophysical models presented in the second part aim to overcome this issue and directly relate microstructural features to the diffusion data. Thus, depending on the complexity and assumptions of the model, tissue features such as cellular size, volume fraction, orientation distribution, elongation, etc. can be estimated.

Pitfalls of modelling diffusion MRI data

As seen in the last two sections, diffusion MRI is a rich modality with many different possibilities for signal acquisition and data analysis. Most of the models presented above explain the data well, so an immediate question arises: which is the right model?

The answer is not straightforward and it highly depends on the amount and quality of measured data as well as on the application of interest. If the acquisition protocol is very limited with only one b-value and several directions, then only the simplest models such as ADC and DTI are supported. DTI derived metrics such as ADC and FA have been used in various clinical applications, such as studying normal brain maturation and aging, cerebral ischemia, multiple sclerosis, epilepsy, tumours, etc [**?**]. Increase or decrease in ADC and/or FA can correlate with various pathologies, however the measure is not specific enough to understand the processes that cause the change. More recent work shows that using higher-order models improves significantly white matter tractography for clinical applications, e.g. [191, 192]. Moreover, when multi-shell data is available, the DTI model does not generalize well to higher b-values [150, 164]. For cancer imaging, a decrease in ADC is usually correlated with higher cellularity, however, the presence of vasogenic edema and/or focal necrosis within the tumour can revert this effect increasing ADC [3]. Thus, having a multi-compartment model can better differentiate between tumour types/grades[3, 2]. Nevertheless, due to the short acquisition times and robustness to noise, ADC and DTI are still widely used in clinical studies, however the estimates are not specific to the tissue microstructure.

When a rich data set with various b-values is available, more complex data analysis is supported. Signal models explain the measured data and the additional parameters can be correlated with some histological features, however they are not very specific. Biophysical models account for water diffusing in different compartments which have a histological correspondence and aim to explain the acquired data by including more tissue features and/or compartments. In order to prevent overfitting, the simplest model with the least number of parameters that fits the data is preferred. Moreover, the different compartments as well as the estimated parameters need to be in line with histological findings. This approach was considered when comparing various white matter models [150, 193] as well as choosing an appropriate cancer model [2, 63]. If the model aims to recover more complex tissue features, such as pore elongation or size distribution, then an improved diffusion acquisition is required in order to support the additional parameters. One drawback of modelling tissue microstructure is the fact that the most appropriate model depends on the imaging application as well as the richness and quality of the data, thus a model comparison needs to be performed in order to assess the results.

2.5 Conclusions

The first section of this chapter provides a brief description of brain and cancer microstructure, two applications of interest for the imaging methods we develop. A thorough understanding of tissue histology is essential in developing accurate biophysical models to analyse the diffusion MRI data.

The second section covers the basics of NMR phenomenon as well as signal generation, detection and localization, which are the foundation for modern MRI systems. These aspects are important in order to understand the data acquisition and analysis, as well as the practical implications for the DW-MRI techniques we develop.

The third section presents the theoretical aspects of diffusion MRI, with a focus on modelling restricted diffusion. Additionally, it introduces the advanced diffusion sequences which are of interest for this work, namely ODE and DDE sequences.

The last section provides an overview of the most popular modelling techniques for analysing DW-MRI data. It covers models developed for both brain and cancer imaging, presents various approaches for analysing ODE and DDE data, and discusses possible pitfalls of microstructure imaging.

The next chapters of this thesis present my own contribution on developing more advanced DW-MRI sequences and complex tissue models in order to improve the estimation of pore size and shape.

Chapter 3

Oscillating diffusion encoding

In chapter 2 we discussed the importance of estimating microstructural biomarkers and we illustrated that diffusion MRI provides the right tools to extract this information from non-invasive MR measurements. By developing biophysical models of the tissue and relating them to the measurement data, features such as pore size, shape and volume fraction can be estimated. Most microstructure imaging techniques presented in section 2.4.2 use single diffusion encoding (SDE) sequences with a combination of gradient strengths and diffusion times. Nevertheless, the sensitivity of the measurements to the tissue parameters can be increased by using more advanced diffusion acquisition as presented in section 2.3.6.

This chapter derives analytical signal models for oscillating diffusion encoding (ODE) sequences and improves the sequence design for diffusion spectrum imaging. This work has been published in [90].

3.1 Motivation

Oscillating diffusion encoding sequences (ODE) illustrated in Figure 2.11, measure diffusion on a shorter time scale which improves the estimation of intrinsic diffusivity and gives access to smaller structures, such as cell nuclei. The majority of studies involving ODE sequences, for estimating microstructural features or for measuring the diffusion spectrum, use sinusoidal gradient waveforms. Recent work [93, 94], which optimises the diffusion gradient waveform for pore size estimation, suggests that square oscillating gradients maximise sensitivity to small pore size as they yield the highest diffusion weighting within one period compared to other periodic waveforms. Moreover, in temporal diffusion spectroscopy experiments, square waves yield a higher amplitude of the power modulation spectrum which improves the diffusion contrast. When considering the finite slew rate of the diffusion gradients, trapeziodal waveforms, which account for the rise time of the gradient, are the practical implementation of square waves.

In this chapter I present the derivation of analytical signal models for square, trapezoidal and sinusoidal (with arbitrary phase) ODE sequences. Then I discuss how to improve the choice of sequence parameters for diffusion spectrum imaging, when the gradient slew rate is not negligible.

3.2 GPD approximations for ODE sequences

This study uses the GPD approximation described in section 2.3.4 to derive signal models of restricted diffusion for ODE sequences. The GPD approximation provides analytical expression which are fast to compute and enable parameter fitting in every voxel of an image volume.

3.2.1 Aims and objectives

The specific aims of this work are the following:

1. derive GPD approximations for ODE sequences with square, trapezoidal and sinusoidal (with arbitrary phase) waveforms.
2. validate the analytical expressions against MC numerical simulations which are highly accurate [101]
3. approximate the signal model for trapezoidal waveforms with the much simpler expressions for square or sinusoidal waveforms.

3.2.2 Theory

This section presents the mathematical description of the new oscillating gradients, namely square and trapezoidal waveforms, the derivation of the corresponding b-values for free diffusion and the signal attenuation computed using the GPD approximation for restricted diffusion.

Oscillating gradients - definition

Figure 3.1 illustrates the standard SDE sequence, as well as the square and trapezoidal waveforms that will be used in the subsequent derivations of the diffusion signal.

The diffusion gradient for ODE sequences with constant gradient orientation can be generally described as:

$$g(t) = \begin{cases} G \cdot f(2t\nu - \frac{\phi}{\pi}) & \text{if } 0 \le t < \delta \\ G \cdot f(2(t-\Delta)\nu - \frac{\phi}{\pi}) & \text{if } \Delta \le t < \Delta + \delta \\ 0 & \text{otherwise} \end{cases} \tag{3.1}$$

where G is the amplitude of the gradient, ν is the oscillation frequency, ϕ is the phase and $f(x)$ denotes the waveform.

For square and trapezoidal ODE sequences, the gradient waveform $f(x)$ is:

$$f(x) = (-1)^{\lfloor x \rfloor} \cdot \begin{cases} \frac{1}{2\nu}\frac{1}{t_r}(x - \lfloor x \rfloor) & \text{if } \lfloor x \rfloor \le x < \lfloor x \rfloor + 2\nu \cdot t_r \\ 1 & \text{if } \lfloor x \rfloor + 2\nu \cdot t_r \le x < \lfloor x \rfloor + 1 - 2\nu \cdot t_r \\ \frac{1}{2\nu}\frac{1}{t_r}(\lfloor x \rfloor + 1 - x) & \text{if } \lfloor x \rfloor + 1 - 2\nu \cdot t_r \le x < \lfloor x \rfloor + 1 \end{cases}$$

for a trapezoidal waveform with rise time t_r.

$f(x) = (-1)^{\lfloor x \rfloor}$, for a square waveform

with $\lfloor \rfloor$ denoting the integer part. (3.2)

The parameters of these two pulse sequence are: the gradient amplitude G, the length of the pulse δ, the diffusion time Δ, the frequency of the wave ν, the phase ϕ and the rise time t_r (in the case of the trapezoidal wave). The general formulae computed for an ODE sequence with arbitrary phase and frequency are quite lengthy, therefore we present here the expressions for the special case of integer number of half periods (i.e. $\delta = \frac{N}{2\nu}$, $N = 1, 2, ...$) and $\phi = 0$. Appendices A.3 present the general results for arbitrary frequency and phase, including the extension for sinusoidal waveforms.

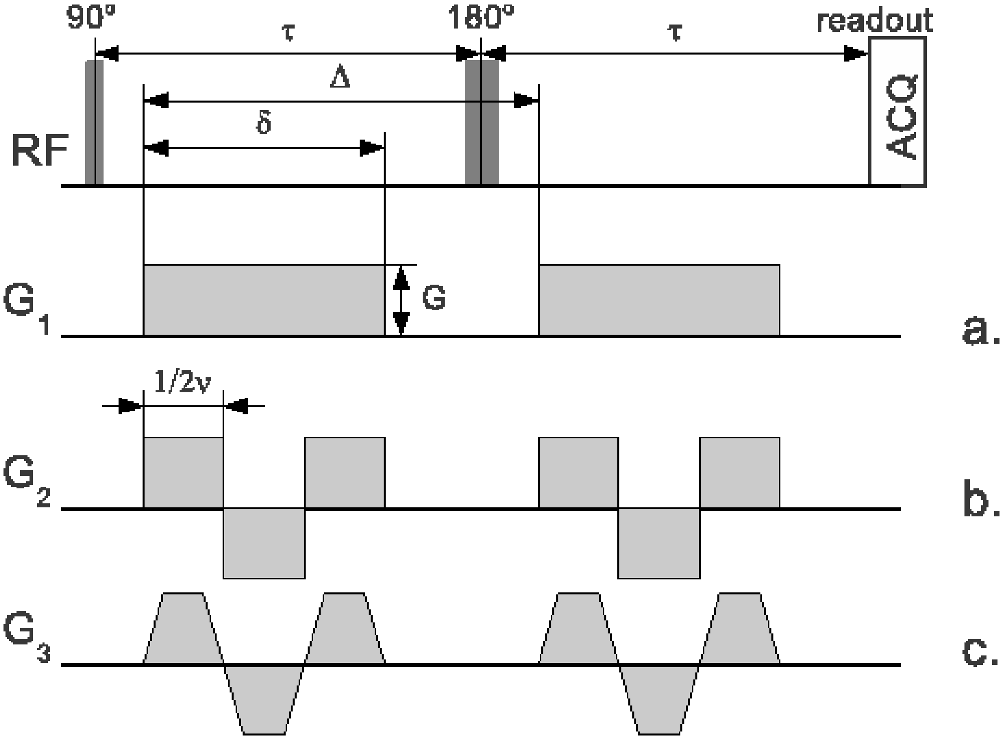

Figure 3.1: Schematic representation of the applied gradient for SDE a), square ODE b) and trapezoidal ODE with zero phase and integer number of half periods $N = 3$

Free diffusion

The expressions for b calculated according to equation 2.32, assuming an integer number of half periods N and $\phi = 0$ are the following:

$$b = \frac{G^2\gamma^2\delta}{6\nu^2} + G^2\gamma^2(\Delta - \delta)\left(\frac{1-(-1)^N}{4\nu}\right)^2, \tag{3.3}$$

for square wave and

$$\begin{aligned} b = G^2\gamma^2(\Delta - \delta)\left(\frac{(1-(-1)^N)(1-2\nu\cdot t_r)}{4\nu}\right)^2 + \\ \frac{G^2\gamma^2\delta}{30\nu^2}(5 - 15t_r\cdot\nu - 5t_r^2\cdot\nu^2 + 32t_r^3\cdot\nu^3), \end{aligned} \tag{3.4}$$

for trapezoidal wave.

If we set the rise time of the trapezoidal wave to be zero $t_r = 0$ in equation 3.4, then we recover the b value for a square wave in 3.3. Moreover, the b value for the square wave in 3.3 has the well-known form $b = G^2\gamma^2\delta^2(\Delta - \delta/3)$ for SDE if we set $2\nu = \delta^{-1}$ and $N = 1$.

The b values for square, sine and cosine ODE with arbitrary frequency and phase are

$$\begin{aligned} b =& G^2\gamma^2\Bigg\{(\Delta-\delta)(\alpha-\theta)^2 + \frac{\delta^3+\alpha^3+(1-(-1)^N)(\theta-\alpha)^3+(-1)^N\beta^3}{3} + \\ &+ \frac{N(1-3\nu\delta+6\nu^2\theta^2)}{12\nu^3} + \frac{N^2}{4\nu^3}\left(\frac{1}{2}-\frac{N}{3}-\nu(\delta-\theta)\right) - \delta\theta(\delta-\theta)\Bigg\}, \quad (3.5) \end{aligned}$$

$$\text{with} \quad \theta = \frac{\phi}{2\pi\nu}, \quad N = \lfloor 2(\delta-\theta)\nu \rfloor, \quad \alpha = (-1)^N\frac{(-1)^N - 1 - 2N + 4\nu(\delta-\theta)}{4\nu}, \quad \beta = \frac{(-1)^N - 1 + 4\nu\theta}{4\nu}$$

for square wave,

$$\begin{aligned} b =& \frac{G^2\gamma^2}{2\omega^3}\Big[2(\Delta-\delta)\omega\left(\cos\phi - \cos(\delta\omega-\phi)\right)^2 + 4\delta\omega - 4\sin(\delta\omega) - \sin 2\phi + \\ & \delta\omega\left(\cos 2\phi + \cos(2\delta\omega - 2\phi)\right) - \sin(2\delta\omega - 2\phi)\Big] \quad (3.6) \end{aligned}$$

for sine wave, and

$$\begin{aligned} b =& \frac{G^2\gamma^2}{2\omega^3}\Big[2(\Delta-\delta)\omega\left(\sin\phi + \sin(\delta\omega-\phi)\right)^2 + 4\delta\omega - 4\sin(\delta\omega) + \sin 2\phi - \\ & \delta\omega\left(\cos 2\phi + \cos(2\delta\omega - 2\phi)\right) + \sin(2\delta\omega - 2\phi)\Big] \quad (3.7) \end{aligned}$$

for cosine wave, with $\omega = 2\pi\nu$.

The b values for square, sine and cosine ODE with arbitrary frequency and $\phi = 0$ are

$$\begin{aligned} b =& G^2\gamma^2\Bigg\{(\Delta-\delta)\alpha^2 + \frac{\delta^3+\alpha^3-(1-(-1)^N)\alpha^3+(-1)^N\beta^3}{3} + \frac{N(1-3\nu\delta)}{12\nu^3} + \\ &+ \frac{N^2}{4\nu^3}\left(\frac{1}{2}-\frac{N}{3}-\nu\delta\right)\Bigg\}, \quad (3.8) \end{aligned}$$

$$\text{with} \quad N = \lfloor 2\delta\nu \rfloor, \quad \alpha = (-1)^N\frac{(-1)^N - 1 - 2N + 4\nu\delta}{4\nu}, \quad \beta = \frac{(-1)^N - 1}{4\nu},$$

for square wave,

$$b = \frac{G^2\gamma^2}{2\omega^3}\Big[2(\Delta-\delta)\omega\left(1-\cos(\delta\omega)\right)^2+5\delta\omega-4\sin\delta\omega+\delta\omega\cos(2\delta\omega)-\sin(2\delta\omega)\Big] \tag{3.9}$$

for sine wave, and

$$b = \frac{G^2\gamma^2}{2\omega^3}\Big[2(\Delta-\delta)\omega\sin^2\delta\omega+3\delta\omega-4\sin\delta\omega-\delta\omega\cos(2\delta\omega)+\sin(2\delta\omega)\Big]. \tag{3.10}$$

for cosine wave.

Restricted diffusion

By substituting the new gradient waveforms, defined above, in equation 2.41, we derived the expressions of Γ_n for square and trapezoidal wave. The results for waveforms with integer number of half periods N and $\phi = 0$ are the following:

$$\begin{aligned}\Gamma_n = G^2\Bigg\{&\left(\frac{e^{\frac{\lambda_n D}{2\nu}}-1}{e^{\frac{\lambda_n D}{2\nu}}+1}\right)^2\Big(1-N(e^{-\lambda_n D/(2\nu)}+1)-(-1)^N e^{-\lambda_n D\delta}-\\ &e^{-\lambda_n D\Delta}\big(1-(-1)^N\cosh(\lambda_n D\delta)\big)\Big)+\lambda_n D\delta+N\big(e^{-\frac{D\lambda_n}{2\nu}}-1\big)\Bigg\}.\end{aligned} \tag{3.11}$$

for square wave, and

$$\begin{aligned}\Gamma_n = \frac{G^2}{2D^2\lambda_n^2 t_r^2}\Bigg[&\frac{(-1)^N}{E_{1+}^2}(e^{\tilde{t_r}}-1)^2(e^{\tilde{t_r}}-e^{\lambda_n D/2\nu})^2 e^{-\tilde{\delta}-2\tilde{t_r}}\Big(e^{-\tilde{\Delta}}\big(-1+(-1)^N e^{\tilde{\delta}}\big)^2-\\ &2\big(1+(-1)^N e^{\tilde{\delta}}(N-1+Ne^{-\lambda_n D/2\nu})\big)\Big)+N\Big(2e^{-\lambda_n D/2\nu}\big(e^{\tilde{t_r}}-1\big)^2-\\ &4(e^{-\tilde{t_r}}-1+\lambda_n D t_r)+\lambda_n^3 D^3 t_r^2(1/\nu-8t_r/3)\Big)\Bigg],\end{aligned} \tag{3.12}$$

where $N = 2\delta\nu, \quad \tilde{\delta} = D\lambda_n\delta, \quad \tilde{\Delta} = D\lambda_n\Delta, \quad \tilde{t_r} = D\lambda_n t_r, \quad E_{1+} = e^{D\lambda_n/(2\nu)}+1$

for trapezoidal wave.

If we take $\lim_{t_r\to 0}\Gamma_n$, expression 3.12 reduces to the formula for square wave in equation 3.11.

3.2.3 Simulations and results

The first simulation validates the formulae presented in the previous section and Appendix A.3 and assesses the accuracy of the GPD approximation for cylindrically restricted diffusion. The second simulation evaluates the accuracy of approximating the full trapezoidal wave formulae with the simpler expressions for square and sine waves.

Validation of GPD formulae

These simulations aim to test the accuracy of the GPD approximation. We compare the analytical expressions of the normalised diffusion signal for square waveforms with the exact solutions obtained using the Monte Carlo diffusion simulator in Camino [101] and a semi-analytical solution provided by the matrix method (MM) described in section 2.3.4. We treat the MC simulation as ground truth since it provides arbitrary precision, depending on the resolution of the simulation, and no bias. The signal for a total diffusion time of 0.12s was computed using $N_W = 200,000$ walkers and $N_T = 6,000$ time steps, yielding a normalized-signal variance on the order of 10^{-6} [101]. For a given simulation complexity (i.e.$N_W \times N_T$), the largest accuracy is obtained when N_T is on the order of 10^3. Moreover, this particular choice of parameters leads to a time step $dt = 0.12$ s/ N_T = 0.02 ms, which corresponds to a step size $dx = \sqrt{2Ddt} \approx 0.3$µm smaller than the cylinder radius.

To validate the GPD approximation for the square waveform, we simulated the normalised diffusion signal with $D = 2 \cdot 10^{-9}$ m^2/s for a wide range of sequence parameters and pore sizes suitable for biomedical applications.

In the main simulation we considered all combinations of $R \in \{1, 2, 5, 10\}$ µm, $G \in \{0.02, 0.04, ...0.1, 0.2, ...1\}$ T/m, $\Delta \in \{25, 35, 45, 55\}$ ms and $\nu \in \{25, 30, ...100, 200, ...500\}$ Hz. In practice ODE sequences are designed to have a long pulse durations limited by the time required for the refocusing pulse. In this simulation we consider a typical duration for the refocusing pulse $\tau_{rf} = 5$ ms and we set $\delta = \Delta - \tau_{rf}$. This choice of parameters covers the range of gradient strengths achievable on both clinical scanners, $G \leq 0.1$ T/m, as well as much higher gradient strengths available only on small-bore high-field scanners not in widespread clinical use, $G \leq 1$T/m. We do not vary the diffusivity, D, as the signal depends only on the ratio D/R^2, so varying R is sufficient.

To visualise the results, Figure 3.2 presents a representative subsample of data, comparing the GPD approximation with the Monte Carlo simulation as a function of the different parameters used in the analysis. Figure 3.2a shows the restricted diffusion signal as a function of frequency for four different values of Δ, fixed gradient strength $G = 0.1$ T/m and cylinder radius $R = 5$ µm. The diffusion signal increases with decreasing Δ and increasing frequency with a sharp jump in slope at values that give integer numbers of half periods. The data points for $\Delta = 25$ ms illustrate how the signal behaves when the frequency is increased from the value corresponding to SDE, $\nu = 25$ Hz to the value corresponding to $N = 4$ oscillations, $\nu = 100$ Hz. Figure 3.2b illustrates the signal as a function of frequency for five different gradient strengths with fixed $\Delta = 25$ ms and cylinder radius $R = 5$ µm. The signal decreases with increasing gradient strength with a similar pattern as the frequency increases to that observed in Figure 3.2a. Figure 3.2c presents the dependence of the diffusion signal on the gradient strength for several frequencies with fixed $R = 5$ µm and $\Delta = 45$ ms and Figure 3.2d shows the dependence of the diffusion signal on the cylinder radius for the same frequencies with fixed $G = 0.1$ T/m and $\Delta = 45$ ms. The signal is less dependent on the radius as the oscillation frequency increases. This plot also shows that low-frequency ODE sequences can better differentiate restriction sizes, however, for the case illustrated here ($G = 0.1$ T/m, no sequence shows sensitivity to radii smaller than 2 µm. The resolution limit, i.e. the smallest restriction size that can be detected for a given gradient strength, is discussed in Chapter 4.

The difference between the GPD approximation of the restricted diffusion signal for the square ODE sequence, the MC simulation and the matrix method (not shown in Figure 3.2) is within 3.5% of the normalised signal, in all cases we considered. The difference between the matrix method and the MC simulation is within 1.1% of the normalised signal. 95% of differences larger than 1% occur when the diffusion signal is between 0.01 and 0.5. The largest differences occur for $R = 5$ µm at low frequencies (Figure 3.2b) and for $R = 10$ µm at high frequencies (not shown). For smaller radii, $R = 1$ µm and $R = 2$ µm, the errors are always less than 1%.

A secondary simulation validates the GPD approximation for arbitrary phase and variable pulse length. For the same gradient strengths and cylinder radii as the main simulation above, first we simulate the diffusion signal from a square waveform with

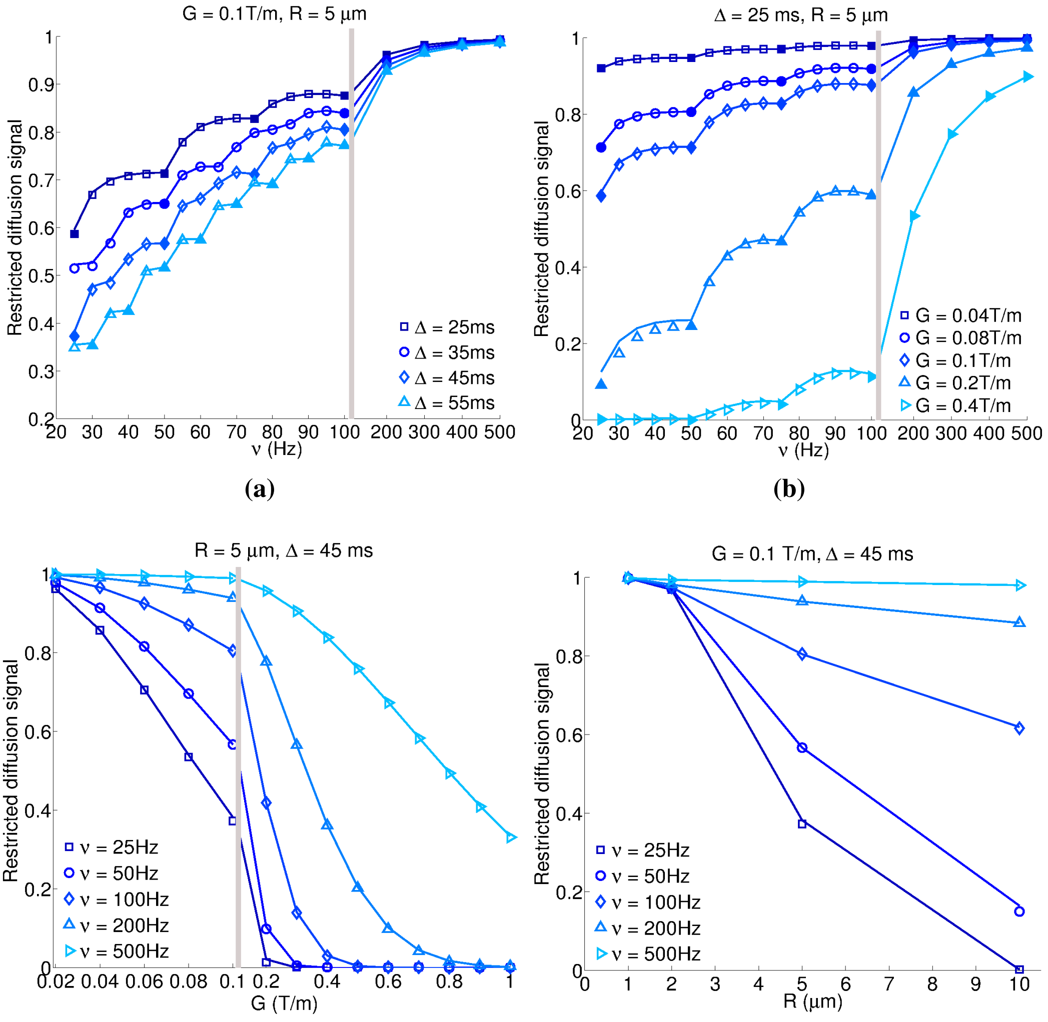

(a) (b)

(c) (d)

Figure 3.2: Restricted diffusion signal as a function of oscillation frequency for a) several values of Δ, $R = 5$ µm and $G = 0.1$ T/m; b) several gradient strengths, $R = 5$ µm and $\Delta = 25$ ms. In a) and b) the filled markers indicate waveforms with integer number of oscillations. Restricted diffusion as a function of c) gradient strength for several frequencies, $R = 5$ µm and $\Delta = 45$ ms; d) cylinder radius for several frequencies, $G = 0.1$ T/m and $\Delta = 45$ ms. The markers show the MC simulation and the solid lines are the GPD approximations. The vertical bar separates different scales on the x-axis.

variable phase $\phi \in \{0^o, 30^o, 45^o, 60^o, 90^o\}$ for fixed $\Delta = 40$ ms, $\delta = 35$ ms and frequency $\nu = 2\delta^{-1}$. Then, we simulate the signal attenuation as a function of the pulse duration $\delta \in \{4, 8, ..., 36\}$ ms with $\phi = 0$ and $\nu = 250$ Hz; the fixed frequency was chosen to have integer number of oscillations for all values of δ.

Figure 3.3a compares the restricted diffusion signal as a function of the gradient strength for waveforms with different phases for a cylinder with radius $R = 5$ µm.

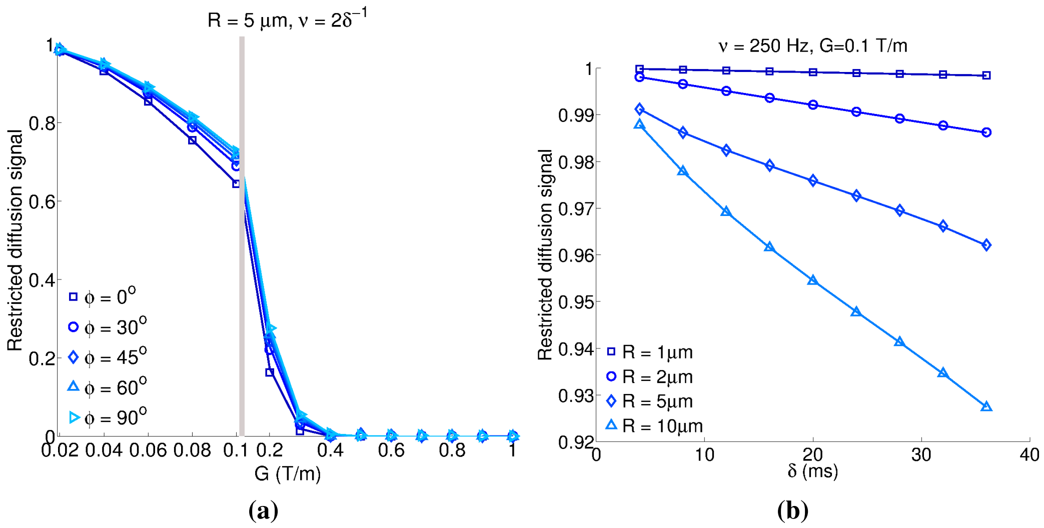

(a) **(b)**

Figure 3.3: Restricted diffusion signal as a function of a) gradient strength for several waveform phases, $R = 5$ µm and $\nu = 2\delta^{-1}$ T/m; b) pulse duration for several cylinder radii, $G = 0.1$ T/m and $\nu = 250$ Hz. The markers show the MC simulation and the solid lines are the GPD approximations.

For all radii the waveforms with $\phi = 90^o$ yield the highest signal and the waveforms with $\phi = 0$ the lowest one, which is consistent with the higher b value of sine-like oscillations compared to cosine-like oscillations. Figure 3.3b illustrates the diffusion signal as a function of δ for several radii and $G = 0.1$ T/m. The signal is approximately linear in δ with all other parameters fixed. Moreover, sequences with a longer pulse can separate better different restriction sizes. For all the parameters considered in the second simulation, the difference between the GPD approximation and MC simulation is less than 1.2%.

Approximation of trapezoidal waveform

This simulation tests the hypothesis that in most practical circumstances the relatively simple square wave or sine wave formulae provide a sufficiently close approximation to the more complex trapezoidal wave expressions. We analyse four different choices of waveform amplitude for the sine and square curves and we discuss separately the cases of waveforms with integer number of half periods and with arbitrary frequency.

For a trapezoidal ODE sequence with integer number of oscillations N, we quantify the shape of the waveform using the ratio $n = N/N_{max}$, where $N_{max} = \lfloor \frac{\delta \cdot S_R}{2G} \rfloor$ is the maximum possible number of oscillations for gradient strength G, slew rate S_R and pulse duration δ. In the extreme cases the trapezoidal wave tends towards a square wave for $n \to 0$ and a triangular wave for $n \to 1$.

We evaluate the absolute difference in signal $|\Delta S|$ between the different waveforms as a function of n in four situations: I. square and sine waves with amplitude equal to that of the trapezoid curve, II. square and sine waves with amplitude chosen so that the area under each function for half a period is the same, III. square and sine waves with amplitudes chosen so that the area under each *squared* function for a half period is the same, and IV. square and sine waves with amplitudes chosen so that the b value per oscillation is the same. The parameters used in this analysis are the following: $R \in \{1, 2, 5, 10\}$ µm, $G \in \{0.02, 0.04..., 0.4\}$ T/m, $2\nu \in \{1, 2, ..., N_{max}\} \cdot \delta^{-1}$, $\Delta = 40$ ms, $\delta = 35$ms and $S_R \in \{200, 1000\}$ T/m/s.

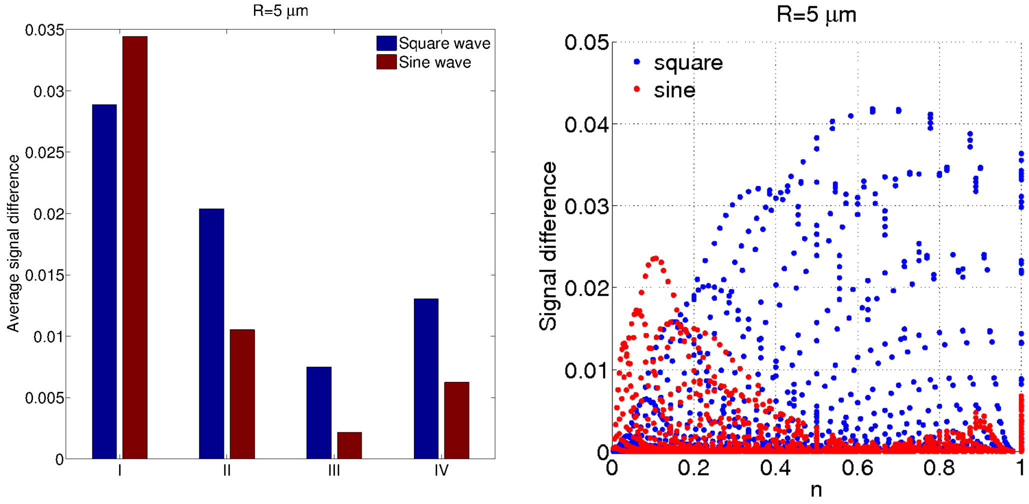

(a) (b)

Figure 3.4: a) Average normalized signal difference between square and sine approximations and the full trapezoidal expression considering: I - same amplitude, II - same area under the curves, III - same area under the *squared* curves and IV - same b value per oscillation; b) Scatter plot of the differences between square and sine approximations and the full trapezoidal expressions as a function of n. The differences are given for all combinations of gradient strengths and oscillation frequencies for trapezoidal waveforms with $S_R = 200$ T/m/s and cylinder radius $R = 5$ µm

Figure 3.4a shows the average normalized signal difference over all combinations of pulse sequence settings in the four cases for a cylinder with radius $R = 5\mu$m. Although in the case of free diffusion, approximation IV ensures the same diffusion signal for waveforms with integer number of periods, in the case of restricted diffusion the simulation shows that approximation III provides a lower error bound. The results are consistent for all the radii in the simulation. Thus approximation III is used in all the following analysis.

Figure 3.4b illustrates the normalized signal difference between the trapezoidal waveform and the square and sine waves as a function of n for slew rate $S_R = 200$ T/m/s and radius $R = 5$ µm. The results of the simulation show that with this approximation, for larger radii, $R = 5$ µm and $R = 10$ µm, the error between the trapezoidal waveform and the square or sine wave is less than 2% of the normalised signal, for $R = 2$ µm the error is on the order of 10^{-3} and for $R = 1$ µm the error is on the order of 10^{-4}. A similar pattern to the one illustrated in Figure 3.4b was obtained for $S_R = 1000$ T/m/s. Thus, at low gradient strengths and frequencies, i.e. $n \approx 0.1$, the square wave is the better approximation, while as n increases the sine wave approximation is better. However, for the cases considered here, the errors are small suggesting that either approximation is probably adequate in practice.

The optimised waveforms presented in [93] do not necessarily have integer number of oscillations. Thus, to determine how the errors for the square and sine approximations behave in this case, we extend the previous analysis for arbitrary frequency when δ is no longer a multiple of half periods. To quantify the deviation from the integer case, we define the new frequencies as $2\nu' = 2\nu + \alpha \cdot \delta^{-1}$, where $0 \leq \alpha < 1$ gives the ratio between the duration of the last oscillation and a full half a period at the corresponding frequency. Then we repeat the simulation with the same parameters and $\alpha \in [0, 0.1, ...0.9]$.

Figure 3.5a illustrates the average signal difference over all combinations of pulse sequence parameters between the full trapezoidal GPD approximation and the surrogate sine or square approximations as a function of α for two cylinder radii, $R = 10\mu$m and $R = 2\mu$m. Figure 3.5b plots the restricted diffusion signal from the three waveforms as a function of frequency ν' for $R = 5\mu$m and two gradient strengths $G = 60$ mT/m and $G = 200$ mT/m. On average, the sine wave is usually a better approximation for $\alpha < 0.5$, and the square is usually better for $\alpha > 0.5$, which can also be observed for the specific cases in Figure 3.5b, i.e. the red line is close to the green line for $\alpha < 0.5$, and departs from it for $\alpha > 0.5$. However, the precise value of alpha at the transition is not exactly at 0.5 and depends on the frequency and gradient strength.

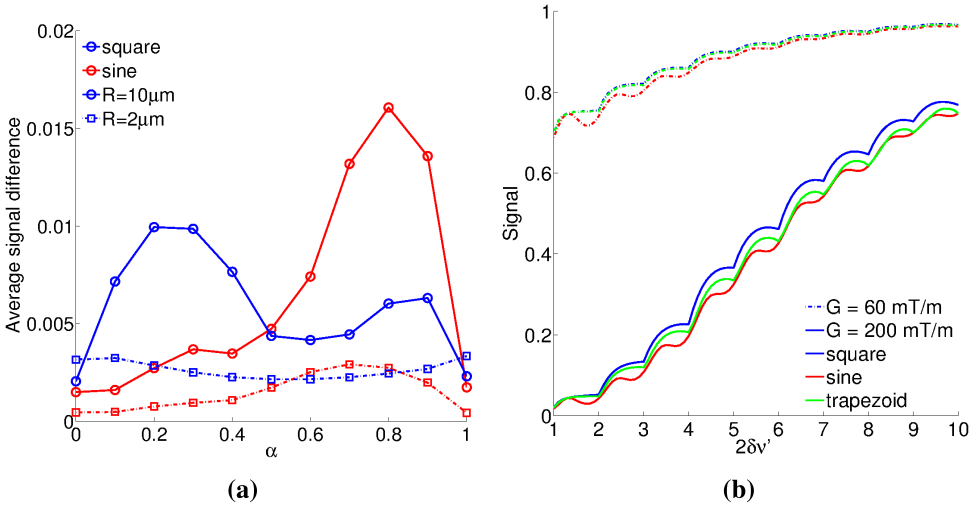

Figure 3.5: a) Average signal difference between square and sine approximations and the full trapezoidal expressions as a function of α for $R = 2\mu$m (- -) and 10μm (—); b) Diffusion signal for $R = 5\mu$m for the three waveforms with gradient strength $G = 60$mT/m (- -) and 200mT/m (—) as a function of oscillation frequency

3.2.4 Discussion

In this section we provide and validate analytical formulae of the free and restricted diffusion MR signal for trapezoidal, square and generalised sinusoidal oscillating gradients. These expressions enable the adaptation of many widely used diffusion MRI techniques for oscillating gradients.

The b-value expressions, given in section 3.2.2 for ODE sequences, support Diffusion Tensor Imaging (DTI) [50] or other mathematical models which describe the signal in terms of b-value, such as Ball and Stick [147], Diffusion Kurtosis Imaging [137], NODDI [12], etc., using ODE. The expressions of the restricted diffusion signal, given in section 3.2.2 for ODE measurements, are relevant for techniques which explicitly aim to estimate pore size, such as ActiveAx [9] or VERDICT [2]. The restricted diffusion signal can be calculated for simple geometries where the factors B_n and λ_n are known, i.e. parallel planes, cylinders, spheres [80, 78, 81] and spherical shells [87]. These simple shapes are the building blocks of more complex tissue models which are increasingly used in biomedicine, as explained in section 2.4.

We test the accuracy of the analytical signal approximations by comparison with exact values provided by MC simulations and a semi-analytical signal model provided by the matrix method (MM) formalism. The maximum difference between the GPD approximation and the MC or MM signal values is less than 3.5% of the normalised diffusion signal, for all the parameters considered in the simulation. Most of the errors larger than 1% occur when the normalised diffusion signal is between 0.01 and 0.5. Thus, for small radii, $R = 1$ µm and 2 µm, which yield lower signal attenuation the errors are less than 0.5%. For $R = 5$ µm the largest errors occur at low frequencies and for $R = 10$ µm at high frequencies when the gradients yield a normalised diffusion signal $S \approx 0.2$. From the data points with normalised diffusion signal in the range $0.01 < S < 0.7$, 89% have an error less than 1% and 73% have an error less than 5%. Differences of up to 1% between the MC and MM signals arise from numerical instabilities in the techniques. The accuracy of GPD for the other waveforms is similar, as demonstrated indirectly in the subsequent comparison in figures 3.4b. In general, the voxel-wise signal-to-noise (SNR) ratio in diffusion MRI data is approximately 20, which leads to a noise related standard deviation of 5% which is larger than the maximum error of the GPD approximation. Even for larger values of SNR up to 100, which can be obtained if the the acquired data is denoised or the signal is averaged over a region of interest (ROI), the GPD approximation is accurate for $\approx 90\%$ of the investigated sequence parameters. This work shows the accuracy of the GPD approximation by comparison with signal values from MC simulations. The validation of the analytical expressions in terms of estimating pore size in a microcapillary phantom is presented in chapter 4.

We showed that in the case of restricted diffusion, sine and square wave approximations to the trapezoidal waveform work well with the amplitude chosen so that the squared areas under each half period match. With this approximation, for larger radii, $R = 5$ µm and $R = 10$ µm, the error between the trapezoidal waveform and the square or sine wave is less than 2%, for $R = 2$ µm the error is on the order of 10^{-3} and for $R = 1$ µm the error is on the order of 10^{-4}. If δ is a multiple of half periods, the square wave is a better approximation for small n, i.e. small gradient amplitude, low frequency, large slew rate, while the sine wave is a better approximation for large n, when the trapezoid wave becomes more triangular. Approximating the trapezoid wave model with the square and sine wave models roughly halves computation time.

For an arbitrary frequency, we see in Figure 3.4b that the average error for square and sine waves depends on α. Broadly, the sine wave is a better approximation when

$\alpha < 0.5$ and the square wave is better when $\alpha > 0.5$, although the cut-off varies with frequency and gradient strength. However, either approximation is reasonable particularly in the vicinity of $\alpha = 0.5$, so the precise choice of transition point is not crucial. For a typical clinical scanner with $S_R = 200$ T/m/s and $G = 0.04$ T/m the maximum number of oscillations is $N = 87$. For this gradient strength, the optimized waveforms in [93] have a small number of oscillations $N < 5$ for $R = 5$ µm, a larger number of oscillations $N \approx 20$ for $R = 2\ up\mu$m and very high frequency for $R < 1$ µm. This suggests that for the waveforms optimized for larger radii the square wave is a better approximation ($n < 0.06$), while for the waveforms optimized for smaller radii the sine wave is better ($n \approx 0.25$ for $R = 2$ µm and $n \to 1$ for $R < 1$ µm).

The main advantage of the analytical expressions for the signal from GPD is the reduced computational complexity and running time. For the entire data set, the MC simulation took over 10 hours, the matrix method took 480 s, while the analytical values were computed in less than one tenth of a second, which enables model fitting applications, e.g. to generate whole brain parameter maps as in [9, 11]. When modelling the diffusion signal we assume that background gradients do not contribute to the cumulative waveform. A limitation of the GPD approximation is that the expression of restricted diffusion signal can be calculated analytically only when the gradient $G(t)$ has a form for which Equation (2.41) has solutions. In case of arbitrary gradient waveforms, the double integrals in Equation(2.41) need to be calculated numerically, losing the advantage of computational speed. In this case, using semi-analytical approaches such as the matrix method or multiple correlation function presented in section 2.3.4 is preferred, as they provide more accurate signal values.

3.3 Sequence design for diffusion spectrum imaging

Temporal diffusion spectroscopy uses cosine-like ODE sequences of various frequencies to probe the diffusion spectrum, as detailed in section 2.3.5. The dependence of diffusivity on frequency, which is inversely proportional to diffusion time, reflects the restriction lengthscale without assuming an explicit biophysical model. This is advantageous when there is no prior knowledge of the tissue microstructure.

A desirable feature of ODE sequences is to have the main peak in the power modulation spectrum at the same frequency as the oscillating gradient and no zero frequency peak [81]. This allows the sampling of the diffusion spectrum $D(\omega)$ by varying the frequency of the ODE sequence. This property is satisfied by cosine ODE, however, a practical problem with this waveform is that it requires instantaneous rise to maximum gradient strength at the start of the pulse. Using a sine ODE instead introduces a significant peak at the zero frequency (long diffusion time), which corrupts estimates of short-time ADC. To overcome this problem, Does et al introduced the apodised cosine waveform in which the first quarter of period is replaced by a sine function of double frequency [106].

The amplitude of the power modulation spectrum can be further increased if the apodised cosine waveforms are replaced with trapezoidal waveforms which take advantage of the maximum gradient slew rate.

3.3.1 Aims and objectives

This study aims to:

1. apodise trapezoidal waveforms in a comparable way to cosine waveforms in order to have the main peak at the oscillation frequency and no zero-frequency peak.
2. analyse the diffusion signal and ADC estimates as a function of frequency for different ODE waveforms.

3.3.2 Simulations and results

As detailed in section 2.3.5, when investigating the dependence of the estimated ADC on oscillation frequency, an important tool is the power modulation spectrum [105]

$$\mathbf{F}'(\omega) = \int_0^{2\tau} e^{i\omega t}\mathbf{F}(t)dt, \tag{3.13}$$

which is the Fourier transform of the gradient integral and indicates the diffusion times contributing to the ADC value.

The apodised cosine pulse avoids a peak at $\omega = 0$ in the power spectrum, by ensuring the integral of the first oscillation is equal to half of the integral of the second oscillation. We satisfy the same condition for the trapezoidal waveform by extending the duration of the first and last oscillations by half the rise time, $t_r/2$. Thus, the total duration of the trapezoidal waveform is $\delta + t_r$. Figure 3.6a shows the three waveforms with angular frequency $\omega = 8\pi/\delta = 718$ s^{-1} and Figure 3.6b plots the corresponding power spectra. The main peaks for all three waveforms are at the desired frequency. The peak heights are similar for square and apodised trapezoid and lower for the apodised cosine, indicating less focus on the desired diffusion time.

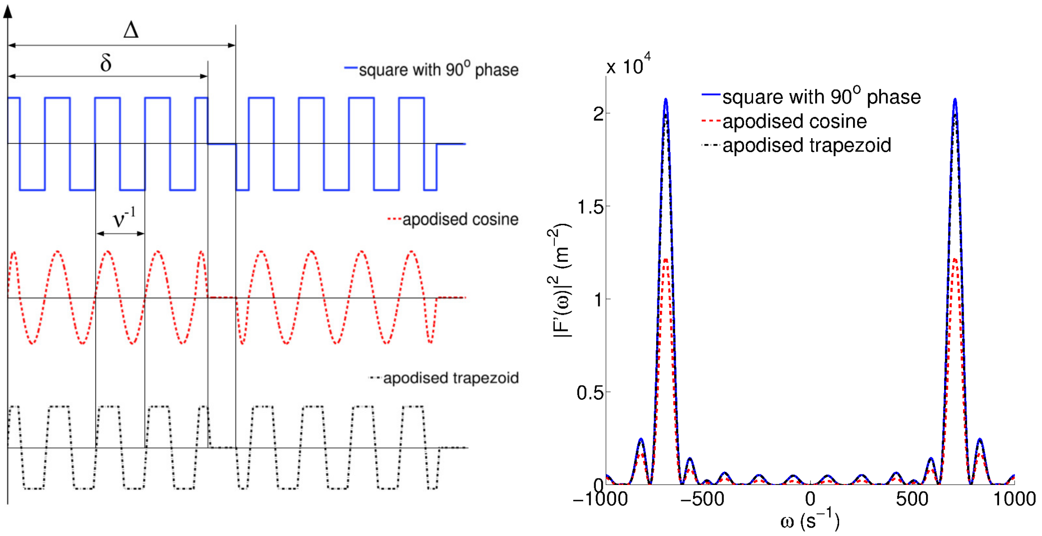

(a) **(b)**

Figure 3.6: a) Example waveforms with $\omega = 718\text{s}^{-1}$ b) Corresponding power modulation spectra

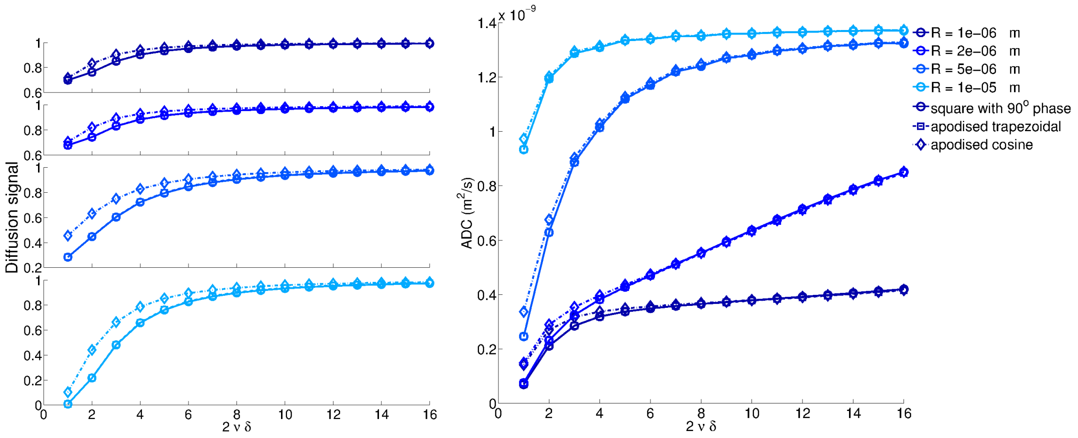

(a) **(b)**

Figure 3.7: a) Diffusion signal for different waveforms: square with 90^o phase, apodised cosine and apodised trapezoid as a function of oscillation frequency for four different sizes of the restricted compartment; b) corresponding extracted ADC values. The diffusion signal and ADC for apodised trapezoid and square wave are very similar and are plotted on top of each other.

To better understand the effects of different gradient waveforms, we use the GPD approximation to simulate the dependence of the ADC on oscillation frequency for a two-compartment Zeppelin and Cylinder [150] model: $S(2\tau) = f \cdot S_r + (1 - f) \cdot S_h$, where f is the volume fraction of axons, S_r is the signal from the restricted compartment and S_h is the signal from the hindered compartment which exhibits Gaussian diffusion with parallel diffusivity D_r and perpendicular D_h. The parameter settings used in the simulation are $f = 0.7$, $D_r = 1.7 \times 10^{-9}$ m^2/s, $D_h = 1.2 \times 10^{-9}$ m^2/s, $\Delta = 40$ ms, $\delta = 35$ ms, $G = 0.1$ T/m and $2\nu \in \{1, 2, ..., 16\}\delta^{-1}$.

Figure 3.7a illustrates the dependence of the diffusion signal on frequency for different cylinder radii $R \in \{1, 2, 5, 10\}$µm and different gradient waveforms, square wave with 90^o phase, apodised cosine and trapezoidal and Figure 3.7b shows the corresponding extracted ADC values. The calculated ADC increases with frequency and the rate of change depends on the size of the restricted compartment which is consistent with recent experimental studies [173, 174, 109]. The ADC values are similar for all waveforms, nevertheless square and trapezoidal waves provide higher diffusion weighting which increases the contrast. At low frequencies the ADC value is higher for the apodised cosine waveform than for either square or trapezoidal due to the influence of the extracellular compartment. Because the b-value is lower, slightly more extracellular signal remains so the weighting of the restricted contribution is lower.

3.3.3 Discussion

The original motivation for square and trapezoidal wave pulses [93] is for model-based applications to improve sensitivity to intrinsic diffusivity and pore size. We note the usual caveat about these approaches that modelling does not necessarily reflect the actual compartmentation of water and should be assigned with care. In this section, however, we explore wider applicability of these waveforms in non-model based applications. We showed that trapezoidal oscillating gradients can be apodised in a similar way to cosine waveforms, which have been used to study the dependence of estimated ADC on frequency [106, 174, 173]. The benefit of apodised trapezoid over the standard cosine gradients is the higher diffusion weighting at the same gradient strength. This feature improves the SNR in substrates with small pore sizes, where higher diffusion weighting is desirable. Figure 3.7b suggests that the advantages of the trapezoid waves are only minor when estimating ADC, but their use has no cost and may prove significant in some applications.

Most of ODE theory has been developed with the quantification of $D(\omega)$ in mind. Nevertheless, optimizing each time point of a generalized diffusion gradient [93, 94] for estimating intrinsic diffusivity and pore size, resulted in oscillating gradients. The link between ODE sequences and sensitivity to pore size which aims to better understand previous results in [93, 94] is analyzed in chapter 4.

3.4 Conclusions

This chapter analyses square, trapezoidal and generalized sinusoidal ODE sequences.

The first section provides analytical expressions of the free and restricted diffusion signal for the various oscillating gradient waveforms and validates them against numerical MC simulations which provide arbitrarily high precision. The results show that the GPD approximation is accurate enough when the SNR of the acquired data is lower than ≈ 100, which is the case in the majority of practical applications. Moreover, the signal expression for trapezoidal waveforms can be approximated with the simpler expressions for sine or square waveforms, which roughly halves the computational time.

The second simulation shows that trapezoidal waveforms can be apodised in a similar way to cosine waveforms. Thus, they are beneficial for temporal diffusion spectroscopy, as they provide a power modulation spectrum with narrow peaks at the frequency of interest and higher amplitude compared to the apodised cosine. The higher diffusion weighting improves the signal contrast, however, the effect on the estimated ADC is only minor. A similar apodisation strategy is presented in [108], and was reported after this work was published in JMR. Moreover, the experiments in [108] show the applicability of trapezoidal waveforms for in-vivo clinical studies.

Overall, this work provides the necessary tools to analyse square and trapezoidal ODE data in order to estimate pore size using a model-based approach and it presents the benefits of trapezoidal waveforms for temporal diffusion spectroscopy.

In the next chapter I present collaborative work on ODE sequences. The first study analyses the sensitivity of DODE sequences to axon diameter, while the second experiment validates the model-based estimation of pore size using ODE sequences in glass microcapillaries.

Chapter 4

Oscillating diffusion encoding - associated work

The previous chapter described a theoretical framework which provides the restricted signal model for ODE sequences. The results were validated against numerical MC simulations, showing that the GPD approximation for ODE sequences is accurate enough for practical situations.

This chapter presents two collaboration studies that extend the analysis of ODE sequences. The first study investigates in simulation the sensitivity of SDE and ODE sequences with respect to axon diameter, and is published in [153]. The second study provides experimental validation for the ActiveAx framework using ODE sequences, and has been presented at the ISMRM conference [194]. My main role in this work is providing the theoretical and computational framework for simulating and analysing data, but I have also been involved in other aspects of the research, as detailed in the statement of intellectual contribution at the beginning of the thesis.

4.1 Sensitivity to axon diameter

This section provides a broad understanding of signal sensitivity to axon diameter and determines the most effective ways to maximize sensitivity of SDE and ODE sequences in idealized and practical conditions. Here I present the experiments that I have been directly involved in, while an extensive discussion of sensitivity for various SNR levels can be found in [153].

4.1.1 Motivation

Many diffusion studies use off-the-shelf sequences, try to achieve the ideal conditions for short gradient pulsed or, in the case of ODE sequences, try to use the highest possible frequency. Previous work [151, 8, 93] showed the importance of optimising the acquisition protocol in order to maximise its potential given the hardware constraints of a scanner. An automatic optimisation framework gives the final acquisition protocol, however, it does not provide a clear understanding of the result, especially in the case of more complex sequences.

In this study we use a standard two-compartment white matter model (non-permeable cylindrical axons) to investigate the signal sensitivity of SDE and ODE sequences to axon diameter, in detail. In white matter, axons are rarely coherent and models of fibre dispersion (discussed in section 2.4) have been in the literature to describe a more realistic distribution of axons at the voxel scale. Here, we consider both the idealised situation of parallel axons with known orientation (central to several white matter models, e.g. AxCaliber) as well as more realistic cases of unknown orientation or dispersed fibres.

4.1.2 Aims and objectives

The simulations of this study aim to:

1. analyse the sequence sensitivity to axon diameter in the idealised condition of parallel fibres and gradient perpendicular to the fibre
2. analyse the effects of T2 decay on the sequence sensitivity.
3. analyse the sequence sensitivity to axon diameter when the fibre orientation is unknown, i.e. the gradient is not perpendicular to the fibre direction.
4. analyse the sequence sensitivity to axon diameter when in the more realistic scenario of dispersed fibres.

4.1.3 Methods

This section outlines the diffusion MR signal model for white matter, introduces the pulse sequences, and develops the concept of signal sensitivity to axon diameter we use here.

MR signal model

In this study we use two-compartment models of white matter which describe the diffusion signal as a weighted sum of intra-axonal space (restricted diffusion) and extra-axonal space (hindered diffusion):

$$S^* = S_0(fS_r + (1-f)S_h) \tag{4.1}$$

where S_0 is the MR signal with no diffusion weighting and $f \in [0,1]$ is the proportion of water molecules inside the axons.

The first model is a simplified version of the CHARMED model [195, 149] where the intra-axonal compartment is described by parallel, non-abutting cylinders with a single radius. The second one is more realistic and explicitly accounts for axon dispersion which is modelled with a Wason distribution parametrized by a scalar concentration parameter κ, as proposed in [11].

The intra-axonal signal S_r is the product of parallel $S_{r,||}$ and perpendicular $S_{r,\perp}$ components and is calculated using the matrix method as described in section 2.3.4. The hindered compartment is described by a symmetric diffusion tensor model [50], with diffusion coefficient $D_{||}$ in the direction of the axons and $D_{\perp}$ in the perpendicular plane. The parallel diffusivity, $D_{||}$, is the same as the intrinsic diffusivity inside the cylinders in the model for S_r, following [151]. A simple tortuosity model [152] sets $D_{\perp} = D_{||}(1-f)$.

Pulse sequences

Figure 4.1 illustrates the SDE and ODE sequences showing the set of variables for each. Following this parametrization, ODE sequences have one additional variable compared to SDE sequences, namely the number of lobes N. We include the time constant τ_1 as the time between the middle of the RF pulse and the beginning of the first gradient waveform; τ_2 as the time between the end of the second waveform and the readout at the centre of k-space; $P180$ is the time required for the 180^o RF pulse and accounts for the surrounding crusher gradients and additional time delays; and $P90$ is the duration of the 90^o RF pulse.

Here we consider trapezoidal ODE sequences with integer number of oscillations N, which is typically used in ODE experiments [175, 173]. When N=1, the trapezoidal

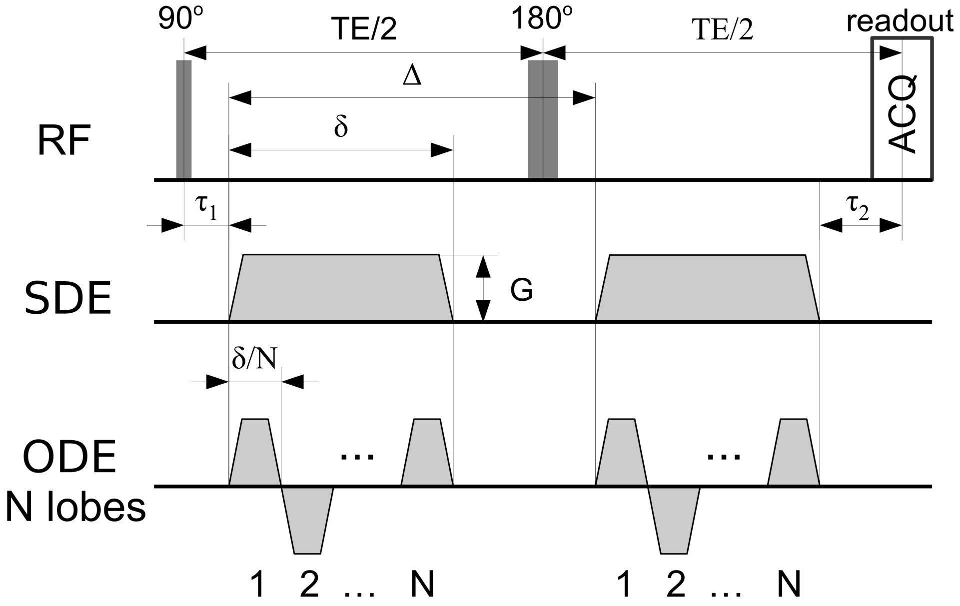

Figure 4.1: An illustration of SDE (middle) and ODE (bottom) sequence showing all the variables. ODE sequences are of trapezoidal shape with minimum achievable rise time to maximise diffusion weighting. The SDE sequence is a special case of ODE for N=1. Figure adapted from [153]

oscillating gradient reduces to an SDE sequence, thus we refer to all sequences as ODE. The b-values for these sequences are given by equation 3.4, which can be rewritten in terms of the number of lobes N:

$$b = \frac{2|\mathbf{G}|^2\gamma^2\delta^3}{15N^2}(5 - \frac{15t_rN}{2\delta} - \frac{5t_r^2N^2}{4\delta^2} + \frac{4t_r^3N^3}{\delta^3}) + |\mathbf{G}|^2\gamma^2(\Delta - \delta)\left(\frac{(1-(-1)^N)(\delta - N\cdot t_r)}{2N}\right)^2 \tag{4.2}$$

where t_r is the rise time and γ is the gyromagnetic ratio.

Sensitivity

We define the sensitivity of a measurement to axon diameter as a rate of signal change with axon diameter, i.e. the derivative $S^{*'}(a)$. From equation 4.1 we have:

$$S^{*\prime}(a) = S_0 f S_r'(a). \tag{4.3}$$

In both models we assume that the signal coming from the extra-axonal space does not depend on the diameter, thus it has no contribution to the signal sensitivity in equation 4.3. S_0 in general depends on both repetition time (TR) and echo time (TE). However, since $T1$ for white matter, typically around 800ms [196], is much smaller than the typical TR values (about 10s), hereafter we simplify the equation for S_0 by assuming infinite TR. If we additionally normalise by proton density, S_0 will depend on TE and T2: $S_0 = \exp(-\text{TE}(\delta, \Delta)/T2)$, where $\text{TE}(\delta, \Delta) = \delta + \Delta + \tau_1 + \tau_2$ and $T2$ is the relaxation time of the white matter. Hence, assuming independence of $T2$ on axon diameter, we have:

$$S^{*\prime}(a) = \exp(-\frac{\text{TE}(\delta, \Delta)}{T_2}) f S_r'(a) \tag{4.4}$$

and use it as a measure of sensitivity of the full signal $S^*(a)$.

Implementation

The simulations in this manuscript were performed using MISST simulation software described in chapter 7.

4.1.4 Results

This section presents the main results that investigate the sensitivity of ODE sequences to axon diameter for the two white matter models discussed above. It aims to find the key features of ODE sequences that drive the sensitivity and it assesses their impact for both ideal and more practical situations.

Simulations investigate a wide space of sequence parameters Λ, feasible on current human imaging systems: $G \in [0, 300]$mT/m ($G = |\mathbf{G}|$), $\delta \in [0, 60]$ms, $\Delta \in [\delta + P180, 100]$ms, $N \in [1, 10]$. We set typical values for time constants $\tau_1 = 10$ms, $\tau_2 = 20$ms, $P180 = 10$ms, and slew rate $SR = 200$T/m/s. Experiments use tissue models described in the Methods section and assume $f = 0.7$, $D_{||} = 1.7 \times 10^{-9}\text{m}^2/\text{s}$ [9], axon diameter $a \in [0, 10]\mu$m and $T2 = 70$ms [196] to match standard values in the white matter (at 3T). Note that b-value, q-value and TE are not fixed and the sequence parameters are allowed to take any values in space Λ.

The first two experiments maximise the sensitivity of restricted signal $S_r'(a)$ for a white matter model with parallel cylinders assuming known fibre orientation and gradients perpendicular to the fibre direction. The first simulation assumes infinite $T2$, while the second one includes the effects of $T2$ decay. Subsequent experiments relax the assumption of known fibre orientation and investigate sensitivity for a range of angles $\angle(\mathbf{n}, \mathbf{G})$ and as well as a more complex white matter model with fibre dispersion.

Maximising sensitivity of the restricted signal ($\mathbf{n} \perp \mathbf{G}$)

This section investigates the impact of ODE sequence parameters on the restricted signal in the ideal conditions of parallel fibres with diffusion gradient perpendicular to them ($\mathbf{n} \perp \mathbf{G}$). The effect of $T2$ relaxation is analysed separately in order to better understand the link between the diffusion signal and sequence parameters. As ODE sequences are defined by four parameters, G, δ, Δ and N, we aim to find in a systematic way which combination yields the largest $S'_r(a)$. The choice of the optimal gradient separation is detailed in [153] and all subsequent experiments use a fixed time interval between the two gradients given by the duration of the refocusing RF pulse, yielding an optimal Δ:

$$\Delta = \delta + P180. \tag{4.5}$$

Sensitivity without $T2$ relaxation This experiment simulates $S'_r(a)$ for the range of sequence parameters in Λ, and with Δ constrained according to Equation 4.5 in order to analyse the impact of gradient strength G, gradient durations δ and the number of lobes N.

Figure 4.2 plots $S'_r(a)$ for different values of axon diameter $a \in \{2, 4, 6, 8\}\mu\text{m}$. The absolute value of $S'(a)$ is colour coded, the horizontal axis gives the pulse duration δ, the vertical axis gives the gradient strength G and the different planes represent different number of oscillation. Maximum intensity points are marked with a black star. The values of δ which did not satisfy the slew rate constraint ($\delta > G/2SR \times N$, SR is the slew rate) were excluded.

The results show that in the case of parallel fibres and perpendicular diffusion gradient the maximum sensitivity occurs for SDE sequences (ODE with $N = 1$) for all axon diameters considered in this study. In the case of small axon diameters, the largest gradient amplitude and longest pulse duration are preferred, emphasizing the need for stronger diffusion weighting when probing smaller length scales. For larger diameters, the increased signal attenuation is compensated by a preference for lower

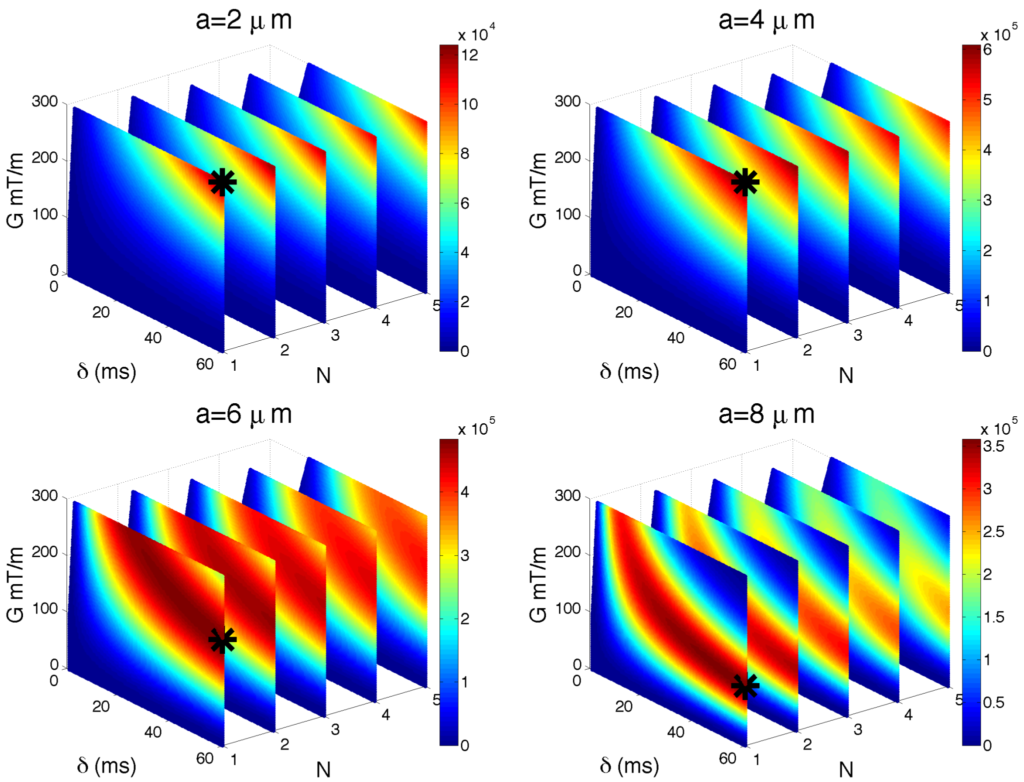

Figure 4.2: Impact of G, δ and N on sensitivity. Figure shows $S_r'(a)$ for $a \in \{2, 4, 6, 8\}$ μm and $\mathbf{n} \perp \mathbf{G}$. The absolute value of S_r' is colour coded, with dark red being the highest value. Maximum intensity points are marked with a black star. Note that the plots are not perfectly rectangular due to excluded values of δ that did not satisfy the slew rate constraint. Unit of $S_r'(a)$ is $1/\mu$ m. Figure from [153]

gradient strength with the longest pulse duration. The overall sensitivity varies with the axon size, however they are all of the same order of magnitude. This figure also shows that the sensitivity of sequences with $N > 1$ is similar, even though their b-values are an order of magnitude lower.

Sensitivity with $T2$ relaxation This experiment takes into account $T2$ relaxation and the effect of echo time on the signal sensitivity given by equation 4.4 which assumes independence of a and T_2. Increasing the pulse duration δ and separation Δ increases the echo time which reduces the sensitivity of the overall signal. Figure 4.3 shows $S^{*\prime}(a)$ for $a \in \{2, 4, 6, 8\}$ μm when the effect of $T2$ relaxation is taken into account and maximum intensity points are marked with a black star.

Accounting for $T2$ relaxation has two main effects: it decreases the pulse duration δ and increases the gradient strength G, which hits the upper boundary considered in this study. Nevertheless, the maximum sensitivity point is still obtained by SDE sequences for all diameters.

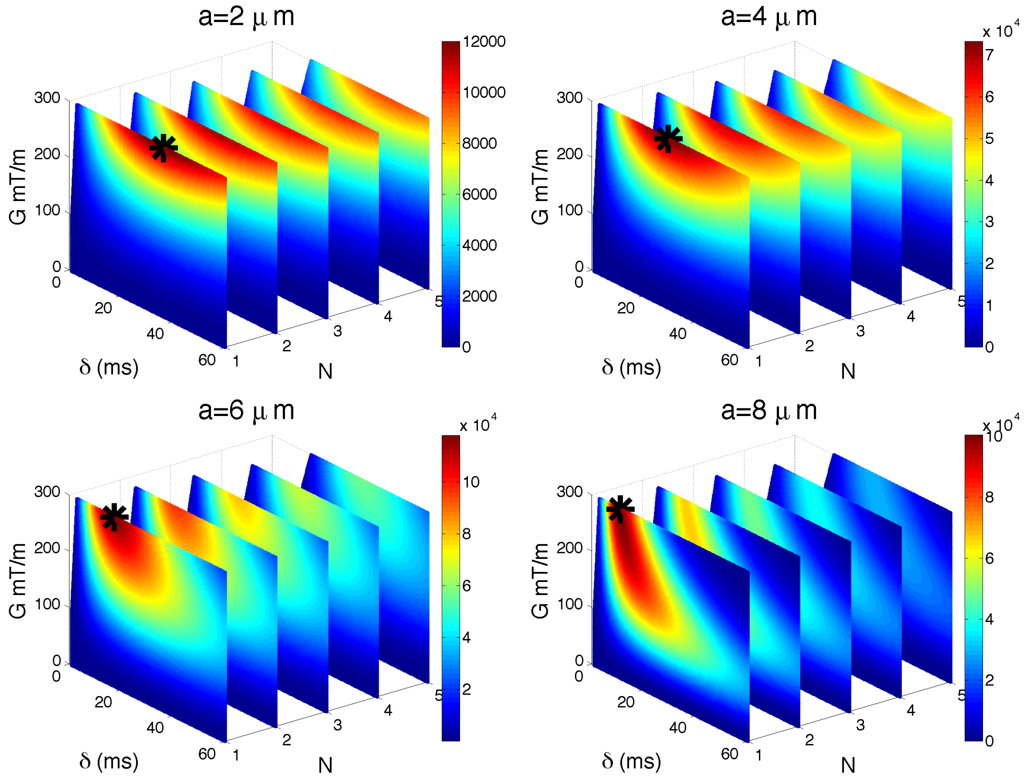

Figure 4.3: Impact of T_2 decay on sensitivity. As Figure 4.2 but with $T_2 = 70$ms. Unit of $S^{*\prime}(a)$ is $1/\mu$ m. Figure from [153]

Gradient not perpendicular to fibre direction ($\mathbf{n} \not\perp \mathbf{G}$)

This section investigates signal sensitivity when diffusion gradients are not perfectly perpendicular to the fibres: $\angle(\mathbf{n}, \mathbf{G}) = 90^o \pm \theta$, where θ measures the deviation from the orthogonality. This is the case in many practical situations such as fibres with unknown orientation or HARDI acquisitions. The effects of T_2 relaxation are also considered.

Figure 4.4 shows $S^{*\prime}(a)$ for $a \in \{2, 4, 6\}$μm and different deviations from orthogonality $\theta \in \{1^o, 6^o, 10^o\}$ and maximum intensity points are marked with a black star. The optimal combination of G and δ are relatively similar to the perpendicular case, however the choice of N is different.

The results show that the optimal N is strongly affected by the deviation from orthogonality. For the diameters illustrated in Figure 4.4 (i.e. $a < 6$ μm) the optimal N increases with increasing θ, however for $a > 7$ μm the choice of $N = 1$ is still preferred.

As seen in the methods, the restricted diffusion signal is the product of parallel and perpendicular components. As θ increases, the effect of the parallel signal component, which exponentially decays with b-value, increases as well, affecting the overall signal sensitivity. Consequently, the sensitivity of sequences with $N = 1$, which have significantly higher b-values for similar combinations of G and δ, drops as θ increases. This effect is visible for small pore diameters ($a < 7$ µm) that require sequences with high b-value for optimal sensitivity in the perpendicular gradient case. For larger pore diameters ($a > 7$ µm), where the initial parameter combination did not yield sequences with a very high b-value, this effect is not present and the optimal sequence has $N = 1$.

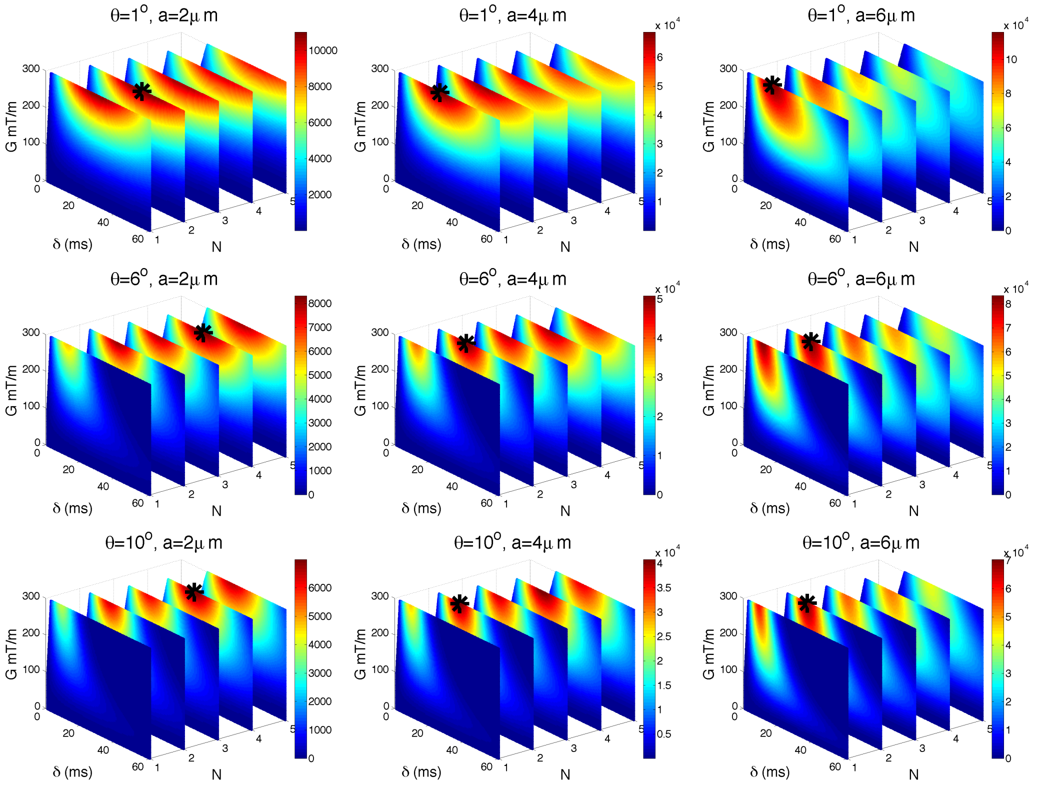

Figure 4.4: Impact of θ on sensitivity. As Figure 4.3 but for $\theta = 1^o$ (top), $\theta = 6^o$ (middle), $\theta = 10^o$ (bottom). Unit of $S^{*\prime}(a)$ is $1/\mu$ m. Figure from [153]

Fibre dispersion

The experiment analyses $S^{*\prime}(a)$ for the model with fibre dispersion described in Methods section, in the same range of sequence parameters. The tissue model has axon diameters in the range $a \in [0, 10]\mu$m and concentration parameter of the Watson distribution $\kappa \in [0, 32]$. The principal orientation of the fibres is perpendicular to the gradient vector and the concentration parameter of the Watson distribution describes the amount of dispersion around the principal direction (anisotropy increases with increasing κ). Figure 4.5 shows the sensitivity of the full signal $S^{*\prime}(a)$ (with T_2 relaxation) for

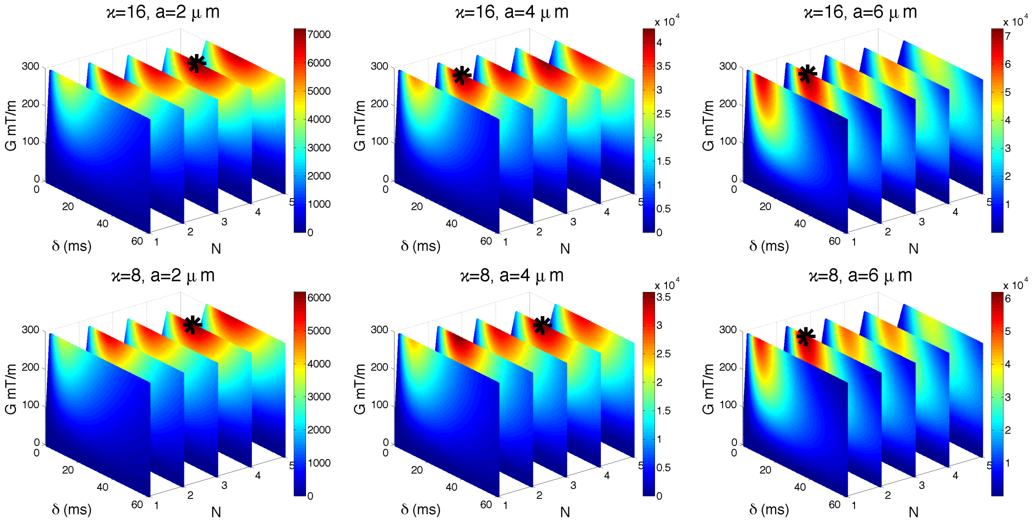

Figure 4.5: Impact of fibre dispersion on sensitivity. Figure shows $S^{*\prime}(a)$ for $\kappa = 16$ (top row) and $\kappa = 8$ (bottom row). $a \in \{2,4,6\}$µm and $T_2 = 70$ms. As in previous figures: the absolute value of $S^{*\prime}(a)$ is color coded, with dark red being the highest value; maximum intensity points are marked with black stars; plots are not perfectly rectangular due to the slew rate constraint.Unit of $S^{*\prime}(a)$ is $1/$µ m. Figure from [153]

$a \in \{2,4,6\}$µm and $\kappa \in \{8,16\}$, with the maximum intensity points marked with a black star.

The optimal combination of G, δ and N are similar to the case of non-perpendicular gradients discussed above. Sequences with $N > 1$ yield the highest sensitivity for the parameter space considered in this study for small axon diameters ($a < 7$ µm), while SDE sequences are optimal for larger axon diameters ($a > 7$ µm). This effect is more pronounced for smaller values of κ which indicate higher dispersion.

4.1.5 Discussion

The aim of this study is to explore optimal combinations of ODE sequence parameters for sensitivity to axon diameter in an intuitive way. Thus we use simulations and simple white matter models of non-permeable cylindrical axons, with either parallel or dispersed configurations. The results show that in the case of parallel fibres with known orientation (i.e. $\mathbf{n} \perp \mathbf{G}$), the optimal parameter combination has $N = 1$ (a standard SDE sequence) for the entire range of axon diameters considered ($a \in [0,10]/$µm). When the effects of $T2$ decay are not considered, the optimal sequences have the longest gradient duration $\delta = 60$ms and the gradient strength is decreasing with axon diameter in order to preserve the signal. If $T2$ decay is included, then the optimal sequences have the shorter gradient duration and the largest gradient strength $G = 300$mT/m.

In practice, fibre orientation varies across the brain, which makes it unlikely for the gradient to be perpendicular for different regions. Even if we are interested in a particular area, such as corpus callosum which is very homogeneous, there is still dispersion at the voxel level. In the case of non-perpendicular gradients and/or dispersed fibres, the maximum sensitivity is achieved for $N > 1$ for small diameters $a < 7/\mu$m, which, for example, represents the majority of axon diameters in the human corpus callosum [35]. ODE sequences with $N > 1$ are beneficial in these situations because they yield high sensitivity at a modest b-value. The lower b-value retains signal sensitivity in the cases of unknown fibre direction and/or dispersion by avoiding excessive signal attenuation due to freely diffusing water in the parallel direction. This is particularly advantageous for systems with high performance gradients. For larger pores which do not require sequences with a high b-value to maximise sensitivity, SDE sequences ($N = 1$) provide maximum sensitivity.

The effect of SNR on signal sensitivity is thoroughly discussed in [153]. The results illustrate that ODE sequences with $N > 1$ provide more sensitivity to axon diameter in the case of unknown or dispersed fibre orientation for a wide range of gradient strengths and SNR levels. Moreover, the results show what is the resolution limit (the smallest diameter that can be distinguished) for different SNR levels and gradient strengths. In the case of standard clinical gradient strengths < 80 mT/m, the resolution limit of axon diameter is around 5 μm, while for larger gradient strengths of 300 mT/m which could be achieved on the Connectome scanner [154] the resolution limit decreases to 2.5 μm. Although the majority of axon diameters are smaller than the resolution limit, there are also axons which are above the limit, biasing the estimated indices to larger values, e.g. in ActiveAx[9]. A recent study fits a Poisson size distribution instead of a single axon diameter index [10], and reports mean axon diameter values bellow 2 μm for a gradient strength less than 100 mT/m. As the Poisson distribution has only one parameter, having measurements that are sensitive to the tail of the distribution directly influences its mean, which results in smaller estimates of the mean diameter, even below the resolution limit.

In this study, we assume a simple tortuosity model for the extracellular space, which has been previously used for estimating indices of axon diameter in the human brain [9, 11]. In some situations this model cannot capture the complexity of the extracellular space, and recent studies have shown a time dependent diffusivity in the extracellular space, which reflects restricted diffusion [197, 10]. If the signal contribution from the extracellualr space is modeled independently of the inner axon diameter, as in [10], or there is only a weak dependence, these results should not be significantly affected; however, a significant amount of restriction in the extracellular space would impact on the axon diameter estimation, affecting the results presented here. Including a more complex model for extracellular space and myelin thickness is the subject of ongoing research.

All in all, this study shows the importance of optimising the acquisition protocol for a particular application and choosing the diffusion sequences that are sensitive to the tissue features of interest.

4.2 Phantom validation

This section presents the experimental validation of the ActiveAx framework [9] using ODE sequences on a clinical scanner. The data was acquired in glass micro-capillaries array plates (MAP) and has been analysed using the signal model presented in chapter 3.

4.2.1 Motivation

Phantom validation is a crucial step in developing new acquisition sequences for MRI. The theoretical signal model can be easily validated using numerical simulations, as detailed in section 3.2.3, however implementing novel sequences on the scanner and acquiring experimental data pose additional challenges such as susceptibility artefacts, Eddy current distortions, limited SNR, etc. This work shows the feasibility of using ODE sequences on a clinical scanner to estimate microstructural parameters such as pore size.

4.2.2 Aims and objectives

Specifically, this study aims to:

1. implement ODE sequences on a clinical scanner.

2. estimate water diffusivity and capillary diameters using the ActiveAx framework.
3. compare the parameter estimates from ODE sequences with various number of oscillations.

4.2.3 Methods

This section outlines the diffusion MR model, the preparation of the micro-capillaries array plates, the imaging protocols and data processing pipeline.

Diffusion MR model

The phantom consists of glass micro-capillary arrays filled with water which is confined inside cylindrical pores. Thus, we simplified the ActiveAx framework and we use only one compartment of restricted diffusion in parallel, non-abutting cylinders, with equal radii and impermeable walls. The model has the following parameters: intrinsic diffusivity (D_i), capillary diameter (a) and direction $\mathbf{n}$.

As diffusion in parallel and perpendicular direction are uncorrelated, the restricted diffusion signal, $S_r = S_{r||}S_{r\perp}$, is the product of components arising from displacements parallel, $S_{r||}$, and perpendicular, $S_{r\perp}$, to the long axis of the cylinder [195]. The signal model for $S_{r\perp}$ is computed using the GPD approximation and $S_{r||}$ describes free diffusion with D_i. The signal model and b-values for the ODE sequences are given in section 3.2.2. The total signal accounting for both components is:

$$S = S_0 S_r = S_0 S_{r||} S_{r\perp}. \tag{4.6}$$

where S_0 is the MR signal without diffusion weighting.

Phantom Description

Sample Preparation: The micro-capillaries array plates (as shown in Figure 4.6a) are thin square plates (20mm × 20mm × 1mm) made up of borosilicate glass (Incom, inc). This experiment uses three pairs of plates with nominal capillary diameters, 5, 10 or 20 µm. (Figure 4.6b, c and d).

Acquisition

Trapezoidal ODE diffusion sequences were implemented on a Phillips Achieva 3.0T TX MRI system (University College London Hospital, London, UK). The sequence

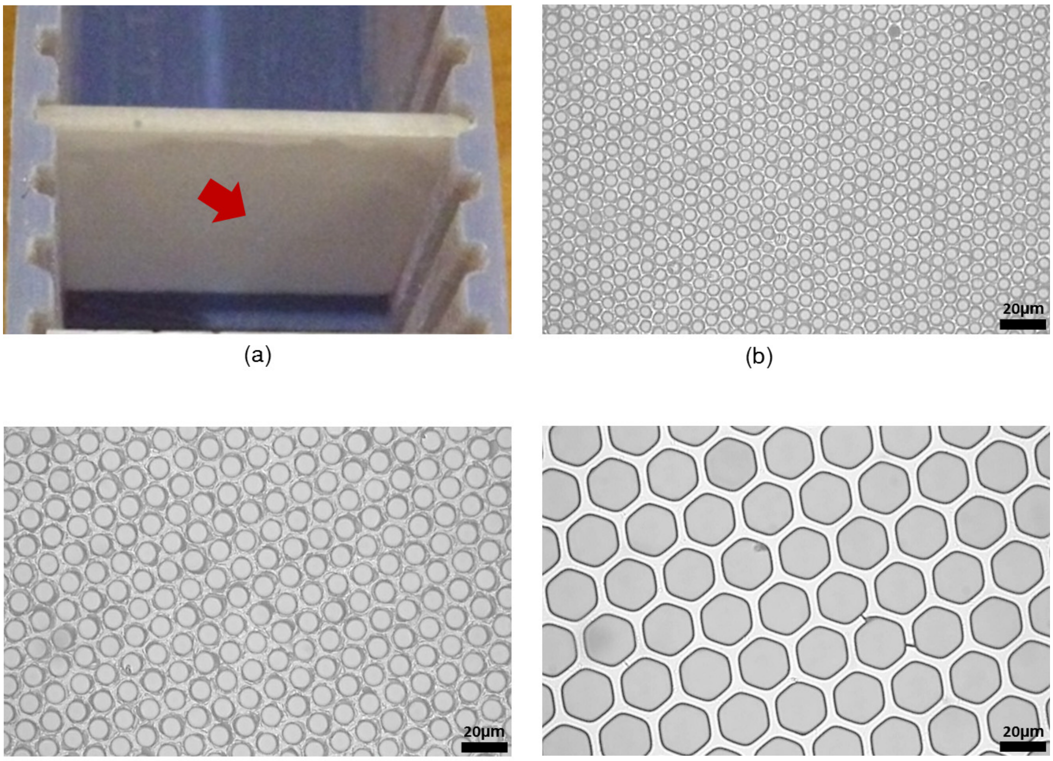

(a) (b) (c) (d)

Figure 4.6: (a) Photograph of the micro-capillaries array plates with capillary diameters of 5 µm (plate 1). Light microscopy images of (b) 5 µm (plate 1), (c) 10 µm (plate 1) and (d) 20 µm (plate 1). Images courtesy of Lebina Kakkar

parameters that can be controlled are: echo time (TE), pulse duration (δ), gradient separation (Δ) and number of half period oscillations, referred to as 'lobes' (N). Gradient strength, **G**, and slew rate were fixed in all experiments at 62mT/m and 68.9mT/m/ms, respectively, and they comply with the safety values for peripheral nervous stimulation (PNS). During the experiment the temperature was kept constant at 20^o.

The diffusion protocol consisted of 9 HARDI shells of ODE measurements with b-values ranging from 120 to 20000s/mm^2, each with 32 gradient directions and one b=0s/mm^2. For all ODE shells, the pulse duration and gradient separation were fixed to $\delta = 39$ms and $\Delta = 63$ms, respectively, and the number of lobes was varied from N=1 to N=9. Consequently, the b-values varied. An additional SDE diffusion sequence (N=1, δ=10ms,Δ=92ms) with a b-value of 1860s/mm^2 was included for comparison.

All diffusion protocols were acquired using SS-EPI readout as explained in section 2.2.3. The slice thickness was 10mm with in-plane resolution of 0.4×1.6mm, which ensured that at least one row of voxels was free from partial volume effects. Eddy currents were automatically corrected for by the scanner hardware.

Data Analysis

Data processing: The image registration was performed using FMRIB Software Library (FSL) rigid-body registration [198]. The SNR was calculated per voxel from the $b = 0$ images (mean SNR > 45) and the region of interest (ROI) was manually chosen to avoid partial volume effects.

ActiveAx Model Fitting: Data was fitted using a voxel-wise, two-stage fitting procedure as described in [9], in order to estimate diameter and diffusivity of the plates. The mean and standard deviation of the parameters were calculated for the voxels in each ROI.

4.2.4 Results

This section describes the microstructure parameter estimates of plates, which are obtained from these experiments.

Figure 4.7a and b display the parameter maps of diameter and diffusivity estimates for the different ROIs. The parameter estimates for the plates with diameters of 10 and 20μm plates are accurate and precise, while for the plates with $a = 5$ μm, the fitted diameters are underestimated. Figure 4.7c and d show the mean and standard deviation of the estimated a and D_i calculated across the ROI.

Figure 4.8 illustrates the experimental data and model predictions for the fitted and ground truth parameters for a central voxel of each plate. The ground truth value for diameter was provided by the manufacturer and the diffusivity was set to 2.0 μm^2/ms corresponding to free water at 20^{o}C. There is a good agreement between the measurements, the fitted curve (dashed lines) and the ground truth curve (full lines) for 10 μm and 20 μm plates. Larger differences can be seen for 5 μm plates (Figure 4.8a and b). In this case the signal is noisy ($S/S_0 > 1$) close to $|\mathbf{n.G}|/|\mathbf{G}|=0$ due to the low diffusion weighting for small capillaries. The difference between the signal from the predicted and ground truth parameters is small even if there is a drastic difference in the parameter values, which indicates that the measured signal is not very sensitive to capillaries at or below 5 μm. These parameter estimates were calculated using the entire data set with 9 different shells.

The next experiment investigates the ability of each measurement shell to estimate

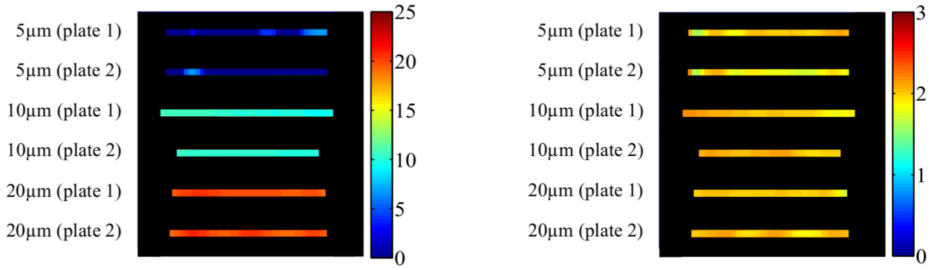

(a) Estimated diameter (μm)

(b) Estimated diffusivity (μm^2/ms)

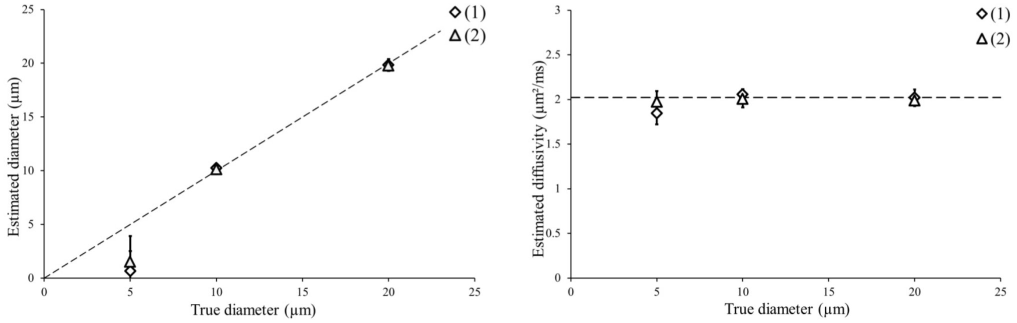

(c) Diameter

(d) Diffusivity

Figure 4.7: The (a) diameter, a, and (b) diffusivity, D_i, maps, respectively, across the ROIs of the 5 μm (plates 1 & 2), 10 μm (plates 1 & 2) and 20 μm (plates 1 & 2) plates. The graphs show the mean and standard deviation of the (c) capillary diameters (μm) and (d) intrinsic diffusivities (μm^2/ms), which are calculated over the ROIs. Image courtesy of Lebina Kakkar

capillary diameter and diffusivity. Figure 4.9 shows the mean and standard deviation of the estimated diameter and diffusivity obtained by analysing each ODE shell. Here, the results from the additional SDE sequence (N=1,δ=10ms) are also included for comparison. The diameter estimates for larger pores (10 and 20 μm) are close to the ground truth values. In this case ODE sequences with low frequency (i.e. $N \in \{2,3,4\}$) perform very well, while the estimates become less accurate and precise for $N > 5$, which happens due to insufficient diffusion weighting as N increases. For the 20 μm diameter plate the fitting fails for N=1 (δ=39ms) due to the strong diffusion weighting which drives the signal to the noise floor. For this particular TE and diffusion gradient duration, we find that N>1 gives better results overall. For the plates with $a = 5$ μm, the pore diameter is highly underestimated for all shells, nevertheless the intrinsic diffusivity, which can be extracted from the free diffusion along the capillary, is in good agreement with the ground truth value especially for $N > 4$. This is the case due to the limited gradient strength that does not provide sufficient sensitivity to small pores. As discussed in section 4.1.5, the resolution limit for a gradient strength of ≈ 60 mT/m, the

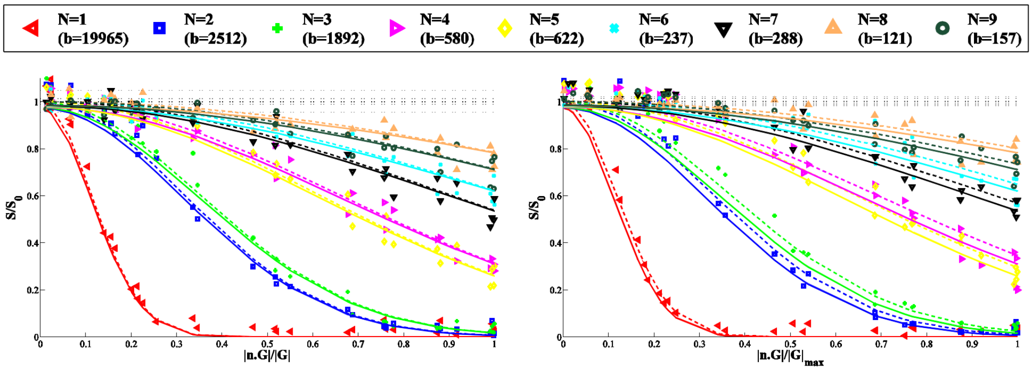

(a) 5μm, plate 1 (b) 5μm, plate 2

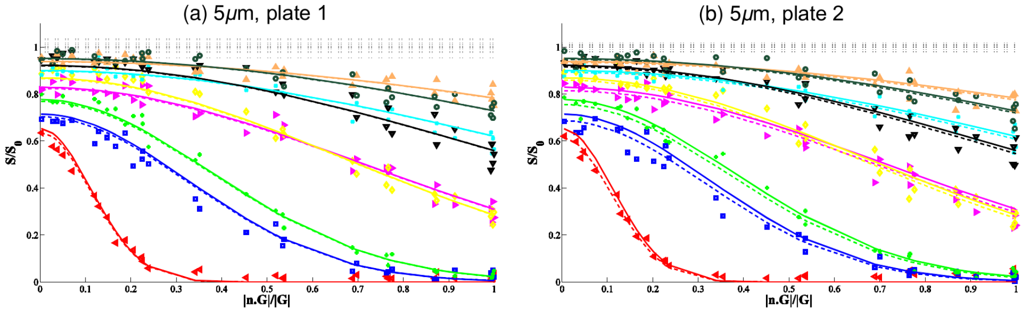

(c) 10μm, plate 1 (d) 10μm, plate 2

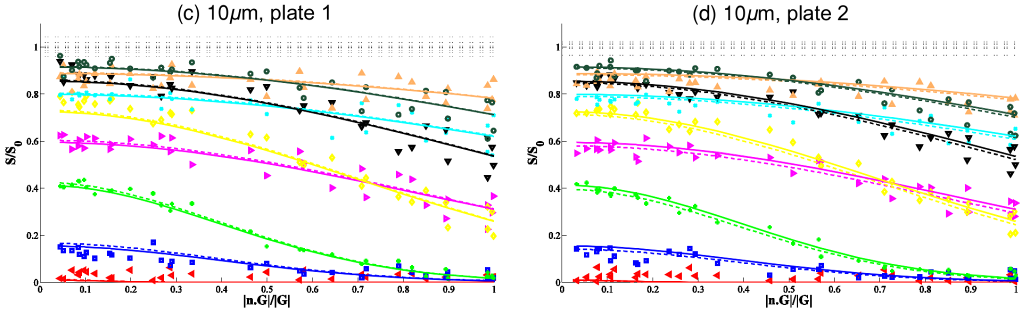

(e) 20μm, plate 1 (f) 20μm, plate 2

Figure 4.8: Plots of normalised signal versus absolute dot product between the gradient directions and the estimated capillary direction from the central voxel of each ROI in Figure 4.7a; the parallel component of the gradient increases from left to right. The measurements are represented by markers, while the solid (—) and dashed (–) lines show the predicted signal from the ground truth and estimated parameters, respectively. The colours indicate the different number of lobes N of the diffusion sequences. Image courtesy of Lebina Kakkar

resolution limit is around $5/\mu\mathrm{m}$. Although theoretically the smallest capillary diameter is on the limit of detectability, in practice it cannot be estimated due to the Rician noise in the experimental data (many values of the normalized diffusion signal are larger than 1 when the gradient is almost perpendicular to the fibres) which decreases the sensitivity.

4.2.5 Discussion

This work experimentally verifies the feasibility of ODE ActiveAX approach on a clinical scanner and provides validation for the theoretical work described in section 3.2.2. Microstructural features such as pore size were estimated for plates with capillary diameters of 5, 10 or 20 µm. This experiment uses a maximum gradient strength of 62T/m, which is sufficient to accurately and precisely estimate diameters of 10 and 20 µm, however the gradient is not strong enough to estimate smaller size, which is shown by poor agreement with ground truth values for the plates with $a = 5$ µm. The experiments also show that ODE with lower frequency ($N \in \{2, 3, 4\}$) provide the most accurate results, and in the cases considered the shell with N=3 yields estimates close to the ones obtained when fitting the entire data set. These results further enforce the importance of optimizing the diffusion acquisition for estimating pore size.

4.3 Conclusions

This chapter presents two collaboration studies that show the benefits of using ODE sequence for estimating axon diameters as well as the feasibility of implementing such an acquisition protocol on clinical scanners.

The first study in section 4.1 investigates the sensitivity of SDE and ODE sequences to axon diameters in various white matter models and aims to find the key parameters that drive this sensitivity. The results illustrate that low frequency ODE sequences are beneficial for estimating pore size in practical situations (dispersed axons, not perfectly perpendicular gradients). Thus a combination of high-frequency and low-frequency ODE sequences are needed for accurate estimation of intrinsic diffusivity and pore size.

The second study in section 4.2 provides experimental validation for ODE signal models and shows the benefits of estimating microstructural features such as pore size

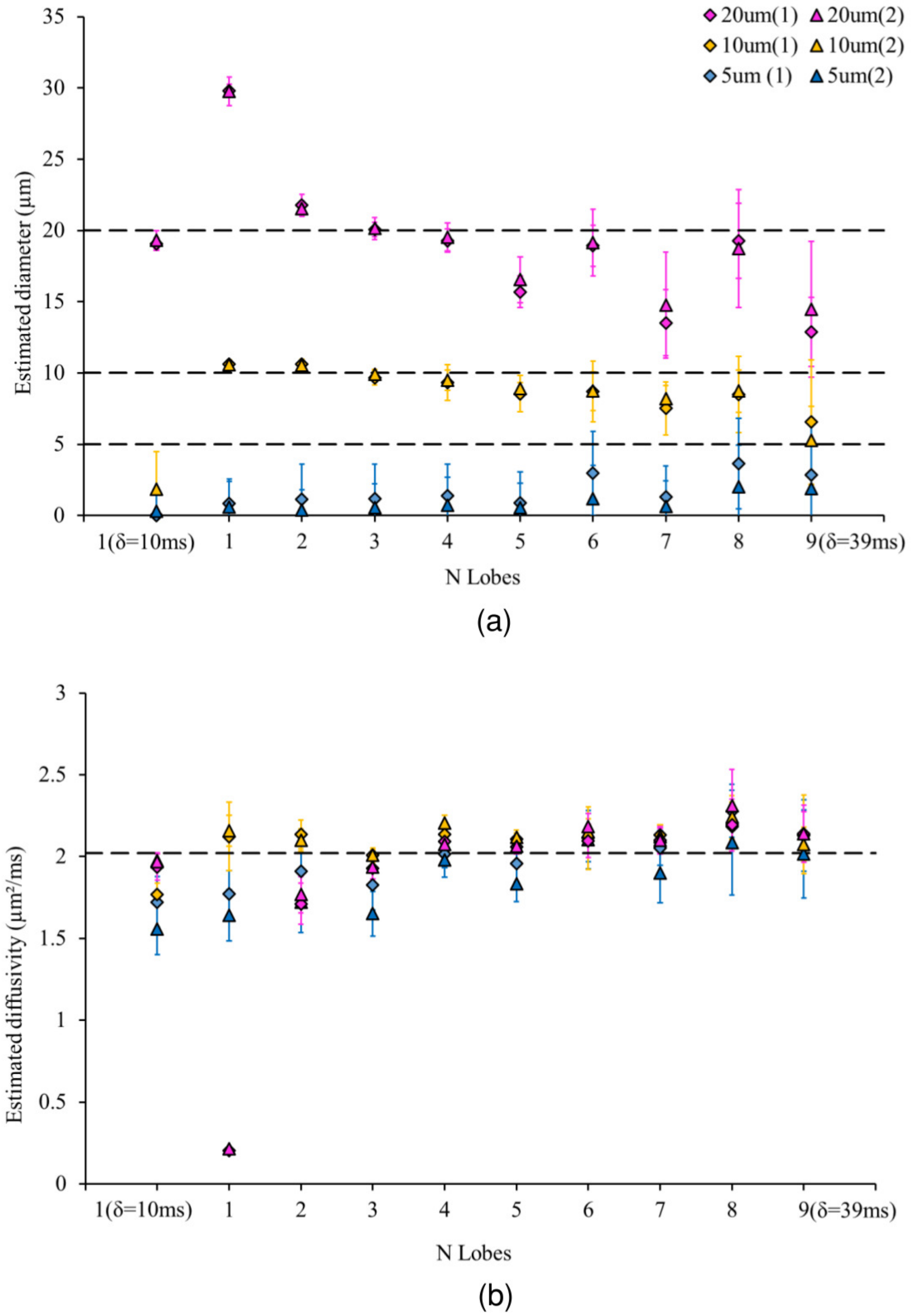

Figure 4.9: Mean diameter (a) and diffusivity (b) estimates calculated for each N from 1 to 9 (with δ = 39ms) and also from the standard SDE sequence (with δ=10ms), for all plates. The same central row of voxels, as in Figure 4.7, is used to calculate the mean and the standard deviation. The dashed lines represents the real nominal diameters in (a), and the calculated diffusivity from [199] in (b). N=3 produces the best diameter and diffusivity for both pairs of 10 µm and 20 µm plates. Image courtesy of Lebina Kakkar

using ODE sequences. The experimental results are in line with the theoretical predictions that low-frequency ODE improve sensitivity to microcapillary diameters. For a limited clinical gradient strength, the smallest pore size was not accurately estimated, which agrees with the detailed SNR analysis from [153].

Furthermore, this chapter illustrates the importance of numerical simulations for a better understanding of diffusion MRI signal in restricted environments in order to improve measurement sensitivity towards different microstructural features.

Chapter 5

Model-based estimation of microscopic anisotropy

The previous two chapters focused on understanding the MRI signal measured with ODE sequences. We derived an analytical signal model of restricted diffusion signal, analysed the sequence sensitivity to axon diameter and validated the ODE ActiveAx framework for estimating diameter in microcapillaries.

This chapter introduces a model-based approach for estimating microscopic anisotropy from DW-MRI data. It explores in simulation complex diffusion substrates with elongated pores and a distribution of sizes and extends the acquisition to a rotationally invariant framework in order to account for macroscopic anisotropy. Part of this chapter has been published in [91].

5.1 Motivation

Estimating complex histological features such as pore size distribution and eccentricity is important for an accurate representation of cancer tumours and brain tissue at the interface between white and grey matter. However, most of current microstructure imaging techniques cannot estimate both of these features. For instance, white matter models [5, 9, 11] discussed in section 2.4.2 assume axons to be infinitely long cylinders, while cancer models assume spherical cells [2, 3]. Therefore, these models cannot accurately represent other cellular shapes that are present in the tissue.

In addition, the above mentioned techniques use a collection of SDE sequences which have limited sensitivity to more complex systems, such as certain configurations of isotropic pores with a size distribution and randomly oriented anisotropic pores

[117]. More advanced pulse sequences, in particular those that have varying gradient orientation within one measurement, such as double diffusion encoding (DDE) [110], can disentangle these effects [111]. The difference between DDE measurements with parallel and perpendicular gradients has been used to derive model-free metrics of microscopic anisotropy [119, 121], however such metrics confound the effects of size and eccentricity and are highly prone to noise. More recent studies that use a model-based approach with DDE acquisition to estimate pore size and eccentricity did not consider the effects of size distribution [179] or assumed a known orientation of pores [189, 190], as discussed in section 2.4.4.

In this chapter we demonstrate in simulation the feasibility of using a model-based approach to provide quantitative microstructural features in complex substrates featuring elongated pores with a distribution of sizes and orientation dispersion. The key benefit of directly modelling microstructure is the ability to provide estimates of intrinsic tissue parameters independent of the acquisition protocol. First, we investigate the dependence of two standard indices of microscopic anisotropy on substrate parameters, then we show that more specific parameters such as pore size and eccentricity can be estimated by fitting a microstructural model to the diffusion data. We test whether a simple model with identical pores can provide a good estimate of volume-weighted mean pore size and eccentricity and we investigate the effects of explicitly modelling the size distribution.

Moreover, we compare the ability of different protocols with SDE and DDE sequences to recover the ground truth parameters and we further extend such a model-based technique to analyse macroscopically anisotropic substrates as well as substrates with various parametric and non-parametric size distributions.

5.2 Data synthesis

To synthesize diffusion data we use the MC simulator in Camino [101] using a mesh-based substrate, with closed pores represented as cuboids. The diffusion meshes have 1000 cuboids with two equal sides ($l_x = l_y$) and a gamma distribution of sizes, as illustrated in Fig. 5.1b in the case of a macroscopically isotropic substrate. The parameters of the model are the mean width of the cuboid $\bar{l_x}$, the ratio between the height and width $E = l_z/l_x$ (eccentricity), which is the same for all pores regardless of size, the gamma distribution shape parameter a and the diffusivity constant D. We choose different geometric models to synthesize and fit the data in order to emphasize the robustness of this approach when the geometry is not a perfect match. Moreover, we prefer cuboids over ellipsoids due to the reduced computational complexity of the mesh.

All MC simulations have 1000 time steps and 200000 walkers located inside the pores. Thus the synthesized data has intracellular signal only. Noise, with a Rician distribution and SNR = 50, was added to the data to create 100 different data sets for each substrate.

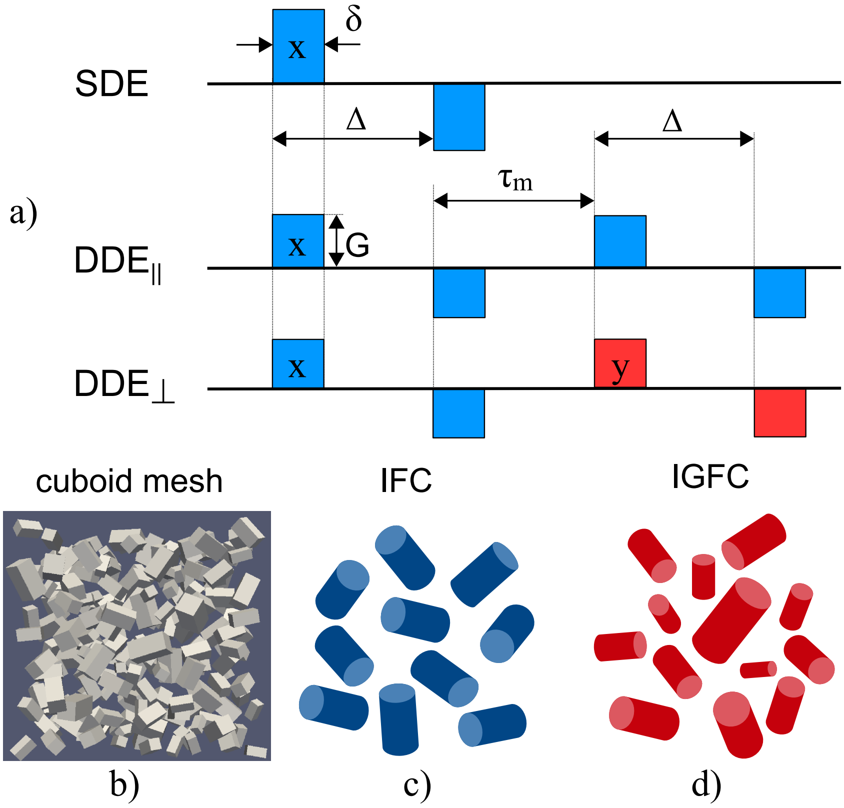

Figure 5.1: a) Effective diffusion gradient waveforms (accounting for the effect of 180^o rf pulses) for SDE, DDE with parallel gradients and with perpendicular gradients. b) Isotropic mesh based diffusion substrate for MC simulations ($\bar{l_x} = 6\mu$m, $E = 2$, $a = 2.5$). c) Schematic representation of the IFC model. d) Schematic representation of the IGFC model

5.3 Signal model and fitting

For fast signal computation, we expand the Gaussian Phase Distribution (GPD) approximation [80] for DDE sequences and a restriction model of finite cylinders with various sizes. Previous work [200] derived analytical expressions for DDE sequences and a similar restriction model keeping terms up to second order in $2\pi qR$, where q is the wavenumber and R is the radius. Here we keep second order terms in the expansion of the signal logarithm (cumulant expansion) which has a wider range of applicability than the same order of the Taylor series [201]. The GPD approximation provides analytical expressions of the signal $S(\mathbf{u}, R, E)$ for a finite cylinder with orientation $\mathbf{u}$, radius R and length $2RE$. We use the same framework presented in [90] for oscillating gradients.

To calculate the signal for an ensemble of finite cylinders, we numerically integrate the signal over orientation and size distribution weighted by volume, to obtain the overall signal $S = \int_{\mathbf{u}} \int_0^{\infty} \mathcal{P}(R)\mathcal{F}(\mathbf{u})S(\mathbf{u}, R, E)d\mathbf{u}R^3dR$. $\mathcal{P}(R)$ is the probability distribution of radii, $\mathcal{F}(\mathbf{u})$ is the probability distribution of cylinder orientation and E is the same for all sizes. The factor R^3 arises because the diffusion MRI signal from each pore depends on the amount of spins it contains and in our model the length of the cylinder is proportional to the radius. Assuming independence of parallel and perpendicular displacements [195], the signal for one cylinder is then $S(\mathbf{u}, R, E) = S_{\perp}(\mathbf{u}, R, E)S_{\|}(\mathbf{u}, R, E)$ with

$$
\begin{aligned}
\ln S_{\perp}(\mathbf{u}, R, E) =& \frac{\gamma^2}{2} \sum_n B_{cyl,n} \int_0^{TE} dt_1 \int_0^{TE} dt_2 \exp\left(-\lambda_{cyl,n} D|t_2 - t_1|\right) \\
& \mathbf{G}_{\perp}(t_1) \cdot \mathbf{G}_{\perp}(t_2) \\
\ln S_{\|}(\mathbf{u}, R, E) =& \frac{\gamma^2}{2} \sum_n B_{plane,n} \int_0^{TE} dt_1 \int_0^{TE} dt_2 \exp\left(-\lambda_{plane,n} D|t_2 - t_1|\right) \\
& G_{\|}(t_1) G_{\|}(t_2)
\end{aligned}
\tag{5.1}
$$

where γ is the gyromagnetic ratio B_n and λ_n are geometry related factors for cylindrical and planar restriction [78] which depend on R and E, $G_{\perp}$ and $G_{\|}$ are the components of the diffusion gradient perpendicular and parallel, respectively, to the cylinder axis and TE is the echo time. The full expressions of the signal are provided in Appendix A.4 .

We fit the models to data in Matlab, using a two-step procedure: a grid search of predefined values, which gives a rough estimate of parameters, followed by a gradient descent which minimizes the difference between the data and the model given Rician noise. During all stages of fitting D is fixed to its true value. For numerical stability, the lower limit of the gamma distribution shape parameter a is set to 1 and the upper limit to 10000. All other parameters are estimated with no constraints. We also ensure that the parameter values used in the grid search do not overlap with simulation parameters. For the anisotropic substrates, the main orientation is estimated from the DTI-like data set, by fitting a linear diffusion tensor model, and fixed afterwards. This reduces the computational complexity of the gradient descent without compromising on accuracy.

5.4 Simulation 1: Metrics of microscopic anisotropy

This experiment investigates the dependence of two model-free metrics of microscopic anisotropy on pore elongation for various diffusion substrates. Specifically, we study ϵ and the corresponding normalized fractional eccentricity FE, introduced in [121]. Nevertheless, we expect similar behaviour for other metrics of microscopic anisotropy based on the difference between DDE measurements with parallel and perpendicular gradients, which were discussed in section 2.4.4. As detailed in [121], ϵ is an additive measure of compartment eccentricity and it depends on pore size to the fourth power. FE aims to remove this dependency and normalizes ϵ with respect to pore size. Here we aim to analyse the effect of pore size distribution as well as the influence of noise on the calculated ϵ and FE.

5.4.1 Aims and objectives

The specific objectives of this simulation are:

1. study the dependence of ϵ and FE on pore elongation.
2. investigate the effect of pore size distribution on the estimated metrics.
3. analyse the effect of different noise levels.

5.4.2 Methods

Derivation of ϵ and FE

We use the expressions derived in [121], simplified for a macroscopically isotropic substrate. In this case only two DDE sequences with parallel and perpendicular gradients are necessary to derive ϵ and FE based on the difference between the two measurements:

$$\log(S_{\|}) - \log(S_{\perp}) = q^4\epsilon, \tag{5.2}$$

where $S_{\|}$ is the signal for the DDE sequence with parallel gradients, $S_{\perp}$ is the signal for the DDE sequence with perpendicular gradients, $q = \gamma G\delta$ is the wavenumber, γ the gyromagnetic ratio , G the gradient strength, δ the pulse duration and ϵ depends on pore size and eccentricity. For spherical pores $\epsilon = 0$. Fractional eccentricity normalizes ϵ with respect to size:

$$FE = \sqrt{\frac{\epsilon}{\epsilon + 3\Delta^2 ADC^2/5}} \tag{5.3}$$

which varies between 0 (spherical pores) and 1 (elongated pores), where Δ is the diffusion time and ADC is the apparent diffusion coefficient which reflects the length scale of the substrate.

Diffusion substrates

To analyse the dependence of ϵ and FE on pore eccentricity we construct diffusion substrates as explained in section 5.2 with the following parameters: $\bar{l_x} = \{4, 8, 12\}\mu$m, $a = \{2.5, 10, \infty\}$ ($a \to \infty$ yields identical pores) and E varying between 1 and 3.

Measurement protocol

Further, we choose DDE sequences with parallel and perpendicular gradients with long diffusion and mixing times ($\Delta D/\bar{l_x}^2 \gg 1$, $\tau_m D/\bar{l_x}^2 \gg 1$) and pulse duration of $\delta = 5$ ms. To have a similar diffusion attenuation for all substrates and to be in the same diffusion regime we keep constant $\gamma\delta G\bar{l_x}$ and $\Delta D/\bar{l_x}^2$, respectively, as explained in [83]. The gradient duration is the same for all measurements $\delta = 5$ms. The gradient strength corresponding to the substrates with $\bar{l_x} = 4\mu$m is $G = 300$mT/m, and decreases accordingly for larger pores. This ensures the signal attenuation is above the noise floor for all substrates, with values between 0.2 and 0.9. The diffusion and mixing times, which are $\tau_m = \Delta = 100$ms for the substrates with $\bar{l_x} = 4\mu$m, are increased for larger pores, yielding a constant ratio $\Delta D/\bar{l_x}^2 = 12.5$. Additionally, we investigate the effect of noise with three different SNR levels of 50, 100 and ∞. As $S_{\|} - S \perp \geq 0$ [117], negative values of ϵ occur solely due to noise and are set to 0, in order to obtain real-valued FE.

5.4.3 Results

Figure 5.2a) plots FE against cuboid eccentricity in the range $E \in [1, 3]$ for substrates of various sizes, with mean $\bar{l_x} = \{4, 8, 12\}\mu$m and gamma distribution shape parameter $a = \{2.5, 10, \infty\}$. Figure 5.2b) shows a similar dependence for ϵ normalized with the pore size $\bar{l_x}^4$. The plots present the median values over 100 noise trials with SNR = 50 (left), 100(middle) and ∞ (right). Figure 5.2c) illustrates the FE values pooled from substrates with different l_x and a for different eccentricities $E = \{1, 1.5, 2, 2.5, 3\}$. The simulations show that FE is very noisy, especially for pores with low eccentricity where the difference between the DDE measurements with parallel and perpendicular gradients is smaller than the noise floor. ϵ, which is a direct measure of the signal difference, is less affected by noise, however it depends strongly on pore size.

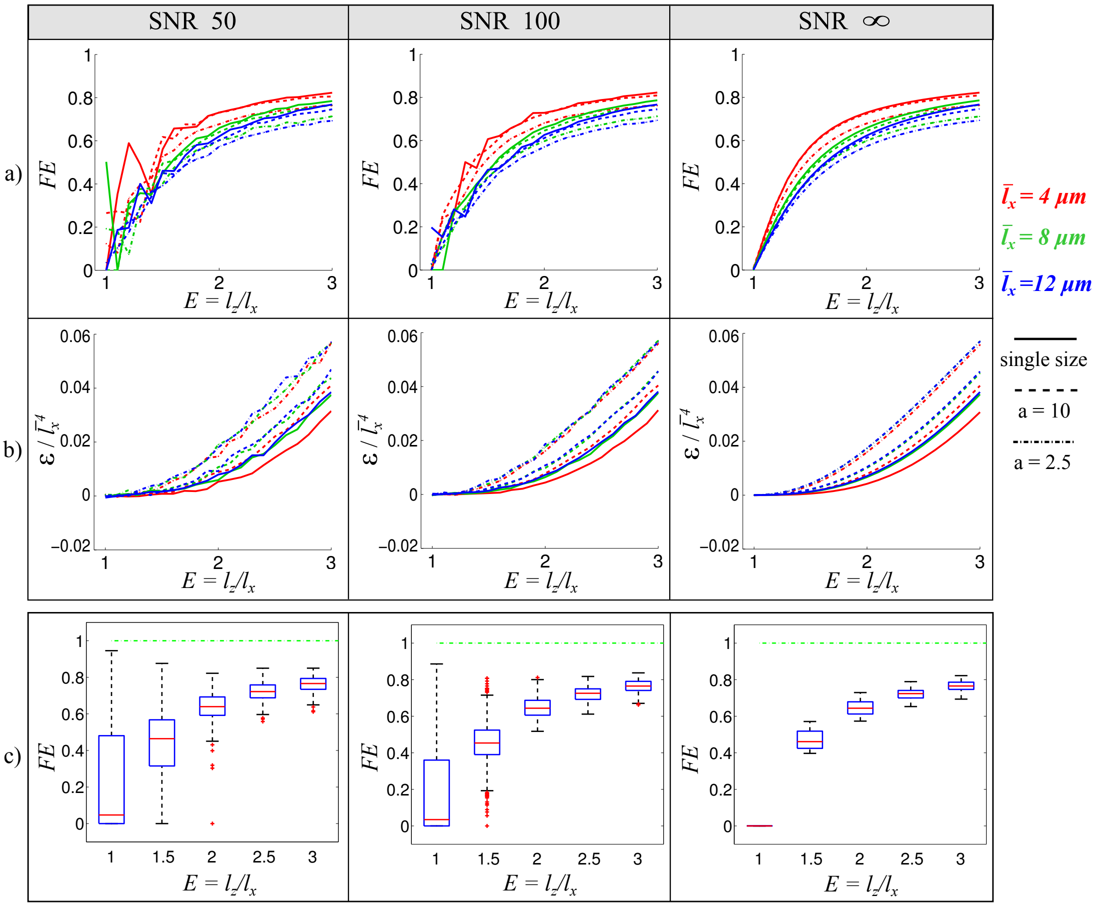

Figure 5.2: Dependence of a) FE and b) ϵ on pore eccentricity. The plot illustrates the average values over 100 instances of noise with SNR = $\{50, 100$ and $\infty\}$. The standard deviations were large (> 1) especially for pores with low eccentricity and are not shown for clarity. Different colours represent different sizes and different line styles represent different shapes of the gamma distribution.

5.4.4 Discussion

This section investigates the dependence of two model-free metrics of microscopic anisotropy on pore elongation for various diffusion substrates. The first metric, ϵ, confounds the effects of pore size and eccentricity, while FE, which normalizes ϵ with respect to pore size, is highly influenced by noise. The effect of noise is especially pronounced for pores with low eccentricity, when the signal difference between the two DDE measurements is below the noise level. In this case the microscopic anisotropy is likely to be overestimated. These findings are consistent with the original results presented in [121] which show noisy estimates in the grey matter of monkey brain.

Moreover, if we keep the diffusion time the same for all substrates ($\tau_m = \Delta =$ 100ms), both FE and ϵ are underestimated for the larger pores ($\bar{l_x} = 12\mu$m) (data not shown), which shows the importance of having the sequence parameters in the correct diffusion regime. This analysis is focused on FE and ϵ , but these observations hold for similar indices presented in [119] which are based on signal differences.

5.5 Simulation 2: Macroscopically isotropic substrates

This simulation explores a model-based approach for estimating pore size and eccentricity in macroscopically isotropic substrates that have a distribution of pore sizes. Here, we fit a microstructural model directly to the diffusion signal, avoiding the increased noise variance of the signal difference.

5.5.1 Aims and objectives

In this simulation we aim to:

1. test whether a simple model with identical pores can recover accurate estimates of volume-weighted mean size and eccentricity, in a similar way the axon diameter index from ActiveAx correlates with the volume-weighted mean axon diameter.
2. investigate the effects of explicitly modelling pore size distribution.
3. compare four diffusion protocols with SDE and DDE sequences and their ability to recover the ground truth parameters.

5.5.2 Methods

Diffusion substrates

We use MC simulations to synthesize the diffusion signal in a variety of macroscopically isotropic substrates, as explained in section 5.2. Thus, we construct separate meshes for each combination with the following parameter values: $\bar{l_x} = \{2, 4, ...12\}\mu$m, $E = \{1, 1.5, 2, 2.5, 3\}$, $a = \{2.5, 10, \infty\}$ and $D = 2 \cdot 10^{-9}$ m^2/s. The smaller pores have similar sizes to axons and dendrites in brain tissue [35, 202], while larger pores are closer to certain cancer cells, e.g. [203]. For intrinsic diffusivity we chose a value similar to the principal eigenvalue of the diffusion tensor measured at short diffusion time in the human brain [175].

Signal model

For the model-based estimation of pore size and eccentricity in a macroscopically isotropic substrate, we construct two signal models. The first one has identical pores and aims to test whether a simpler model can recover the average volume weighted size and eccentricity, in a similar way ActiveAx [9] yields an index of axon diameter. The second model explicitly accounts for pore size distribution. As we are investigating macroscopically isotropic substrates, the probability distribution of cylinder orientation is the 0th order spherical harmonic ($\mathcal{F}(\mathbf{u}) = 1/4\pi$). The two models are:

1. **Isotropic finite cylinders** (IFC) consists of randomly oriented identical finite cylinders and is illustrated in Fig.5.1c. This model has three parameters: cylinder radius R, ratio between cylinder length and diameter E (eccentricity) and diffusivity constant D. In this case the probability distribution of radii is a delta function $\mathcal{P}(R) = \delta(R)$.

2. **Isotropic gamma finite cylinders** (IGFC) consists of randomly oriented finite cylinders with a volume weighted gamma distribution of radii, so explicitly accounts for a size distribution, as illustrated in Fig. 5.1d. This model has four parameters: D, mean radius $\bar{R}$, the gamma distribution shape parameter a, and eccentricity E, which is the same across all sizes. In this case the probability distribution of radii is $\mathcal{P}(R) = \frac{1}{C}\frac{R^{a-1}(a/\bar{R})^a \exp(-Ra/\bar{R})}{\gamma[a]}$, where $\gamma(a)$ is the gamma function and $C = \int_0^\infty \frac{R^{a-1}(a/\bar{R})^a \exp(-Ra/\bar{R})}{\gamma[a]} R^3 dR$ is a normalization constant that accounts for volume weighting. The variance of the distribution is

$\text{var}\{\mathcal{P}(R)\} = \bar{R}^2/a$.

Measurement protocol

For estimating microstructural parameters, we test four different measurement protocols, constructed from basic SDE and DDE sequences shown in Fig. 5.1a. We construct a rich protocol for each sequence type to ensure sensitivity across as wide a range of pore sizes as possible. As the substrates are macroscopically isotropic, the diffusion gradients are only in x direction (parallel) and y direction (perpendicular). To make the comparison as fair as possible, we choose sequence parameters that yield the same maximum diffusion weighting (b-value) and number of measurements in each protocol. The protocols are:

1. **SDE** protocol. This has the following parameters: pulse duration $\delta = \{5, 10, , ...25\}$ ms, gradient strength $G = \{25, 50, 75, 100, 300, 500\}\sqrt{2}$ mT/m and time interval between the beginning of the first and second gradients $\Delta = \delta + \{5, 10, 20, 30, 40\}$ ms with two repetitions for each measurement. The gradient strength for SDE measurements is higher by a factor of $\sqrt{2}$ in order to have the same b-value as the other protocols.
2. **DDE**$_{||}$ protocol. This has DDE sequences with parallel gradients of equal amplitudes. The other parameters are: $\delta = \{5, 10, , ...25\}$ ms, $\Delta = \delta + \{5, 10, 20, 30, 40\}$ ms, $G = \{25, 50, 75, 100, 300, 500\}$ mT/m, and mixing time $t_m = \Delta$, with two repetitions for each measurement.
3. **DDE**$_{\perp}$ protocol. This has DDE sequences with perpendicular gradients of equal amplitudes. The rest of the parameters are the same as for **DDE**$_{||}$.
4. **DDE**$_{||\&\perp}$ protocol. This has DDE sequences with both parallel and perpendicular gradients for each combination of parameters in the DDE$_{||}$. Including only one repetition rather than two, as in the SDE, DDE$_{||}$ and DDE$_{\perp}$ protocols, ensures the same number of measurements in all protocols.

Protocol comparison

For a quantitative protocol comparison, we use an objective function derived from the Cramer-Rao Lower Bound (CRLB) to rank the four protocols. The CRLB provides a lower bound on the variance of the parameter estimates given a set of measurements, and is often closely correlated to the true variance. Thus, objective functions based on the CRLBs are a standard optimality criterion and have been previously used in diffusion MRI experiment design [151, 93]. To ensure similar scale, we use the sum of the normalized CRLBs to compare the four protocols:

$$F = \sum_{i}^{P} (J^{-1})_{ii}/p_i^2 \tag{5.4}$$

where p_i are the model parameters with $i = 1, ...P$, J is the Fisher information matrix and $(J^{-1})_{ii}$ is the CRLB for p_i. For example, in the IFC model we fit two parameters (R and E) and in the IGFC model we fit three parameters (R, E and a).

5.5.3 Results

This section focuses on the results for macroscopically isotropic substrates. First we investigate the ability of a signal model with identical pores (IFC) to recover ground truth microstructural features in the case of substrates with a single pore size or a distribution of sizes. Then we analyse a signal model which directly accounts for the size distribution (IGFC). The last part of this section compares the ability of the four protocols to recover model parameters.

IFC model: Figure 5.3a illustrates the relative error of the parameter estimates ($\Delta R = (R_{est} - R_{g.t.})/R_{g.t.}$) and $\Delta E = (E_{est} - E_{g.t.})/E_{g.t.}$) from the IFC model for different ground truth values used in the MC simulation. When computing the relative errors, the ground truth parameter values are adapted to account for the difference in geometry between cuboids (MC simulation) and finite cylinders (signal model) by matching cylinder radius to give the same pore volume. Thus, for a cuboid with width l_x and $E = l_z/l_x$, the corresponding radius of a finite cylinder is $l_x/\sqrt{\pi}$ and eccentricity is $E\sqrt{\pi}/2$. The results are shown for SDE and $\text{DDE}_{\parallel\&\perp}$ protocols. The relative errors are separated according to the ground truth values of the parameters, with radius estimates in the middle column and eccentricity estimates in the right column.

The relative errors of the IFC model parameter estimates (R and E) are reported in Table 5.1a) and 5.1b). As the values are not normally distributed, we report non-parametric statistics to control for outliers. The median, lower quartile and upper quartile of the relative errors are presented separately for each measurement protocol and

		IFC - relative error of estimated radius $R : Md\ (q_1, q_3)$		
		$a \to \infty$	$a = 10$	$a = 2.5$
		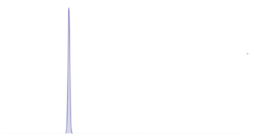	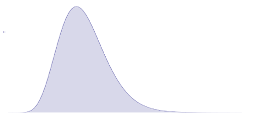	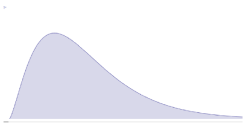
a)	SDE	$3.6\ (1.6, 6.3)\%$	$-9.6\ (-20, -2.9)\%$	$-20\ (-32, -13)\%$
	DDE$_{\|\|}$	$2.1\ (0.6, 4.0)\%$	$-12\ (-22, -5.7)\%$	$-22\ (-33, -16)\%$
	DDE$_{\perp}$	$0.4\ (-3.1, 3.9)\%$	$-18\ (-52, -11)\%$	$-29\ (-68, -20)\%$
	DDE$_{\|\|\&\perp}$	$1.6\ (-0.5, 3.1)\%$	$-12\ (-20, -5.8)\%$	$-20\ (-31, -14)\%$

		IFC - relative error of estimated eccentricity $E : Md\ (q_1, q_3)$		
		$a \to \infty$	$a = 10$	$a = 2.5$
b)	SDE	$-0.8\ (-5.5, 1.4)\%$	$28\ (16, 72)\%$	$103\ (58, 192)\%$
	DDE$_{\|\|}$	$-1.7\ (-4.6, 0.1)\%$	$27\ (11, 77)\%$	$87\ (38, 186)\%$
	DDE$_{\perp}$	$0.9\ (-3.8, 7.5)\%$	$35\ (18, 140)\%$	$92\ (47, 329)\%$
	DDE$_{\|\|\&\perp}$	$-0.2\ (-3.2, 1.4)\%$	$20\ (8.5, 58)\%$	$50\ (25, 105)\%$

Table 5.1: Median (Md), lower quartile (q_1) and upper quartile (q_2) of the relative error of estimated parameters from the IFC model: a) radius and b) eccentricity. For each measurement protocol and ground truth shape parameter a, the data is pooled from substrates with different mean radii and eccentricities.

size distribution. The results show that, if the diffusion substrate consists of identical pores, then a simple model of microscopic anisotropy, such as IFC, can be used to measure average size and eccentricity using any of the four protocols. Most outliers illustrated in Figure 5.3a) occur for the substrates with $l_x = 2\mu$m which reaches the lower sensitivity bound for a gradient strength $G_{max} = 500\sqrt{2}$mT/m, as described in [8]. A key observation is that, for these simple substrates, the estimates based on SDE sequences have similar accuracy to those from DDE sequences, when a suitable model has been assumed. This happens because, for the subset of identical pores, the apparent size distribution in any given direction is generated solely by pore elongation.

Figure 5.3b) illustrates the relative errors of the parameter estimates from the IFC model for a substrate with a gamma distribution of sizes, with shape parameter $a = 2.5$. The results are presented for SDE and DDE$_{||\&\perp}$ sequences. In this case, when computing the relative errors, the ground truth parameter values are adapted to account both for the geometric correction explained above, as well as for a volume-weighted size distribution, as discussed in section 5.3. The figure shows that, in the presence of a distribution of sizes, the IFC model does not give consistent size and eccentricity estimates from either protocol, and most outliers occur for pores with small size ($l_x = 2\mu$m). The volume-weighted average radius is underestimated and the pore eccentricity is overestimated for all diffusion protocols for both $a = 10$ and $a = 2.5$ as detailed in Table 5.1a) and 5.1b). The bias in parameter estimation increases with the variance of the size distribution. This effect is especially pronounced for pores with low eccentricity, when the IFC model explains the size variation as coming from elongated pores.

IGFC model: Figure 5.4 presents the relative errors of $\bar{R}$ and E estimates from fitting the IGFC model to data synthesized from gamma distributed cuboids with the largest variance ($a = 2.5$). The results are presented for all four protocols and are separated according to the ground truth values of the parameters. The parameter values are adapted to account for the geometric correction, and the volume-weighting is incorporated in IGFC model. In comparison to the IFC model, explicitly accounting for size distribution improves the parameter estimates in more complex substrates. Fitted parameters from all protocols are in good agreement with the ground truth values used in the MC meshes. Outliers occur for either very small pores, close to the lower bound of sensitivity [8], or for very large pores, when the longest diffusion time is too short to observe restriction. DDE$_{\|\&\perp}$ sequences yield the smallest errors for both radius and eccentricity estimates. However, when an appropriate model is assumed, as it is the case here, all the protocols, including SDE, show reasonable sensitivity and enable estimation of all the parameters of the system. The effect of fitting a different size distribution to the one used in the synthetic data is analysed in Simulation 4 (section 5.7).

Although not shown in Figure 5.4, the shape parameter of the gamma distribution was fitted as well. As the variance of the gamma distribution is inversely proportional to the shape parameter (var$\{\mathcal{P}(R)\} = \bar{R}^2/a$, see section 5.3), quantifying the error of the variance is more meaningful than quantifying the error of the shape parameter. Thus, the relative errors of mean radius, eccentricity and variance are reported in Table 5.2a), 5.2b) and 5.2c) for all substrates and measurement protocols. The SDE protocol yields the highest relative errors in estimating the size distribution variance which is also reflected by poorer estimates of $\bar{R}$ and E. The relative errors of the estimated variance are slightly higher, as it depends on both mean radius and shape parameter estimates.

Protocol comparison: For a more quantitative protocol comparison, we use the objective function F, defined in equation 5.4 as the sum of the normalized CRLBs

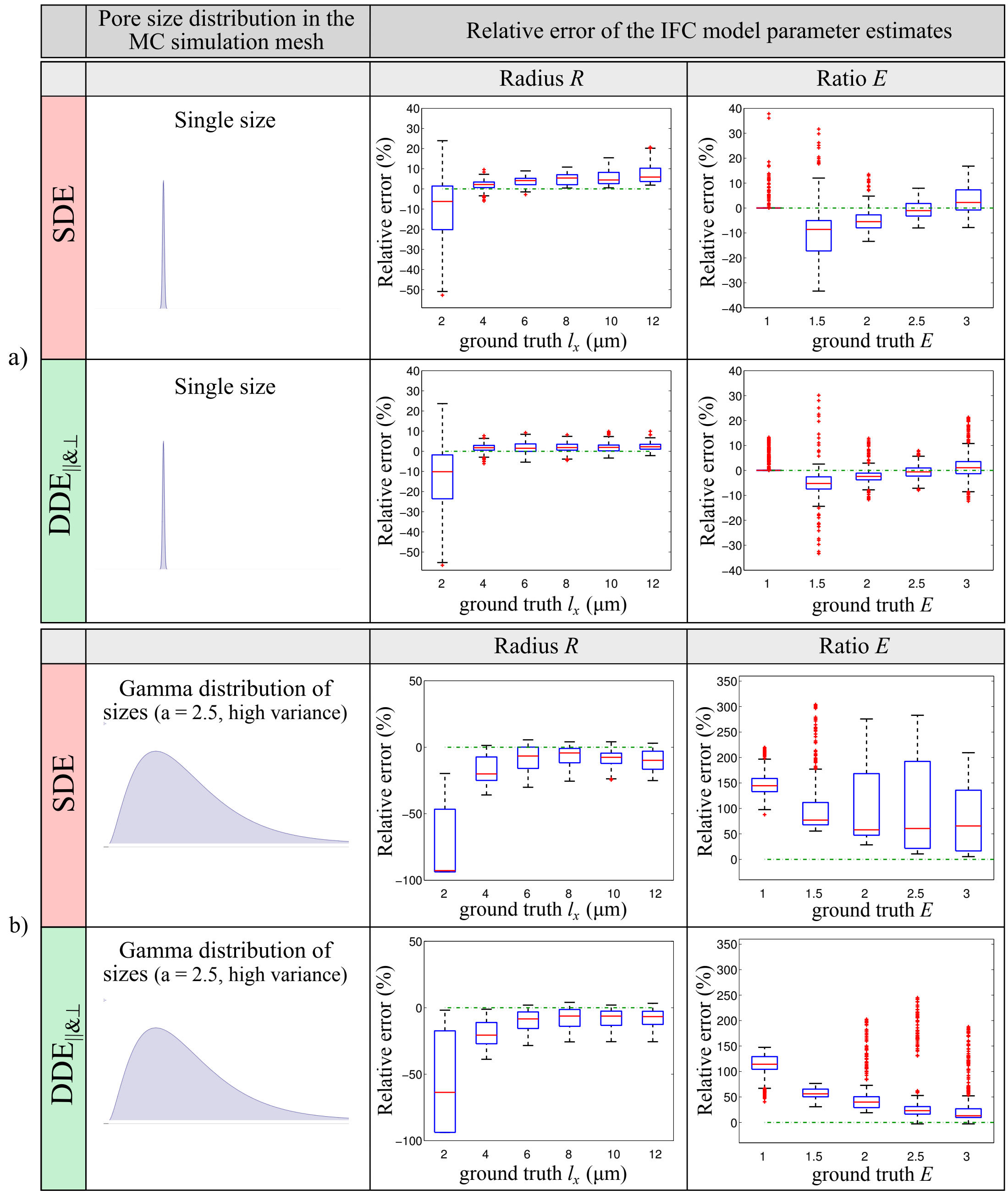

Figure 5.3: Relative errors of estimated parameters of the IFC model for different ground truth values in MC simulations, for a) a substrate with identical pores and b) a gamma distribution of sizes. The data is pooled across all substrates with a given size (middle column) or eccentricity (right column) and 100 noise trials. The box plots present the median, 25th percentile (lower quartile) and 75th percentile (upper quartile) as well as data points that extent up to 1.5 × inter-quartile range.

of the model parameters. The lower the objective function, the smaller the expected variance of the estimated parameters. For the ICF model, Figure 5.5a) illustrates F for the four protocols as a function of eccentricity for substrates with identical pores ($a \to \infty$) and two different radii $R = \{2, 4\}\mu$m. The plots show that DDE$_\perp$ protocol has the

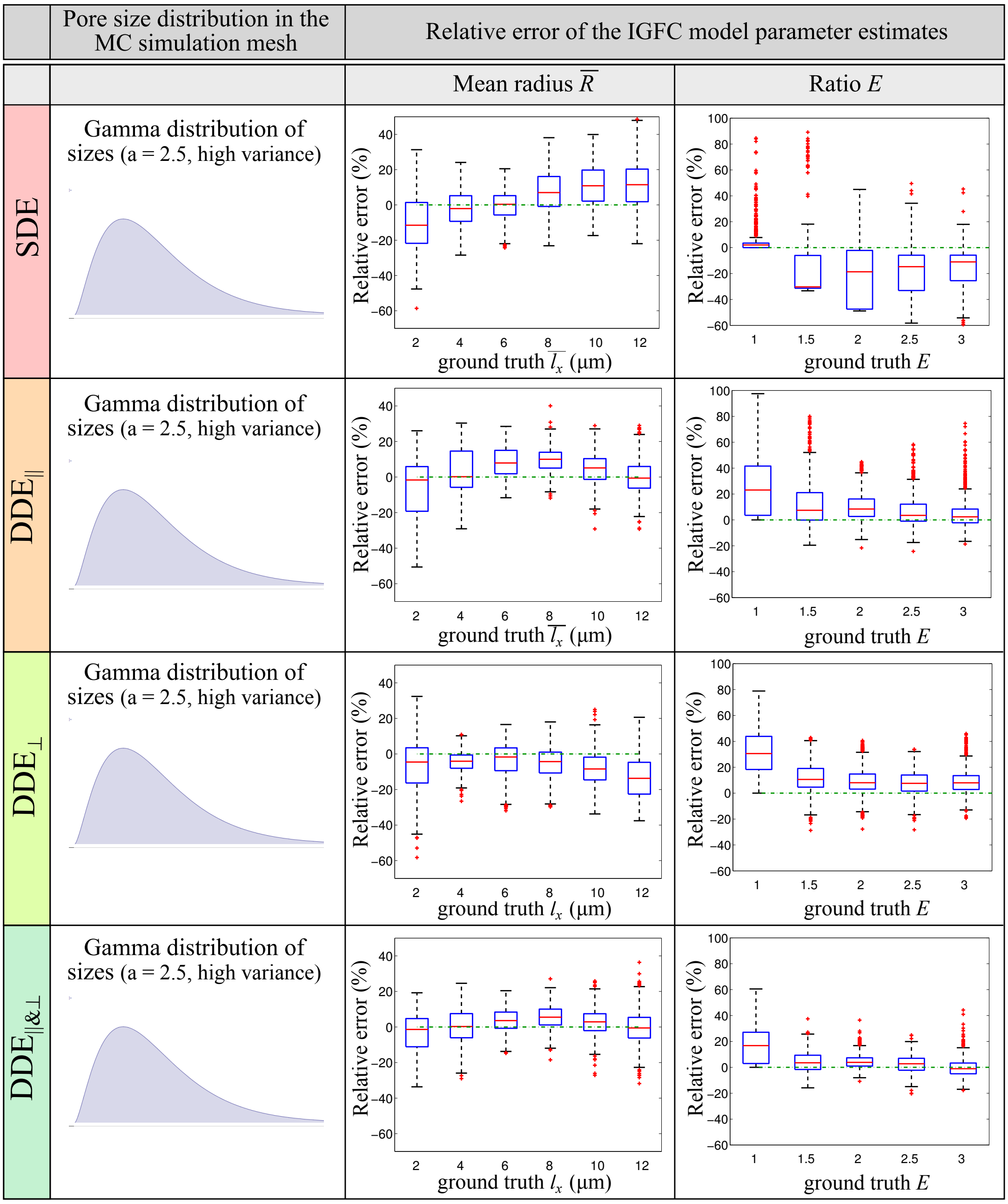

Figure 5.4: Relative errors of estimated parameters ($\bar{R}$ and E) of the IGFC model for different ground truth values in MC simulations, for substrates with a gamma distribution of sizes (a = 2.5). The data is pooled across all substrates with a given size (middle column) or eccentricity (right column) and 100 noise trials.

highest F (i.e. lowest sensitivity), while the other protocols have similar performance. The same trend appears for the other substrates. This result reflects the data presented in Table 5.1 for $a \to \infty$, where DDE$_{\perp}$ has the largest interquartile range for both radius and eccentricity estimates. Figure 5.5b) presents the objective function values for the IGFC model for substrates with $\bar{R} = \{2, 4\}\mu$m and $a = 2.5$. In this case a)

	IGFC - relative error of estimated mean radius $\bar{R}$: $Md\ (q_1, q_3)$		
	$a \to \infty$ 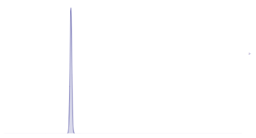	$a = 10$ 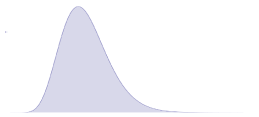	$a = 2.5$ 
SDE	$2.8\ (0.5, 6.6)\%$	$4.0\ (-0.3, 7.5)\%$	$2.8\ (-5.9, 12)\%$
DDE$_{\|\|}$	$2.0\ (0.5, 4.0)\%$	$3.0\ (-0.4, 5.6)\%$	$4.2\ (-3.4, 11)\%$
DDE$_{\perp}$	$0.4\ (-4.6, 4.1)\%$	$-2.1\ (-6.7, 1.4)\%$	$-5.6\ (-13, 0.8)\%$
DDE$_{\|\|\&\perp}$	$1.4\ (-1.3, 2.9)\%$	$1.8\ (-1.0, 4.1)\%$	$1.9\ (-3.7, 7.4)\%$

b)

	IGFC - relative error of estimated eccentricity E : $Md\ (q_1, q_3)$		
	$a \to \infty$	$a = 10$	$a = 2.5$
SDE	$-4.4\ (-14, 0.1)\%$	$-6.7\ (-20, 0.1)\%$	$-9.2\ (-31, 0.1)\%$
DDE$_{\|\|}$	$-1.8\ (-4.9, 0.1)\%$	$4.6\ (0.1, 12)\%$	$7.4\ (0.1, 23)\%$
DDE$_{\perp}$	$0.6\ (-4.3, 7.1)\%$	$8.5\ (2.3, 17)\%$	$11\ (4.2, 23)\%$
DDE$_{\|\|\&\perp}$	$-0.2\ (-3.2, 1.4)\%$	$1.9\ (-1.0, 6.7)\%$	$1.5\ (-5.6, 7)\%$

c)

	IGFC - relative error of estimated variance $Md\ (q_1, q_3)$		
	$a \to \infty$	$a = 10$	$a = 2.5$
SDE	$119\ (5.8, 373)\%$	$38\ (-8, 87)\%$	$38\ (10, 61)\%$
DDE$_{\|\|}$	$4.8\ (2.1, 10)\%$	$-32\ (-52, -12)\%$	$-19\ (-32, -2)\%$
DDE$_{\perp}$	$5.0\ (-1.9, 39)\%$	$-19(-31, -2.6)\%$	$-8.5\ (-19, 4.4)\%$
DDE$_{\|\|\&\perp}$	$4.4\ (0.8, 9.5)\%$	$-16\ (-29, -0.5)\%$	$-8.6\ (-18, 3.4)\%$

Table 5.2: Median (Md), lower quartile (q_1) and upper quartile (q_2) for the relative errors of the estimated parameters from the IGFC model: a) radius and b) eccentricity and c) variance. For each measurement protocol and ground truth shape parameter a, the data is pooled from substrates with different mean radii and eccentricities. For the substrates with identical pores, the upper limit of a ($a = 10000$) from the signal model was used to compute the variance.

the DDE$_{||\&\perp}$ and DDE$_{\perp}$ protocols perform better than the protocols with one single gradient orientation. Table 5.2 supports this finding where, for substrates with $a = 2.5$, the last two protocols have smaller interquartile ranges.

5.5.4 Discussion

This section presents a model-based approach for estimating pore size and eccentricity in macroscopically isotropic substrates which consist of randomly oriented elongated pores with a distribution of sizes. In the model-based approach, we fit a geometric model to the diffusion signal itself, avoiding the increased noise variance of the signal difference. Moreover, we explicitly account for the finite gradient duration and we do not assume long mixing and diffusion times. Simulation 2 is focused on estimating

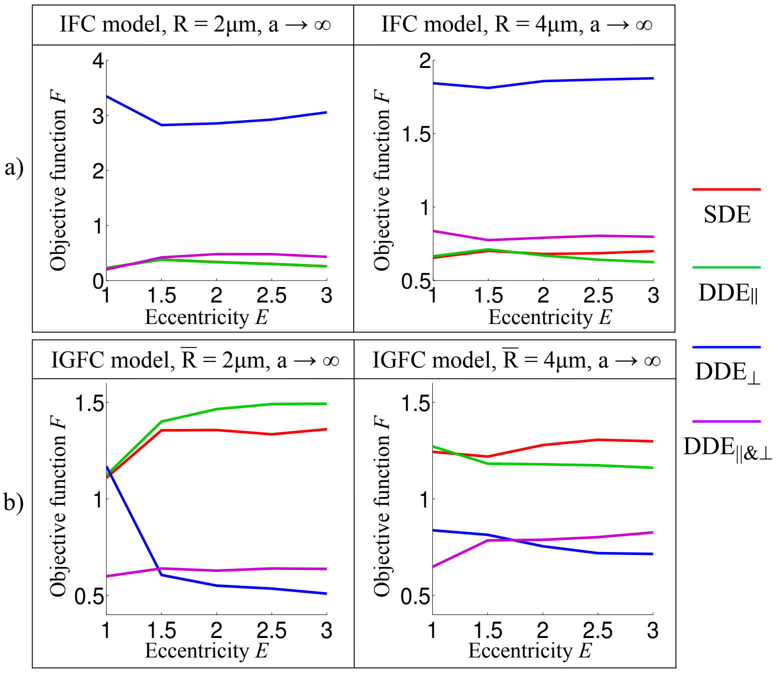

Figure 5.5: Dependence of the objective function F on pore eccentricity for the four protocols for a) the IFC model and b) the IGFC model.

microstructural parameters in isotropic substrates and we investigated the sensitivity of four different protocols: SDE, DDE$_{||}$, DDE$_{\perp}$ and DDE$_{||\&\perp}$. For fair comparison, all protocols were adjusted to have the same maximum diffusion weighting (b-value) and number of measurements. First we test whether a simple model with identical pores (IFC) can provide good estimates of the volume-weighted mean pore size and eccentricity. In the elementary case when the underlying substrates have identical pores, the IFC model provides accurate parameter estimates. In this situation, DDE sequences offer no clear advantage over SDE sequences. However, this model underestimates radius and overestimates eccentricity if the substrates have a distribution of pore sizes for both types of protocols. Directly accounting for size distribution, i.e. the IGFC model, overcomes this problem and provides accurate microstructural estimates. The DDE$_{||\&\perp}$ protocol yields the smallest relative errors for all parameter estimates, with 50% of data points having a relative error less than 10% for mean radius and eccentricity estimates. From all IGFC model parameters, the shape of the gamma distribution a has the largest variability which translates to larger interquartile range for the relative error of the size distribution variance compared to the other parameters, as illustrated in Table 5.2. Nevertheless, explicitly accounting for size distribution improves the accuracy of mean radius and eccentricity estimates. During fitting, D was fixed to its ground truth value. For the protocols considered, additionally fitting for D does not affect results significantly and provides good estimates of D, but increases the computational time, as the restricted signal depends on the ratio D/R^2.

When probing an ensemble of pores with a size distribution, the SDE protocol provides sensitivity to mean size and eccentricity, although the $\text{DDE}_{\|\&\perp}$ and $\text{DDE}_{\perp}$ protocols improve the accuracy. The DDE protocols yield smaller errors when estimating the variance of the size distribution, which is consistent with previous studies [189, 190]. The sensitivity of the SDE protocol arises from the fact that choosing a specific model for parameter fitting resolves ambiguity in the underlying measurements. If the diffusion substrate is unknown, DDE measurements contain information to distinguish different cases. Moreover, a non model-based approach can be used to provide prior information in order to select a relevant model. If an appropriate model is assumed, then SDE measurements can estimate microstructural parameters. This is important in practice as the SDE sequence is much simpler to implement and generally returns higher signal by keeping the echo time shorter. Previous work [204] showed that DDE sequences preserve information from the diffusion-diffraction patterns in the presence of size distribution and can be used to recover more subtle features of pore shape, differentiating between various geometries [205, 206]. However, for estimating pore size and eccentricity in the diffusion regime considered here, the differences in performance among the protocols are quite small and further work is required to determine if they reflect genuine sensitivity differences. When comparing SDE and DDE sequences it is not trivial to define a fair comparison, and here we choose to have the same maximum diffusion weighting (b-value). Using the same maximum gradient strength would provide more diffusion weighting for DDE sequences, increasing sensitivity to small pore sizes. On the other and, the longer pulse duration for DDE reduces SNR if the effects of T2 decay are considered. A better comparison can be achieved if the protocols are optimised in order to fully explore the parameter space of each sequences, given practical constraints for total duration and gradient strength, as described in [151] or [153].

One limitation of the models described here is that they assume the same eccentricity for all sizes. In some tissues, such as gray matter, cellular structures of different sizes have different shapes. For example, cell bodies, which have a diameter on the order of tens of microns [29], and dendritic spines, which are much smaller ($0.5 - 2\mu$m [207]), are nearly spherical structures, while dendrites, which are several microns in diameter [208] are elongated structures. To be more realistic, the models could include a distribution of eccentricity and/or several populations with different size/shape characteristics.

The protocols used in this study provide sensitivity over a wide range of pores and are not designed for practical application. The maximum gradient strength we use in the simulation is $500\sqrt{2}$ mT/m for SDE sequences and the maximum echo time required for the DDE protocols is 250ms. These values can be achieved on preclinical scanners, however, the range of values is more limited on a clinical scanner. The lower gradient strengths (80mT/m for a standard scanner or 300mT/m for the Connectome scanner [154]) decrease the sensitivity to small pore size, while the short diffusion times affect the estimates for larger pores. The same features which are desired for such a simulation study (large measurement space, high gradient strength, long diffusion and mixing times) are a drawback for practical applications which require short acquisitions and limited diffusion time to prevent signal loss from $T2$ decay. When designing such a protocol for practical applications all these aspects should be considered. Additionally, to preserve the sensitivity over a wide range of pore sizes for practical situations, rectangular gradients can be replaced with oscillating ones [153], or if there is prior knowledge of the system, the diffusion protocol can be substantially shortened using numerical optimisation [151], including diffusion gradients with varying orientation [94].

5.6 Simulation 3: Macroscopically anisotropic substrates

This simulation presents an extension of the model-based approach to estimate pore size and eccentricity in macroscopically anisotropic substrates.

5.6.1 Aims and objectives

Given the results from Simulation 2, the objectives of this study are the following:

1. develop a rotationally invariant protocol of DDE sequences.

2. incorporate pore orientation in the tissue models in order to account for macroscopic anisotropy.

5.6.2 Methods

Diffusion substrates

This simulation tests the hypothesis that a model-based approach can be extended to a rotationally invariant framework for estimating pore size and eccentricity in the presence of macroscopic anisotropy. To this end, we construct diffusion substrates consisting of cuboids oriented according to a Watson distribution, as explained in section 5.2. The substrates have the largest size variance ($a = 2.5$) and all combinations of $\bar{l_x}$ and E presented in Simulation 2, as well as various concentration parameters of the Watson distribution $\kappa = \{2, 4, 8, 16, 32\}$.

Signal model

For a macroscopically anisotropic substrate, in order to recover rotationally invariant indices of pore size and eccentricity, we explicitly model the orientation distribution of the pores as a Watson distribution, i.e. $\mathcal{F}(\mathbf{u}) = W(\frac{1}{2}, \frac{3}{2}, \kappa)^{-1} e^{\kappa(\boldsymbol{\mu}\cdot\mathbf{u})^2}$, where W is a confluent hypergeometric function, κ is the concentration parameter and $\boldsymbol{\mu}$ is the main orientation. Thus, the new models are:

1. **Watson finite cylinders** (WFC) has three additional parameters compared to the IFC model: concentration parameter of the Watson distribution κ and the angles θ and ϕ in spherical coordinates describing the main direction $\boldsymbol{\mu}$.
2. **Watson gamma finite cylinders** (WGFC) has three additional parameters compared to the IGFC model: concentration parameter of the Watson distribution κ and the angles θ and ϕ in spherical coordinates describing the main direction $\boldsymbol{\mu}$.

Measurement protocol

In this experiment we extend the measurement protocol to provide directional information. To measure the dominant orientation of pores, we use a DTI-like measurement set with 32 isotropic directions and a b-value of 2000 mm^2/s (G = 100 mT/m, δ = 10 ms and Δ = 31 ms). We chose a higher b value compared to the standard b = 1000 mm^2/s DTI measurements as we are probing restricted diffusion only. To measure pore size and eccentricity as well as orientation dispersion we use DDE sequences with 6 gradient orientations (xx,xy,xz,yy,yz,zz) for each combination of parameters in protocol $\textbf{DDE}_{||}$. This is the minimum number of gradient directions to ensure that parallel and perpendicular measurements along the three orthogonal axes are acquired. We name this combined, rotationally invariant protocol $\textbf{DDE}_{RI}$.

5.6.3 Results

This section presents the results for macroscopically anisotropic substrates. Having a rotationally invariant acquisition protocol and explicitly incorporating directional information in the tissue model allows for estimating size and eccentricity in the presence of macroscopic anisotropy. Thus we investigate the ability of signal models with a Watson distribution of pore orientation to recover ground truth microstructural features.

As in the case of isotropically oriented pores, the WFC model with identical pores underestimates the radius and overestimates the eccentricity, especially in the case of pores with low eccentricity (data not shown). After accounting for the size distribution of the pores, the WGFC model accurately recovers the ground truth values for these parameters. Figure 5.6a) illustrates the relative errors of estimated radius and eccentricity given by the WGFC model for substrates with two different orientation distributions ($\kappa = \{2, 4\}$). The shape parameter of the gamma distribution is $a = 2.5$ for all substrates (largest variance considered in this study). The results show accurate estimates for mean radius and eccentricity for all κ values. The median relative error of the estimated shape parameter a is 9.4%, with lower and upper quartiles of -3.5% and 22%, respectively. As for the isotropic substrates, larger errors occur for very small pores, close to the lower bound of sensitivity of the maximum gradient strength in this study.

Figure 5.6b) illustrates the estimates of the concentration parameter of the Watson distribution. For pores with low eccentricity (E = 1,1.5) the estimates of kappa are not accurate, as the choice of κ becomes increasingly redundant as the pores approach isotropy. For elongated pores the estimated values of κ are closer to the ground truth values from the MC simulations. As noted in [12], high κ is hard to estimate precisely as the numerical value has an exponentially decreasing effect as $\kappa \to \infty$.

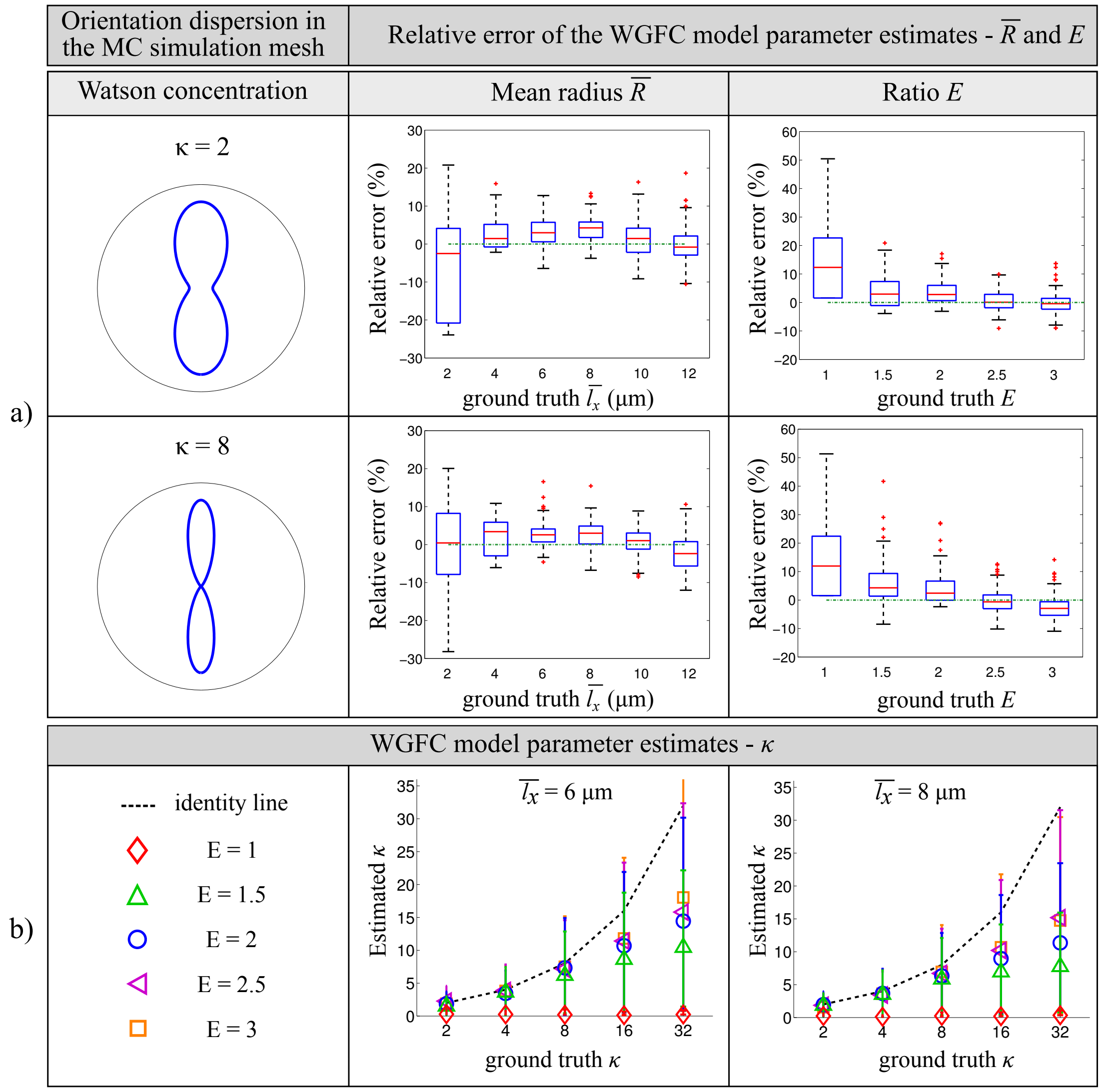

Figure 5.6: a) Relative error of the estimated size and eccentricity parameters from fitting the WGFC model a function of ground truth values in MC simulations, for a substrate with a gamma distribution of sizes ($a = 2.5$) and two different concentration parameters of the orientation distribution ($\kappa = 2$ and 8). The data is pooled across all substrates with a given size (middle column) or eccentricity (right column) and 100 noise trials. b) Estimated concentration parameter κ of the WGFC model as a function of ground truth values used in MC simulations, for substrates with gamma distributed sizes ($l_x = 6$ and 8 μm with $a = 2.5$) and various eccentricities. The values were computed as the mean estimates over 100 noise trials.

5.6.4 Discussion

This section shows that a model-based approach can be extended to estimate pore size and eccentricity in macroscopically anisotropic substrates.

In Simulation 3 we used an extended protocol DDE$_{RI}$ consisting of a SDE shell with 32 isotropic directions and DDE sequences with 6 gradient orientations (xx,xy,xz,yy,yz,zz). The SDE shell is used to determine the main orientation of the pores, which is subsequently fixed, while fitting the rest of the model parameters. Fitting the WFC model to substrates with a size distribution, yields biased parameter estimates which underestimate mean radius and overestimate eccentricity. Accounting for size distribution, i.e. the WGFC model, provides accurate estimates of size and eccentricity, however an accurate value of the concentration parameter κ is recovered only for pores with high eccentricity. For pores with low eccentricity, the influence of κ on the overall diffusion signal is small, which is reflected in the poor estimate of this parameter at E close to 1.

5.7 Simulation 4: Varying size and orientation distribution

In Simulation 2 and 3, both the diffusion substrates and the signal model use a gamma distribution for pore sizes and a Watson distribution for pore orientation. In this section we aim to relax these assumptions and test the applicability of a model-based approach when the simulated data and signal model have different distributions of pore size and orientation.

5.7.1 Aims and objectives

Specifically, we test whether:

1. the IGFC model can provide accurate parameters estimates when the underlying substrates have different parametric or non-parametric size distributions.
2. the WGFC model can recover microstructural features when the underling substrates have a different orientation distribution.

5.7.2 Results

Different size distributions

Here we investigate the effects of fitting the IGFC model to substrates consisting of elongated cuboids that have different size distributions. First we test a different parametric distribution, namely the inverse Gaussian distribution, then a realistic histological distribution taken from histology of the SW-620 cell line of colorectal cancer [209]. In both cases we simulate the diffusion signal from the $\text{DDE}_{||\&\perp}$ protocol.

In the first simulation we analyse diffusion substrates consisting of randomly oriented cuboids with eccentricity $E = 2$ and an inverse Gaussian size distribution with mean value $\bar{l_x} = 6\mu m$ and shape parameter $\lambda = \{10, 50, 100\}\mu$m. The variance of the inverse Gaussian is given by $\bar{l_x}^3/\lambda$. Fitting the IGFC model to the diffusion data synthesized from the three meshes provides accurate estimates of mean radius and eccentricity, while the relative errors of the variance are larger. The size distribution of the cuboids as well as the mean relative errors of the parameter estimates over 10 noise trials with SNR = 50 are shown in Table 5.3a).

a)

Diffusion substrates with an inverse Gaussian distribution of pore sizes (ground truth parameters: $\overline{l_x}$ = 6μm, E = 2)			
Relative error of parameter estimates (IGFC model)	Initial distribution of sizes		
	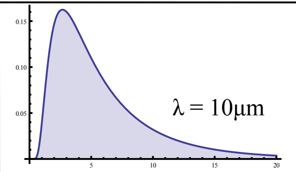	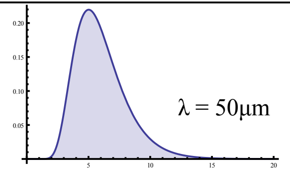	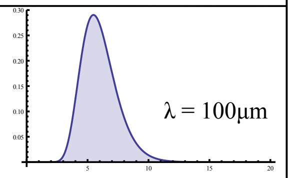
$\overline{\Delta R}$	-15 ± 7.1 %	1.9 ± 1.6 %	2.9 ±1.4 %
$\overline{\Delta E}$	5.2 ± 2.7 %	0.9 ±3.4 %	3.9 ± 3.3 %
$\overline{\Delta \text{Var}}$	74 ± 20 %	52 ± 27 %	-68 ± 38 %

b)

Diffusion substrates with different orientation distributions (ground truth parameters: $\overline{l_x}$ = 6μm, E = 3, a = 2.5)			
Relative error of parameter estimates (WGFC model)	Volume fraction of coherently oriented pores f 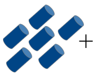 + (1-f) 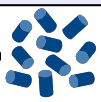		
	f = 25%	f = 50%	f = 75%
$\overline{\Delta R}$	-3.3 ± 3.8 %	-9.4 ± 2.6 %	-12 ± 6.8 %
$\overline{\Delta E}$	1.3 ± 1.5 %	1.6 ± 1.0 %	4.9 ± 1.6 %
$\overline{\Delta \text{Var}}$	-5.3 ± 9.1 %	-4.3 ± 7.5 %	12 ± 17 %

Table 5.3: a) Average relative error of estimated mean radius and eccentricity provided by the IGFC model when fitted to pores that have an inverse Gaussian distribution of sizes. b) Average relative error of estimated mean radius, eccentricity and shape parameter of the gamma distribution provided by the WGFC model when fitted to substrates with different volume fractions of coherently oriented pores. The mean value and standard deviation are computed over 10 noise trails with $SNR = 50$.

In the second simulation we investigate a more realistic distribution. We construct a cuboid mesh with the discrete size distribution from histology of SW-620 colorectal cancer cells [209], which has a mean value $\bar{l_x} = 10.8\mu$m and we assume a smaller eccentricity $E = 1.5$. In this case, the average relative errors of the estimated IGFC model parameters over 10 noise trials with SNR = 50 are: $\overline{\Delta \bar{R}} = 5.3 \pm 2.1\%$ for the mean radius, $\overline{\Delta E} = 1.1 \pm 3.8\%$ for the eccentricity and $\overline{\Delta \text{Var}} = -22 \pm 54\%$ for the variance.

Overall, the results show that fitting the IGFC model to diffusion substrates with a different size distribution provides accurate estimates of average size and eccentricity, for both parametric and non-parametric distributions. The estimated variance has the largest relative errors, which are higher compared to the values in Simulation 2 and 3 due to the mismatch between the distributions.

Different orientation distributions

In this experiment we relax the assumption that the diffusion substrate and signal model have the same orientation distribution. Thus, we analyse the effect of fitting the Watson orientation distribution to diffusion signal originating from substrates with a combination of coherently oriented cuboids occupying a volume fraction $f = \{0.25, 0.5, 0.75\}$ and randomly oriented cuboids with volume fraction $1 - f$. The cuboids have a gamma distribution of sizes with shape parameter $a = 2.5$ and mean value $\bar{l_x} = 6\mu$m. To maximize the effect of orientation distribution we choose the largest eccentricity used in previous simulations $E = 3$. The diffusion signal is synthesized for the DDE$_{RI}$ protocol and we fit the WGFC model.

The results presented in Table 5.3 show a good agreement between the estimated parameters of the WGFC model (mean radius, eccentricity and variance of the size distribution) and the ground truth values from the cuboid meshes. The estimated concentration parameter of the Watson distribution κ increases ($\bar{\kappa} = 1.5, 2.7, 4.9$) with the volume fraction of the coherently oriented pores, reflecting the more anisotropic orientation distribution. These results illustrate that the WGFC model yields accurate estimates of pore size and eccentricity, even when the orientation distribution in the underlying substrate is different.

5.7.3 Discussion

The first simulation in this section shows that a microstructural model which explicitly accounts for pore size distribution yields accurate estimates of average pore size and eccentricity even when the distribution in the underlying substrate is different. Specifically, here we investigated two distinct cases, a uni-modal parametric distribution, namely inverse Gaussian, and a histologically plausible distribution of cancer cells

[209]. One limitation of this approach is the inability to characterize a more complex distribution, for instance a multi-modal one. In this case a model with non-parametric size distribution, as the ones proposed in [189, 210], which accounts for the signal contribution from various sizes, would better characterize the underlying microstructure.

In the second simulation we investigated the accuracy of the WGFC model parameter estimates when the underlying substrate has a different orientation distribution. For substrates with a combination of coherently and randomly oriented pores, the WGFC model yields accurate estimates of average pore size and eccentricity. The Watson distribution introduces only one additional parameter on top of the dominant orientation, which stabilizes the fitting procedure. However, this distribution cannot explain the diffusion signal coming from complex tissue configurations with multiple orientation peaks, such as crossing fibres in the brain. A more general configuration can be recovered if the orientation distribution is expanded in terms of spherical harmonics as explained in [117], however, this approach introduces many additional parameters, making the fit less stable.

5.8 Simulation 5: Relaxing assumption

This section presents preliminary results that aim to relax some of the assumptions from Simulations 2-4.

5.8.1 Aims and objectives

The objectives of this simulation are the following:

1. investigate the effects of diffusion in extra-cuboidal space.
2. reduce the number of diffusion measurements, while retaining the accuracy of parameter estimates.

5.8.2 Results

Effect of extra-cuboidal space

The main challenge for analysing the effect of extra-porous space is creating a diffusion mesh with a realistic intra-cuboidal volume fraction around 0.7 [2], as expected in biological tissue. With the current algorithm that randomly packs non-intersecting cuboids, the largest volume fraction we obtained was around 15%. We analysed the diffusion signal for a mesh with randomly oriented cuboids ($f = 0.153$, $\bar{l_x} = 6\mu$m, $a = 2.5$ and $E = 1.5$) and the DDE$_{||\&\perp}$ protocol. We model the extra-cuboidal space using an isotropic tensor and the intra-cuboidal space using the IGFC model and we fit all parameters. The mean relative errors of the parameter estimates over 10 noise trials with SNR = 50 are: $\Delta f = 3.8 \pm 8.5\%$, $\Delta D = 6.3 \pm 30\%$, $\Delta \bar{R} = 9.9 \pm 23\%$ and $\Delta E = 11 \pm 30\%$. The estimates of a were unstable with a median value of 6.25. Including extra-cuboidal space decreases sensitivity, which is mainly reflected by a poor estimate of the shape parameter of the gamma distribution. Nevertheless, the other parameters (f, R and E) are close to the ground truth even for a substrate with a very low volume fraction. Extending the analysis to a broader range of volume fractions is part of future work.

Reduced number of measurements

This simulation investigates the possibility of reducing the number of diffusion measurements. Thus, for a substrate of randomly oriented cuboids with a gamma distribution of sizes ($\bar{l_x} = 6\mu m$, $a = 2.5$, $E = 2$), we analyse the data from a subset of the DDE$_{||\&\perp}$ protocol with 25 measurements (10 different sequences with parallel and perpendicular gradients and 5 b0 measurements). We choose the measurements from the full protocol following a greedy algorithm to maximize sensitivity to this particular substrate. For the reduced protocol, the average relative errors of the parameter estimates over 100 noise trials are $\Delta \bar{R} = 10 \pm 17\%\mu$m, $\Delta a = 23 \pm 94\%$ and $\Delta E = 3.3 \pm 7.9\%$, while for the full protocol the errors are $\Delta \bar{R} = 2.2 \pm 3.8\%\mu$m, $\Delta a = 8.8 \pm 14\%$ and $\Delta E = 9.1 \pm 2.8\%$. The values overlap within standard deviation, however reducing the number of measurements increases the variability of the estimates. The size and eccentricity are robustly recovered, while the shape of the gamma distribution estimate is more influenced by noise.

5.8.3 Discussion

A first step towards practical applications, such as cancer imaging, is to account for signal from the extracellular space. For low volume fractions, a simple extracellular model with hindered diffusion is accurate enough, while for higher volume fractions models that account for a time-dependent diffusivity which reflects the restriction length-scale [15] are preferable. Compartment models, as in [2, 5, 9, 164], can separate extracellular and intracellular contributions to the signal.

The first simulation analyses the effect of including diffusion in the extra-porous space. The results show that estimates of average pore size, eccentricity and volume fraction are close to the ground truth values, while the estimates of the shape parameter are unstable. The volume fraction we used was quite small $f = 15\%$, and with the current packing algorithm it was not possible to achieve a higher, more realistic value. Studying the ability to recover microstructural features for a wider range of pore sizes and volume fractions is part of future work.

The second experiment shows that we can recover microstructural parameters with a reduced acquisition protocol. Specifically, we analysed a DDE$_{\|\&\perp}$ protocol with 25 measurements and 10 unique parameter combination. The parameter estimates from the short protocol overlap within standard deviation with the values obtained from the full protocol, however the estimates have higher variability. Thus, the right balance between acquisition time and measurement precision is necessary depending on the application. In this simulation the 10 measurements were chosen from the initial set of measurements, however, more accurate results can be obtained if the protocol is optimised over the entire parameter space of the sequence, as detailed in [151, 93].

5.9 Conclusions

This work is a proof of concept showing that microstructural parameters such as pore size and eccentricity can be estimated from diffusion MRI using a geometric model of restriction even in the presence of macroscopic anisotropy and a distribution of pore sizes.

In Simulation 1 we investigated two metrics of microscopic anisotropy, FE and ϵ, which are calculated from DDE measurements with parallel and perpendicular gradients. The results show that FE is highly affected by noise, especially for pores with low eccentricity, while ϵ, which is less prone to noise, strongly depends on pore size distribution as well as eccentricity, making it difficult to separate the two effects.

Simulation 2 presents a model-based approach for estimating average pore size and eccentricity in macroscopically isotropic substrates. When the underlying substrates have a distribution of pore sizes, a simple model with identical pores yields biased estimates and explicitly accounting for size distribution is necessary to improve accuracy. Moreover, in substrates with a size distribution, the protocols with DDE sequence provide more accurate estimates. Nevertheless, all protocols show sensitivity when an appropriate tissue model has been selected. Simulation 3 extends the acquisition protocol and signal model to a rotationally invariant framework in order to estimate pore size and eccentricity in macroscopically anisotropic substrates.

The last two simulations relax some of the assumptions in the previous experiments. Simulation 4 demonstrates that accurate parameter estimates can be recovered when the diffusion substrate and signal model have different size and orientation distributions, while Simulation 5 studies the effects of diffusion in the extra-cuboidal space and reducing the number of measurements.

In the simulations from this chapter, the diffusivity D was fixed to its ground-truth value during fitting. Nevertheless, we have also tested the effects of fitting all model parameters. For the protocols considered here, additionally fitting for D does not affect results significantly and provides good estimates of D but increases the computational time, as the restricted signal depends on the ratio D/R^2.

The protocols thoroughly analysed in this work in Simulation 2 and 3 have a large number of measurements and long diffusion time in order to provide sensitivity over a wide range of pore sizes. Such a technique could be adapted for practical applications by using optimised measurement protocols that maximise the sensitivity to tissue microstructure [151] or the diffusion weighting [211], while taking into account physical scanner constraints such as maximum gradient strength, slew rate, maximum echo time, gradient heating, etc. To allow for longer diffusion times without loosing SNR due to T2 decay, a stimulated echo preparation could be used instead of the standard spin-echo preparation.

Future work will focus on more realistic substrates which include extracellular space with various volume fractions, in order to mimic different tissue configurations, as well as using improved measurement protocols which could be used in practice.

Chapter 6

Double oscillating diffusion encoding

In the previous chapter we explored a model-based approach for estimating pore size distribution and eccentricity in a large variety of diffusion substrates. Further, we compared the sensitivity of SDE and DDE sequences and the results showed that DDE protocols, with a combination of parallel and perpendicular gradients, provide the most accurate parameter estimates.

In this chapter we introduce a novel class of diffusion sequences, namely double oscillating diffusion encoding (DODE). These sequences consist of gradients with oscillating waveforms and varying orientation in one acquisition. We analyse the DODE signal dependence on sequence parameters and the sensitivity to microstructural features. Moreover we present an application of DODE sequences for comparing model-free metrics of microscopic anisotropy. Parts of this work have been presented at two conferences [212, 213].

6.1 Motivation

Accurate estimation of microscopic anisotropy (µA) requires sequences with varying gradient orientation, such as DDE, while sequences with oscillating gradients improve the sensitivity to intrinsic diffusivity and pore size.

In this chapter we combine the benefits of both DDE and ODE sequences in a double oscillating diffusion encoding (DODE) acquisition, which concatenates two oscillating waveforms and allows the angle between the two gradients to vary, as illustrated in Fig. 6.1. Such an acquisition aims to improve sensitivity to pore size in more complex substrates featuring microscopic anisotropy.

Here we explore the DODE signal in the case of restricted diffusion and we investigate the sensitivity with respect to pore size and length. In the first simulation we analyse the dependence of the DODE signal on sequence parameters for substrates with isotropic pores as well as randomly oriented anisotropic pores in order to evaluate the effect of microscopic anisotropy. In the subsequent experiment we compare the DODE and DDE sensitivity with respect to pore size and length for a wide range of substrates. Then, we show the potential to extend the DODE acquisition to a rotationally invariant framework. In the last section we use the new sequences to compare two existing metrics of microscopic anisotropy for substrates featuring restricted or Gaussian diffusion.

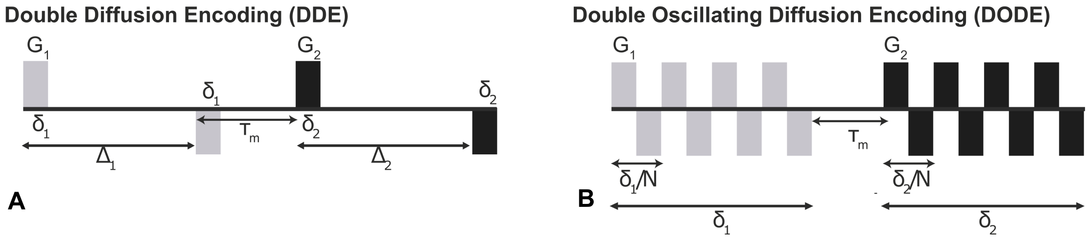

Figure 6.1: a) Typical double diffusion encoding sequence with gradient amplitude $G_{1,2}$, gradient duration $\delta_{1,2}$, diffusion time $\Delta_{1,2}$ and mixing time τ_m. b) Double oscillating diffusion encoding sequence (DODE) with oscillation frequency $\delta_{1,2}/N_{1,2}$ where N is the number of periods.

6.2 Theory

This section presents the derivation of b-values and q-values for DODE sequences. These quantities are necessary in order to extend the derivation of rotationally invariant metrics of microscopic anisotropy, e.g. fractional eccentricity (FE) [121] for an acquisition protocol consisting of DODE sequences.

When both encoding gradients have the same amplitude ($G_1 = G_2$), duration ($\delta_1 = \delta_2$) and number of oscillations ($N_1 = N_2$), DODE with parallel or anti-parallel gradient orientations are the same diffusion sequences as ODE. Thus, rewriting the b-value for an ODE sequence defined in equation 3.3 in terms of the DODE sequence parameters defined in Figure 6.1b), we get:

$$b = \gamma^2 G^2 \frac{\delta^3}{6N^2}, \tag{6.1}$$

where $N = N_1 = N_2$ is the number of periods, $G = G_1 = G_2$ is the gradient strength and $\delta = \delta_1 = \delta_2$ is the gradient duration. When DODE sequences have gradients with different orientations, the diffusion weighting has half the contribution in equation 6.1 along each direction of the gradient.

There is no definition of the q-value for oscillating gradients, therefore, in order to define the q-value of a DODE sequence, we make the following assumption: we write the b-value of a DDE sequence in terms of its q-value and diffusion time and we assume that the equation will have the same form for a DODE sequence. The b-value of a DDE sequence is

$$b = 2\gamma^2 G^2 \delta^2 (\Delta - \frac{\delta}{3}) = (2\pi)^2 q^2 2\tau_{diff}, \tag{6.2}$$

with $q = (2\pi)^{-1}\gamma G\delta$ and diffusion time $\tau_{diff} = \Delta - \delta/3$. Following the steps in [106], the diffusion time of a DODE sequence is $\tau_{diff} = \frac{\delta}{3N}$, thus we define the q-value

$$q = \frac{1}{2\pi}\frac{\gamma G\delta}{2\sqrt{N}}, \tag{6.3}$$

which ensures equation 6.2 holds for DODE sequences as well.

The formulae of b-value and q-value are presented for DODE sequences with $G_1 = G_2$, $\delta_1 = \delta_2$ and $N_1 = N_2$ which are used for all simulations in this chapter. However, similar expressions can be derived for the general case presented in Figure 6.1b), when the two diffusion encoding periods will have different b-values and q-values.

6.3 Diffusion substrates and simulation framework

This section explains the diffusion substrates and signal model that have been used to explore the DODE acquisition.

Substrates with a range of different microscopic anisotropy values, from highly anisotropic ones (cylinders, Fig. **??**c) to isotropic ones (spheres, Fig. 6.1d)) are considered. We characterize µA through pore dimensions, namely diameter d and length L. In all simulations we set the intrinsic diffusivity to $D = 2 \cdot 10^{-9}$m^2/s, a value similar to the principal eigenvalue of the diffusion tensor measured at short diffusion time in the human brain in vivo [175]. To reduce the parameter space, in the first part we investigate macroscopically isotropic substrates, and limit the acquisition protocols to a single orientation of the first gradient pulse. In the second part we construct orientationally invariant DODE protocols in a similar way to orientationally invariant DDE protocols, as in [121].

All the simulations in this study are performed using the MISST software which is described in detail in chapter 7. It uses the matrix method presented in section 2.3.4 to compute the restricted diffusion signal in various substrates using an acquisition protocol with DODE sequences. In all the experiments we assume that the first and second gradient waveforms have the same parameters except for gradient orientation which can vary. As illustrated in Fig. 6.1, the DODE sequences are parametrized by the gradient strength G, gradient duration δ, number of oscillation periods N, mixing time τ_m, as well as the orientation of the two gradient directions, which can be expressed in terms of the first gradient orientation and the relative angle ψ between the two gradients. In the case of DODE sequences the mixing time is somewhat loosely defined and we chose it to be the time interval between the two gradients. *Note:* For DODE sequences N represents the number of periods, as opposed to the number of lobes which is used in chapter 3. In the current representation of DODE sequences, each gradient requires an integer number of periods in order to satisfy the gradient echo constraint.

6.4 Simulation 1: Qualitative comparison of DODE and DDE signal

The first simulation compares the dependence of DODE and DDE signal on sequence parameters in substrates featuring microscopic diffusion anisotropy and tests whether DODE gives similar trends as DDE when the angle between the two gradients, ψ, is varied. Specifically, we analyze the amplitude of the signal modulation as a function of ψ for sequences with different mixing times and oscillation frequencies.

6.4.1 Aims and objectives

Specifically, we aim to:

1. investigate the effect of varying mixing time on the DODE and DDE signal.
2. investigate the effect of varying oscillation frequency on the DODE signal.

6.4.2 Simulations and results

Effect of varying mixing time:

In the first simulation we compare the effect of increasing mixing time τ_m on the amplitude of the signal modulation for DODE and DDE sequences in a substrate featuring randomly oriented anisotropic pores with diameter $d = 4$ µm and length $L = 12$ µm. To study a similar diffusion regime, we fix the b-values for both sequences to $b = \{5000, 10000\}$ s/mm^2 and modify the gradient strength accordingly. For DODE we consider the following parameters: gradient duration $\delta = 50$ ms, mixing time $\tau_m = \{0, 10, 20, 30, 50\}$ ms, and number of periods $N = \{1, 4\}$ with corresponding gradient amplitude $G = \{58, 232\}$ mT/m for $b = 5000$ s/mm^2 and $G = \{82, 327\}$ mT/m for $b = 10000$ s/mm^2. The DODE sequence with $N = 1$ is equivalent to a DDE sequence with $\delta = \Delta = 25$ ms and $\tau_m = \{25, 35, 45, 55, 75\}$ ms. The DDE sequence parameters are: gradient amplitude $G = \{137, 193\}$ mT/m, pulse duration $\delta = 6.25$ ms (which correspond to the duration of each half period for the DODE sequence with $N = 4$), diffusion time $\Delta = 50$ ms and mixing time $\tau_m = \{0, 10, 20, 30, 50\}$ ms.

Figure 6.2 illustrates the dependence of the DODE and DDE signal on the angle between the two gradients, ψ, for various mixing times, for a substrate of randomly oriented finite cylinders with diameter $d = 4$ µm and length $L = 12$ µm. The signal itself as well as the normalized signal with respect to the measurements with parallel gradients are plotted in Figure 6.2a) for sequences with $b = 5000$ s/mm^2 and in Figure 6.2b) for sequences with $b = 10000$ s/mm^2. Both the DODE and DDE signals exhibit an angular dependence on ψ, however, the influence of the mixing time differs for the two sequences. For zero mixing time (τ_m = 0ms), DDE sequences exhibit the well-described [214, 116, 215] bell-shaped signal dependence, with the largest signal difference between measurements with parallel and anti-parallel gradients, which is an indication of restricted diffusion [116, 118, 216]. As the mixing time increases, the signal dependence resembles the expected cos(2ψ) function [214, 117, 217], with the largest signal difference corresponding to measurements with parallel and perpendicular gradients. This amplitude modulation is a signature of µA. [116, 118, 216].

For DODE sequences, the angular dependence has a similar trend, however, the influence of mixing time becomes less pronounced as the frequency is increased, which is illustrated in Figure 6.2 for DODE with $N = \{1, 4\}$. For sequences with $N = 4$, the signal difference between measurements with parallel and anti-parallel gradients becomes close to zero even for short time intervals between the two gradient waveforms, which, for the standard DDE sequences, is characteristic of the long mixing time regime. In case of DODE sequences, the accumulated phase is refocused dur-

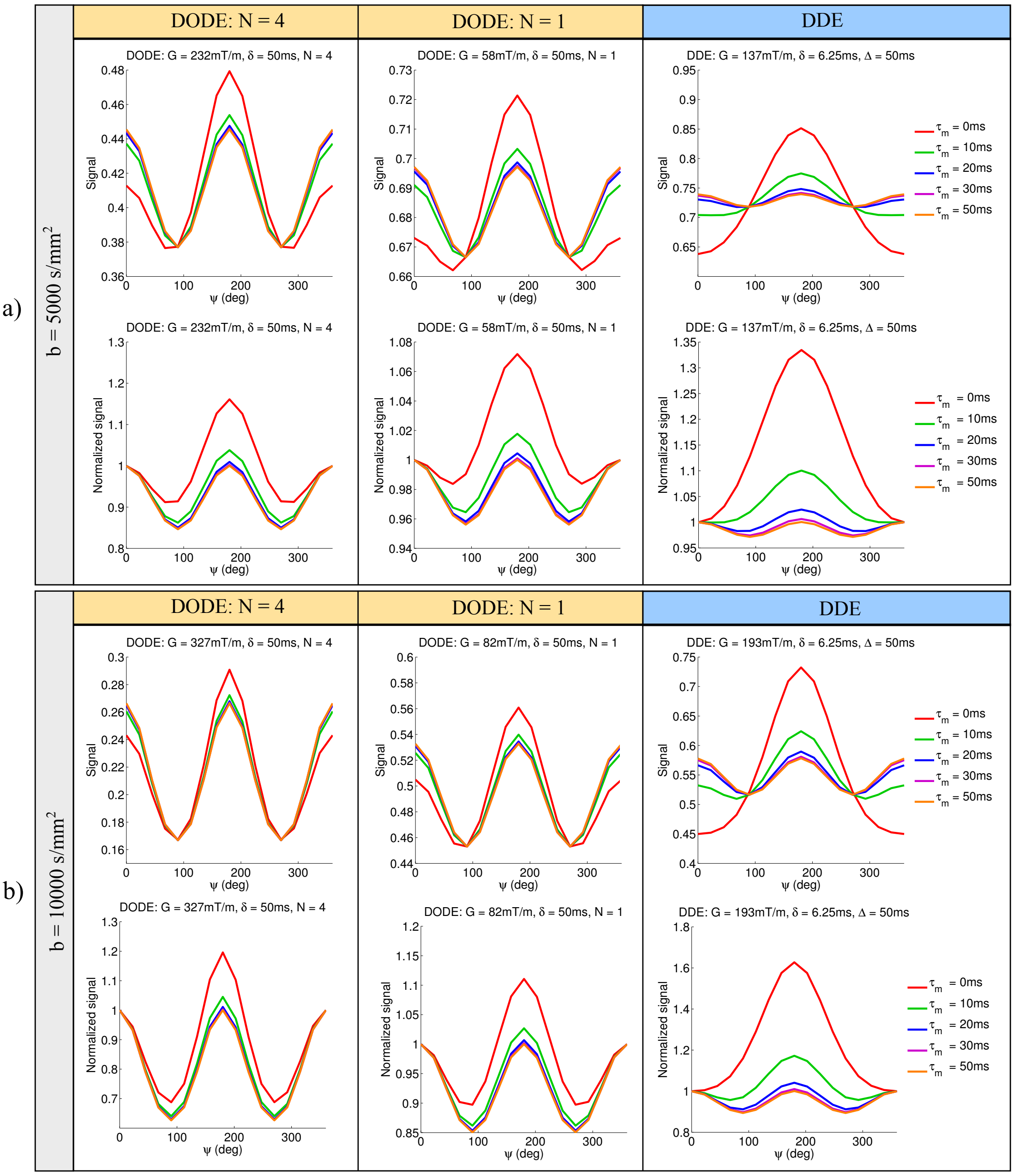

Figure 6.2: Signal and normalized signal as a function of the angle between gradients for DODE and DDE sequences with various mixing times and a) $b = 5000$ s/mm^2 and b) $b = 10000$ s/mm^2. The diffusion substrate consists of randomly oriented finite cylinders with diameter $d = 4$ μm and length $L = 12$ μm.

ing each period, which reduces the effective diffusion time and increases the effective mixing time.

Effect of varying oscillation frequency:

In the second simulation we investigate the effect of varying the number of oscillation periods N on the amplitude of the DODE signal modulation, in substrates with different degrees of diffusion anisotropy. We consider randomly oriented finite cylinders with diameter $d = 4$ µm and two different lengths $L = \{12, 8\}$ µm as well as spherical pores with $d = 4$ µm. First, to understand the effect of varying the gradient frequency, rather than decreasing the amount of diffusion weighting, we analyse sequences that have the same $b = 5000$ s/mm^2. We evaluate the dependence of the DODE signal on ψ for various number of oscillation periods $N = \{1, 2, 4, 8, 12\}$. The rest of the sequence parameters used in the simulation are: $\delta = 50$ ms, $\tau_m = 20$ ms and gradient strength $G = \{58, 116, 232, 463, 695\}$ mT/m which is adjusted to yield the same b-value. As in practice there is a physical constraint on the maximum gradient strength, we also investigate the case when DODE sequences with different N have the same gradient strength $G = 300$ mT/m.

Figure 6.3a) plots the signal itself as well as the normalized signal with respect to the measurements with parallel gradients for DODE sequences with the same $b = 5000$ s/mm^2. In this case the amplitude modulation initially increases with N, then it decreases, a trend that can be explained by analyzing which components of the diffusion spectrum D are sampled. In case of restricted diffusion, $D(\omega)$ increases with frequency, reaching the free diffusivity value for $\omega \to \infty$. The DODE sequences used in this simulation have sine-like waveforms and exhibit two peaks in the power modulation spectrum, one at zero frequency and one at the oscillation frequency. Thus, DODE sequences with $N = 1$ probe the smaller values of the diffusion spectrum at low frequencies, i.e. long diffusion times, and yield little signal attenuation for the given b-value. DODE sequences with medium values of N start probing larger values of $D(\omega)$ and provide a higher signal attenuation as well as sensitivity to restriction. As the number of oscillations is further increased, DODE sequences probe even larger values of $D(\omega)$ which approach free diffusivity as $\omega \to \infty$, and loose sensitivity to restriction. In case of restricted diffusion $D(0) = 0$ and the zero frequency peak does not influence the sensitivity to pore size.

Analyzing sequences with the same b-values is important for understanding the effects of varying oscillation frequency, however, these sequences cannot be readily achieved in practice, as there is a physical constraint on the maximum gradient strength. Figure 6.3b) presents the same dependence in a more practical situation, when the DODE sequences have the same gradient amplitude $G = 300$ mT/m. In this case,

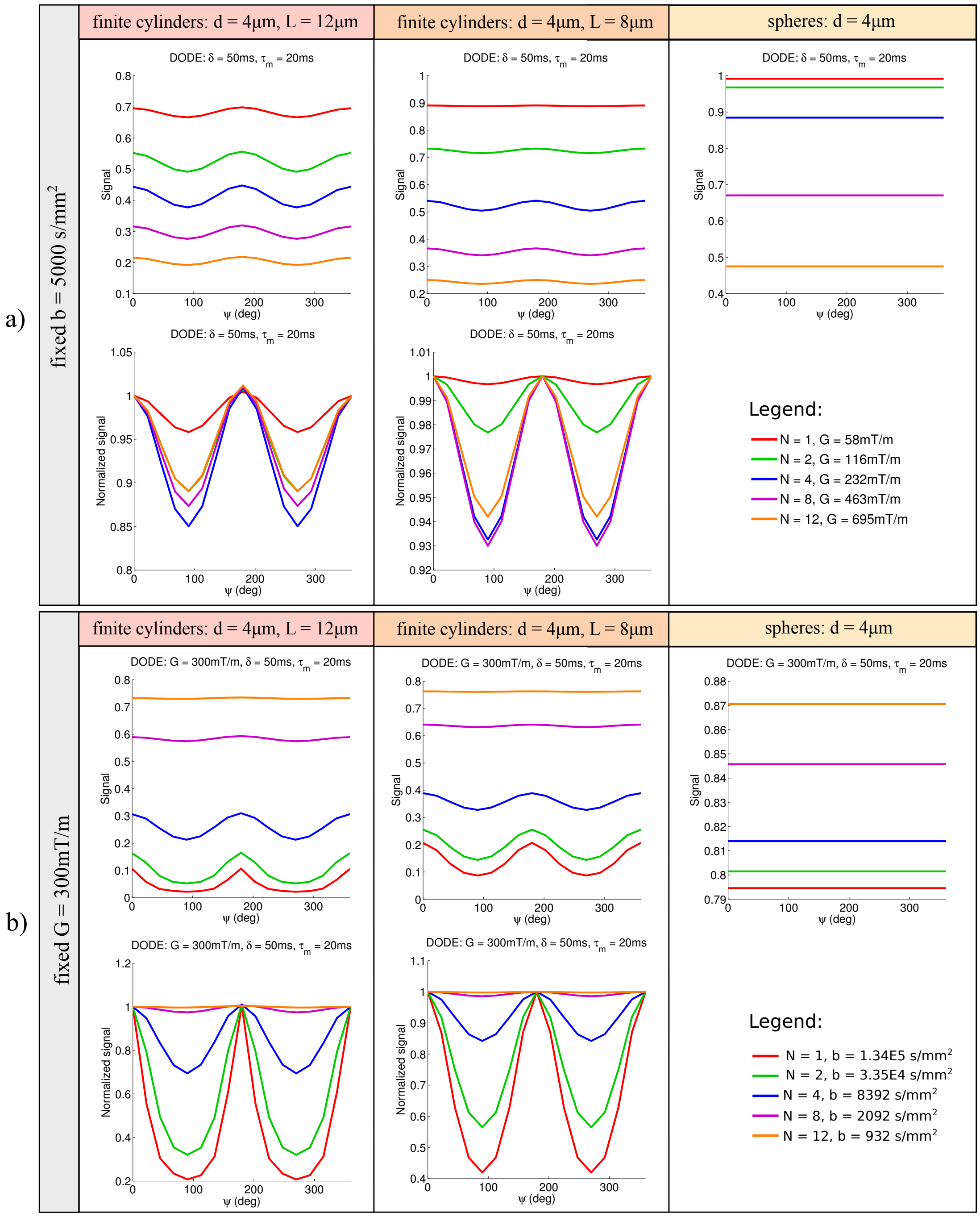

Figure 6.3: Signal and normalized signal as a function of the angle between gradients for pores with different eccentricities and DODE sequences with various number of periods N and a) the same $b = 5000$ s/mm^2 or b) the same gradient strength $G = 300$ mT/m

the diffusion weighting (b-value) of different sequences varies over several orders of magnitude. The DODE sequences with a large number of oscillations yield little signal attenuation, while the DODE sequence with $N = 1$ attenuates the signal close to the noise floor in substrates with elongated pores. As illustrated in Figure 6.3b) DODE sequences with an intermediate frequency yield the highest signal modulation amplitude. In all cases the amplitude of the signal modulation decreases as the pores become more isotropic, as expected from previous studies on DDE sequences.

6.4.3 Discussion

In this section we compared the DODE and DDE signal for sequences with various mixing times and oscillation frequencies. As the angle ψ between the two gradient waveforms varies, the DODE measurements also exhibit the characteristic amplitude modulation, which is well-known for DDE sequences. However, as the frequency of DODE sequences increases, the effect of varying mixing time becomes less pronounced compared to DDE. The oscillating gradient waveforms refocus the phase during each period, which leads to a decrease in the effective diffusion time and an increase in the effective mixing time.

The effect of different oscillation frequencies was investigated for DODE measurements with the same b-value or the same gradient strength. For sequences with the same b-value, the peak amplitude in the power modulation spectrum is the same for different frequencies, however, as N increases the gradients probe the higher diffusivity values corresponding to less restricted diffusion and the signal attenuation increases. For large N, the amplitude of the signal modulation as a function of ψ decreases and microscopic anisotropy is underestimated. When DODE sequences have the same gradient strength, their diffusion weighting (b-value) varies over several orders of magnitude, and a fine balance between signal attenuation and sensitivity to restriction needs to be achieved.

6.5 Simulation 2: Sensitivity and specificity analysis of DODE and DDE sequences

The second set of simulations explores the sensitivity of DODE and DDE measurements to pore diameter and length in substrates of randomly oriented anisotropic pores. Here we chose to investigate pore diameter and length (as opposed to pore diameter and eccentricity in chapter 5) as they affect the diffusion signal independently, which makes the results easier to interpret.

6.5.1 Aims and objectives

Extending the concept of sequence sensitivity discussed in chapter 4.1, the objectives of this simulation are the following:

1. compare the sensitivity of DODE and DDE sequences for a wide range of substrates:
    - sensitivity to pore diameter in randomly oriented infinite cylinders.
    - sensitivity to pore diameter and length in randomly oriented finite cylinders.
2. analyse the sensitivity over a practical range of sequence parameters and incorporate the effects of T2 decay.
3. investigate the difference between DODE and DDE sequences with parallel and perpendicular gradients and identify which substrates are distinguishable from isotropic pores for various SNR levels.

6.5.2 Simulations and results

Sensitivity definition

In case of ODE sequences we defined the sensitivity to pore diameter as the absolute value of the partial signal derivative with respect to the parameter of interest. In the case of DODE sequences both measurements with parallel and perpendicular gradients are of interest, and we define the total sensitivity as the sum of sensitivities for these two measurements:

$$\mathcal{S}_d = \left|\partial_d\left(S_{\|}(d,L)\right)\right| + \left|\partial_d\left(S_{\perp}(d,L)\right)\right|, \tag{6.4}$$

with respect to pore diameter and

$$\mathcal{S}_L = \left|\partial_L\left(S_{\|}(d,L)\right)\right| + \left|\partial_L\left(S_{\perp}(d,L)\right)\right|, \tag{6.5}$$

with respect to pore length, where d is the pore diameter, L is the pore length, $S_{\|}$ is the diffusion signal measured from sequences with parallel gradients and $S_{\perp}$ is the signal obtained from measurements with perpendicular gradients.

Sensitivity for a wide range of substrates:

The first simulation compares the sensitivity of several DODE and DDE sequences in substrates with a large variety of parameters. We consider randomly oriented infinite cylinders with diameter d between 1 and 12 μm as well as randomly oriented finite cylinders with $d = \{4, 6\}$ μm and a range of lengths L between 4 and 40 μm. We analyze DODE sequences with various numbers of oscillations, DDE sequences with finite gradient duration as well as ideal DDE sequences with short gradient duration. As in practice the gradient strength is a physical constraint, in this simulation, we fix the gradient strength of the DODE sequences to $G = 300$ mT/m, corresponding to the Connectome scanner [218]. The rest of the DODE parameters are: $\delta = 50$ ms, $\tau_m = 20$ ms and $N = \{1, 2, 4, 8, 12\}$. For the DDE sequences, we look at 2 different scenarios, and in all cases $\Delta = \tau_m = 50$ ms:

1. DDE sequences have the same gradient amplitude $G = 300$ mT/m and various pulse durations equal to half the oscillation period of the DODE sequences: $\delta = \{25, 12.5, 6.3, 3.1, 2.1\}$ ms.
2. The gradient amplitude of idealized DDE sequences with $\delta = 1$ ms is adjusted to get matching b-values with the DODE sequences for each N. The resulting gradient strengths are $G = \{4.34, 2.17, 1.09, 0.54, 0.36\}$ T/m. Although the gradient strength for matching the b-values becomes unrealistically high, it provides a useful theoretical comparison.

Figure 6.4 presents the dependence of sensitivity to pore diameter, $\mathcal{S}_d$, for randomly oriented infinite cylinders. The sensitivity is calculated for DODE sequences with various N and the corresponding DDE sequences with the same gradient strength and finite duration as well as ideal DDE sequences with short gradient pulses and the same b-value. To match b-value, the gradient amplitude of the idealized short-pulse DDE sequence must reach over 4T/m which is not practical even in most preclinical settings, but we include the results for theoretical comparison. DODE sequences show higher sensitivity than DDE for a range of pore diameters between 2 and 8 μm, as noted by the higher values of $\mathcal{S}_d$. On the other hand, DDE sequences, both with finite pulses as well as with short pulses, have higher sensitivity for larger pore diameters $d > 8$ μm. For these pore sizes, a longer diffusion time, which is achieved using DDE sequences,

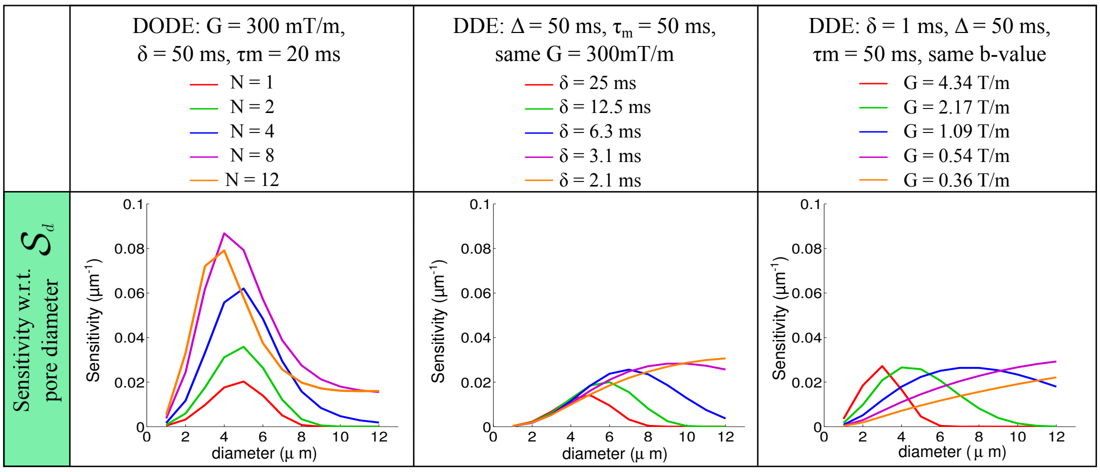

Figure 6.4: Sensitivity of DODE and DDE sequences with respect to pore diameters $\mathcal{S}_d$ for substrates consisting of randomly oriented infinite cylinders. For each DODE sequence with number of periods N, the parameters of the DDE sequences were chosen as explained in section **??**: DDE with finite pulses (2$^{\text{nd}}$ column) and DDE with short gradient pulses and the same b-value (3$^{\text{rd}}$ column).

is necessary to better probe the pore boundaries. It is interesting to note that these results also hint at increased specificity, for example when $N = \{8, 12\}$, the signal is most sensitive to small diameters, and less sensitive to larger sizes. Nevertheless, for the range of pore diameters analyzed here, these sequences retain some sensitivity to larger pore diameters as well.

Figure 6.5 illustrates the DODE and DDE sensitivities with respect to pore diameter and length, $\mathcal{S}_d$ and $\mathcal{S}_L$, in substrates consisting of randomly oriented finite cylinders. For elongated pores with $L > 8$ μm, DODE sequences with $N = 8$ provide the highest sensitivity to pore diameter, $\mathcal{S}_d$, for both $d = \{4, 6\}$ μm, which is consistent with the results in Figure 6.4. For less eccentric pores ($L < 8$ μm), DODE sequences have no net advantage. Nevertheless, the maximum sensitivity of DODE and DDE sequences with finite pulses is higher compared to values obtained from DDE sequences with sort gradient pulses (3rd column). For all sequences, the sensitivity $\mathcal{S}_d$ decreases as the pores become more elongated. This happens because in a finite cylinder the restricted diffusion signal is the product of perpendicular and parallel components, which depend on pore diameter and length, respectively. Thus, the sensitivity to pore diameter is weighted by the parallel signal. As the pore length increases, there is more attenuation from the parallel component and the sensitivity $\mathcal{S}_d$ decreases.

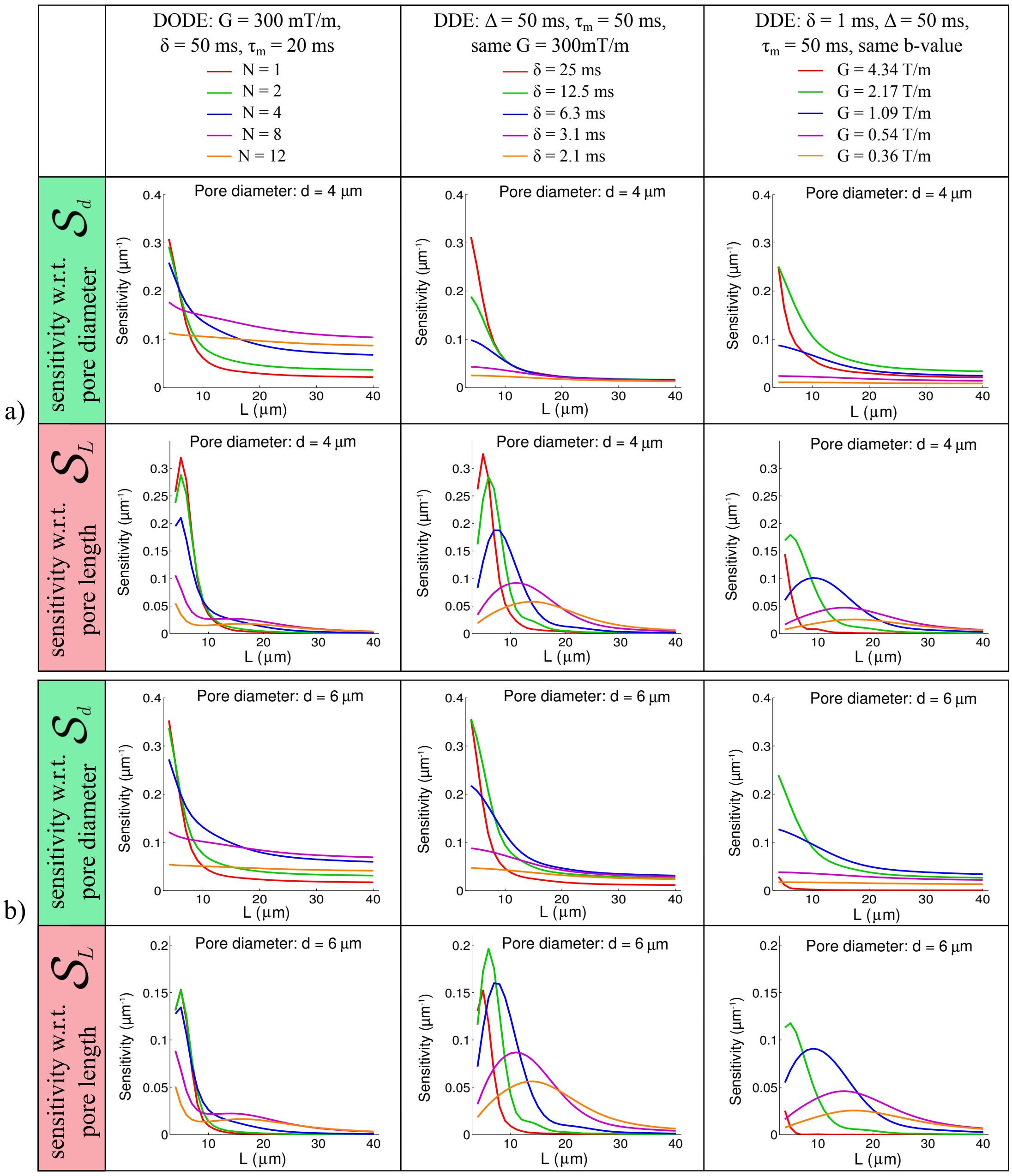

Figure 6.5: Sensitivity of DODE and DDE sequences with respect to pore size, $\mathcal{S}_d$, and length, $\mathcal{S}_L$, for randomly oriented finite cylinders with various lengths and two different diameters a) $d = 4$ μm and b) $d = 6$ μm. Different columns illustrate different sequences as explained in Figure 6.4.

When considering sensitivity to pore length $\mathcal{S}_L$, DDE sequences with finite gradient duration provide the highest sensitivity in all substrates. The simulations show that ideal DDE sequences with short gradient pulses do not have any advantages in terms of sensitivity to microstructural features. For the diffusion times and gradient strengths considered in this study, the sensitivity $\mathcal{S}_L$ of all sequences decreases almost to 0 for pores with $L > 20$ μm.

These results show that ideal DDE sequences with short gradient duration are not the best choice for estimating pore length and diameter and stress the importance of choosing the correct sequence parameters for a given application.

Sensitivity for a wide range of sequence parameters:

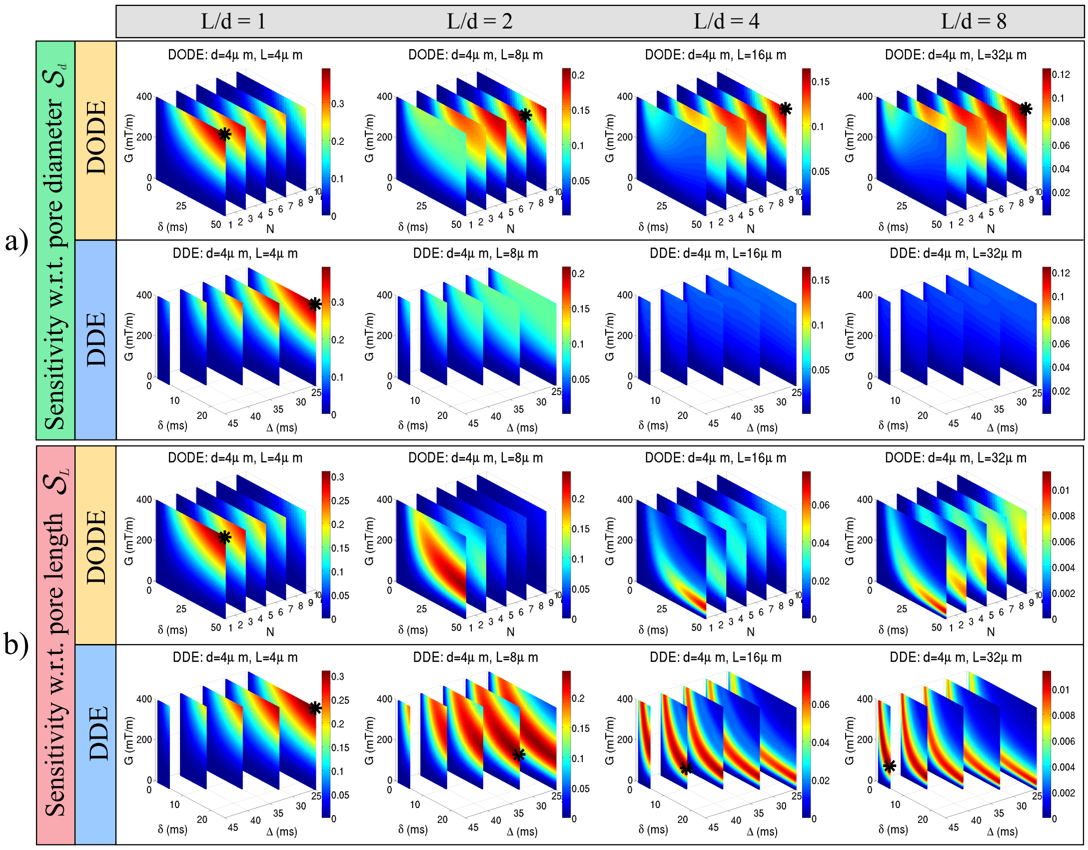

Figure 6.6: Signal sensitivity of DODE and DDE sequences with respect to a) pore diameter $\mathcal{S}_d$ and b) pore length $\mathcal{S}_L$ for substrates of finite cylinders with diameter $d = 4\mu$m and different lengths $L = \{4, 8, 16, 32\}\mu$m. The eccentricity of the pores increases from left to right. The sensitivity is colour coded and the maximum value for each substrate is marked with a black asterisk.

In the second experiment, we investigate the sensitivity of DODE and DDE sequences over a wide range of practical sequence parameters in several substrates, which consist of randomly oriented finite cylinders with diameter $d = \{4, 6\}$ µm and eccentricities of $L/d = \{1, 2, 4, 8\}$. We make the two sequences equally practical by ensuring the same maximum gradient strength and maximum duration for both DODE and DDE sequences. The range of parameters for DODE sequences are: $G = [0, 400]$ mT/m, $\delta_{DODE} = [0, 50]$ ms and $N = \{1, 2, ..., 10\}$. For the DDE sequences the range of gradient strengths is the same $G = [0, 400]$ mT/m and we consider five different

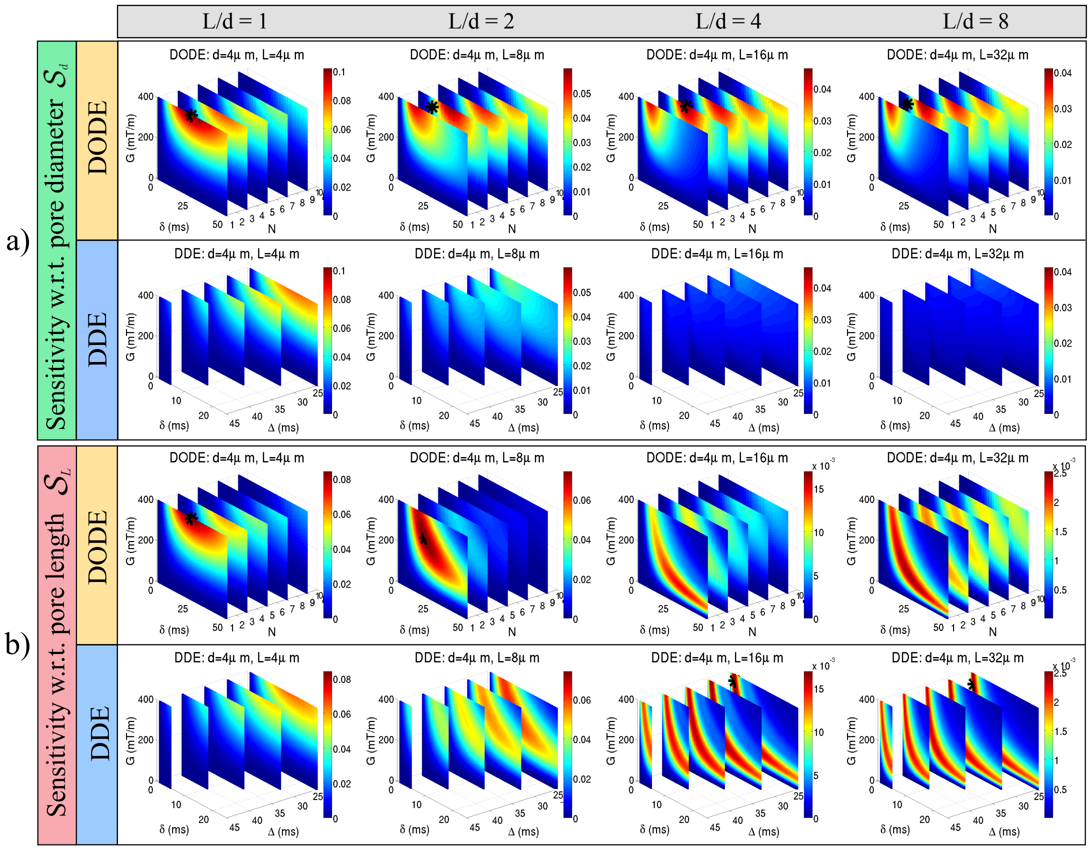

Figure 6.7: Signal sensitivity of DODE and DDE sequences with respect to a) pore diameter $\mathcal{S}_d$ and b) pore length $\mathcal{S}_L$ in the presence of T2 decay with time constant $T2 = 70$ms. The substrates consist of finite cylinders with diameter $d = 4\mu$m and different lengths $L = \{4, 8, 16, 32\}\mu$m.

diffusion times $\Delta = \{25, 30, 35, 40, 45\}$ ms. For each Δ we have a different range of gradient durations δ in order to limit the total duration of each gradient pair $(\delta + \Delta)$ at 50 ms. In order to reduce the dimensionality of the problem, the time interval between the first and second gradient waveforms is fixed to 20 ms for all sequences. We also analyze the effect of T2 relaxation with a constant of 70 ms, which is in the range of values for gray matter at 3T.

Figure 6.6 illustrates the sensitivities $\mathcal{S}_d$ and $\mathcal{S}_L$ for substrates with diameter $d = 4$ μm and various eccentricities, when the effects of T2 decay are not considered. The asterisk depicts the most sensitive sequences for each substrate. For the configurations considered in this study, DODE sequences with $N = 9$ periods are the most sensitive to pore diameter in elongated pores ($L > 8$ μm). In substrates with isotropic pores of diameter $d = 4$ μm, DODE sequences with $N = 1$, which are equivalent to DDE sequences with $\Delta = \delta$ have the highest sensitivity to pore size. When considering the sensitivity to pore length, DDE sequences with a low gradient strength and the longest pulse duration for the corresponding diffusion time are the best choice. The plots also illustrate that the diffusion time of the most sensitive DDE sequence increases with pore length, as larger length scales need to be probed.

Figure 6.7 presents the sensitivity of DODE and DDE sequences, when the effects of T2 relaxation are taken into account with a relaxation constant T2 = 70ms. In this case, DODE sequences with a lower number of oscillations ($N = \{2, 3\}$) and shorter gradient duration, compared to the results in Figure 6.6a), show the highest sensitivity to pore diameter in elongated pores. The optimal sensitivity to pore length in elongated pores ($L > 16$ µm) is still achieved by DDE sequences with $\Delta > \delta$, while for less elongated pores DDE sequences with $\Delta = \delta$ are preferred. Nevertheless, the optimal parameter values are different. When T2 decay is considered, the preferred DDE sequences have larger gradient strength and shorter pulse duration and diffusion time compared to the results in Figure 6.6b).

Overall, the results show that a combination of DODE and DDE sequences provides complementary sensitivity to different microstructural features such as pore diameter and length.

Specificity to microscopic anisotropy

As the difference between DODE/DDE measurements with parallel and perpendicular gradients is a signature of microscopic anisotropy, the last simulation investigates how different sequence parameters influence this contrast in a large variety of substrates. This facilitates the design of experiments which improve the specificity to the microstructural features of interest. Thus, we analyze the signal difference between the two sets of measurements for DODE and DDE sequences with different varying parameters in a wide range of substrates with pore diameters $0.5\mu\text{m} < d < 10\mu\text{m}$ and eccentricities $1 < L/d < 10$. For DODE sequences we vary independently G, N and δ, while for DDE we vary G, δ and Δ. For both sequences the time interval between the two gradients has a constant value of 20 ms. We also analyze the effect of noise and label the regions where the difference is larger than the standard deviation of the noise for different levels of $SNR = \{20, 50, 100, 1000\}$. This highlights which substrates can be distinguished from isotropic pores, given the diffusion sequence and SNR level.

As in the previous simulation, the time interval between the first and second gradient waveforms is fixed to 20ms for all sequences.

Figure 6.8 presents the signal difference as a function of pore size and eccentricity. Different rows in panels a) and b) have sequences with different varying parameters. Sequences with large gradient strength are more sensitive to smaller pore sizes, and decreasing G shifts sensitivity to larger and more elongated pores for both DODE and DDE sequences. For DODE with varying N, we see a slightly different pattern which enhances the sensitivity to pore diameter for elongated pores, i.e. there is a stronger color gradient in vertical direction for the entire range of eccentricities. Decreasing the gradient duration has an overall effect of reducing the sensitivity due to a decrease in diffusion weighting. For DDE sequences, decreasing δ while having a long diffusion time has a similar effect to increasing N for DODE, nevertheless, the effect is less pronounced. For DDE sequences, increasing diffusion time improves sensitivity to pore elongation, which can be seen as a sharper gradient in panel b) bottom row. All in all, this simulation shows that DODE and DDE sequences with different parameters are required in order to estimate different microstructural properties. Thus, for substrates with unknown microstructural features or in areas with a superposition of cellular structures, measurements with a range of different parameters are needed. A careful choice of sequence parameters can also be used to enhance the signal acquired from a certain tissue configuration, while suppressing the signal from different ones.

6.5.3 Discussion

This section investigates the sensitivity and specificity of DODE and DDE sequences with respect to pore diameter and length.

The first experiment compares the sensitivity of DODE and DDE sequences, with the aim of identifying regimes where each sequence is beneficial. Thus, the analysis is focused on sequences with several parameter combinations and a large variety of diffusion substrates. In randomly oriented infinite cylinders, we found that DODE sequences improve the sensitivity to pore diameter for a range of values between 2 and 8 μm. This is consistent with the findings from Chapter 4, showing higher sensitivity for ODE sequences in cylindrical pores with orientation dispersion. The advantage of DODE arises from less attenuation due to diffusion along the long axis of the pore,

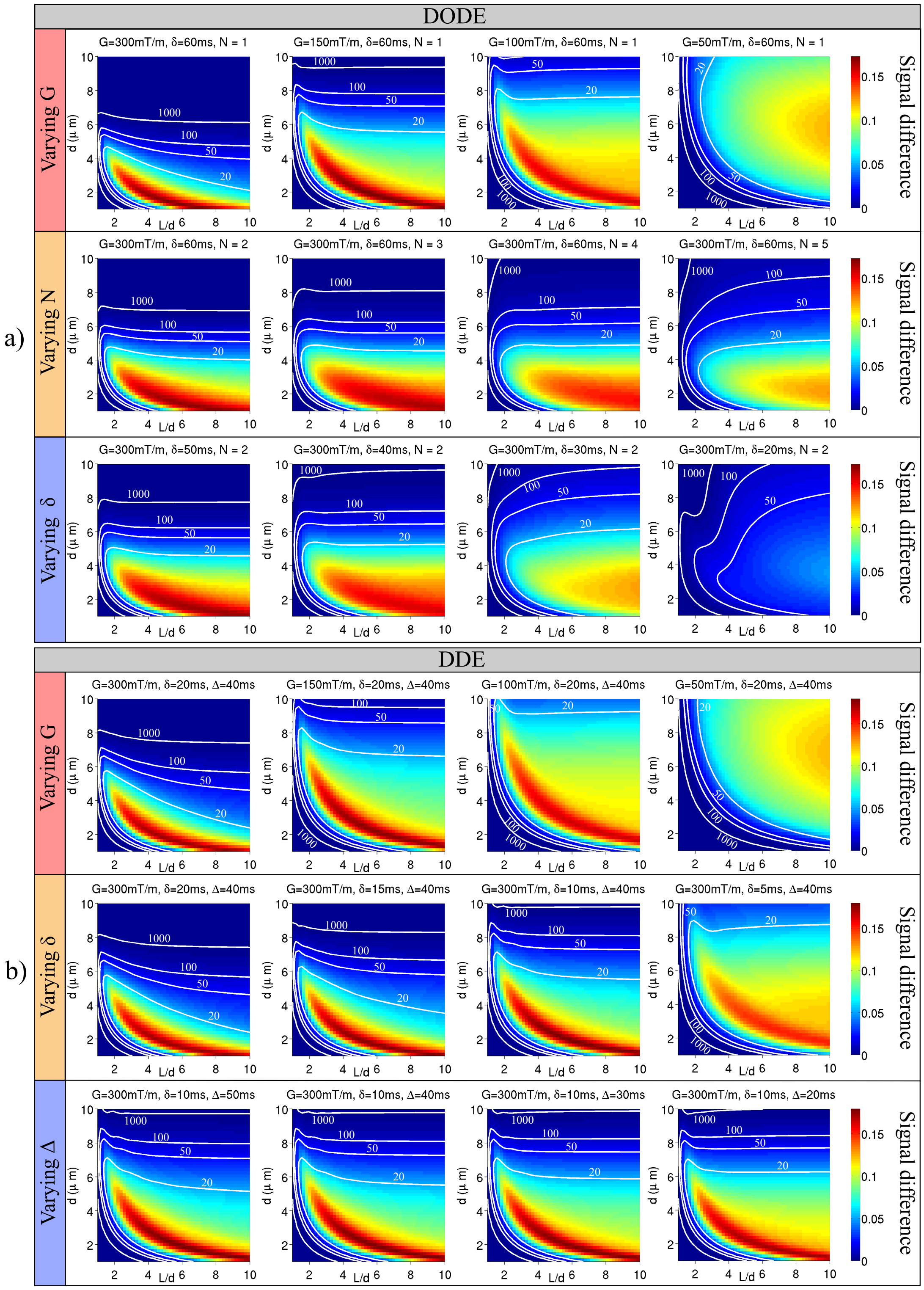

Figure 6.8: Difference between parallel and perpendicular measurements of a) DODE and b) DDE sequences as a function of pore size and eccentricity. In each row a different sequence parameter is varying, while all the other parameters are constant. The white contours indicate the limit where the difference is equal to the standard deviation of noise for $SNR = \{20, 50, 100, 1000\}$.

while preserving sensitivity to restriction. When considering substrates of finite cylinders, DODE sequences improve sensitivity to pore diameter in elongated pores, while DDE acquisitions have higher sensitivity to pore length. Furthermore, we found that ideal DDE sequences with short gradient duration and the same b-value do not necessarily have an advantage with respect to sensitivity to microstructural features.

The subsequent simulation examined the sensitivity of sequences over a wide range of practical sequence parameters in several substrates. This analysis further demonstrates that DODE sequences show higher sensitivity to pore diameter in elongated pores, while DDE sequences have larger sensitivity to pore length. This trend was observed both when T2 decay was neglected or considered in the sensitivity measure, however, the optimal parameters look different in the two cases. When the effects of T2 are neglected, the maximum sensitivity for DODE sequences occurs at long pulse durations and higher oscillation frequency ($N = 9$). For sensitivity to pore length, the optimal DDE measurements have a low gradient strength and the longest pulse duration which can be achieved for the preferred diffusion time. When T2 effects are considered, the optimal DODE sequences have shorter pulse duration and a lower number of oscillations ($N = 2, 3$), and the optimal DDE sequences have shorter duration and higher gradient strength compared to the case of infinite T2. DDE sequences with $\Delta = \delta$ have the highest sensitivity to small, isotropic pores, as they maximize the amount of diffusion weighting for a given duration. Their advantage is perhaps a bit surprising, as many DDE-based studies to date have opted using DDE sequences resembling as much as possible to the ideal SGP limits [121, 217], although others used longer gradient durations due to gradient amplitude constraints [219, 120, 220, 221]. These results suggest that diffusion protocols which combine DODE and DDE measurements would be sensitive to a wide range of configurations and pore-sizes. Moreover, when there is prior knowledge of the substrates, the sequences can be optimized to improve the sensitivity to a particular configuration.

The last simulation points to a potential specificity of DDE/DODE sequences towards different μA. A given pixel within brain tissues, particularly gray matter, will reflect a superposition of several very different environments for water diffusion. For instance, large and approximately spherical cell bodies may co-exist with randomly oriented neurites [222]. The results presented in Figure **??** show that by changing the sequence parameters we can manipulate which substrates the sequence would be most sensitive to, based on the respective signal differences between parallel and perpendicular gradients. Although the plots in Figure **??** do not show very localized maxima, further investigations optimizing these signal differences in DDE/DODE towards specific microstructures could be beneficial. This approach would be especially useful for estimating model-free metrics based on the signal difference.

In these simulations we mostly focus on practically feasible sequence parameters, rather than achieving the theoretical conditions of long diffusion and mixing times for all substrates. A direct consequence of this fact, is the decreased sensitivity to pore length for $L > 20\mu$m in Figure 6.5, as diffusion and mixing times of 50ms are not long enough to fully probe this length scale. The same fact explains the smaller value of the sensitivities in Figures 6.6 and 6.7 in the rightmost panels which feature pores with $L = 32\mu$m.

This analysis is concentrated on comparing DODE and DDE type acquisitions in the context of angular experiments as well as their sensitivity to microstructural parameters. Although the search space is limited to several parameters, previous work, which optimized a generalized diffusion sequence (i.e. $\mathrm{g}(t)$) for axon diameter estimation [94], showed that oscillating gradients of various frequencies consistently appeared to be the optimal waveforms. A thorough analysis of other diffusion techniques that have been recently presented in the literature for estimating microscopic anisotropy [223, 177, 180, 224]) is outside the scope of this work and will be considered in future research.

6.6 Simulation 3: Rotationally invariant extension

The previous simulations consider only macroscopically isotropic substrates, however, in order to have a wider range of applicability we require a rotationally invariant acquisition. This work aims to extend the DODE acquisition in order to estimate a rotationally invariant metric of microscopic anisotropy following the approach described by Jespersen et al [121].

6.6.1 Aims and objectives

Specifically, the objectives of this study are:

1. adapt the expression of fractional eccentricity (FE) [121] for DODE sequences using the b-values and q-values derived in the theory section 6.2
2. analyse the dependence of FE on pore elongation for substrates with various levels of macroscopic anisotropy.
3. compare the estimated FE provided by DODE and ideal DDE sequences.

6.6.2 FE derivation

Using the expressions for b-value, q-value and diffusion time provided in section 6.2, fractional eccentricity introduced in [121] can be extended to DODE sequences as follows:

$$\begin{aligned} FE &= \sqrt{\frac{\epsilon}{\epsilon + \frac{3}{5}\left(\frac{\delta}{3N}\right)^2 \left(\frac{Tr(\mathbf{D})}{3}\right)^2}}, \text{ where} \\ \epsilon &= \frac{1}{q^4}\left(\log\left(\frac{1}{12}\sum S_{||}\right) - \log\left(\frac{1}{60}\sum S_{\perp}\right)\right), \end{aligned} \tag{6.6}$$

$\mathbf{D}$ is the diffusion tensor computed from the parallel measurements and $\delta/3N$ is the diffusion time.

6.6.3 Simulations and results

The original protocol proposed in [121] has 12 parallel DDE measurements with gradient directions pointing towards the vertices of an icosahedron and 60 perpendicular DDE measurements with 5 measurements in the normal plane of each parallel direction. Here we replace the DDE measurements with DODE sequences and we use the following parameters: $G = 300$mT/m, $\delta = 60$ms, $\tau_m = 20$ms and $N = 3$. We chose this specific value of N so we can later compare this approach of computing fractional eccentricity to the method presented by Lasic et al [180] that involves isotropic diffusion encoding. To substrates consisting of randomly oriented finite cylinders we add coherently oriented pores which occupy a volume fraction $f = \{0, 0.25, 0.5, 0.75\}$. We compute the fractional eccentricity according to equation 6.6 and we use the adapted b-values and q-values presented in section 6.2. We also compare the DODE derived FE with the values obtained from an ideal DDE sequence with $\delta = 1$ ms, $\Delta = \tau_m = 50$ ms and the same b-value as the DODE measurements.

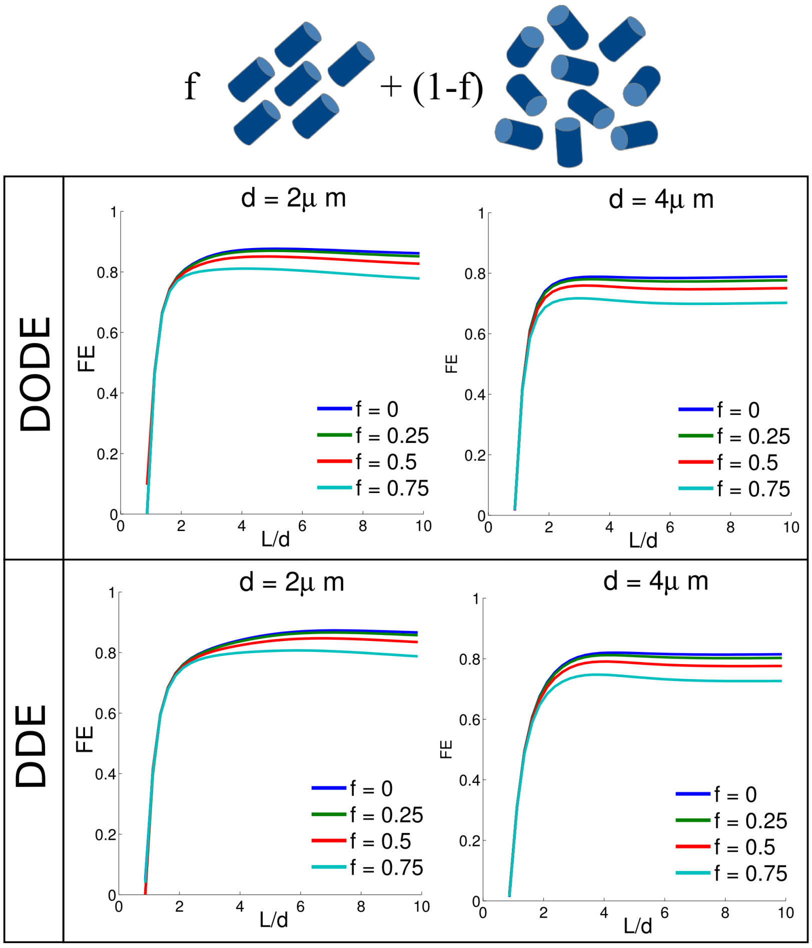

Figure 6.9: Fractional eccentricity as a function of pore elongation for substrates with various volume fractions of coherently oriented pores for DODE and DDE sequences. The DODE protocol consist of sequences with $N = 3$, $G = 300$mT/m, $\delta = 50$ms and $\tau_m = 20$ ms with 72 directions, while the DDE protocol has $\delta = 1$ms, $\Delta = \tau_m = 50$ms and the same b-value as the DODE sequences.

Figure 6.9 illustrates the dependence of fractional eccentricity on pore elongation for substrates with different volume fractions of coherently oriented pores with diameter $d = 2\mu$m and $d = 4\mu$m. FE is computed according to equation 6.1 and the acquisition protocol described above. The results for DODE sequences (top row) show a good agreement with the FE values measured with an ideal DDE protocol (bottom row), which confirms that the new sequences can easily be extended to a rotationally invariant framework. Due to the discrete sampling of gradient orientations (12 parallel directions), there are small differences up to 10% in the calculated FE values for different volume fractions f.

6.6.4 Discussion

In this section we have adapted the derivation of fraction eccentricity [121] for an acquisition consisting of DODE sequences. Furthermore, we have investigated the dependence of FE on pore elongation for macroscopically anisotropic substrates with various volume fractions of coherently oriented pores. The results show that the FE values estimated from DODE measurements are similar to the gold standard FE values given by an ideal DDE protocol with the same b-value. This finding demonstrates that reliable FE values can be measured with sequences that are not necessarily close to the theoretical limit of short gradient pulses.

As seen in the previous section, if there is prior knowledge of the substrate, the sequence parameters can be chosen in order to maximize the difference between parallel and perpendicular measurements, decreasing the impact of noise on the estimation of FE.

6.7 Simulation 4: Comparison of microscopic anisotropy metrics

The last simulation presents an application of DODE sequences for comparing two rotationally invariant metrics of microscopic anisotropy, namely fractional eccentricity (FE) [121] microscopic fractional anisotropy (μFA) [180]. Originally, FE is calculated from DDE sequences and μFA from sequences with isotropic and directional encoding. In order to compare the two metrics we require diffusion sequences that are as similar as possible in terms of gradient waveform, which can be achieved using oscillating gradients with varying direction.

6.7.1 Aims and objectives

This study aims to:

1. adapt the DODE sequences for each approach in order to have comparable data acquisition.
2. compare the two metrics in different diffusion substrates: randomly oriented pores featuring restricted diffusion or randomly oriented microdomains featur-

ing Gaussian diffusion.

6.7.2 Simulations and results

Measurement protocols

In order to compare the two metrics which require different acquisitions, we adapt the DODE protocol for each approach ensuring that the sequences have the same gradient waveform and vary only in direction. Thus we make the two acquisitions as similar as possible.

To estimate FE we use a rotationally invariant protocol with 72 measurements, as discussed in section 6.6. The DODE sequences have three periods $N = 3$, a gradient duration $\delta_{DODE} = 60$ms, mixing time $\tau_m = 20$ms and gradient strength G_{DODE} that we modify depending on the substrates we investigate. For estimating μFA we use 16 different gradient strengths between 0 and G_{DODE}, and for each gradient strength we have 15 isotropically oriented directions to compute the directional average and 15 repeats for the isotropic encoding, to match the acquisition described in [180]. For the sequences providing isotropic encoding, the gradient duration in each direction is $\delta_{DODE}/2N = 10$ ms. The two acquisition protocols have the same gradient waveform and maximum b-value and are illustrated in Figure 6.10a.

FE and μFA expressions

We calculate FE according to equation 6.6 that we derived for DODE acquisition in section 6.6.

To compute μFA, we follow the steps described in [180]. First we perform a non-linear fit to the 2nd order cumulant expansion of the signal $\log(S(b)) = -\bar{D} + \frac{\mu_2}{2}b^2$ in order to obtain the mean diffusion coefficient $\bar{D}$ and its variance μ_2. For better parameter estimates, we use the output of the linear regression as starting points for the non-linear fitting procedure. We find this method to be more numerically stable than fitting a Gamma distribution of diffusivities as explained in [180]. We fit this equation to the isotropically encoded measurements and to the directionally averaged data with two different assumptions:

- We enforce the same mean diffusivity when fitting the isotropic encoded and the directional averaged data, as assumed in [180].

- We fit the cummulant expansion separately to the two data sets and we obtain two different values of mean diffusivity and variance.

Once we have the values for mean diffusivity and variance, we compute μFA according to:

$$\mu FA = \sqrt{\frac{3}{2}} \left(1 + \frac{2}{5\Delta\tilde{\mu}_2}\right)^{-1/2}, \quad \text{where} \tag{6.7}$$

$$\Delta\tilde{\mu}_2 = \frac{\mu_2^{da}}{\bar{D}^{da}} - \frac{\mu_2^{iso}}{\bar{D}^{iso}} \tag{6.8}$$

is the difference of scaled variances for directional averaged data and isotropically encoded data.

Diffusion substrates

We investigate two different types of diffusion substrates and adapt the maximum gradient strength accordingly:

- Randomly oriented anisotropic pores, which exhibit restricted diffusion. The maximum gradient strength for this simulation is $G_{DODE} = 300$mT/m, which yields a b-value of $25,780$ s/mm^2.
- Randomly oriented anisotropic domains which exhibit Gaussian diffusion with different parallel and perpendicular diffusivities. The maximum gradient strength is $G_{DODE} = 100$mT/m, which yields a b-value of 2,865 s/mm^2. This is similar to the simulations in [180, 177].

Results

Figure 6.10 compares the values of fractional eccentricity based on DODE sequences and the values of microscopic fractional anisotropy based on directional and isotropic encoding. With our particular choice of sequence parameters we try to match the two types of acquisitions as well as possible. Figure 6.10b illustrates the dependence of FE and μFA on pore elongation for a substrate of anisotropic pores exhibiting restricted diffusion. In this case, the FE and μFA value computed assuming the same mean diffusivity for isotropic encoding and the directional average overestimates the

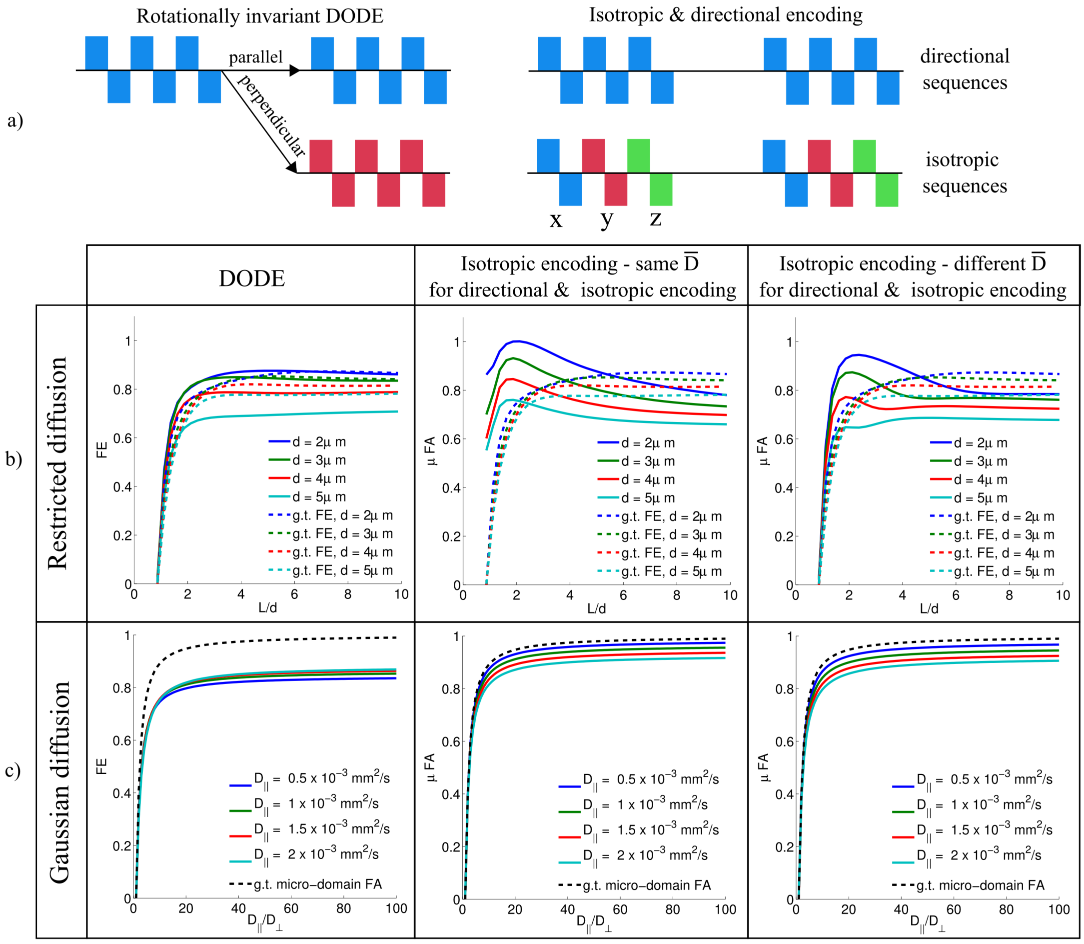

Figure 6.10: a) Schematic representation of diffusion sequences used to compute fractional eccentricity (left) and microscopic fractional anisotropy (right); b) dependence of FE and μFA on pore elongation for substrates which consist of randomly oriented pores featuring restricted diffusion. μFA is calculated in two different ways: data from directional and isotropic encoding is fitted using the same mean diffusivity and different variances, as in [180] (middle) and the data sets from directional and isotropic encoding are fitted separately (right). Gold standard FE values computed from an ideal DDE protocol are shown as well (−−). The maximum gradient strength is 300mT/m corresponding to $b = 25,780$ s/mm^2 c) dependence of FE and μFA on the ratio between parallel and perpendicular diffusivities for substrates which consist of randomly oriented domains featuring Gaussian diffusion. μFA is calculate in two different ways as explained above. The ground truth micro-domain FA is plotted as well (−−). In this case, the maximum gradient strength is 100mT/m, corresponding to $b = 2865$ s/mm^2.

microscopic anisotropy of pores with low eccentricity. Relaxing this assumption improves the values of μFA, nevertheless, it is not monotonically increasing with pore eccentricity. In case of restricted diffusion, the fractional eccentricity computed from DODE measurements is closer to the gold standard values. Figure 6.10c illustrates the dependence of FE and μFA on the ratio between parallel and perpendicular diffusivities in randomly oriented domains which exhibit Gaussian diffusion. In this case μFA is closer to the ground truth FA values of the microdomains compared to FE. Moreover, the assumption that the mean diffusivity is the same for the directional average and isotropic encoding holds. This situation is representative of the simulations from [180, 177].

6.7.3 Discussion

In this simulation we adapted the DODE acquisition in order to compare two different metrics of microscopic anisotropy and we investigated their behaviour in various substrates. The results show that FE and μFA metrics do not provide the same values and behave differently depending on the nature of microscopic anisotropy. In the case of restricted diffusion FE describes better the anisotropy of the system, while for Gaussian diffusion, μFA is closer to the ground truth values of micro-domain FA. Future work aims to investigate the effect of noise on the calculated values of FE and μFA.

6.8 Conclusions

This chapter presents a novel class of diffusion sequences, namely double oscillating diffusion encoding (DODE), that combine the benefits of oscillating gradients and varying gradient orientation in one measurement.

In the first section we investigated the signal dependence of the DODE signal on sequence parameters in substrates featuring microscopic anisotropy. The results show a similar signal pattern to DDE sequences, however the influence of the mixing time is less pronounced. This happens because the phase is already partially refocused due to the oscillating gradient waveform, thus the long mixing time condition can be achieved for shorter time intervals between the two gradients. This is especially beneficial for reducing the total duration of the pulse sequence in order to mediate the effects of T2 decay.

The second section investigates the sensitivity of DODE and DDE signal with respect to microstructural features such as pore diameter and length. The conclusions of these simulations is in line with the results for SDE and ODE sequences discussed in section 4.1. DODE sequences improve the sensitivity to pore diameter with a range of values between 2 and 8μm in randomly oriented elongated pores, while DDE sequences with various diffusion times show higher sensitivity to pore length. Moreover, by adjusting the sequence parameters, we can increase the difference between DDE and DODE sequences with parallel and perpendicular measurements, which is important for mediating the effect of noise when estimating model-free metrics such as fractional eccentricity.

In the third simulation we show that a DODE acquisition can be extend to a rotationally invariant framework in order to estimate model-free metrics such as FE. The values of FE measured using DODE sequences are similar to the gold standard values computed from ideal DDE sequences with the same b-value. These results encourage the optimisation of the acquisition protocol in order to maximise the signal difference and improve the robustness to noise.

In the last section we compared two different metrics of microscopic anisotropy that are based on different acquisition sequences and theoretical grounds. Using DODE sequences allows a fair comparison between the two approaches as the diffusion sequences have the same gradient waveforms. The simulation results suggest that μFA [180] is very close to the ground truth values if the microdomains exhibit Gaussian diffusion, while FE is a better measure of pore elongation in substrates which feature only restricted diffusion. However, to fully understand the similarities and differences between the two methods, more realistic substrates need to be investigated. This will help the design of future studies when deciding on how to measure microscopic anisotropy or what parameters to choose.

The work presented in this chapter investigated the sensitivity of DODE sequences with respect to microstructural features and showed that DODE acquisition can be extended to estimate fractional eccentricity. In substrates with elongated pores and small diameters, DODE sequences provide both higher sensitivity to diameter, which is beneficial for a model based approach as described in chapter 5, as well as a larger difference between parallel and perpendicular measurements, which is important for estimating FE. A desirable feature of DODE sequences is the shorter time interval between the two gradients necessary to reach the long mixing time limit, which is essential in practice when T2 decay decreases SNR. Moreover, these simulations show the importance of choosing the right acquisition parameters for a given applications. This is relevant both for model-based approaches when a tissue model is directly fitted to the signal as well as for model-free metrics of microscopic anisotropy which are based on the signal difference between parallel and perpendicular measurements.

Chapter 7

MISST (Microstructure Imaging Sequence Simulation Toolbox)

This chapter presents MISST (Microstructure Imaging Sequence Simulation Toolbox), an open source research software package I have developed during my PhD. MISST is aimed at researchers in the field of diffusion MRI that are interested in developing new acquisition sequences and understanding their sensitivity to microstructural parameters. As an open source software, MISST can be easily adapted by the user in order to investigate their own research questions, which in turns speeds up the development of new methodologies for diffusion MRI.

7.1 Motivation

Implementing a new acquisition protocol directly on a MRI scanner without having prior knowledge of the expected results is time consuming and very expensive, therefore there is increasing need for fast and reliable simulation tools. A previous diffusion simulator, Multiple Correlation Function Tool, which uses the MCF approach 2.3.4 to compute the restricted diffusion signal, allows the user only to change the parameters of already studied diffusion sequences, while software packages based on Monte Carlo simulations, such as Camino [101] are demanding in terms of memory and computational time.

The novelty of MISST is that it simulates diffusion MRI signal with any user-defined diffusion gradient waveform from a standard SDE to more advanced sequences such as ODE, DDE, q-mas, STEAM and other recently introduced sequences. The user can further combine various basic diffusion substrates to create new multi-compartment

Computational method	Pulse sequence	Restricted diffusion substrate	Performance
SGP approximation	SDE	Simple geometries: parallel planes, cylinder, sphere, ellipse, etc	Very fast to compute; Accurate only for short gradient pulses
GPD approximation	SDE, ODE, DDE	Parallel planes, Cylinder, Sphere, Triangles (eigenvectors of the diffusion propagator are needed)	Very fast to compute; Accurate within limits
Matrix Method (MM), Multiple Correlation Function (MCF)	Any	Parallel planes, Cylinder, Sphere, Triangles (eigenvectors of the diffusion propagator are needed)	Medium fast to compute; Accurate
Monte Carlo (MC)	Any	Any	Slow to compute, especially for more complex substrates; Accurate

Table 7.1: Overview of different computational methods for simulating diffusion MRI signal

tissue models. Its key purpose is to provide a deep understanding of the restricted diffusion MRI signal for a wide range of realistic, fully flexible scanner acquisition protocols, in practical computational time.

7.2 Introduction

Microstructure Imaging Sequence Simulation Toolbox (MISST) is a practical diffusion MRI simulator for development, testing, and optimisation of novel MR pulse sequences for microstructure imaging.

MISST implements the 3D extension of the matrix method described in section 2.3.4, which allows the computation of restricted diffusion signal for very flexible gradient waveforms. A schematic representation of the MISST toolbox is shown in Figure 7.1.

To put our method in perspective, the Table **??** summarizes different computational methods used to simulate diffusion MRI signal in restricted environments. The different methods are described in section 2.3.4.

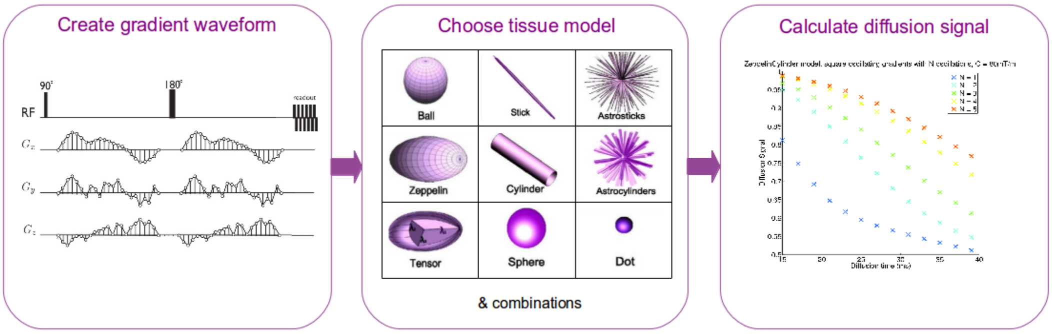

Figure 7.1: Schematic representation of MISST.

7.3 Implementation details

In order to generate the diffusion signal, we need to specify the diffusion pulse sequence and the tissue model.

7.3.1 Diffusion pulse sequence

The information about the pulse sequence is stored in a structure, commonly denoted as "protocol". There are three mandatory fields needed to generate the diffusion signal:

protocol.pulseseq	**='GEN' the name of the sequence required to generate diffusion signal from discrete generalised gradients**
protocol.G	**- discrete gradient waveforms which contain the gradient components (G_x, G_y and G_z) at each point in time from the beginning of the measurement until the readout**
protocol.tau	**- time interval between two consecutive points of the gradient waveform (sampling interval)**

Optional fields:

protocol.smalldel	**- gradient duration**
protocol.delta	**- time interval between the onset of the first and second gradients**
protocol.mirror	**=0 - the 2nd gradient is the same as the 1st gradient; =1 - the 2nd gradient is the mirror of the 1st gradient**

Specifying the fields 'smalldel' and 'delta' if the diffusion sequence has two gradient intervals reduces computation time.

The gradient waveform (protocol.G) is a M x 3K matrix, where M is the number of diffusion measurements and K is the number of gradient points in one measurement.

The gradient waveform has the following structure:

meas 1:	$G_x(1)$	$G_y(1)$	$G_z(1)$	$G_x(2)$	$G_y(2)$	$G_z(2)$	...	$G_x(K)$	$G_y(K)$	$G_z(K)$
meas 2:	$G_x(1)$	$G_y(1)$	$G_z(1)$	$G_x(2)$	$G_y(2)$	$G_z(2)$	...	$G_x(K)$	$G_y(K)$	$G_z(K)$
...	...	...	...	...	...	...	...	...	...	...
meas M:	$G_x(1)$	$G_y(1)$	$G_z(1)$	$G_x(2)$	$G_y(2)$	$G_z(2)$	...	$G_x(K)$	$G_y(K)$	$G_z(K)$

For a diffusion MRI experiment the integral of the gradient at the echo time must be 0.

Note: The gradient waveform (protocol.G) should contain the effective gradient, i.e. for a SDE sequence the second gradient is the negative of the first one. Where necessary, imaging gradients should be included for more accuracy.

Example waveforms

We provide a set of examples how to generate the discrete gradient waveforms for several diffusion sequences. We use the old naming convention in order to match this description with the names implemented in the software. The examples we offer include:

- pulsed gradient spin echo sequences (PGSE); *Note: New name used throughout this thesis is SDE*
- sinusoidal oscillating gradients (OGSE); *Note: New name used throughout this thesis is sinusoidal ODE*
- square oscillating gradients (SWOGSE); *Note: New name used throughout this thesis is square ODE*
- trapezoidal oscillating gradients (TWOGSE); *Note: New name used throughout this thesis is trapezoidal ODE*
- square oscillating gradients with multiple orientations (SWOGSE_3D)
- double pulsed field gradients (dPFG); *Note: New name used throughout this thesis is DDE*
- stimulated echo sequences (STEAM)
- helical gradients (Helical)

Note: If the sequence you are interested in is not listed here, you have to create it yourself. We show how to do this in example 2 on our web page our web page: `http://cmic.cs.ucl.ac.uk/mig//index.php?n=Tutorial.MISST`.

For these examples, the discrete gradients required to generate the diffusion signal are created as follows: `G = wave_form(protocol)`. In this case the "protocol" structure contains information about the sequence which is being discretised and has the following fields:

PGSE

standard pulsed gradient spin echo sequence

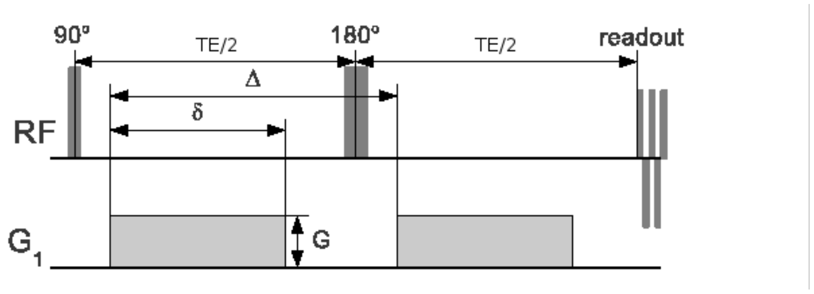

Field name	Description	Units
protocol.pulseseq	the name of the sequence	-
protocol.G	gradient amplitude	T/m
protocol.grad_dirs	direction of each gradient	unit vector
protocol.smalldel	gradient duration	s
protocol.delta	duration between the onset of the first and second pulses	s
protocol.tau	sampling interval of the gradient; recommended value 1E-4 s	s

OGSE

sinusoidal oscillating gradients

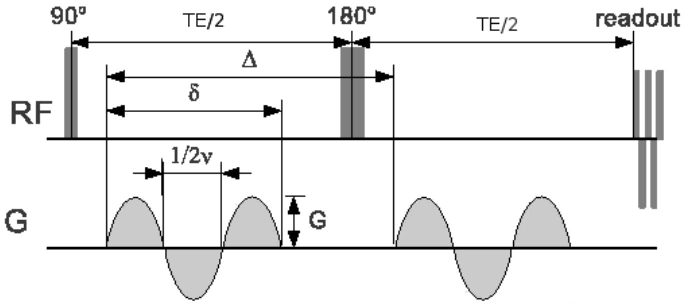

Field name	Description	Units
protocol.pulseseq	the name of the sequence	-
protocol.G	gradient amplitude	T/m
protocol.grad_dirs	direction of each gradient	unit vector
protocol.smalldel	gradient duration	s
protocol.delta	duration between the onset of the first and second pulses	s
protocol.omega	$= 2\pi\nu$ - gradient angular frequency	1/s
protocol.tau	sampling interval of the gradient; recommended value 1E-4 s	s
Optional		
protocol.phase	phase of the gradient waveform; default value 0	-
protocol.mirror	=0 - the 2nd gradient is the same as the 1st gradient; =1 - the 2nd gradient is the mirror of the 1st gradient; default value 0	-
protocol.apodisedcos	=1 - returns an apodised cosine waveform, in which the first quarter of a period is replaced by a sine wave with double frequency. This is needed for practical implementations of OGSE sequences. A detailed explanation can be found in [106]; This option works only if the angular frequency of the waveform corresponds to a integer number of lobes. If the phase is specified, it must be $\pi/2$ or $-\pi/2$	-

SWOGSE

square wave oscillating gradients

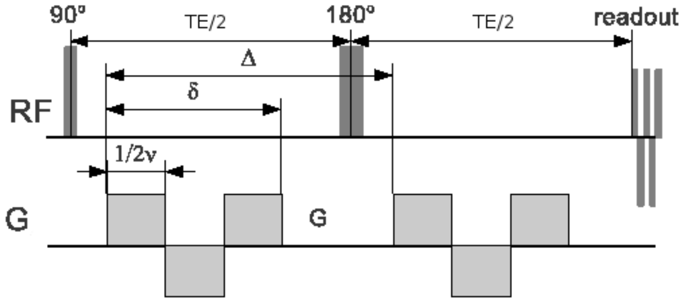

Field name	Description	Units
protocol.pulseseq	the name of the sequence	-
protocol.G	gradient amplitude	T/m
protocol.grad_dirs	direction of each gradient	unit vector
protocol.smalldel	gradient duration	s
protocol.delta	duration between the onset of the first and second pulses	s
protocol.omega	$= 2\pi\nu$ - gradient angular frequency	1/s
protocol.tau	sampling interval of the gradient; recommended value 1E-4 s	s
Optional		
protocol.phase	phase of the gradient waveform; default value 0	-
protocol.mirror	=0 - the 2nd gradient is the same as the 1st gradient; =1 - the 2nd gradient is the mirror of the 1st gradient; default value 0	-

TWOGSE

trapezoidal wave oscillating gradients

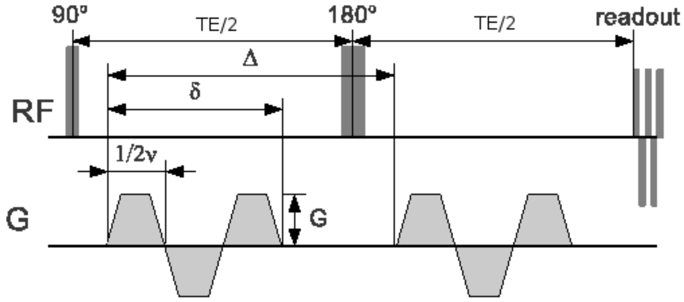

Field name	Description	Units
protocol.pulseseq	the name of the sequence	-
protocol.G	gradient amplitude	T/m
protocol.grad_dirs	direction of each gradient	unit vector
protocol.smalldel	gradient duration	s
protocol.delta	duration between the onset of the first and second pulses	s
protocol.omega	$= 2\pi\nu$ - gradient angular frequency	1/s
protocol.slew_rate	the slew rate of the gradient	T/m/s
protocol.tau	sampling interval of the gradient; recommended value 1E-4 s	s
Optional		
protocol.phase	phase of the gradient waveform; default value 0	-
protocol.mirror	=0 - the 2nd gradient is the same as the 1st gradient; =1 - the 2nd gradient is the mirror of the 1st gradient; default value 0	-
protocol.apodisedcos	=1 - returns an apodised trapezoidal waveform with a slightly increased duration $\delta + rt$ and $\Delta + rt$ ($rt = G/slew\_rate$ is the rise time of the gradient). This ensures that the area of the first lobe is half the area of a full lobe in order to have a similar diffusion spectrum to a cosine waveform. A detailed explanation can be found in [90]. This option works only if the angular frequency of the waveform corresponds to a integer number of lobes. If the phase is specified, it must be $\pi/2$ or $-\pi/2$	-

SWOGSE_3D square wave oscillating gradients with different components in different directions		
Field name	Description	Units
protocol.pulseseq	the name of the sequence	-
protocol.smalldel	gradient duration	s
protocol.delta	duration between the onset of the first and second pulses	s
protocol.Gx	gradient amplitude in x direction	T/m
protocol.Gy	gradient amplitude in y direction	T/m
protocol.Gz	gradient amplitude in z direction	T/m
protocol.omegax	angular frequency of the gradient in x direction	1/s
protocol.omegay	angular frequency of the gradient in y direction	1/s
protocol.omegaz	angular frequency of the gradient in z direction	1/s
protocol.tau	sampling interval of the gradient; recommended value 1E-4 s	s
Optional		
protocol.phix	phase of the gradient waveform in x direction	-
protocol.phiy	phase of the gradient waveform in y direction	-
protocol.phiz	phase of the gradient waveform in z direction	-
Note: If the gradient is not desired in a certain direction, then the respective gradient strength, frequency and phase should be set to 0;		

dPFG

double pulsed field gradient

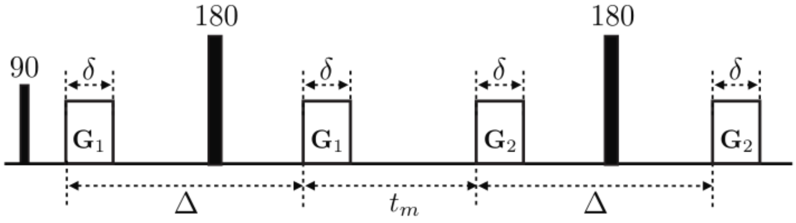

Field name	Description	Units
protocol.pulseseq	the name of the sequence	-
protocol.G	gradient amplitude (same for both gradient pairs)	T/m
protocol.smalldel	gradient duration (same for both gradient pairs)	s
protocol.delta	duration between the onset of the first and second pulses (same for both gradient pairs)	s
protocol.tm	mixing time	s
protocol.tau	sampling interval of the gradient; recommended value 1E-4 s	s
protocol.theta	Angle between the first gradient direction and z axis.	-
protocol.phi	Azimuthal angle of the first gradient direction; $G_z = G \times \cos(theta); G_x = G \times \sin(theta) \times cos(phi); G_y = G \times \sin(theta) \times \sin(phi);$	-
protocol.theta1	Angle between the second gradient direction and z axis.	-
protocol.phi1	Azimuthal angle of the second gradient direction; $G_z = G \times \cos(theta1); G_x = G \times \sin(theta1) \times cos(phi1); G_y = G \times \sin(theta1) \times \sin(phi1);$	-

STEAM

pulsed gradient with stimulated echo sequence

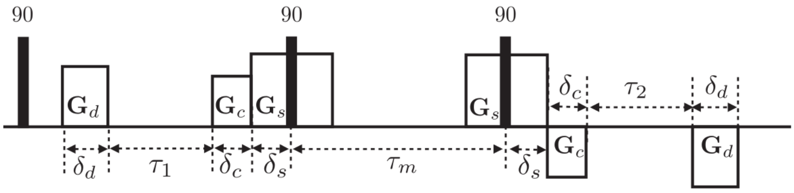

Field name	Description	Units
protocol.pulseseq	the name of the sequence	-
protocol.G	diffusion gradient amplitude	T/m
protocol.grad_dirs	direction of diffusion gradients	unit vector
protocol.Gc	crusher gradient amplitude - fixed direction along z	T/m
protocol.Gs	slice select gradient amplitude - fixed direction along z	T/m
protocol.smalldel	diffusion gradient duration	s
protocol.sdelc	crusher gradient duration	s
protocol.sdels	slice select gradient duration	s
protocol.tau1	time interval between the first diffusion gradient and crusher gradient	s
protocol.tau2	time interval between the second crusher gradient and the second diffusion gradient	s
protocol.tm	mixing time	s
protocol.tau	sampling interval of the gradient; recommended value 1E-4 s	s

Helical

helical gradient waveforms

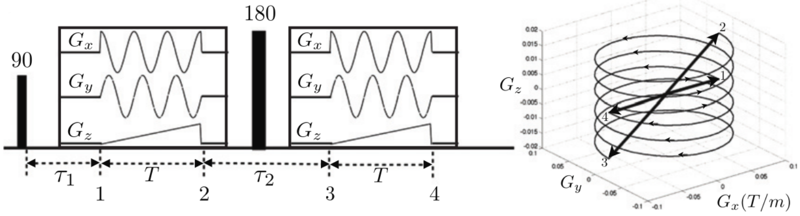

Field name	Description	Units
protocol.pulseseq	the name of the sequence	-
protocol.G	gradient amplitude	T/m
protocol.smalldel	gradient duration	s
protocol.delta	duration between the onset of the first and second pulses	s
protocol.omega	gradient angular frequency: $G_x = G \times \cos(omega \times t), G_y = G \times \sin(omega \times t)$	1/s
protocol.slopez	slope of Gz: $G_z = G \times slopez \times t$	1/s
protocol.tau	sampling interval of the gradient; recommended value 1E-4 s	s

Limitations

The signal is accurate up to the level of discretization. If the imaging parameters are on the order of ms, then a sampling interval tau = 0.1 ms should be enough. However if you want to see the effect on a sorter time scale, then tau should be decreased.

7.3.2 Tissue models

For the diffusion substrates, we follow the naming scheme presented in [150]. The following substrates are available in MISST:

Basic compartments with Gaussian diffusion:

- Ball (isotropic free diffusion)
- Zeppelin (anisotropic, cylindrically symmetric diffusion tensor)
- Tensor (full diffusion tensor)
- Stick (Unidirectional diffusion)
- AstroSticks (isotropically oriented sticks)

Basic compartments with restricted diffusion:

- Cylinder (diffusion inside a cylinder)
- AstroCylinders (isotropically oriented cylinders)
- Sphere (diffusion inside a sphere)
- Dot (no diffusion at all)

Multi-compartment models:

- ZeppelinCylinder
- TortZeppelinCylinder (same as ZeppelinCylinder, but with tortuosity constraint on volume fraction)
- TortZeppelinCylinderBall

Other substrates can be easily implemented by combining different compartments. All the information related to the diffusion substrate is stored in a structure called "model". For the purpose of signal generation, "model" has only two fields:

model.name - the name of the model

model.params - the values of the model parameters in S.I. (m, s, etc.); the order of the parameters is the same as in the next table.

The next table summarizes the parameters of different models:

Model name	Parameters	Units
Ball	d - free diffusivity	m/s^2
Zeppelin	d$_{\|\|}$ - parallel diffusivity d$_h$ - hindered diffusivity θ - angle from z axis φ - azimuthal angle from x axis	m/s^2 m/s^2 rad rad
Tensor	d$_1$ - diffusivity along main direction d$_2$ - diffusivity along second direction d$_3$ - diffusivity along third direction θ - angle from z axis φ - azimuthal angle from x axis ψ - angle giving the third direction of the tensor	m/s^2 m/s^2 m/s^2 rad rad rad
Stick	d$_{\|\|}$ - parallel diffusivity θ - angle from z axis φ - azimuthal angle from x axis	m/s^2 rad rad
AstroSticks	d$_{\|\|}$ - parallel diffusivity along each stick	m/s^2
Cylinder	d$_{\|\|}$ - diffusivity R - cylinder radius θ - angle from z axis φ - azimuthal angle from x axis	m/s^2 m rad rad
AstroCylinders	d$_{\|\|}$ - diffusivity R - cylinder radius	m/s^2 m
Sphere	d$_{\|\|}$ - diffusivity R - sphere radius	m/s^2 m
Dot	No parameters	-
ZeppelinCylinder	f - volume fraction of intracellular compartment d$_{\|\|}$ - parallel diffusivity d$_h$ - hindered diffusivity R - cylinder radius θ - angle from z axis φ - azimuthal angle from x axis	- m/s^2 m/s^2 m rad rad
TortZeppelinCylinder	f - volume fraction of intracellular compartment d$_{\|\|}$ - parallel diffusivity R - cylinder radius θ - angle from z axis φ - azimuthal angle from x axis	- m/s^2 m rad rad
TortZeppelinCylinderBall	f$_i$ - volume fraction of intracellular compartment from the anisotropic part (1-fiso) d$_{\|\|}$ - parallel diffusivity R - cylinder radius f$_{iso}$ - volume fraction of isotropic space (eg CSF) d$_{iso}$ - parallel diffusivity θ - angle from z axis φ - azimuthal angle from x axis	- m/s^2 m - m/s^2 rad rad

7.3.3 Running the code

- A step-by-step guide can be found on our web page: `http://cmic.cs.ucl.ac.uk/mig//index.php?n=Tutorial.MISST`
- Run the script files corresponding to the examples shown on our web page. They are located in the folder MISST/example. RunMISST.m includes Example 1 (square waveforms) and Example 2 (random waveforms) and PublishedExamples.m includes the waveforms used in [96].

7.4 Conclusions

This chapter introduces MISST, a software package that simulates the diffusion MRI signal from a variety of pulses sequences and diffusion substrates. Being open source, the user can easily tailor the software to explore their own research question, allowing faster development of this research field.

MISST implements the 3D extension of the matrix method described in section 2.3.4, which allows the computation of restricted diffusion signal for flexible, user defined, gradient waveforms. We provide details of the implementation, as well as examples of tissue models and gradient waveforms. Due to its modular construction, the user can easily combine various diffusion compartments to create models that are representative of various tissue types, such as grey matter, white matter or tumours.

One limitation of the matrix method is that it can be used to calculate the restricted diffusion signal only for basic geometries with well known solution of the diffusion equation such as parallel planes, cylinders, spheres, spherical shells as well as triangles [206]. Another limitation is the fact that diffusion in extracellular needs to be computed separately, thus the accuracy of the signal depends on the complexity of the chosen model. Although boundary relaxation effects can be accounted for in the matrix mathod formalism, the exchange between intra and extracellular spaces cannot be readily incorporated.

Nevertheless, MISST software is a useful tool for analysing restricted diffusion signal as well as the sensitivity of various sequences to substrate parameters and has been used to produce the results in chapter 4.1 and 6.

Chapter 8

Conclusions and future work

This chapter discusses the contributions of this thesis from a general perspective and details possible future extensions based on the current work.

8.1 Summary

This thesis presents my work on developing and analysing novel diffusion MRI sequences and modelling frameworks to improve the accuracy of pore size and eccentricity estimation. The motivation of this research is developing biomedical imaging techniques which can be applied to both brain and cancer imaging.

The first part of this work is focused on applications of microstructure imaging for white matter, and specifically for estimating axon diameter. Abnormal development and degeneration of white matter or cortex regions affects the properties of axons in different tracts. For instance, there are indications that variations in axon diameter are present in autism spectrum disorders [225, 226], amyotrophic lateral sclerosis [227] as well as during the aging process [228]. Moreover, the axon thickness affects nerve function as it determines the conduction velocity [229]. Thus, measuring axon diameter can provide potential biomarkers for different diseases affecting white matter tracts, as well as for better understanding the link between brain structure and function.

Most of current techniques for mapping axon diameter, such as AxCaliber [5] or ActiveAx [9], use a collection of standard single diffusion encoding sequences, which do not provide the optimal sensitivity to axon diameter. There are claims in the literature, e.g. [230], that replacing the pulsed gradients in the SDE sequence with oscillating waveforms which measure diffusion at shorter time scales can improve the estimating of pore size, however, the ability of the two sequences to estimate axon diameter has not been directly compared.

In chapter 4.1 we compared in simulation the sensitivity of SDE and ODE sequences with respect to pore size, in a range applicable for axon diameter mapping. The results show that in the ideal case of parallel fibres and gradient perpendicular to the fibre direction SDE sequences are the most sensitive, while in the practical situation of unknown fibre orientation and/or dispersion, low frequency ODE sequences improve sensitivity.

This work also gave us a clearer perspective on the previous results of numerically optimizing the diffusion acquisition in [93, 94, 231]. When optimizing a gradient perpendicular to the fibre direction for estimating both axon diameter and intrinsic diffusivity [93], there are measurements with high frequency oscillations. These measurements have a short diffusion time and are important for estimating the intrinsic diffusivity, while the SDE measurements provide the highest sensitivity to pore diameter. When the measurement protocol has gradients with multiple directions (e.g. [231]), optimal sequences include low frequency oscillations which provide improved sensitivity to pore diameter. In this case, intrinsic diffusivity can be estimated from the gradient components parallel to the fibre. This brief analysis is based on a simple model of white matter which consists of parallel infinite cylinders. In practice the parallel diffusivity measured as the largest eigenvalues of the diffusion tensor depends on diffusion time [175], which can be explained by a variety of factors such as dispersion, neurite beading, restricted diffusion in glial cells, etc.

Chapter 3 presents my theoretical work on oscillating diffusion encoding sequences. I provide expressions of the free and restricted diffusion MRI signal for square, trapezoidal and sinusoidal oscillating gradients. This enables the adaptation of various microstructure imaging techniques described in section 2.4 for an acquisition consisting of ODE sequences. Together with my colleagues we experimentally validated the ODE ActiveAx framework in a microcapillary array phantom, which is presented in chapter 4.2. The results show that ODE sequences can be implemented on a clinical scanner and can be used for estimating pore size. For a gradient strength of 62 mT/m, pore diameters of 10 and 20 μm were accurately estimated, while smaller pore diameters of 5 μm could not be measured and were clearly below the resolution limit discussed in 4.1.5. Moreover, the experimental results are in line with the theoretical predictions of sensitivity, showing that in the given range of measurements, low frequency ODE sequences provide the most accurate estimates of pore size.

The second part of this thesis is focused on diffusion acquisition and modelling techniques for estimating pore size and eccentricity, with potential applications for both cancer and brain imaging. Cellular anisotropy is an important microstructural feature, that has the potential to differentiate various tumour types [177] as well as cytoarchitectures in the grey matter. A widely used sequence in the literature for estimating microscopic anisotropy is double diffusion encoding, however, most studies do not recover intrinsic estimates of pore size and eccentricity.

Chapter 5 illustrates a model-based framework for estimating pore size and eccentricity. We investigate complex substrates featuring elongated pores with a distribution of size in both macroscopically isotropic and anisotropic ensembles. The results show that it is necessary to explicitly account in the model for the size distribution in order to recover accurate estimates of mean radius and eccentricity. This is also the case when the fitted model and the underlying substrate have different pore size distributions. Moreover, the results indicate that a protocol which consists of DDE sequences with both parallel and perpendicular measurements provide the most accurate results. This finding is consistent with previous theories that sequences which have multiple gradient orientation within one measurement provide additional information on pore eccentricity compared to SDE sequences [111]. Nevertheless, in the situation analysed in this work we choose a specific model to fit the data, thus we introduce constrains on the possible substrate configurations, and protocols which consist of SDE sequences also show some sensitivity towards the model parameters.

Chapter 6 introduces and analyses DODE sequences, which combine the benefits of oscillating gradients and varying gradient orientation. We investigate the dependence of the restricted diffusion MRI signal as a function of sequence parameters, analyse the sequence sensitivity to microstructural parameters and extend the acquisition to a rotationally invariant framework. The results indicate that DODE sequences yield higher sensitivity to pore diameter in elongated pores, while DDE sequences are more sensitive to pore length. Moreover, by adapting the sequence parameters to the substrates of interest, we can improve sensitivity to various microstructural features compared to the standard way of acquiring DDE measurements (short gradient pulse, long diffusion and mixing time). Furthermore, we use DODE sequences to compare two model-free metrics of microscopic anisotropy. Simulations indicate that μFA better characterizes microdomains featuring Gaussian diffusion, while FE is more accurate for restricted diffusion, nevertheless, a more theoretical approach would be necessary for a thorough comparison.

Chapter 7 presents MISST, the research software I have developed for simulating restricted diffusion MRI signal in various substrates. MISST is open source and allows the user to test novel diffusion sequences in order to better understand the mechanisms of restricted diffusion. MISST has been successfully used to produce the results presented in chapters 4.1 and 6.

This work provides a thorough understanding of the restricted diffusion MR signal for various diffusion acquisitions, and is important for developing novel imaging techniques that will make the estimating of tissue microstructure more accurate for both brain and cancer imaging.

8.2 Discussion

The work presented in this thesis provides a theoretical framework for improving the accuracy of microstructure imaging technique. ODE acquisition can improve the estimation of pore size in elongated pores which are dispersed and/or have unknown orientation, while DDE and DODE sequences provide necessary information for estimating more complex features such as size distribution and eccentricity. Such information is valuable for studies that try to characterize tissue structure both for brain imaging as well as cancer imaging.

For brain imaging such techniques can be adapted to increase specificity towards cellular structure, which can be used to distinguish between cortical layers in grey matter or to follow tracts with similar morphology in white matter. This can provide a novel insight into the link between tissue structure and function and improve tractography results. Moreover, estimates of tissue features, such as axon diameter, intracellular volume fraction, orientation dispersion, etc, can constitute valuable biomarkers for diagnosing and monitoring various pathologies as discussed in section 2.1.1.

For cancer imaging, advanced acquisition sequences and more complex models can be incorporated into the existing VERDICT framework. This will provide a more detailed characterization of tissue features such as cell elongation and size which vary between different tumour types [177] and grades. For example, in prostate cancer the connective tissue (stroma) surrounding the glands consists of elongated muscle fibres which are locally very anisotropic. Moreover, the amount and organization of stroma varies significantly between different cancer grades. Thus, we believe that sensitizing the diffusion measurements to microscopic anisotropy will constitute a valuable biomarker for prostate cancer grading.

Modelling assumptions

Impermeable membranes: The tissue models analysed in this work assume restricted diffusion inside pores with non-permeable membranes, as modelling both effects is extremely challenging. In healthy white matter the exchange between intra- and extra-axonal space is slow and the effects of permeability become important for diffusion times on the order of seconds[171]. Thus, for commonly used diffusion times which are in the range of tens of milliseconds, assuming tissue models with impermeable membranes is reasonable. For cancer cells, the exchange time is shorter, on the order of hundres of milliseconds, and can depend on the cell line and/or tumour grade [171, 232]. Nevertheless when the diffusion time is at least one order of magnitude smaller than the exchange time, the effects of permeability become negligible [172]. This is the case for oscillating gradients as well as for SDE sequences with a diffusion time up to 20-30ms [172, 232]. For longer diffusion times, assuming impermeable membranes can lead to biased estimates, i.e. increased pore size and/or decreased volume fraction to compensate for the effects of permeability. When exchange rate is the parameter of interest, using DDE sequences, e.g. in a filter exchange (FEXI) experiment [114, 170, 232], can provide additional contrast to SDE measurements.

Hindered diffusion in the extracellular space: The two-compartment models presented here assume hindered diffusion in the extracellular space. However, recent work has shown that a time dependant diffusivity can be more appropriate for characterizing extracellular space when measurements are acquired at different diffusion times[230, 197, 10]. For in-vivo measurements of human white matter acquired with SDE sequences, a more pronounced time dependence of the extracellular diffusivity is visible for diffusion times larger than 100ms [10]. For ODE sequences, Burcaw et al showed that in ex-vivo brain data $D(\omega)$ exhibits a linear dependence at low ω which is characteristic for disordered diffusion in the extracellular space rather than a parabolic dependence (ω^2) which is characteristic for the intracellular diffusion. Therefore, accounting for time dependent diffusivity in the extracellular space can improve the analysis for both ODE and SDE measurements.

Practical implications

:

In this work we analyze various diffusion sequences, such as SDE, ODE, DDE and DODE sequences. All these sequences can be easily implemented on pre-clinical scanners, which usually provide high gradient amplitudes and slew-rates. However, on clinical scanners, the gradient amplitude and slew-rate are much lower, limiting the frequencies that can be achieved in ODE and DODE sequences. Although the new Connectome scanner provides much higher values compared to standard clinical scanner, i.e. 300mT/m gradient strength and 200T/m/s slew-rate, peripheral nerve stimulation (PNS) prevents the application of waveforms combining both high strength and high slew rate [**?**]. Nevertheless, as seen in Chapters 4 and 6, the ODE and DODE sequences which provide the highest sensitivity to pore diameter have low frequency oscillations, thus they can be achieved without exceeding the PNS threshold.

Another important factor to consider in practice is the total duration of the scan. The protocols presented in chapter 5 have a large number of measurements which provide sensitivity over the wide range of substrates analyzed. For practical implementation, the total scan time can be significantly reduced by choosing measurements which are the most sensitive to the application of interest. Moreover, a balance between the timings of the diffusion gradients and $T2$ decay needs to be considered in order to have sufficient SNR. For sequences with very long diffusion time, the spin echo preparation can be replaced with a stimulated echo one in order to mitigate the effects of $T2$ decay. As some of these sequences are gradient-intensive, duty cycle constraints can lead to an increase in repetition time and/or a decrease in the number of slices, compared to standard acquisitions.

8.3 Future work

Further to the contributions presented in this thesis, there are improvements and modifications that will bring this work closer to the goal detailed in chapter 1, namely to accurately estimate tissue microstructure from diffusion MRI data. This section looks at some of these directions:

Modelling

White matter model: One limitation of the white matter model used in chapters 3 and 4 is the assumption of hindered diffusion in the extracellular space. Accounting for time-dependent diffusivity is important when deriving the signal model, investigating the sensitivity to axon diameter or using the tissue model to fit experimental data. A future project, which aims to compare optimized SDE and ODE sequences for estimating axon diameter in the monkey brain and rat sciatic nerve, will include a time a dependent diffusivity in the extracellular space. This extension of the white matter model is also supported by preliminary results from my colleague Lebina Kakkar which demonstrate that accounting for this dependence reduces the fitting error and variability of the parameter estimates.

Cancer model: One limitation of the model-based approach for estimating microscopic anisotropy in chapter 5 is the fact that the tissue models include only intracellular space. For applying this framework in practice, diffusion in the extracellular space needs to be considered. Preliminary results presented in section 5.8 show that microstructural parameters can be accurately estimated in the presence of extra-cuboidal diffusion, and additional compartments need to be incorporated in future work. Moreover, for cancer imaging, the model could incorporate an additional compartment accounting for the effect of vasculature [2].

Model fitting

Current implementations of the white matter model in chapters 3 and 4, as well as the microscopic anisotropy model in chapters 5 and 6 use iterative non-linear fitting for estimating model parameters. The computational time for fitting a model of parallel cylinders with one radius is on the order of seconds, while fitting the more complex IGFC model which has a distribution of pore sizes and orientations takes a couple of hours. The long computational time arises from the fact that at each iteration the signal is summed over different orientations and pore sizes. In case of SDE sequences, the integration over orientation can be calculated analytically for both isotropic and Watson distribution, however, this is not the case for sequences with varying gradient orientation such as DDE or DODE. The long computational time of the current fitting routine is an obvious limitation for analysing the data using more complex models. Recent work developed the AMICO (Accelerated Microstructure Imaging via Convex Optimization) framework for fitting diffusion MRI data, which drastically reduces the computational time. Future work aims to implement the AMICO framework for all tissue models presented in this thesis.

Diffusion sequences

Another limitation of the simulations in chapters 5 and 6, which compare the sensitivity of various sequences, is the choice of sequence parameters itself. The simulations for ODE acquisition in chapter 4 cover the entire range of sequence parameters within the physical constraints of gradient strength and acquisition time, however, DDE and DODE sequences have more degrees of freedom and we cannot vary all of them at the same time. Thus we had to make a set of assumptions: in section 5.5 we compare the sensitivity of the four different protocols with SDE and DDE sequences enforcing the same maximum b-value, while in section 6.5 we choose sequence parameters which enforce the same total duration for DDE and DODE sequences. Future work can make a better comparison by studying optimised SDE, DDE and DODE protocols that fully explore the parameter space of each sequence within the physical constraints for gradient strength and acquisition time.

Validation

An important step in the development of any imaging technique, which was not performed for the studies in chapters 5 and 6, is experimental validation. One option for validating the estimation of pore size and shape as well as the implementation of DODE sequences is to use microstructural phantoms, such as biomimetic materials [233, 234], biological phantoms (yeast cells [115], asparagus [180, **?**, **?**]), liquid crystals [180] or glass microcapillaries [179]. Another option for validating this technique is to image brain or cancer tissue in a pre-clinical set-up and to compare the estimated parameters with histology. Imaging real tissue will capture the entire microstructural complexity which cannot be achieved in phantoms.

Applications

Developing imaging techniques which provide high specificity to microstructural features has many potential applications, both in basic science for a better understanding of brain structure as well as for diagnosing and monitoring various pathologies. Here I describe some these potential applications.

Brain imaging: One application of ODE sequences for brain imaging is axon diameter mapping, as these sequences improve the sensitivity in the realistic situations of fibres with unknown direction and/or dispersed orientation. Another possibility is to use the advanced diffusion acquisition and modelling framework for characterizing different cortical layers in the brain. Although the resolution might not be enough to do this on standard clinical scanners, it can be used in pre-clinical set-ups to gain more information about brain structure and its connectivity in vivo.

Cancer imaging: The proposed methodology could be used for cancer imaging to distinguish between tumour types and grades. For instance, different types of brain tumours have distinct histological features: meningiomas, which are usually benign tumours, exhibit a fascicular pattern of growth with elongated tumour cells, while glioblastomas, which are highly malignant, are usually hypercellular with mostly rounded cells of various sizes and scattered necrotic areas [177]. In the case of brain tumours, both cellularity and microscopic anisotropy are relevant indicators of tumour grade and treatment outcome.

Another application of this framework is for prostate cancer grading. As illustrated in section 2.1.3, the tissue structure changes significantly as the cancer becomes more aggressive, which is captured by the Gleason grading system. As the grade increases, the tissue becomes less structured, epithelial cells proliferate faster and the amount of lumen space and connective tissue decreases. Connective tissue consists of elongated muscle fibres and recent ultra-high resolution prostate images show large anisotropy at the sub-voxel scale [**?**]. Therefore, using the methodology proposed in this thesis to estimate cell size and eccentricity might provide the right tools to achieve the goal of non-invasive prostate cancer grading.

This section details future work related to biomedical imaging, nevertheless, such techniques can be used for a wider range of applications to estimate microstructure in porous media.

Appendices

Appendix A

Diffusion MRI - explicit signal models

This section aims to complement section 2.3 and provides explicit equation of the diffusion signal for various sequences that have been previously analysed in the literature and are of interest for this work.

A.1 GPD approximations presented in the literature

Geometric factors λ_n and B_n

The restricted diffusion signal computed from the GPD approximation in equation 2.40 depends on the geometry of the confining domain which is reflected through the geometric factors λ_n and B_n.

Cylindrical geometry

For diffusion inside a cylinder with radius R and the gradient perpendicular to the cylinder axis, the geometric factors are [78]

$$B_n = \frac{2(R/\mu_n)^2}{\mu_n^2 - 1} \text{ and } \lambda_n = \left(\frac{\mu_n}{R}\right)^2 \tag{A.1}$$

where μ_n is the n^{th} root of the equation $J_1' = 0$ and J_1 is a Bessel function of first kind.

Spherical geometry

For diffusion inside a sphere with radius R [78]

$$B_n = \frac{2(R/\mu_n)^2}{\mu_n^2 - 2} \text{ and } \lambda_n = \left(\frac{\mu_n}{R}\right)^2 \tag{A.2}$$

where μ_n is the n^{th} root of the equation $\mu J_{3/2}'(\mu) - \frac{1}{2}J_{3/2}(\mu) = 0$.

Planar geometry

For diffusion restricted in between parallel planes [78] separated by a distance d

$$B_n = \frac{8d^2}{(2n-1)^4\pi^4} \text{ and } \lambda_n = \frac{\pi^2(2n-1)^2}{d^2}. \tag{A.3}$$

GPD approximations for common gradient waveforms

This section provides the expressions of Γ_n for the most common waveforms that have been published so far in the literature.

Each term of the GPD approximation given in equation 2.41 can be factored into a purely geometric part, B_n/λ_n^2, and a part that also includes the gradient waveform Γ_n. If we denote the exponent in equation 2.41 as $\beta(2\tau)$, the we can rewrite it as:

$$\beta(2\tau) = \frac{2\gamma^2}{D^2}\sum_{n=0}^{\infty}\frac{B_n}{\lambda_n^2}\Gamma_n \tag{A.4}$$

For the SDE sequence [78]

$$\Gamma_n = G^2\{\lambda_n D\delta - 1 + e^{-\lambda_n D\delta} + e^{-\lambda_n D\Delta}(1-\cosh(\lambda_n D\delta))\}, \tag{A.5}$$

for sine ODE with integer number of periods [87]

$$\Gamma_n = \frac{G^2\omega^2/(\lambda_n D)^2}{(1+\omega^2/(\lambda_n D)^2)^2}\left\{\frac{\lambda_n D\delta(\lambda_n^2 D^2+\omega^2)}{2\omega^2} + 1 - e^{-\lambda_n D\delta} - \right.$$
$$\left. e^{-\lambda_n D\Delta}(1-\cosh(\lambda_n D\delta))\right\}, \tag{A.6}$$

and for cosine ODE

$$\Gamma_n = \frac{G^2}{(1+\omega^2/(\lambda_n D)^2)^2}\left\{\frac{\lambda_n^2 D^2+\omega^2}{\lambda_n D}\left[\frac{\delta}{2}+\frac{\sin(2\omega\delta)}{4\omega}\right] - 1 + e^{-\lambda_n D\delta} + \right.$$
$$\left. e^{-\lambda_n D\Delta}(1-\cosh(\lambda_n D\delta))\right\}. \tag{A.7}$$

The expressions for square and trapezoidal waveform are presented separately as they are part of my contribution.

A.2 b-values for oscillating gradient waveforms

This section presents the b-values for sinusoidal oscillating gradients that have been previously used in temporal diffusion spectroscopy studies.

For sine ODE with integer number of periods [106]

$$b = \frac{3G^2\gamma^2\delta}{(2\pi\nu)^2}, \tag{A.8}$$

for cosine ODE with integer number of periods [106]

$$b = \frac{G^2\gamma^2\delta}{(2\pi\nu)^2}. \tag{A.9}$$

and for apodized cosine with integer number of periods [106]

$$b = \frac{G^2\gamma^2\delta}{(2\pi\nu)^2}\left(1 - \frac{1}{8\nu\delta}\right). \tag{A.10}$$

A.3 GPD approximations for oscillating gradient waveforms with arbitrary phase and frequency

This appendix provides the explicit formulae of GPD approximations I have derived for square, sine and cosine waveforms with arbitrary frequency (i.e. non-integer number of periods) and phase and is an addition to section 3.2.2.

The Γ_n factors for these waveforms are

$$\begin{aligned}\Gamma_n =& \frac{G^2}{2}\Bigg\{2\tilde{\delta} - 4 + e^{-\tilde{\theta}}\left(2 - e^{-\tilde{\Delta}}E_\theta^2\right) - (-1)^N E_0 E_\theta A\left(-1 + 2e^{\tilde{\Delta}} - e^{\tilde{\delta}+\tilde{N}}\right) \\ & - E_0 A^2 + 2e^{-\tilde{\delta}+\tilde{N}+\tilde{\theta}} + 2N(e^{-\lambda_n D/2\nu} - 1)+ \\ & \frac{E_{1-}}{E_{1+}} E_0 E_\theta e^{\tilde{\delta}}\Big[(-1)^N\left(-1 + 2e^{\tilde{\Delta}} - e^{2\tilde{N}+\tilde{\theta}}\right) + e^{\tilde{N}}\left(1 - 2e^{\tilde{\Delta}} + e^{\tilde{\theta}}\right)\Big]+ \\ & \frac{E_{1-}}{E_{1+}} E_0 (-1)^N A\Big[e^{\tilde{\delta}}\left((-1)^N - e^{\tilde{N}}\right) + e^{\tilde{\theta}}(2e^{\tilde{\Delta}} - 1)\left(1 - (-1)^N e^{\tilde{N}}\right)\Big]+ \\ & \frac{E_{1-}^2}{E_{1+}^2}\Big[(-1)^N e^{-\tilde{N}}(-2 + e^{2\tilde{N}-\tilde{\Delta}} + e^{\tilde{\Delta}}) - 2e^{-\tilde{\Delta}} - 2N(e^{-\lambda_n D/2\nu} + 1) + 2\Big]\Bigg\},\end{aligned} \tag{A.11}$$

where $\theta = \dfrac{\phi}{2\pi\nu}$, $\quad N = \lfloor 2(\delta - \theta)\nu \rfloor, \quad \tilde{\delta} = D\lambda_n\delta, \quad \tilde{\Delta} = D\lambda_n\Delta, \quad \tilde{N} = D\lambda_n N/(2\nu)$

$$\begin{aligned}
&\tilde{\theta} = D\lambda_n\theta, \quad E_0 = e^{-(\tilde{\Delta}+\tilde{\delta}+\tilde{\theta}+\tilde{N})}, \quad E_{1+} = e^{D\lambda_n/(2\nu)} + 1, \quad E_{1-} = e^{D\lambda_n/(2\nu)} - 1 \\
&E_\theta = e^{D\lambda_n\theta} - 1, \quad A = e^{\tilde{\delta}} - e^{\tilde{N}+\tilde{\theta}}.
\end{aligned}$$

for square wave,

$$\begin{aligned}
\Gamma_n =& \frac{G^2 e^{-D\lambda_n\Delta}}{2(1+\Omega^2)^2}\Big(A_- - \Omega B_-\Big) \cdot \Big(A_+ + \Omega B_+\Big) + \frac{G^2}{4(1+\Omega^2)^2}\Big(2(\Omega^2-1) + \\
& (1+\Omega^2)\big(2D\lambda_n\delta + C_1 - \frac{1}{\Omega}C_2\big) - 2e^{-D\lambda_n\delta}\big((\Omega^2-1)\cos\delta\omega + \\
& (\Omega^2+1)\cos(2\phi - \delta\omega) + 2\Omega\sin\delta\omega\big)\Big) \qquad \text{(A.12)}
\end{aligned}$$

$$\begin{aligned}
\text{where } \Omega =& \omega/(D\lambda_n), \quad A_- = \sin\phi + e^{-D\lambda_n\delta}\sin(\delta\omega - \phi), \quad A_+ = \sin\phi + e^{D\lambda_n\delta}\sin(\delta\omega - \phi) \\
B_- =& \cos\phi - e^{-D\lambda_n\delta}\cos(\delta\omega - \phi), \quad B_+ = \cos\phi - e^{D\lambda_n\delta}\cos(\delta\omega - \phi) \\
C_1 =& \cos 2\phi + \cos(2\delta\omega - 2\phi), \quad C_2 = \sin 2\phi - \sin(2\delta\omega - 2\phi)
\end{aligned}$$

for sine wave, and

$$\begin{aligned}
\Gamma_n =& \frac{G^2 e^{-D\lambda_n\Delta}}{2(1+\Omega^2)^2}\Big(\Omega A_- + B_-\Big) \cdot \Big(-\Omega A_+ + B_+\Big) + \frac{G^2}{4(1+\Omega^2)^2}\Big(2(\Omega^2-1) + \\
& (1+\Omega^2)\big(2D\lambda_n\delta - C_1 + \frac{1}{\Omega}C_2\big) - 2e^{-D\lambda_n\delta}\big((\Omega^2-1)\cos\delta\omega - \\
& (\Omega^2+1)\cos(2\phi - \delta\omega) + 2\Omega\sin\delta\omega\big)\Big) \qquad \text{(A.13)}
\end{aligned}$$

for cosine wave.

The Γ_n function for square, sine and cosine waveforms with arbitrary frequency and $\phi = 0$ are

$$\begin{aligned}\Gamma_n =&\frac{G^2}{2}\Bigg\{2\tilde{\delta} - 2 - E_0A^2 + 2e^{-\tilde{\delta}+\tilde{N}} + 2N(e^{-\lambda_n D/2\nu} - 1)+\\ &\frac{E_{1-}}{E_{1+}}E_0(-1)^N A\Big[e^{\tilde{\delta}}\left((-1)^N - e^{\tilde{N}}\right) + (2e^{\tilde{\Delta}} - 1)\left(1 - (-1)^N e^{\tilde{N}}\right)\Big]+\\ &\frac{E_{1-}^2}{E_{1+}^2}\Big[(-1)^N e^{-\tilde{N}}(-2 + e^{2\tilde{N}-\tilde{\Delta}} + e^{\tilde{\Delta}}) - 2e^{-\tilde{\Delta}} - 2N(e^{-\lambda_n D/2\nu} + 1) + 2\Big]\Bigg\},\end{aligned} \tag{A.14}$$

where $N = \lfloor 2\delta\nu \rfloor, \quad \tilde{\delta} = D\lambda_n\delta, \quad \tilde{\Delta} = D\lambda_n\Delta, \quad \tilde{N} = D\lambda_n N/(2\nu), E_0 = e^{-(\tilde{\Delta}+\tilde{\delta}+\tilde{N})}$,

$$E_{1+} = e^{D\lambda_n/(2\nu)} + 1, \quad E_{1-} = e^{D\lambda_n/(2\nu)} - 1, \quad A = e^{\tilde{\delta}} - e^{\tilde{N}}$$

for square wave,

$$\begin{aligned}\Gamma_n =&\frac{G^2e^{-D\lambda_n\Delta}}{2(1+\Omega^2)^2}\Big(- \Omega + e^{-D\lambda_n\delta}(\sin\delta\omega + \Omega\cos\delta\omega)\Big)\cdot\Big(\Omega + e^{D\lambda_n\delta}(\sin\delta\omega -\\ &\Omega\cos\delta\omega)\Big) + \frac{G^2}{4(1+\Omega^2)^2}\Big(2(\Omega^2 - 1) + (1+\Omega^2)\big(2D\lambda_n\delta + 1 + \cos 2\delta\omega +\\ &\frac{1}{\Omega}\sin 2\delta\omega\big) - 2e^{-D\lambda_n\delta}\big(- 2\cos\delta\omega + 2\Omega\sin\delta\omega\big)\Big)\end{aligned} \tag{A.15}$$

where $\Omega = \omega/(D\lambda_n)$

for sine wave, and

$$\begin{aligned}\Gamma_n =&\frac{G^2e^{-D\lambda_n\Delta}}{2(1+\Omega^2)^2}\Big(1 + e^{-D\lambda_n\delta}(\Omega\sin\delta\omega - \cos\delta\omega)\Big)\cdot\Big(1 - e^{D\lambda_n\delta}(\Omega\sin\delta\omega +\\ &\cos\delta\omega)\Big) + \frac{G^2}{4(1+\Omega^2)^2}\Big(2(\Omega^2 - 1) + (1+\Omega^2)\big(2D\lambda_n\delta - 1 - \cos 2\delta\omega -\\ &\frac{1}{\Omega}\sin 2\delta\omega\big) - 2e^{-D\lambda_n\delta}\big(- 2\cos\delta\omega + 2\Omega\sin\delta\omega\big)\Big)\end{aligned} \tag{A.16}$$

for cosine wave. If we set $N = 1, \ \theta = 0$ and $1/(2\nu) = \delta$ in equations A.12 and A.14, we obtain the results for the SDE sequence in equation A.5. If we set $\delta\omega = 2\pi N, \ N = 1, 2, ...$ in equations A.15 and A.16 and additionally $\phi = 0$ in equations A.12 and A.13 we recover the expression in equation A.6 published in [87].

A.4 GPD approximations for DDE sequences

The section presents the analytical expressions we derive to calculate the restricted diffusion signal parallel and perpendicular to the cylinder axis for DDE sequences. The following expressions assume that both gradient pulses have the same gradient amplitude (G), duration (δ) and diffusion time (Δ). In order to express the signal as a function of the angle between the two gradient pulses ψ, we write the dot product between the perpendicular components of the gradient in equation 3 as $\mathbf{G}_{1\perp} \cdot \mathbf{G}_{2\perp} = G^2 \cos\psi - G_{1\|}G_{2\|}$. We consider parallel orientation ($\psi = 0$) when first gradients of each pair have the same orientation.

$$\begin{aligned}\Gamma_{cyl,n} =&(G_{1\perp}^2 + G_{2\perp}^2)\{\lambda_{cyl,n}D\delta - 1 + e^{-\lambda_{cyl,n}D\delta} + \\ &e^{-\lambda_{cyl,n}D\Delta}(1 - \cosh(\lambda_{cyl,n}D\delta))\} + \\ &(G^2\cos\psi - G_{1\|}G_{2\|})\{e^{-\lambda_{cyl,n}D\tau_m}(1 - \cosh(\lambda_{cyl,n}D\delta))\} \cdot \quad (1 - e^{-\lambda_{cyl,n}D\Delta})^2\end{aligned} \tag{A.17}$$

$$\begin{aligned}\Gamma_{plane,n} =&(G_{1\|}^2 + G_{2\|}^2)\{\lambda_{plane,n}D\delta - 1 + e^{-\lambda_{plane,n}D\delta} + \\ &e^{-\lambda_{plane,n}D\Delta}(1 - \cosh(\lambda_{plane,n}D\delta))\} + \\ &G_{1\|}G_{2\|}\{e^{-\lambda_{plane,n}D\tau_m}(1 - \cosh(\lambda_{plane,n}D\delta))\} \cdot \quad (1 - e^{-\lambda_{plane,n}D\Delta})^2\end{aligned} \tag{A.18}$$

where $G_{1\perp}$ and $G_{2\perp}$ are the components of the two gradient pulses perpendicular to the cylinder axis and $G_{1\|}$ and $G_{2\|}$ are the parallel components, respectively.

Bibliography

[1] J. I. Epstein, W. C. Allsbrook, M. B. Amin, L. L. Egevad, and the ISUP Grading Committee. The 2005 international society of urological pathology (ISUP) consensus conference on gleason grading of prostatic carcinoma. *American Journal of Surgical Pathology*, 29:1228–1242, 2005.

[2] E. Panagiotaki, S. Walker-Samuel, B. Siow, S. P. Johnson, V. Rajkumar, R. B. Pedley, M. F. Lythgoe, and D. C. Alexander. Noninvasive quantification of solid tumor microstructure using VERDICT MRI. *Cancer Research*, 74:1902–1912, 2014.

[3] N. S. White, C. McDonald, N. Farid, J. Kuperman, D. Karow, N. M. Schenker-Ahmed, H. Bartsch, R. Rakow-Penner, D. Holland, A. Shabaik, A. Bjø rnerud, T. Hope, J. Hattangadi-Gluth, M. Liss, J. K. Parsons, C. C. Chen, S. Raman, D. Margolis, R. E. Reiter, L. Marks, S. Kesari, A. J. Mundt, C. J. Kane, B. S. Carter, W. G. Bradley, and A. M. Dale. Diffusion-weighted imaging in cancer: physical foundations and applications of restriction spectrum imaging. *Cancer research*, 74:4638–52, 2014.

[4] M. A. Liss, N. S. White, J. K. Parsons, N. M. Schenker-Ahmed, R. Rakow-Penner, J. M. Kuperman, H. Bartsch, H. W. Choi, R. F. Mattrey, W. G. Bradley, A. Shabaik, J. Huang, D. J. Margolis, S. S. Raman, L. S. Marks, C. J. Kane, R. E. Reiter, A. M. Dale, and D. S. Karow. MRI-Derived Restriction Spectrum Imaging Cellularity Index is Associated with High Grade Prostate Cancer on Radical Prostatectomy Specimens. *Frontiers in oncology*, 5:30, 2015.

[5] Y. Assaf, T. Blumenfeld-Katzir, Y. Yovel, and P. J. Basser. AxCaliber: a method for measuring axon diameter distribution from diffusion MRI. *Magnetic Resonance in Medicine*, 59:1347–1354, 2008.

[6] D. Barazany, P. J. Basser, and Y. Assaf. In-vivo measurement of the axon diameter distribution in the corpus callosum of a rat brain. *Brain*, 132:1210–1220, 2009.

[7] H. H. Ong and F. W. Wehrli. Quantifying axon diameter and intra-cellular volume fraction in excised mouse spinal cord with q-space imaging. *NeuroImage*, 51:1360–1366, 2010.

[8] T. B. Dyrby, L. V. Søgaard, M. G. Hall, M. Ptito, and D. C. Alexander. Contrast and stability of the axon diameter index from microstructure imaging with diffusion MRI. *Magnetic Resonance in Medicine*, 70:711–721, 2013.

[9] D. C. Alexander, P. L. Hubbard, M. G. Hall, E. A. Moore, M. Ptito, G. J. M. Parker, and T. B. Dyrby. Orientationally invariant indices of axon diameter and density from diffusion MRI. *NeuroImage*, 52:1374–1389, 2010.

[10] S. De Santis, D. K. Jones, and A. Roebroek. Including diffusion time dependence in the extra-axonal space improves in vivo estimates of axonal diameter and density in human white matter. *NeuroImage*, 130:91–103, 2016.

[11] H. Zhang, P. L. Hubbard, G. J. M. Parker, and D. C. Alexander. Axon diameter mapping in the presence of orientation dispersion with diffusion MRI. *NeuroImage*, 56:1301–1315, 2011.

[12] H. Zhang, T. Schneider, C. A. M. Wheeler-Kingshott, and D. C. Alexander. NODDI: Practical in vivo neurite orientation dispersion and density imaging of the human brain. *NeuroImage*, 61:1000–1016, 2012.

[13] M. Nilsson, J. Lätt, F. Ståhlberg, D. van Westen, and H. Hagslätt. The importance of axonal undulation in diffusion MR measurements: a Monte Carlo simulation study. *NMR in Biomedicine*, 25:795–805, 2012.

[14] M. Kleinnijenhuis, V. Zerbi, B. Küsters, C. H. Slump, M. Barth, and A. van Cappellen van Walsum. Layer-specific diffusion weighted imaging in human primary visual cortex in vitro. *Cortex*, 25:2569–82, 2013.

[15] D. S. Novikov, J. H. Jensen, J. A. Helpern, and E. Fieremans. Revealing mesoscopic structural universality with diffusion. *Proceedings of the National Academy of Sciences*, 11:5088–5093, 2014.

[16] E. O. Stejskal and T. E. Tanner. Spin diffusion measurements: spin echoes in the presence of a time-dependent field gradient. *Journal of Chemical Physics*, 42:288–292, 1965.

[17] Y. Liu, S. M. Sadowski, A. B. Weisbrod, E. Kebebew, R. M. Summers, and J. Yao. Patient specific tumor growth prediction using multimodal images. *Medical image Analysis*, 18:555–566, 2014.

[18] C. A. Cuenod and D. Balvay. Perfusion and vascular permeability: Basic concepts and measurement in DCE-CT and DCE-MRI. *Diagnostic and Interventional Imaging*, 94:1187–1204, 2013.

[19] R. M. Kessler, J. C. Goble, J. H. Bird, M. E. Girton, J. L. Doppman, S. I. Rapoport, and J. A Barranger. Measurement of blood-brain barrier permeability with positron emission tomography and [^{6}8Ga]edta. *Journal of Cerebral Blood Flow and Metabolism*, 4:323–328, 1984.

[20] M. A. Mintun, D. R. Dennis, M. J. Welch, C. J. Mathias, and D. P. Schuster. Measurements of pulmonary vascular permeability with PET and gallium-68 transferrin. *Journal of Nuclear Medicine*, 28:1704–16, 1987.

[21] H. B. W. Larsson, E. Courivaud, F.and Rostrup, and A. E. Hansen. Measurement of brain perfusion, blood volume, and blood-brain barrier permeability, using dynamic contrast-enhanced T1-weighted MRI at 3 tesla. *Magnetic Resonance in Medicine*, 62:1270–1281, 2009.

[22] M. Ugander, A. J. Oki, L. Y. Hsu, P. Kellman, A. Greiser, A. H. Aletras, C. T. Sibley, M. Y. Chen, W. P. Bandettini, and A. E. Arai. Extracellular volume imaging by magnetic resonance imaging provides insights into overt and subclinical myocardial pathology. *European Heart Journal*, 2012.

[23] G. J. Stanisz, A. Szafer, G. A. Wright, and M. Henkelman. An analytical model of restricted diffusion in bovine optic nerve. *Magnetic Resonance in Medicine*, 37:103–111, 1997.

[24] H. Watabe, Y Ikoma, Y. Kimura, M Naganawa, and M Shidahara. Pet kinetic analysisâĂŤcompartmental model. *Annals of Nuclear Medicine*, 20:583–588, 2006.

[25] D. Richards, T. Clark, and C. Clarke. *The Human Brain and its disorders*. Oxford University Press, 2007.

[26] Science photo library. http://www.sciencephoto.com, [Accessed on 16.08.2015].

[27] BartsMS Blog. http://multiple-sclerosis-research.blogspot.com/2015/01/education-whats-mri.html, [Accessed on 16.08.2015].

[28] The brain bank. http://thebrainbank.org.uk/wp-content/uploads/2012/08/neuron.jpg, [Accessed on 16.08.2015].

[29] E. M. Marcus, S. Jacobson, and T. D. Sabin. *Cerebral Cortex: Cytoarchitecture, Physiology, and Overview of Functional Localization*. Oxford University Press, 2014.

[30] K. Brodmann. *Vergleichende Lokalisationslehre der Grosshirnrinde*. Verlag von Johann Ambrosius Barth, 1909.

[31] B. Fischl and A. M. Dale. Measuring the thickness of the human cerebral cortex from magnetic resonance images. *Proceedings of the National Academy of Sciences*, 97:11050–55, 2000.

[32] J. L. Golberg. How does an axon grow? *Genes and development*, 17:941–958, 2003.

[33] C. Filley. *White Matter Structure and Function*. Oxford University Press, 2013.

[34] S. G. Waxman, J. D. Kocsis, and P. K. Stys. *The axon. Structure, Function and Pathophysiology*. Oxford University Press, New York, 1995.

[35] F. Aboitiz, A. B. Scheibel, R. S. Fisher, and E. Zaidel. Fiber composition of the human corpus callosum. *Brain Research*, 598:143–153, 1992.

[36] J. Guy, A. E. Ellis, K. Kelley, and M. G. Hope. Spectra of G ratio, myelin sheath thickness, and axon and fiber diameter in the guinea pig optic nerve. *The Journal of Comparative Neurology*, 287:446–454, 1989.

[37] N. Stikov, J. S. W. Campbell, T. Stroh, M. Lavelée, S. Frey, J. Novek, S. Nuara, M. K. Ho, B. J. Bedell, R. F. Dougherty, I. R. Leppert, M. Boudreau, S. Narayanan, T. Duval, J. Cohen-Adad, P. A. Picard, A. Gasecka, Côté, and G. B. Pike. Quantitative analysis of the myelin g-ratio from electron microscopy images of the macaque corpus callosum. *Data Brief*, 4:368 – 373, 2015.

[38] S. Tomasi, R. Caminiti, and Innocenti G. M. Areal differences in diameter and length of corticofugal projections. *Cerebral Cortex*, 22:1463–72, 2012.

[39] C. Filley. *Neurobiology of White Matter Disorders*. Oxford University Press, 2013.

[40] S. Ramon y Cajal. *Textura del sistema nervioso del hombre y los vertebrados*. 1890-1904.

[41] C. Kobberta, R. Appsb, I. Bechmannc, J. L. Lanciegod, J. Meye, and S. Thanosa. Current concepts in neuroanatomical tracing. *Progress in Neurobiology*, 62:327–351, 2000.

[42] K. A. Walhovd, H. Johansen-Berg, and R.T. Karadottir. Unraveling the secrets of white matter - Bridging the gap between cellular, animal and human imaging studies. *Neuroscience*, 276:2–13, 2014.

[43] T. M. Shepherd, J. Flint, P. E. Thelwall, G. J. Stanisz, T. H. Mareci, A. T. Yachnis, and S. J. Blackband. Postmortem interval alters the water relaxation and diffusion properties of rat nervous tissue âĂŞ Implications for MRI studies of human autopsy samples. *NeuroImage*, 44:820–826, 2009.

[44] D. A. Mouritzen. Shrinkage of the brain during histological procedures with fixation in formaldehyde solutions of different concentrations. *Journal fur Hirnforschung*, 20:115–9, 1979.

[45] E. Seeram. *Computed Tomography, Physical Principles, Clinical Applications and Quality Control*. Elsevier, 2005.

[46] G. B Saha. *Basics of PET Imaging*. Springer, 2010.

[47] D. S. Williams, J. A. Detre, J. S. Leigh, and A. P. Koretsky. Magnetic resonance imaging of perfusion using spin inversion of arterial water. *Proceedings of the National Academy of Science*, 89:212–16, 1992.

[48] R. B. Buxton, L. R. Frank, E. C. Wong, B. Siewert, S. Warach, and R. R. Edelman. A general kinetic model for quantitative perhsion imaging with arterial spin labeling. *Magnetic Resonance in Medicine*, 40:383–396, 1993.

[49] S. Ogawa, T. M. Lee, A. R. Kay, and D. W. Tank. Brain magnetic resonance imaging with contrast dependent on blood oxygenation. *Proceedings of the National Academy of Sciences*, 87:9868–9872, 1990.

[50] P. J. Basser, J. Matiello, and D. Le Bihan. MR diffusion tensor spectroscopy and imaging. *Biophysical Journal*, 66:259–267, 1994.

[51] M. Nilsson, D. Westen, F. Stahlberg, P. C. Sundgren, and J. Lätt. The role of tissue microstructure and water exchange in biophysical modelling of diffusion in white matter. *MAGMA Magnetic Resonance Materials in Physics, Biology and Medicine*, 2013.

[52] F. O. Stephens and R Aigner, K. *Basics of Oncology*. Springer, 2009.

[53] A. Fritz, C. Percy, A. Jack, K. Shanmugaratnam, L. Sobin, D. M. Parkin, and S. Whelan, editors. *International Classification o diseases for Oncology*. World Health Organization, 3rd edition, 2013.

[54] D. Gleason and G. Mellinger. Prediction of prognosis for prostatic adenocarcinoma by combined histological grading and clinical staging. *Journal of Urology*, 111:58–64, 1972.

[55] C. W. Elston and I. O. Ellis. Pathological prognosis factors in breast cancer. *HistoPathology*, 19:403–410, 1991.

[56] Cancer research uk. http://www.cancerresearchuk.org, [Accessed on 10.08.2015].

[57] University of Utah, Health Science Library. http://library.med.utah.edu/WebPath/HISTHTML/STAINS/STAINS.html, [Accessed on 10.08.2015].

[58] G. W. Lenz, E. M. Haacke, and R. D White. Retrospective cardiac gating: A review of technical aspects and future directions. *Magnetic Resonance in Medicine*, 7:445–455, 1989.

[59] J. G Pipe. Motion correction with PROPELLER MRI: Application to head motion and free-breathing cardiac imaging. *Magnetic Resonance in Medicine*, 52:963–969, 1999.

[60] S. Walker-Samuel, R. Ramasawmy, F. Torrealdea, M. Rega, V. Rajkumar, P. S. Johnson, S. Richardson, M. GonÃğalves, H. G. Parkes, E. Arstad, D. L. Thomas, B. R. Pedley, M. F Lythgoe, and X. Golay. In vivo imaging of glucose uptake and metabolism in tumors. *Nature Medicine*, 19:1067–72, 2013.

[61] P. Kozlowski, S. D. Chang, E. C. Jones, K. W. Berean, H. Chen, and S. L. Goldenberg. Combined diffusion-weighted and dynamic contrast-enhanced mri for prostate cancer diagnosis–correlation with biopsy and histopathology. *Journal of Magnetic Resonance Imaging*, 24:108–13, 2006.

[62] M. Merz, L. Seyler, M. Bretschi, W. Semmler, and T. Bauerle. Diffusion-weighted imaging and dynamic contrast-enhanced mri of experimental breast cancer bone metastases–a correlation study with histology. *European journal of Radiology*, 84:623–30, 2015.

[63] E. Panagiotaki, R. W. Chan, N. Dikaios, H. U. Ahmed, J. O'Callaghan, A. Freeman, D. Atkinson, S. Punwani, D. J. Hawkes, and D. C. Alexander. Microstructural characterization of normal and malignant human prostate tissue with vas-

cular, extracellular, and restricted diffusion for cytometry in tumours magnetic resonance imaging. *Investigative Radiology*, 50:218–27, 2015.

[64] F. Bloch, W. W. Hansen, and M. Packard. Nuclear induction. *Physical Review*, 70:460–474, 1946.

[65] E. M. Purcell, H. C. Torrey, and R. V. Pound. Resonance absorption by nuclear magnetic moments in a solid. *Phsical Review*, 69:26–44, 1946.

[66] L. G. Hanson. Is quantum mechanicsnecessary forunderstanding magneticresonance? *Concepts in Magnetic Resonance Part A*, 32(A):329–340, 2008.

[67] R. B. Buxton. *Introduction to Functional Magnetic Resonance Imaging*. Cambridge University Press, 2009.

[68] University college london, NMR lecture notes. https://www.ucl.ac.uk/nmr/NMRlecturenotes/L53SHwebshortened.pdf, [Accessed on 21.07.2015].

[69] Z Liang and P. Lauterbur. *Principles of Magnetic Resonance Imaging: A Signal Processing Perspective*. Wiley-IEEE Press, 2000.

[70] H. Johansen-Berg and T. E. J. Behrens. *Diffusion MRI: from quantitative measurement to in vivo neuroanatomy*. Academic Press, 2009.

[71] S. T. Skare and R. Bammer. *EPI-Based Pulse Sequences for Diffusion Tensor MRI. Diffusion MRI*. Oxford, 2011.

[72] P.T. Callaghan. *Physics of Diffusion. Diffusion MRI: Theory, Methods and Applications*. Oxford University Press, 2011.

[73] W. S. Price. Pulsed-field gradient nuclear magnetic resonance as a tool for studying translational diffusion: Part 1. basic theory. *Concepts in Magnetic Resonance*, 9:299–336, 1997.

[74] A. Einstein. On the theory of brownian movement. *Annalen der Physik*, 19:371–381, 1906.

[75] N. Shemesh, S. N. Jespersen, D. C. Alexander, Y. Cohen, I. Drobnjak, T. B. Dyrby, J. Finsterbusch, M. A. Koch, T. Kuder, F. Laun, M. Lawrenz, H. Lundell, P. P. Mitra, M. Nilsson, E. Özarslan, D. Topgaard, and C. F. Westin. Conventions and nomenclature for double diffusion encoding (DDE) NMR and MRI. *Magnetic Resonance in Medicine*, 75:82–87, 2016.

[76] H. C. Torrey. Bloch equations with diffusion terms. *Physical Review*, 104:563–565, 1956.

[77] P. T. Callaghan. *Principles of Magnetic Resonance Microscopy*. Oxford, UK: Oxford Science Publications, 1991.

[78] J. Stepisnik. Time-dependent self-diffusion by NMR spin echo. *Physica B*, 183:343–350, 1993.

[79] J. E. Tanner and E. O. Stejskal. Restricted SelfâĂŘDiffusion of Protons in Colloidal Systems by the PulsedâĂŘGradient, SpinâĂŘEcho Method. *Journal of Chemical Physics*, 49, 1968.

[80] C. H. Neuman. Spin echo of spins diffusing in a bounded medium. *Journal of Chemical Physics*, 60:4508–4511, 1974.

[81] P. T. Callaghan. Pulsed-gradient spin-echo NMR for planar, cylindrical and spherical pores under conditions of wall relaxation. *Journal of Magnetic Resonance*, 113:53–59, 1995.

[82] D. Grebenkov. Laplacian eigenfunctions in NMR. i. a numerical tool. *Concepts in Magnetic Resonance Part A*, 32:277–301, 2008.

[83] B. Balinov, B. Jonsson, P. Linse, and O. Soderman. The NMR self-diffusion method applied to restricted diffusion. Simulation of echo attenuation from molecules in spheres and between planes. *Journal of Magnetic Resonance. Series A.*, 104:17–25, 1993.

[84] E. O. Stejskal. Use of spin echoes in a pulsed magnetic-field gradient to study anisotropic, restricted diffusion and flow. *The Journal of Chemical Physics*, 43:3597–3603, 1965.

[85] J Kärger and W. Heink. The propagator representation of molecular transport in microporous crystallites. *Journal of magnetic Resonance*, 51:1–7, 1983.

[86] J. Stepisnik. Validity limits of gaussian approximation in cumulant expansion for diffusion attenuation of spin echo. *Physica B*, 270:110–117, 1999.

[87] J. Xu, M. D. Does, and J. C. Gore. Sensitivity of MR diffusion measurements to variations in intracellular structure: effects of nuclear size. *Magnetic resonance in medicine*, 61:828–833, 2009.

[88] D. C. Alexander and T. Dyrby. Diffusion imaging with stimulated echoes: signal models and experiment design. *ArXiv*, arXiv:1305.7367v2 [physics.med-ph], 2013.

[89] J. D. Clayden, Z. Nagy, M. G. Hall, C. A. Clark, and D. C. Alexander. Active imaging with dual spin-echo diffusion MRI. In *Proc. IPMI, LNCS 5636*, pages 264–275, Williamsburg, 2009. Springer.

[90] A. Ianuş, B. Siow, I. Drobnjak, H. Zhang, and D. C. Alexander. Gaussian phase distribution approximations for oscillating gradient spin-echo diffusion (MRI). *Journal of Magnetic Resonance*, 227:25–34, 2013.

[91] A. Ianuş, I. Drobnjak, and D. C. Alexander. Model-based estimation of microscopic anisotropy in macroscopically isotropic substrates using diffusion MRI. In *Proc. IPMI, LNCS 9123*, pages 699–710. Springer, 2015.

[92] P. T. Callaghan. A simple matrix formalism for spin echo analysis of restricted diffusion under generalized gradient waveforms. *Journal of Magnetic Resonance*, 129:74–84, 1997.

[93] I. Drobnjak, B. Siow, and D. C. Alexander. Optimizing gradient waveforms for microstructure sensitivity in diffusion-weighted MRI. *Journal of Magnetic Resonance*, 206:41–51, 2010.

[94] I. Drobnjak and D. C. Alexander. Optimising time-varying gradient orientation for microstructure sensitivity in diffusion-weighted MR. *Journal of Magnetic Resonance*, 212:344–354, 2011.

[95] S. L. Codd and P. T. Callaghan. Spin echo analysis of restricted diffusion under generalized gradient waveforms: Planar, cylindrical and spherical pores with wall relaxivity. *Journal of Magnetic Resonance*, 137:358–372, 1999.

[96] I. Drobnjak, H. Zhang, M. G. Hall, and D. C. Alexander. The matrix formalism for generalised gradients with time-varying orientation in diffusion NMR. *Journal of Magnetic Resonance*, 210:151–157, 2011.

[97] D. Grebenkov. NMR survey of reflected brownian motion. *Reviews of Modern Physics*, 79:1077–1137, 2007.

[98] D. C. Alexander and G. J. Barker. Optimal imaging parameters for fibre-orientation estimation in diffusion MRI. *NeuroImage*, 27:357–367, 2005.

[99] M. Nilsson, E. Alerstam, R. Wirestam, F. Ståhlberg, S. Brockstedt, and J. Lätt. Evaluating the accuracy and precision of a two-compartment karger model using monte carlo simulations. *Journal of Magnetic Resonance*, 206:59–67, 2010.

[100] M. Nilsson, J. Lätt, E. Nordh, R. Wirestam, F. Ståhlberg, and S. Brockstedt. On the effects of a varied diffusion time in vivo: is the diffusion in white matter restricted? *Magnetic Resonance Imaging*, 27:176–187, 2009.

[101] M. G. Hall and D. C. Alexander. Convergence and parameter choice for Monte-Carlo simulations of diffusion MRI. *IEEE Trans. Medical Imaging*, 28:1354–1364, 2009.

[102] E. Panagiotaki, H. Fonteijn, B. Siow, M. G. Hall, A. Price, M. F. Lythgoe, and D. C. Alexander. Two-compartment models of the diffusion MR signal in brain white matter. In *Proc. MICCAI, LNCS 5761*, pages 329–336, London, 2009. Springer.

[103] G. L. Nedjati-Gilani, T. Schneider, M. G. Hall, C. A. M. Wheeler-Kingshott, and D. C. Alexander. Machine learning based compartment models with permeability for white matter microstructure imaging. In *Proc. MICCAI*, 2014.

[104] J. Stepisnik. Analysis of NMR self-diffusion measurements by a density matrix calculation. *Physica B*, 104:350–364, 1981.

[105] P. T. Callaghan and J. Stepisnik. Frequency domain analysis of spin motion using modulated-gradient NMR. *Journal of Magnetic Resonance A*, 117:118–122, 1995.

[106] M. D. Does, E. C. Parsons, and J. C. Gore. Oscillating gradient measurements of water diffusion in normal and globally ischemic rat brain. *Magnetic Resonance in Medicine*, 49:206–215, 2003.

[107] B. Gross and R. Kosfeld. Anwendung der spin-echo-methode der messungder selbstdiffusion. *Messtechnik*, 77:171–177., 1969.

[108] A. T. Van, S. J. Holdsworth, and R. Bammer. In vivo investigation of restricted diffusion in the human brain with optimized oscillating diffusion gradient encoding. *Magnetic Resonance in Medicine*, 71:83–94, 2014.

[109] H. Li, J. C. Gore, and J. Xu. Fast and robust measurement of microstructural dimensions using temporal diffusion spectroscopy. *Journal of Magnetic Resonance*, 242:4–9, 2014.

[110] D. G. Cory, A. N. Garroway, and J. B. Miller. Applications of spin transport as a probe of local geometry. *Polymer Preprints*, 31:149–150, 1990.

[111] P. P. Mitra. Multiple wave-vector extensions of the NMR pulsed-field-gradient spin-echo diffusion measurement. *Physical Review B*, 51(21):15074–15078., 1995.

[112] E. Özarslan and P. J. Basser. MR diffusion/diffraction phenomenon in multi-pulse-field-gradient experiments. *Journal of Magnetic Resonance*, 188:285–294, 2007.

[113] P. T. Callaghan, S. Godefroy, and B.N. Ryland. Use of the second dimension in PGSE NMR studies of porous media. *Magnetic Resonance Imaging*, 21:243–248, 2003.

[114] P. T. Callaghan and I. Furo. Diffusion-diffusion correlation and exchange as a signature for local order and dynamics. *Journal of Chemical Physics*, 120:4032–4037, 2004.

[115] Y. Cheng and D. Cory. Multiple scattering by NMR. *J. Am. Chem. Soc*, 121:7935–7396, 1999.

[116] M. A. Koch and J. Finsterbusch. Compartment size estimation with double wave vector diffusion-weighted imaging. *Magnetic Resonance in Medicine*, 60:90–101, 2008.

[117] E. Özarslan. Compartment shape anisotropy (CSA) revealed by double pulsed field gradient MR. *Journal of Magnetic Resonance*, 199:56–67, 2009.

[118] N. Shemesh and Y. Cohen. Microscopic and compartment shape anisotropies in grey and white matter revealed by angular bipolar double-PFG. *Magnetic Resonance in Medicine*, 65:1216–1227, 2011.

[119] M. Lawrenz, M. A. Koch, and J. Finsterbusch. A tensor model and measures of microscopic anisotropy for double-wave-vector diffusion-weighting experiments with long mixing times. *Journal of Magnetic Resonance*, 202:43–56, 2010.

[120] M. Lawrenz and J. Finsterbusch. Double-wave-vector diffusion-weighted imaging reveals microscopic diffusion anisotropy in the living human brain. *Magnetic Resonance in Medicine*, 69:1072–1082, 2013.

[121] S. N. Jespersen, H. Lundell, C. K. Sonderby, and T. B. Dyrby. Orientationally invariant metrics of apparent compartment eccentricity from double pulsed field gradient diffusion experiments. *NMR in Biomedicine*, 26:1647–1662, 2013.

[122] S. N. Jespersen, C. D. Kroenke, L. Østergaard, J. J. H. Ackerman, and D. A. Yablonskiy. Modeling dendrite density from magnetic resonance diffusion measurements. *NeuroImage*, 34:1473–1486, 2007.

[123] Bashar Issa. In vivo measurement of the apparent diffusion coefficient in normal and malignant prostatic tissues using echo-planar imaging. *Journal of Magnetic Resonance Imaging*, 16(2):196–200, 2002.

[124] F. Yamasaki, K. Kurisu, K. Satoh, Arita. K., K. Sugiyama, M. Ohtaki, J. Takaba, A. Tominaga, R. Hanaya, H. Yoshioka, S. Hama, Y. Ito, Y. Kajiwara, K. Yahara,

T. Saito, and MA. Thohar. Apparent diffusion coefficient of human brain tumors at MR imaging. *Radiology*, 235:985–91, 2005.

[125] P. J. Basser and E. Özarslan. *Anisotropic diffusion: From the Apparent Diffusion Coefficient to the apparent Diffusion Tensor. Diffusion MRI: Theory, Methods and Applications*. Oxford University Press, 2011.

[126] D. K. Jones and P. J. Basser. Squashing peanuts and smashing pumpkins: How noise distorts diffusion-weighted MR data. *Magnetic Resonance in Medicine*, 52:979–993, 2004.

[127] S. Mori and J.D. Tournier. *Introduction to Diffusion Tensor Imaging and Higher Order Models*. Elsevier, 2014.

[128] P. J. Basser. Inferring microstructural features and the physiological state of tissues from diffusion-weighted images. *NMR in Biomedicine*, 8:333–44, 1995.

[129] D. S. Tuch, T. G. Reese, M. R. Wiegell, N Makris, J. W. Belliveau, and V. J. Wedeen. High angular resolution diffusion imaging reveals intravoxel matter fiber heterogeneity. *Magnetic Resonance in Medicine*, 48:577–582, 2002.

[130] V. J. Wedeen, T. G. Reese, D. S. Tuch, J.-G. Dou, R. M. Weiskoff, and D. Chessler. Mapping fiber orientation spectra in cerebral white matter with Fourier-transform diffusion MRI. In *Proc. 7th Annual Meeting of the ISMRM*, page 321, Philadelphia, 1999. Berkeley, USA: ISMRM.

[131] V. J. Wedeen, P. Hagmann, W. Y. I. Tseng, T. G. Reese, and R. M. Weisskoff. Mapping complex tissue architecture with diffusion spectrum magnetic resonance imaging. *Magnetic Resonance in Medicine*, 54:1377–1386, 2005.

[132] D. S. Tuch, T. G. Reese, M. R. Wiegell, and V. J. Wedeen. Diffusion MRI of complex neural architecture. *Neuron*, 40:885–895, 2003.

[133] D. S. Tuch. Q-ball imaging. *Magnetic resonance in medicine*, 52:1358–1372, 2004.

[134] A. Anderson and Z. Ding. Sub-voxel measurement of fiber orientation using high angular resolution diffusion tensor imaging. In *Proc. 10th Annual Meeting of the ISMRM*, page 440, Honolulu, 2002. Berkeley, USA: ISMRM.

[135] J-D. Tournier, F. Calamante, D. G. Gadian, and A. Connelly. Direct estimation of the fiber orientation density function from diffusion-weighted MRI data using spherical deconvolution. *NeuroImage*, 23:1176–1185, 2004.

[136] S. De Santis, A. Gabrielli, M. Palombo, B. Maravigli, and S. Capuani. Non-gaussian diffusion imaging: a brief practical review. *Magnetic Resonance Imaging*, 29:1410–1416, 2011.

[137] J. H. Jensen, J. A. Helpern, A. Ramani, H Lu, and K. Kaczinsky. Diffusional kurtosis imaging: The quantification of non-Gaussian water diffusion by means of magnetic resonance imaging. *Magnetic Resonance in Medicine*, 53:1432–1440, 2005.

[138] J. Veraart, W. Van Hecke, and J. Sijbers. Constrained maximum likelihood estimation of the diffusion kurtosis tensor using a rician noise model. *Magnetic Resonance in Medicine*, 66:678–86, 2011.

[139] C.M. Tax, W.M. Otte, M.A. Viergever, R.M. Dijkhuizen, and A. Leemans. Rekindle: robust extraction of kurtosis indices with linear estimation. *Magnetic Resonance in Medicine*, 73:794–808, 2015.

[140] E. Fiermans, J. H. Jensen, and J. A. Helpern. White matter characterization with diffusional kurtosis imaging. *NeuroImage*, 58:177–88, 2011.

[141] C. A. Clark, M. Hedehus, and M. E. Moseley. In vivo mapping of the fast and slow diffusion tensors in human brain. *Magnetic Resonance in Medicine*, 47:623–8, 2002.

[142] Denis Le Bihan, Eric Breton, Denis Lallemand, ML Aubin, J Vignaud, and M Laval-Jeantet. Separation of diffusion and perfusion in intravoxel incoherent motion mr imaging. *Radiology*, 168(2):497–505, 1988.

[143] D. A. Yablonskiy, G. L. Bretthorst, and J. J. H. Ackerman. Statistical model for diffusion attenuated MR signal. *Magnetic Resonance in Medicine*, 50:664–669, 2003.

[144] K. M. Bennett, K. M. Schmainda, R. T. Bennett, D. B. Rowe, H. Lu, and J. S. Hyde. Characterization of continuously distributed cortical water diffusion rates with a stretched-exponential model. *Magnetic Resonance in Medicine*, 50:727–34, 2003.

[145] M. G. Hall and T. R. Barrick. From diffusion-weighted MRI to anomalous diffusion imaging. *Magnetic resonance in medicine*, 59:447–455, 2008.

[146] J. Karger, H. Pfeifer, and W. Heink. Principles and application of self-diffusion measurements by NMR. *Advances in Magnetic Resonance*, 12:1–89, 1988.

[147] T. E. J. Behrens, M. W. Woolrich, M. Jenkinson, H. Johansen-Berg, R. G. Nunes, S. Clare, P. M. Matthews, J. M. Brady, and S. M. Smith. Characterization and propagation of uncertainty in diffusion-weighted MR imaging. *Magnetic Resonance in Medicine*, 50:1077–1088, 2003.

[148] T. E. J. Behrens, H. Johansen-Berg, S. Jbabdi, M. F. S. Rushworth, and M. W. Woolrich. Probabilistic diffusion tractography with multiple fibre orientations: What can we gain? *NeuroImage*, 34:144–155, 2006.

[149] Y. Assaf and P. J. Basser. Composite hindered and restricted model of diffusion (CHARMED) MR imaging of the human brain. *NeuroImage*, 30:1100–1111, 2005.

[150] E. Panagiotaki, T. Schneider, B. Siow, M. G. Hall, M. F. Lythgoe, and D. C. Alexander. Compartment models of the diffuison MR signal in brain white matter: a taxonomy and comparison. *NeuroImage*, 59:2241–2254, 2012.

[151] D. C. Alexander. A general framework for experiment design in diffusion MRI and its application in measuring direct tissue-microstructure features. *Magnetic Resonance in Medicine*, 60:439–448, 2008.

[152] A. Szafer, J. Zhong, and J. C. Gore. Theoretical model for water diffusion in tissues. *Magnetic Resonance in Medicine*, 33:697–712, 1995.

[153] I. Drobnjak, H. Zhang, A. Ianuş, E. Kaden, and D. C. Alexander. PGSE, OGSE, and sensitivity to axon diameter in diffusion MRI: Insight from a simulation study. *Magnetic Resonance in Medicine*, 75:688–700, 2016.

[154] J. A. McNab, B. L. Edlow, T. Witzel, S. Y. Huang, H. Bhat, K. Heberlein, T. Feiweier, K. Liu, B. Keil, J. Cohen-Adad, M. D. Tisdal, R.D. Folkerth, H. C. Kinney, and L. L. Wald. The human connectome project and beyond: initial applications of 300 mt/m gradients. *NeuroImage*, 80:234–45, 2013.

[155] U. Bürgel, K. Amunts, L. Hoemke, H. Mohlberg, J.M. Gilsbach, and K. Zilles. White matter fiber tracts of the human brain: Three-dimensional mapping at microscopic resolution, topography and intersubject variability. *NeuroImage*, 29:1092–1105, 2006.

[156] G. P. Winston, C. Micallef, M. R. Symms, D. C. Alexander, J. S. Duncan, and H Zhang. Advanced diffusion imaging sequences could aid assessing patients with focal cortical dysplasia and epilepsy. *Epilepsy Research*, 108:336–339, 2014.

[157] I. Timmers, H. Zhang, M. Bastiani, B. M. Jansma, A. Roebroeck, and M. E. Rubio-Gozalbo. White matter microstructure pathology in classic galactosemia revealed by neurite orientation dispersion and density imaging. *Journal of Inherited Metabolic Disease*, pages 1–10, 2014.

[158] N. Kunz, H. Zhang, L. Vasung, O'Brien K. R., Y. Assaf, F. Lazeyras, D. C. Alexander, and P. S. Hüppi. Assessing white matter microstructure of the newborn with multi-shell diffusion MRI and biophysical compartment models. *NeuroImage*, 96:288–299, 2014.

[159] Z. Eaton-Rosen, A. Melbourne, E. Orasanu, M. J. Cardoso, M. Modat, A. Bainbridge, G. S. Kendall, N. J. Robertson, N. Marlow, and S. Ourselin. Longitudinal measurement of the developing grey matter in preterm subjects using multi-modal MRI. *NeuroImage*, 111:580 – 589, 2015.

[160] K. V. Mardia and P. E. Jupp. *Directional Statistics*. Wiley, 2000.

[161] E. Kaden, T. R. Knösche, and A. Anwander. Parametric spherical deconvolution: Inferring anatomical connectivity using diffusion MR imaging. *NeuroImage*, 37:474–488, 2007.

[162] S. N. Sotiropoulos, T. E. J. Behrens, and S. Jbabdi. Ball and rackets: Inferring fiber fanning from diffusion-weighted MRI. *NeuroImage*, 60:1412–1425, 2012.

[163] M. Tariq, T. Schneider, D. C. Alexander, C. A. Wheeler-Kingshott, and H. Zhang. In vivo estimation of dispersion anisotropy of neurites using diffusion MRI. In *Proc. MICCAI*, pages 241–248, Boston, 2014. Springer.

[164] U. Ferizi, T. Schneider, E. Panagiotaki, G. Nedjati-Gilani, H. Zhang, C. A. M. Wheeler-Kingshott, and D. C. Alexander. A ranking of diffusion MRI compartment models with in vivo human brain data. *Magnetic Resonance in Medicine*, 72:1785–92, 2014.

[165] U. Ferizi, T. Schneider, M. Tariq, C. A. Wheeler-Kingshott, H. Zhang, and D. C. Alexander. The importance of being dispersed: A ranking of diffusion mri models for fibre dispersion using in vivo human brain data. In *Proc. MICCAI*, pages 74–81, Nagoya, 2013. Springer.

[166] N. S. White, T. B. Leergaard, H. DÁrceuil, J. G. Bjaalie, and A. M. Dale. Probing tissue microstructure with restriction spectrum imaging: Histological and theoretical validation. *Human Brain Mapping*, 34:327–346, 2013.

[167] A. W. Anderson. Measurement of fiber orientation distributions using high angular resolution diffusion imaging. *Magnetic Resonance in Medicine*, 54:1194–1206, 2005.

[168] J. Pfeuffer, U. Flogel, W. Dreher, and L. Dieter. Restricted diffusion and exchange of intracellular water: theoretical modelling and diffusion time dependence of 1H NMR measurements on perfused glial cells. *NMR in Biomedicine*, 11:19–31, 1998.

[169] O. Dietrich, A. Hubert, and S. Heiland. Imaging cell size and permeability in biological tissue using the diffusion-time dependence of the apparent diffusion coefficient. *Physics in Medicine and Biology*, 59:3081–3096, 2014.

[170] S. Lasič, M. Nilsson, J. Lätt, F. Ståhlberg, and D. Topgaard. Apparent exchange rate mapping with diffusion MRI. *Magnetic Resonance in Medicine*, 66:356–365, 2011.

[171] M. Nilsson, J. Lätt, D. van Westen, S. Brockstedt, S. Lasič, F. Ståhlberg, and D. Topgaard. Non-invasive mapping of water diffusional exchange in the human brain using filter-exchange imaging. *Magnetic Resonance in Medicine*, 69:1573–1581, 2013.

[172] H. Li, X. Jiang, J. Xie, J. O. McIntyre, J. C. Gore, and J. Xu. Time-dependent influence of cell membrane permeability on mr diffusion measurements. *Magnetic Resonance in medicine*, Early View, 2015.

[173] Manisha Aggarwal, Melina V. Jones, Peter A. Calabresi, Susumu Mori, and Jiangyang Zhang. Probing mouse brain microstructure using oscillating gradient diffusion mri. *Magnetic Resonance in Medicine*, 67(1):98–109, 2012.

[174] J. Portnoy, J. J. Flint, S. J. Blackband, and G. J. Stanisz. Oscillating and pulsed gradient diffusion magneticresonance microscopy over an extended b-valuerange: Implications for the characterizationof tissue micr ostructure. *Magnetic Resonance in Medicine*, 69:1131–1145, 2013.

[175] C. A Baron and C. Beaulieu. Oscillating gradient spin-echo (OGSE) Diffusion Tensor Imaging of the human brain. *Magnetic Resonance in Medicine*, 72:726–736, 2014.

[176] J. Xu, M. D. Does, and J. C. Gore. Dependence of temporal diffusion spectra on microstructural properties of biological tissues. *Magnetic resonance imaging*, 29:380–390, 2011.

[177] F. Szczepankiewicz, S. Lasič, D. van Westen, P.C. Sundgren, E. Englund, C. F. Westin, F. Ståhlberg, J. Lätt, D. Topgaard, and M. Nilsson. Quantification of

microscopic diffusion anisotropy disentangles effects of orientation dispersion from microstructure: applications in healthy volunteers and in brain tumors. *NeuroImage*, 104:241–52, 2015.

[178] M. A. Koch and J. Finsterbusch. Numerical simulation of double-wave vector experiments investigating diffusion in randomly oriented ellipsoidal pores. *Magnetic Resonance in Medicine*, 62:247–254, 2009.

[179] N. Shemesh, E. Özarslan, P. J. Basser, and Y. Cohen. Accurate noninvasive measurement of cell size and compartment shape anisotropy in yeast cells using double-pulsed field gradient MR. *NMR in Biomedicine*, 25:236–246, 2012.

[180] S. Lasič, F. Szczepankiewicz, S. Eriksson, M. Nilsson, and D. Topgaard. Microanisotropy imaging: quantification of microscopic diffusion anisotropy and orientational order parameter by diffusion MRI with magic-angle spinning of the q-vector. *Frontiers in Physics*, 2, 2014.

[181] C. F. Westin, F. Szczepankiewicz, O. Pasternak, E. Özarslan, D. Topgaard, H. Knutsson, and M. Nilsson. Measurement tensors in diffusion mri: Generalizing the concept of diffusion encoding. In *Proc. MICCAI*, pages 209–216, Boston, 2014. Springer.

[182] J. P. de Almeida Martins and D. Topgaard. Two-dimensional correlation of isotropic and directional diffusion using NMR. *Physical Review Letters*, 116:087601, 2016.

[183] E. Kaden, F. Kruggel, and D. C. Alexander. Quantitative mapping of the per-axon diffusion coefficients in brain white matter. *Magnetic Resonance in Medicine*, Early View, 2015.

[184] F. Aboitiz, E. Rodriguez, R. Olivares, and E. Zaidel. Age-related changes in fibre composition of the human corpus callosum: sex differences. *NeuroReport*, 7:1761–4, 1996.

[185] K. J. Packer and C. Rees. Pulsed NMR studies of restricted diffusion I. droplet size distributions in emulsions. *Journal of Colloid and Interface Science*, 40:206–218, 1972.

[186] P. T. Callaghan, K. W. Jolley, and R. S. Humphrey. Diffusion of fat and water in cheese as studied by pulsed field gradient nuclear magnetic resonance. *Journal of Colloid and interface Science*, 93(2):521–529, 1983.

[187] B. Balinov, 0. Urdahl, O. Soderman, and J. Sjoblom. Characterization of water-in-crude oil emulsions by the nmr self-diffusion technique. *Colloids and Surfaces A*, 82:173–181, 1994.

[188] K. G. Hollingsworth and M. L. Johns. Measurement of emulsion droplet sizes using pfg nmr and regularization methods. *Journal of Colloid and Interface Science*, 258(2):383–389, 2003.

[189] D. Benjamini, M. E. Komlosh, P. J. Basser, and U. Nevo. Nonparametric pore size distribution using d-PFG: Comparison to s-PFG and migration to MRI. *Journal of Magnetic Resonance*, 246:36–45, 2014.

[190] D. Benjamini and P. J. Basser. Joint radius-length distribution as a measure of anisotropic pore eccentricity: an experimental and analytical framework. *Journal of Chemical Physics*, 141:214202, 2014.

[191] S. Farquharson, J. D. Tournier, F. Calamante, Fabinyi G., M. Schneider-Kolsky, G. D. Jackson, and A. Connelly. White matter fiber tractography: why we need to move beyond DTI. *Journal of Neurosurgery*, 118:1367–77, 2013.

[192] A. M. Auriat, M. R. Borish, N. J. Snow, K. P. Wadden, and L. A. Boyd. Comparing a diffusion tensor and non-tensor approach to white matter fiber tractography in chronic stroke. *NeuroImage: Clinical*, 7:771–781, 2015.

[193] U. Ferizi, T. Schneider, T Witzel, L. L. Wald, H. Zhang, C. A. M. Wheeler-Kingshott, and D. C. Alexander. White matter compartment models for in vivo diffusion mri at 300mt/m. *NeuroImage*, 118:468–83, 2015.

[194] A. J. Sherbondy, M. C. Rowe, and D. C. Alexander. Kakkar, l. and atkinson, d. and chan, r. w. and drobnjak, i. In *Proc. ISMRM*, Milan, 2014.

[195] Y. Assaf, R. Z. Freidlin, G. K. Rohde, and P. J. Basser. New modeling and experimental framework to characterize hindered and restricted water diffusion in brain white matter. *Magnetic Resonance in Medicine*, 52:965–978, 2004.

[196] G. J. Stanisz, E. E. Odrobina, J. Pun, M. Escaravage, S. J. Graham, M. J. Bronskill, and R. M. Henkelman. T1, T2 relaxation and magnetization transfer in tissue at 3T. *Magnetic Resonance in Medicine*, 54:507–512, 2005.

[197] L. M. Burcaw, E. Fieremans, and D. S. Novikov. Mesoscopic structure of neuronal tracts from time-dependent diffusion. *NeuroImage*, 114:18–37, 2015.

[198] M. Jenkinson, P. Bannister, M. Brady, and S. Smith. Improved optimization for the robust and accurate linear registration and motion correction of brain images. *NeuroImage*, 17:825–841, 2002.

[199] M. Holz, S. R. Heil, and A. Sacco. Temperature-dependent self-diffusion coefficients of water and six selected molecular liquids for calibration in accurate 1h nmr pfg measurements. *Physical Chemistry Chemical Physics*, 2:4740–4742, 2000.

[200] E. Özarslan and P. J. Besser. Microscopic anisotropy revealed by NMR double pulsed field gradient experiments with arbitrary timing parameters. *Journal of Chemical Physics*, 128:154511, 2009.

[201] S. N. Jespersen and N. Buhl. The displacement correlation tensor: Microstructure, ensemble anisotropy and curving fibers. *Journal of Magnetic Resonance*, 208:34–43, 2011.

[202] J. C. Fiala and K. M. Harris. *Dendritic Structures*. Oxford University Press, 1999.

[203] G. Vona, A. Sabile, M Louha, V. Sitruk, S. Romana, K. Schutze, F. Capron, D. Franco, M. Pazzagli, M. Vekemans, B. Lacour, C. Brechot, and P. Paterlini-Brechot. Isolation by size of epithelial tumor cells. *American Journal of Pathology*, 156:57–63., 2000.

[204] N. Shemesh, E. Özarslan, P. J. Basser, and Y. Cohen. Detecting diffusion-diffraction patterns in size distribution phantoms using double-pulsed field gradient NMR: Theory and experiments. *Journal of Chemical Physics*, 132:034703, 2010.

[205] N. Shemesh, C-F. Westin, and Y. Cohen. Magnetic resonance imaging by synergistic diffusion-diffraction patterns. *Physical Review Letters*, 108:058103, 2012.

[206] T. A. Kuder and F. B. Laun. NMR-based diffusion pore imaging by double wave vector measurements. *Magnetic Resonance in Medicine*, 70:836–841, 2013.

[207] H. Hering and M. Sheng. Dentritic spines : structure, dynamics and regulation. *Nature Reviews Neuroscience*, 2:880–888, 2001.

[208] A. U. Larkman. Dendritic morphology of pyramidal neurones of the visual cortex of the rat: Branching patterns. *The Journal of Comparative neurology*, 306:307–319, 1991.

[209] Nexelcom Bioscience LLC, ©2003-2015. Analyzing NCI-60 Cancer Cell Lines. Available from: http://www.nexcelom.com/Applications/Cancer-Cells.html, [Accessed on 07.09.2015].

[210] B. Dhital and R. Turner. MRI measurement of three-dimensional morphological features o axons. In *Proc. ISMRM*, page 2769, Toronto, 2015. ISMRM.

[211] J. Sjölund, F. Szczepankiewicz, M. Nilsson, D. Topgaard, C. F. Westin, and H. Knutsson. Constrained optimization of gradient waveforms for generalized diffusion encoding. *Journal of Magnetic Resonance*, 261:157–68, 2015.

[212] N. Shemesh, A. Ianuş, D. C. Alexander, and I. Drobnjak. Double oscillating diffusion encoding (dode) augments microscopic anisotropy contrast. In *Proc. ISMRM*, page 952, Toronto, Canada, 2015.

[213] A. Ianuş, I. Drobnjak, N. Shemesh, and D. C. Alexander. Metrics of microscopic anisotropy: a comparison study. In *International Conference on Magnetic Resonance Microscopy*, 2015.

[214] P. P. Mitra and B. I. Halperin. Effects of finite gradient-pulse widths in pulsed-field-gradient diffusion measurements. *Journal of Magnetic Resonance*, 113:94–101, 1995.

[215] N. Shemesh, E. Özarslan, P. J. Basser, and Y. Cohen. Measuring small compartmental dimensions with low-q angular double-PGSE NMR: The effect of experimental parameters on signal decay. *Magnetic Resonance in Medicine*, 198:15–23, 2009.

[216] T Weber, C.H. Ziener, T. Kampf, V. Herold, V. R. Bauer, and P. M. Jakob. Measurement of apparent cell radii using a multiple wave vector diffusion experiment. *Magnetic Resonance in Medicine*, 61:1001–1006, 2009.

[217] N. Shemesh, E. Özarslan, T. Adiri, P. J. Basser, and Y. Cohen. Noninvasive bipolar double-pulsed-field-gradient NMR reveals signatures for pore size and shape in polydisperse, randomly oriented, inhomogeneous porous media. *Journal of Chemical Physics*, 133:044705, 2010.

[218] D. C. Van Essen, K. Ugurbil, E. Auerbach, D. Barch, T. E. J. Behrens, R. Bucholz, A. Chang, L. Chen, M. Corbetta, S. W. Curtiss, S. Della Penna, D. Feinberg, M. F. Glasser, N. Harel, A. C. Heath, L. Larson-Pror, D. Marcus, G. Michalareas, S. Moeller, R. Oostenveld, S. E. Petersen, F. Prior, B. L. Schlagger, S. M. Smith, A. Z. Snyder, J. Xu, E. Yacoub, and WU-Minn HCP Consortium. The human connectome project: A data acquisition perspective. *NeuroImage*, 62:2222–2231, 2012.

[219] M. A. Koch and J. Finsterbusch. Towards compartment size estimation in vivo based on double wave vector diffusion weighting. *NMR in Biomedicine*, 24:1422–32, 2011.

[220] M. Lawrenz and J. Finsterbusch. Mapping measures of microscopic diffusion anisotropy in human brain white matter in vivo with double-wave-vector diffusion-weighted imaging. *Magnetic Resonance in Medicine*, Earl view, 2014.

[221] A. V. Avram, E. Özarslan, J. E. Sarlls, and P. J. Basser. In vivo detection of microscopic anisotropy using quadruple pulsed-field gradient (qPFG) diffusion MRI on a clinical scanner. *NeuroImage*, 64:229–239, 2014.

[222] S. N. Jespersen, C. R. Bjarkam, J. R. Nyengaard, M. M. Chakravarty, B. Hansen, T. Vosegaard, L. Östergaard, D. Yablonskiy, Nielsen. N. C., and P. Vestergaard-Poulsen. Neurite density from magnetic resonance diffusion measurements at ultrahigh field: Comparison with light microscopy and electron microscopy. *NeuroImage*, 49:205 – 216, 2010.

[223] S. Eriksson, S. Lasič, M. Nilsson, C. F. Westin, and D. Topgaard. NMR diffusion-encoding with axial symmetry and variable anisotropy: Distinguishing between prolate and oblate microscopic diffusion tensors with unknown orientation distribution. *Journal of Chemical Physics*, 142, 2015.

[224] D. Topgaard. Isotropic diffusion weighting using a triple-stimulated echo pulse sequence with bipolar gradient pulse pairs. *Microporous and Mesoporous Materials*, 205:48–51, 2015.

[225] J. Piven, J. Bailey, B. J. Ranson, and S. Arndt. An MRI study of the corpus callosum in autism. *Am. J. Psychiatry*, 154:1051, 1997.

[226] J. W. Bohland. Toward a multimodal, multiscale understanding of white matter abnormalities in autism spectrum disorder. *Biological Psychiatry*, 79:47–48, 2016.

[227] S. Cluskey and D. B. Ramsden. Mechanisms of neurodegeneration in amyotrophic lateral sclerosis. *Journal of Clinical Pathology: Molecular Pathology*, 54:386–392, 2001.

[228] L. Marner, J. R. Nyengaard, J. Tang, and B. Pakkenberg. Marked loss of myelinated nerve fibers in the human brain with age. *Journal of Comparative Neurology*, 462:144–152, 2003.

[229] J. M. Ritchie. On the relation between fibre diameter and conduction velocity in myelinated nerve fibres. *Proceedings of the Royal Society of London B*, 217:29–35, 1982.

[230] J. Xu, H. Li, K. D. Harkins, X. Jiang, J. Xie, H. Kang, M. D. Does, and J. C. Gore. Mapping mean axon diameter and axonal volume fraction by mri using temporal diffusion spectroscopy. *NeuroImage*, 103:10–19, 2014.

[231] B. Siow, I. Drobnjak, A. Ianuş, I. N. Christie, M. F. Lythgoe, and D. C. Alexander. Axon radius estimation with oscillating gradient spin echo (OGSE) diffusion MRI. *Diffusion Fundamentals*, 18:1–6, 2013.

[232] S. Lasič, S. Oredsson, S. C. Partridge, L. H. Saal, D. Topgaard, M. Nilsson, and K. Bryskhe. Apparent exchange rate for breast cancer characterization. *NMR in Biomedicine*, 29:631–639, 2016.

[233] D. J. McHugh, F. Ahou, P. L. Hubbard Cristinacce, J. H. Naish, and G. J. Parker. Ground truth for diffusion MRI in cancer: A model-based investigation of a novel tissue-mimetic material. In *Information Processing in Medical Imaging*, Isle of Skye, 2015.

[234] P. L. Hubbard, F. L. Zhou, S. J. Eichhorn, and G. J. Parker. Biomimetic phantom for the validation of diffusion magnetic resonance imaging. *Magnetic Resonance in Medicine*, Early view, 2014.